Technische Universität München

TUM School of Life Sciences

Studies of gas permeation mechanisms in thin composite coating layers

Stefan Schiessl

Vollständiger Abdruck der von der TUM School of Life Sciences der Technischen Universität München zur Erlangung eines

Doktors der Naturwissenschaften (Dr. rer. nat.)

genehmigten Dissertation.

Vorsitz: Prof. Dr.-Ing. Heiko Briesen

Prüfende der Dissertation:

1. Hon.-Prof. Dr.-Ing. habil. Peter Eisner
2. Prof. Dr. Stephen Schrettl

Die Dissertation wurde am 05.05.2025 bei der Technischen Universität München eingereicht und durch die TUM School of Life Sciences am 02.08.2025 angenommen.

Danksagung

Jede wissenschaftlich arbeitende Person wird mir beipflichten, dass hinter einer Arbeit wie dieser immer mehrere Personen stecken ohne deren Hilfe und Unterstützung eine Promotion nicht möglich gewesen wäre. Auch wenn das Nennen hier nicht aufwiegen kann in welcher Weise ihr mich unterstützt habt, so möchte ich mich dennoch mit ein paar Zeilen ehrlich und aufrichtig bei euch bedanken.

Bei **Prof. Dr. Peter Eisner**. Ich möchte mich in aller Form bei dir dafür bedanken, dass du der Betreuung einer Doktorarbeit, die thematisch etwas weiter entfernt von deinem Kernthema - den Proteinen – ist, zugestimmt hast. Dein Blick von außen hat viel Klarheit und Struktur in so manche Diskussionen gebracht. Ebenso möchte ich für den stets schnellen Beitrag zu allen Publikationen bedanken, dies ist bei Weitem nicht selbstverständlich.

Bei **Prof. Dr. Stephen Schrettl**. Ich möchte bei Ihnen für das Interesse an meiner Arbeit bedanken und dafür das Sie sich bereiterklärt haben die Prüfung zu übernehmen.

Bei **Dr. Esra Kücükpinar**. Der größte Dank gilt natürlich der Betreuerin der Doktorarbeit. Ich möchte mich bei dir für dein Vertrauen in mich von dem Tag der Einstellung bis hin zu dem Tag der Abgabe der Doktorarbeit bedanken. Jede einzelne Diskussionsminute, jedes Gespräch, jedes Projekt und jede Versuchsplanung haben diese Arbeit zu dem gemacht, was sie ist.

Bei **Dr. Cornelia Stramm**. Ich möchte mich bei dir als Abteilungsleiterin dafür bedanken, dass du es ermöglicht hat eine Doktorandenstelle zu schaffen. Ebenso ist zu bemerken, dass du zu jeder Zeit ein offenes Ohr für jegliche Probleme hattest und mit deiner beruhigenden Art auch meinen Puls in so mancher Situation gesenkt hast.

Bei **Prof. Dr. Horst-Christian Langowski**. Unserem ehemaligen Institutsleiter Prof. Langowski möchte ich dafür danken, dass er als Experte für Permeation zu jeder Zeit ein offenes Ohr für Diskussionen hatte und bei sämtlichen Publikationen ohne Zögern mitgewirkt und mitgeholfen hat.

Bei meinen Mitautoren, Stéphane Cross, Oliver Miesbauer, Noémie Rivollier, und Rene Schwidessen möchte ich mich für ihren Beitrag zu den drei wissenschaftlichen Veröffentlichungen bedanken, welche durch die eingebrachte Fackexpertise enorm an Qualität gewonnen haben.

Bei meinen Studenten Deeksha Arya Margapuram, Selina Haller, Svenja Zösmair, Sandra Diener, Anna Tichy, Michael Sommer, Bernhard Baumann und Anna Kimadze möchte ich mich für ihren Einsatz und Engagement mit vielen Stunden im Labor und Technikum bedanken, dies hat wesentlich zur Arbeit bei-

getragen.
Bei der ganzen Abteilung Materialentwicklung, angefangen bei Christiane, über das Laborteam unter Leitung von Zuzi und Marius und das Team im Technikum unter der Leitung von Norbert, bis hin zu allen Wissenschaftlern. Ich möchte mich ganz herzlich für die freundliche Aufnahme bedanken, dafür das ihr mich zu jeder Zeit mit Rat und Tat unterstützt habt und dafür dass die familiäre Atmosphäre in der ME so manche persönlich Krise abdämpfen kann.
Abseits des Instituts möchte ich **meinen Eltern** dafür danken, dass Sie stets ein offenes Ohr für mich hatten und mir bedingungslos vertrauen. Diese familiäre Sicherheit, ist das Fundament meiner Einstellung zur Arbeit.

Contents

Zusammenfassung

Flexible Polymerfolien sind aufgrund ihres geringen Gewichts, ihrer Vielseitigkeit und ihres wirksamen Schutzes die weltweit am häufigsten verwendeten Verpackungsmaterialien. Im Vergleich zu anderen Materialien wie Glas, Metall oder Papier haben sie in vielen Anwendungen Vorteile in einem oder mehreren Punkten. Jedoch hat ihr öffentliches Image aufgrund von gesteigertem Umweltbewusstsein, insbesondere durch die Medienberichterstattung über Plastikverschmutzung, gelitten. Als Reaktion auf diese Bedenken und um die Nachhaltigkeit von Verpackungen zu verbessern, hat das Europäische Parlament im Dezember 2024 die *Packaging and Packaging Waste Regulation* verabschiedet. Eine zentrale Bestimmung hierin sieht vor, dass nicht recycelbare flexible Verpackungen aus Mulimateriallaminaten bis 2030 durch recycelbare Monomateriallaminate ersetzt werden müssen.

Um gemäß der Verordnung als Monomaterial eingestuft zu werden, müssen mindestens 90 Gew% des Laminats aus einem einzigen Polymertyp bestehen, während sich die restlichen 10 Gew% auf Komponenten wie Druckfarben, Klebstoffe und Barrierebeschichtungen belaufen. Die Herausforderung besteht darin, die erforderliche Funktionalität — insbesondere in Bezug auf die Gasbarriereeigenschaften — unter Einhaltung dieser strengen Anforderungen an die Zusammensetzung zu erreichen. Während häufig verwendete Folienmaterialien, beispielsweise Polyolefine, eine hohe Barriere gegen polaren Wasserdampf bieten, ist ihre Barriere gegen unpolare Gase wie Sauerstoff gering. Um die Produktqualität und -haltbarkeit zu erhalten, müssen daher dünne, effiziente Gasbarriereschichten integriert werden, ohne die Recyclingfähigkeit zu beeinträchtigen.

Barrierelacke stellen hierfür eine vielversprechende Lösung dar. Im Gegensatz zu Aufdampfverfahren, die spezielle Anlagen erfordern, können Lacke mit weit verbreiteten Rolle-zu-Rolle-Beschichtungsverfahren (R2R) aufgetragen werden, was sie für die Industrie interessant macht. Die Gasbarriere dieser Lacke kann erhöht werden, indem gasundurchlässige Silikatpartikel integriert werden, um einen gewundenen Pfad (*Tortuous Path Effect*) für die Gasdiffusion zu schaffen. Dies verbessert die Barrierewirkung und ermöglicht gleichzeitig das Auftragen dünnerer Schichten, was hinsichtlich der 10 Gew%-Grenze für Fremdmaterialien sehr vorteilhaft ist.

In dieser Arbeit wird die Entwicklung von Komposit-Barrierelacken auf Silikatbasis beschrieben, die für die Kompatibilität mit standardmäßigen R2R-Beschichtungsverfahren ausgelegt sind. Die Arbeit umfasst die Entwicklung der Lackformulierungen, deren Verarbeitung und deren Charakterisierung. Der Schwerpunkt

liegt hierbei auf dem Verständnis der Gaspermeationsmechanismen und ihrer Beziehung zur Füllstoffmorphologie, den Polymer-Füllstoff-Interaktionen und dem Beschichtungsverfahren.
Die Entwicklung der Formulierung konzentrierte sich auf die Auswahl geeigneter Silikatfüllstoffe und die Optimierung von Parametern wie dem Mischungsverhältnis zwischen Polymer und Silikat und dem absoluten Feststoffgehalt. Als Füllstoffe wurden das plättchenförmige Montmorillonit (MMT) und das stäbchenförmige Halloysit gewählt. Eine zentrale Herausforderung bestand darin, eine gleichmäßige Dispersion und Exfolierung der Silikatpartikel zu erreichen. Die Exfolierung — d. h. die Trennung einzelner Silikatplättchen von Silikatstapeln — ist entscheidend für die Maximierung der Barrierewirkung.
Das Mahlen mit einer Kugelmühle führte zu homogen dispergiertem MMT mit einer lateralen Ausdehnung (Plättchendurchmesser) von etwa 500 nm und minimalen Agglomerationen. Im Gegensatz dazu führte die Dispersion mit einem Labordispergiergerät zu einer bimodalen Größenverteilung: exfolierte Plättchen (∼350 nm) und große Agglomerate (∼3000 nm). Die Analyse von Querschnittsbildern im Rasterelektronenmikroskop ergab für beide Dispergiermethoden, dass die Dicke der exfolierten MMT-Plättchen bei etwa 25 nm lag.
Aus dem exfolierten MMT wurden Kompositbarrierelacke hergestellt und deren Barriere gegen Sauerstoff und Helium gemessen. Polyvinyl Alkohol (PVA)/MMT-Schichten mit einem Mischungsverhältnis von 1:1 und kugelgemahlenem MMT erzielten die höchste Barriere: 0,12 $\frac{\mathrm{cm^3\,(STP)\,\mu m}}{\mathrm{m^2\,d\,bar}}$ für Sauerstoff und 51 $\frac{\mathrm{cm^3\,(STP)\,\mu m}}{\mathrm{m^2\,d\,bar}}$ für Helium - 12 bzw. 17 Mal besser als reines PVA. Schichten, basierend auf der MMT-Dispersion des Labordispergiergeräts, wiesen aufgrund der Agglomerationen eine höhere Permeation auf. Agglomerierte Plättchen tragen nicht zur Verlängerung des Permeationspfads bei.
Die Berechnung mit Hilfe des Nielsen-Modells half bei der Beurteilung, ob die experimentellen Werte dem maximalen Barrierepotential der Silikate nahekommen. Das Modell, das ausschließlich auf dem Volumenanteil des Füllstoffs und dem Aspektverhältnis basiert, lieferte eine Möglichkeit für die Bewertung der Dispersionsqualität. MMT-Plättchen mit einem Aspektverhältnis von etwa 20 übertrafen die Halloysit-Stäbchen (Aspektverhältnis von 1), was die Bedeutung der Füllstoffgeometrie für die Schaffung wirksamer Permeationsbarrieren zeigt. Untersuchungen zur Kristallinität zeigten, dass beide Füllstoffe einen ähnlichen Anstieg der Kristallinität von PVA verursachten. Dies implizierte, dass die Tortuosität und nicht die Änderung der Kristallinität der Polymermatrix die Hauptursache bei der Verbesserung der Barriere spielte.
Um das Verständnis der Permeationsmechanismen zu vertiefen, wurden zusätzli-

che Gase - Wasserstoff und Wasserdampf - verwendet, die so ausgewählt wurden, dass sie eine Reihe von Größen und Polaritäten abdecken. Die Ergebnisse zeigten, dass in PVA/MMT-Kompositlackschichten kleinere, unpolare Gase effektiver blockiert wurden. Bei einer 1:1 PVA/MMT-Beschichtung betrugen die Permeationskoeffizienten 5,1 für Helium, 1,2 für Wasserstoff und $4{,}2 \times 10^{-3}$ $\frac{\mathrm{cm^3\,(STP)\,\mu m}}{\mathrm{m^2\,d\,bar}}$ für Sauerstoff, was einer Verbesserung der Barriere von 49, 41 und 26 entspricht. Diese Tendenzen galten sowohl für Acrylat- als auch für Polypropylen (PP)-Matrizen, obwohl die absolute Verbesserung aufgrund der unterschiedlichen Polymer-Füllstoff-Affinitäten variierte.
Bei PP/MMT-Kompositlackschichten führten schwächere Wechselwirkungen zu niedrigeren Verbesserungsfaktoren (z. B. nur 5,8 für Helium). Die Wechselwirkungen wurden z. B. mittels FTIR-Daten bestimmt, welche keine Verschiebungen des Si-O-Doppelpeaks von MMT im Kompositspektrum mit PP zeigten. Im Gegensatz dazu zeigten die Kompositspektren von PVA/MMT eine Blauverschiebung des Peaks bei 1031 und 1009 $\frac{1}{\mathrm{cm}}$. Die Wechselwirkungen sind auch der Grund für die höhere Scherverdünnung dieser Lackformulierungen und für deren geringere Aktivierungsenergie für die Gaspermeation. Die Tatsache, dass die Gasbarriere der Komposite höher war als die der reinen Polymere, die Aktivierungsenergie aber geringer, zeigt folgendes: Die Permeation findet entlang der Bereiche schwacher Wechselwirkung zwischen Silikat und Füllstoff statt, welche einen geringeren Widerstand für die Permeation als das reine Polymer aufweisen. Die Verlängerung des Permeationspfades hat aber einen größeren Einfluss auf den Permeationskoeffizienten als die verringerte Aktivierungsenergie.
Der Permeationsmechanismus für Wasserdampf erwies sich als gänzlich anders. Während unpolare Gase durch gewundene Pfade effektiv blockiert werden, nutzt der polare Wasserdampf die Hydrophilie von MMT und permeiert entlang sich berührender MMT-Partikel in der Kompositschicht - ein Phänomen, das als *Polar Path Effect* bezeichnet wird. Infolgedessen wurde trotz der Integration von Füllstoffen keine signifikante Verbesserung der Barriere für Wasserdampf beobachtet.
Die Lacke wurden für R2R-kompatible Beschichtungsverfahren entwickelt, insbesondere für das Schlitzdüsen- und Reverse-Gravure-Verfahren. Rheologische Untersuchungen ergaben, dass eine Lackformulierung mit 9 Gew% beim Reverse-Gravure-Verfahren eine höhere Scherung erfuhr ($\sim$4000 $\frac{1}{\mathrm{s}}$) als beim Schlitzdüsenverfahren ($\sim$1200 $\frac{1}{\mathrm{s}}$). Trotz der Unterschiede in der Prozessdynamik ergaben beide Verfahren Sauerstoffbarrierewerte, die mit denen von Rakel-Beschichtungen im Labormaßstab vergleichbar waren (0,12 bis 0,14 $\frac{\mathrm{cm^3\,(STP)\,\mu m}}{\mathrm{m^2\,d\,bar}}$).
Jede Beschichtungstechnik stellte unterschiedliche Anforderungen an die Lackfor-

mulierung. Beim Schlitzdüsenverfahren ist ein geringer Feststoffgehalt (<5 Gew%) aufgrund des höheren Wassergehalts, der zur Stabilisierung der Silikatdispersion durch Hydrathüllen beiträgt, vorteilhaft. Beim Reverse-Gravure-Verfahren ist ein höherer Feststoffgehalt (>5 Gew%) vorteilhaft, um ausreichende Schichtdicken (>1 µm) zu erreichen, da die Dicke nicht über den Volumenstrom eingestellt werden kann. Obwohl das Agglomerationsrisiko mit steigendem Feststoffgehalt zunimmt, gleicht das Reverse-Gravure-Verfahren dies teilweise durch mechanische Filterung aus, wobei einige Agglomerate im Reservoir zurückgehalten oder vom Rakel entfernt werden.

Es zeigte sich, dass die Beschichtungstechnik keinen Einfluss auf die endgültige Ausrichtung der Silikatpartikel in der getrockneten Lackschicht hat. Stattdessen hatte die Art des Lacks — Dispersion oder Lösung — einen größeren Einfluss. Bei Lacken auf Dispersionsbasis behinderte das Vorhandensein von Polymerkügelchen die Ausrichtung der Plättchen, was zu einer breiteren Orientierungsverteilung (18 bis 23°) führte. Lacke auf Lösungsbasis, wie PVA oder Polycarboxylsäure, ermöglichten eine bessere Ausrichtung in der Ebene (11 bis 14°), was für die Barriereleistung von Vorteil ist.

Zusammenfassend zeigt diese Arbeit, dass Kompositlacke auf Silikatbasis einen skalierbaren und effektiven Ansatz für die Integration von Gasbarrieren in recycelbare Monomateriallaminate bieten. Das Erreichen einer hohen Barriereleistung hängt entscheidend von der Exfolierung des Füllstoffs, der Polymer-Füllstoff-Kompatibilität und der Optimierung des Beschichtungsprozesses ab. Die Ergebnisse bieten einen soliden Rahmen für die weitere Entwicklung nachhaltiger Verpackungslösungen. Künftige Forschungsarbeiten sollten sich auf Langzeitstabilität, Recyclingfähigkeit und die Entwicklung neuer Polymer-Silikat-Systeme mit verbesserten Wechselwirkungen konzentrieren, um die sich entwickelnden Anforderungen an kreisförmige Verpackungstechnologien zu erfüllen.

Summary

Flexible polymer films are the most widely used packaging materials worldwide due to their light weight, versatility, and efficient protection. Compared to traditional materials such as glass, metal, or paper, they offer superior functionality in many applications. However, their public image has suffered due to environmental concerns, particularly from media coverage of plastic pollution. In response to these concerns and to improve the sustainability of packaging, the European Parliament adopted the *Packaging and Packaging Waste* Regulation in December 2024. A central provision requires that non-recyclable multi-material flexible packaging be replaced by recyclable mono-material laminates by 2030.

To be classified as mono-material under the regulation, at least 90 wt% of the laminate must consist of a single polymer type, while the remaining 10 wt% can include components such as inks, adhesives, and barrier coatings. This presents a challenge: achieving necessary functionality — particularly in terms of gas barrier performance — within strict compositional constraints. While base polymers like polyolefins offer high resistance to polar water vapor, they are ineffective against non-polar gases like oxygen. Thus, to maintain product quality and shelf life, thin, efficient gas barrier layers must be integrated without compromising recyclability.

Barrier lacquers represent a promising solution. Unlike vapor deposition techniques, which require specialized equipment, lacquers can be applied using widely available roll-to-roll (R2R) coating systems, making them more accessible to industry. To increase the effectiveness of these lacquers, gas-impermeable silicate particles can be introduced to create a *tortuous path* for gas diffusion. This strategy improves barrier performance while allowing for thinner layers, which is critical under the 10 wt% limit for non-base-polymer materials.

This thesis investigates the development of silicate-based composite barrier lacquers designed for compatibility with standard R2R coating processes. The work encompasses formulation, processing, and functional characterization, with a focus on understanding gas permeation mechanisms and their relation to filler morphology, polymer-filler interactions, and coating method.

Formulation development focused on selecting appropriate silicate fillers and optimizing parameters such as the polymer-to-silicate mixing ratio and maximum solid content. Montmorillonite (MMT) and halloysite were chosen as fillers, representing platelet and rod geometries, respectively. A key challenge was achieving uniform dispersion and exfoliation of the silicate particles. Platelet exfoliation — i.e., the separation of individual silicate sheets from stacked layers — is critical

for maximizing surface area and barrier effectiveness.

Ball milling produced well-dispersed MMT with lateral sizes around 500 nm and minimal agglomeration. In contrast, high-shear dispersion resulted in a bimodal distribution: exfoliated platelets (∼350 nm) and large aggregates (∼3000 nm). SEM analysis confirmed that exfoliated MMT maintained a thickness of approximately 25 nm.

Barrier performance was evaluated by measuring oxygen and helium permeation through composite coatings. Polyvinyl alcohol (PVA)/MMT films with a 1:1 mixing ratio and ball-milled MMT achieved the best performance: 0.12 $\frac{\mathrm{cm^3\,(STP)\,\mu m}}{\mathrm{m^2\,d\,bar}}$ for oxygen and 51 $\frac{\mathrm{cm^3\,(STP)\,\mu m}}{\mathrm{m^2\,d\,bar}}$ for helium — 12 and 17 times better than pure PVA, respectively. Films made with high-shear-dispersed MMT showed higher permeation due to the presence of agglomerates, which contribute little to the tortuous path.

Theoretical modeling using the Nielsen model helped assess whether experimental values approached the geometric maximum potential of the fillers. The model, based solely on filler volume fraction and aspect ratio, provided a benchmark for evaluating dispersion quality. MMT platelets with aspect ratios around 20 outperformed halloysite rods (aspect ratio of 1), demonstrating the importance of filler geometry in creating effective diffusion barriers. Crystallinity studies showed that both fillers caused a similar increase in polymer crystallinity, suggesting that tortuosity, rather than matrix ordering, played the dominant role in barrier improvement.

To deepen the understanding of permeation behavior, additional gases — hydrogen, oxygen, helium, and water vapor — were used, chosen to span a range of sizes and polarities. Results showed that in PVA/MMT composites, smaller, nonpolar gases were more effectively blocked. For a 1:1 PVA/MMT layer, permeation coefficients were 5.1 for helium, 1.2 for hydrogen, and 4.2×10^{-3} $\frac{\mathrm{cm^3\,(STP)\,\mu m}}{\mathrm{m^2\,d\,bar}}$ for oxygen, corresponding to barrier improvements of 49, 41, and 26. These trends held across acrylate and polypropylene matrices, though the absolute improvement varied due to differing polymer-filler affinities.

In PP/MMT composites, weaker interactions led to lower improvement factors (e.g., 5.8 for helium), consistent with FTIR data showing the absence of shifts in the MMT -Si-O double peaks. In contrast, PVA/MMT spectra revealed a blue shift at 1031 and 1009 $\frac{1}{\mathrm{cm}}$, indicating strong interactions. These interactions also affected rheology, as evidenced by increased shear-thinning behavior and reduced activation energy for gas permeation. Although diffusion paths were longer in MMT-filled layers, the energy required for diffusion was lower, pointing to weak boundary areas between polymer and filler as the primary hindrance to gas flow.

Water vapor permeation behaved differently. While non-polar gases were effectively blocked by tortuous paths, polar water vapor exploited hydrophilic MMT interfaces, forming continuous diffusion pathways — a phenomenon referred to as the *polar path effect*. As a result, no significant barrier improvement was observed for water vapor, despite favorable filler dispersion.

The developed lacquers were scaled to R2R-compatible coating techniques, specifically slot-die and reverse gravure. Rheological studies revealed that a 9 wt% formulation experienced greater shear during gravure coating ($\sim$4000 $\frac{1}{s}$) compared to slot-die ($\sim$1200 $\frac{1}{s}$). Despite differences in viscosity and process dynamics, both methods yielded oxygen barrier values comparable to those of laboratory-scale k-bar coatings (0.12 to 0.14 $\frac{cm^3\,(STP)\,\mu m}{m^2\,d\,bar}$).

Each coating method imposed distinct formulation requirements. Slot-die favored low solid contents (<5 wt%) due to higher water content, which helped stabilize the silicate dispersion via hydrate shells. Gravure required higher solid contents (>5 wt%) to ensure sufficient layer thickness (>1 µm), as thickness cannot be adjusted via flow rate. Though agglomeration risk increases with solid content, the gravure process partially compensates through mechanical filtering, with some agglomerates retained in the reservoir or removed by the doctor blade.

Interestingly, the coating technique did not influence the final orientation of the silicate particles. Instead, the formulation type — dispersion or solution — had a more pronounced effect. In dispersion-based lacquers, the presence of polymer spheres hindered platelet alignment, leading to broader orientation distributions (18 to 23°). Solution-based systems, such as PVA or polycarboxylic acid, promoted better in-plane alignment (11 to 14°), which is advantageous for barrier performance.

In conclusion, this work demonstrates that silicate-based composite lacquers offer a scalable and effective approach for gas barrier integration in recyclable monomaterial laminates. Achieving high barrier performance depends critically on filler exfoliation, polymer-filler compatibility, and coating process optimization. The findings provide a robust framework for further development of sustainable barrier packaging solutions. Future research should focus on long-term stability, recyclability, and the development of new polymer-silicate systems with enhanced interactions to meet the evolving requirements of circular packaging technologies.

List of abbreviations

AF4 Asymmetrical flow field-flow fractionation

ATR Attenuated total reflectance

BIF Barrier improvement factor

BoPP Biaxial oriented polypropylene

EU European Union

EVOH Ethylene vinyl alcohol

fsf Free-standing film

FTIR Fourier transform infrared

LC Liquid crystal

LbL Layer-by-layer

MALLS Multi-angle laser light scattering

MMT Montmorillonite

OLED Organic light emitting diodes

OPV Organic photovoltaics

PA6 Polycaprolactam, known as Nylon 6

PAA Polyacrylic acid

PE Polyethylene

PEN Polyethylene naphthalate

PET Polyethylene terephthalate

PP Polypropylene

PPC-P Polypropylene carbonate-co-phthalate

PPWR Packaging and Packaging Waste Regulation

PVA Polyvinyl alcohol

PVD Physical vapor deposition

PVDC Polyvinylidene chloride

R2R Roll-to-roll

SEM Scanning electron microscopy

STP Standard conditions for temperature (0 °C) and pressure (1.013 bar)

TEM Transmission electron microscopy

VIP Vacuum insulating panel

VOC Volatile organic compound

XRD X-ray diffraction

1. Introduction

The permeation of gases is a fundamental phenomenon with critical implications in scientific fields such as materials science, chemistry, and engineering, as well as industrial applications like gas separation, energy storage, and packaging. The permeation process is defined as the movement of gas molecules through a material, driven by a concentration gradient [1]. An understanding of gas permeation is essential for the design of materials with controlled gas transfer rates and the enabling of applications ranging from food preservation to advanced fuel cells [2]. Figure 1.1 illustrates the comparative barrier properties of common polymeric packaging materials against oxygen and water vapor, as well as the barrier requirements for various applications. The diagram spans eight orders of magnitude, emphasizing the broad range of requirements and applications for these materials. In industries like food, cosmetics, pharmaceuticals, and healthcare, gas permeation properties are pivotal in determining the shelf life and stability of products. By regulating the ingress of oxygen, moisture, and other gases, materials with suitable barrier properties can prevent oxidation, microbial growth, and water uptake, thereby preserving product quality [3]. In electronic applications, such as organic solar cells and flexible organic field-effect transistors, robust barriers against oxygen and moisture are essential in order to protect sensitive organic materials from degradation. The performance and longevity of these devices substantially depend on the optimization of the gas barrier properties of their encapsulation material [4, 5]. In the energy sector, hydrogen storage and transportation present unique challenges closely tied to gas permeation. Materials in these applications must effectively prevent hydrogen leakage while maintaining structural integrity and performance under varying conditions [6].
To establish a basis for discussing gas permeation in packaging materials, the following sections summarize its fundamental principles, define key terms, and present an overview of typical gas barrier materials. The rationale for the established use of multi-material laminates in various applications is explored, and an explanation is provided for the shift toward mono-material laminates in current developments. The introduction then transitions to a discussion of composite barrier layers, emphasizing their advantages, including the enhanced gas barrier

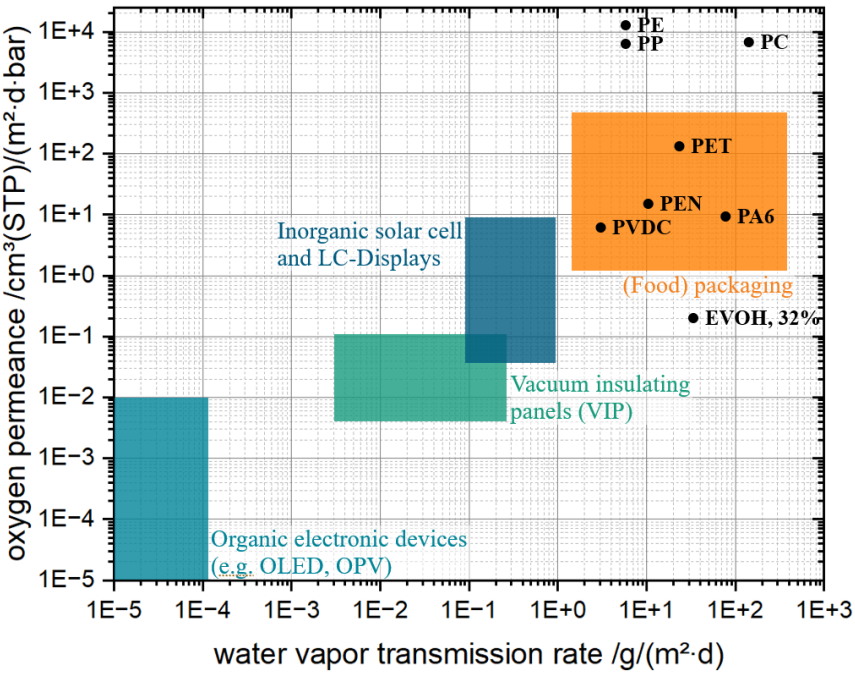

Figure 1.1.: Barrier requirements for oxygen and water vapor in various technical applications and food packaging, in relation to the permeability coefficients normalized to a 100-µm layer thickness for various polymeric materials, e.g. PP, PET, and PVDC (adapted from Langowski [7]).

properties achieved through the tortuous path effect. This section further discusses the polymer matrix, which is composed of gas barrier lacquers, and it describes the inorganic fillers, primarily silicate platelets. It then details the fabrication processes of silicate-based composite layers, and provides an overview of the state-of-the-art advancements in composites based on polyvinyl alcohol (PVA) and other polymer matrices. Finally, the available coating techniques for these lacquers on flat substrates are reviewed, and the latest developments in the coating of composite barrier lacquers are summarized.

Although there is a considerable body of research in the field of composite lacquers as gas barrier layers, critical gaps remain in the understanding and optimization of key aspects of production processes and material combination possibilities in this field. These include the effective dispersion of silicate platelets and their integration with polymer matrices, the permeation mechanisms within composite lacquer layers, and the scaling of coating processes from the laboratory to industrial production. Addressing these challenges is essential and forms the basis for the scientific questions outlined in Section 1.4, as well as the overarching objectives of this thesis.

1.1. Theoretical background on gas permeation

The mass transport of a gas through a homogeneous and dense polymer is described by the solution-diffusion mechanism [8]. This process is driven by a pressure gradient of the permeating gas across the polymeric film, which induces a chemical potential. The gas undergoing transport is referred to as the permeant. Over time, the transport process gradually equalizes the concentration difference across the film [9]. The resulting permeation process at a given temperature is decomposed into three steps [10]:

1. Adsorption of the permeant at the upstream face of the polymer, via chemical affinity
2. Solution and diffusion of the permeant through the polymer's cross-section
3. Desorption of the permeant at the downstream face of the polymer

In a Fickian mechanism, the permeability coefficient P is expressed as the product of the solubility coefficient S and the diffusion coefficient D.

$$P = S \cdot D \tag{1.1}$$

The solubility coefficient of a polymer describes the ability to dissolve a certain amount of gas at a defined pressure according to Henry's law. In the context of a polymeric film, the unit for S is for example expressed as $\frac{\mathrm{cm^3(STP)}}{\mathrm{cm^3(pol)\,bar}}$ [11]. It describes the amount of permeant in volume at standard temperature and pressure ($\mathrm{cm^3(STP)}$), that is dissolved in a defined volume of polymer ($\mathrm{cm^3(pol)}$). The solubility of a gas in a polymer is influenced by the interaction between the permeant and the polymer, the free volume of the polymer, and the condensability of the gas [12].
Diffusion is the process by which the permeant moves through the polymer due to random molecular motions. It is a kinetic term that represents the mobility of the permeant within the polymer phase. The unit for D is typically expressed as $\frac{\mathrm{cm^2}}{\mathrm{d}}$, where the average square of the distance traveled by the permeant is given in $\mathrm{cm^2}$ and the duration is given in days (d). The diffusive flux J of the permeant through a polymer layer with an area A during the time t is given by

$$J = \frac{N}{A \cdot t} \tag{1.2}$$

where N is the total amount of permeant which has passed through the polymer. Fick's first law of diffusion establishes a linear relation between this flux and the

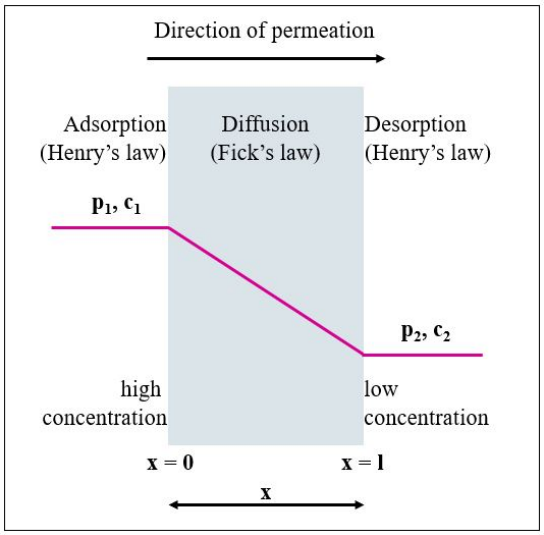

Figure 1.2.: Molecular diffusion perpendicular through a polymer film (adapted from Mahdi et al. [13]).

concentration gradient ∇c between both sides of the film.

$$J = -D\nabla c \tag{1.3}$$

The first Fickian law is applicable when the time-dependent change of the concentration c on both sides of the film is neglected and the flux is constant, that is, the diffusion is in steady state. When the diffusion occurs only in one direction x, the relationship is described as follows

$$J = -D\left(\frac{\partial c}{\partial x}\right) \quad . \tag{1.4}$$

Fick's second law describes the unsteady form of this relationship, with an equation illustrating the rate of change in concentration to the diffusive flux

$$\frac{\partial c}{\partial t} = D\frac{\partial^2 c}{\partial x^2} \quad . \tag{1.5}$$

With a given thickness d of the polymeric film, and under the assumption of steady state and constant diffusion coefficient, the permeant flux is equal to

$$J = -D\frac{(c_1 - c_2)}{d} \tag{1.6}$$

where c_1 and c_2 are the surface concentrations of the gas at the downstream and upstream faces of the polymeric film, respectively. In permeation experiments, it

is not the surface concentration that is usually measured, but the gas pressure on both sides of the film (p_1 and p_2). Henry's law describes the relationship between the equilibrium concentration of the gas c and its partial pressure p, including the solubility coefficient as a function of p.

$$c = S \cdot p \tag{1.7}$$

Following Henry's law in Equation 1.6 leads to

$$J = -DS\frac{(p_1 - p_2)}{d} \tag{1.8}$$

where p_1 and p_2 are the ambient pressures on both sides of the film. Combining the Equations 1.1, 1.2, and 1.8 finally yields

$$P = \frac{d \cdot J}{\Delta p} = \frac{d \cdot N}{A \cdot t \cdot \Delta p} \quad . \tag{1.9}$$

The permeability coefficient P is the most frequently reported quantity characterizing the barrier properties of a polymer film, since it is a material constant [14]. A commonly used unit for P is $\frac{\mathrm{cm^3\,(STP)\,\mu m}}{\mathrm{m^2\,d\,bar}}$. However, the permeability coefficient itself is not a direct measurand. In the case of water vapor, it is calculated from the diffusive flux (also called transmission rate) and the layer thickness of the polymer. In the case of other gases such as hydrogen, helium, or oxygen, it is calculated from the permeance Q and the layer thickness of the polymer [15].

$$Q = \frac{N}{A \cdot t \cdot \Delta p} \tag{1.10}$$

1.2. Multi-material packaging and the shift toward mono-materials

A wide variety of materials and methods are employed to prevent gas permeation in packaging, depending on the specific application [16]. Among these, polymers — particularly flexible polymer films — are the most commonly used due to their unique combination of properties [17]. Polymers are versatile, lightweight, and cost-effective, and they feature essential characteristics such as gas barrier performance, durability, sealability, and transparency [18].

As shown in Figure 1.1, single-layer mono-material polymer films with a thickness of 100 µm are unable to achieve low permeation coefficients. For example, a biaxially oriented polypropylene (PP) film with a thickness of 17.8 µm exhibits an

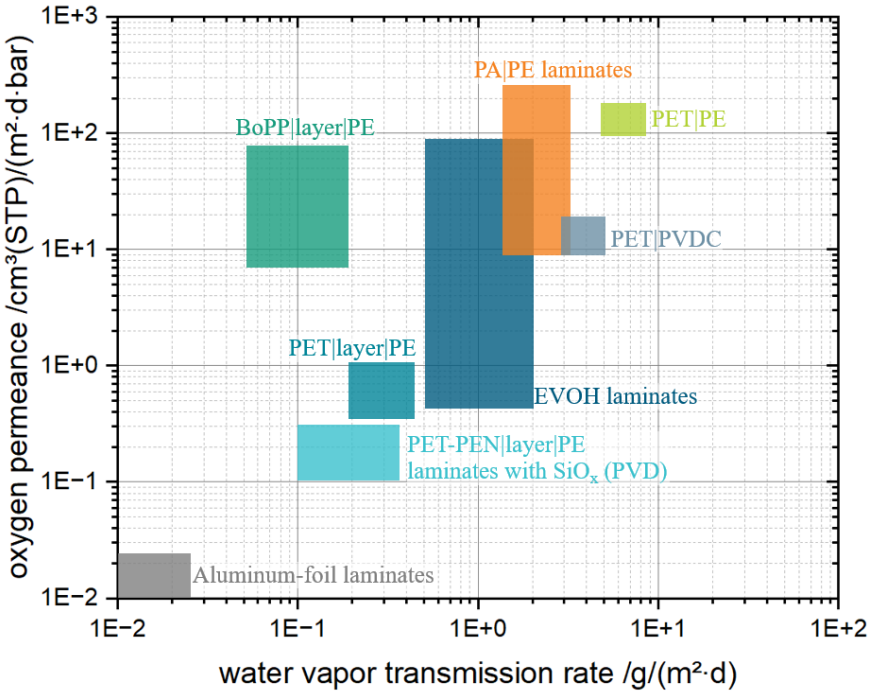

Figure 1.3.: Oxygen permeance and water vapor transmission rates for different gas barrier film laminates (adapted from Langowski [7]).

oxygen permeance of 2511 $\frac{\mathrm{cm^3\,(STP)}}{\mathrm{m^2\,d\,bar}}$ (measured at 23 °C and 50 %RH) and a water vapor transmission rate of 2.5 $\frac{\mathrm{g}}{\mathrm{m^2\,d}}$ (measured at 23 °C and 100 %RH) [19]. According to the diagram, while the water vapor barrier of the PP film is sufficient for packaging most food products, the oxygen barrier is inadequate for all of the applications listed. To address these limitations, modern packaging technologies incorporate advanced solutions with more than one polymer layer, to improve the gas barrier. These polymer films that consist of several layers of partly different materials are generally referred to as laminates, including co-extruded films, laminates with physical vapor deposition (PVD) layers, laminates made of different polymer films, and laminates with metal films (Figure 1.3) [20, 21]. For medium barrier applications, polymer laminates such as PA|PE, PET|PE, PET|PVDC, or laminates with EVOH can be employed. These laminates are typically effective for oxygen permeance values down to 0.3 $\frac{\mathrm{cm^3\,(STP)}}{\mathrm{m^2\,d\,bar}}$ and water vapor transmission rates down to 0.5 $\frac{\mathrm{g}}{\mathrm{m^2\,d}}$. To achieve lower permeability values, additional barrier layers can be deposited using PVD techniques, such as silicon oxide (SiO_x), aluminum oxide (AlO_x), or aluminum metalization. These methods can reduce the oxygen permeance to as low as 0.1 $\frac{\mathrm{cm^3\,(STP)}}{\mathrm{m^2\,d\,bar}}$, and the water vapor transmission rate to 0.1 $\frac{\mathrm{g}}{\mathrm{m^2\,d}}$. The highest barrier performance is obtained by using metallic foils, such as aluminum foils, with thicknesses exceeding 6 µm. While these barrier properties are outstanding, films incorporating aluminum foils lose

their transparency. To achieve both high barrier performance and transparency, highly complex laminate structures are required, often consisting of eight layers or more [22, 23].

Regardless of whether the films are transparent, multi-material laminates present a significant disadvantage: they are not recyclable. This issue has become increasingly relevant, particularly with the introduction of the European Union's (EU) new Packaging and Packaging Waste Regulation (PPWR), published on December 4, 2024 [24]. The regulation mandates that all packaging in the EU must be reusable or recyclable by 2030. In 2016, approximately 20 wt% of all flexible packaging consisted of multi-material laminates [25]. As the volume of packaging material continues to grow, the use of multi-materials in sectors such as food packaging, pharmaceuticals, cosmetics, and electronics is also increasing [26].

Several approaches can be pursued to enable the recyclability of such laminates [27]. One route is to develop advanced recycling processes capable of recovering and reusing different materials within a single recycling step. Examples include chemical recycling, where polymers are broken down into their monomers for reuse, and solvent-based physical recycling, which separates and recovers materials without altering their chemical structure [28, 29]. Another approach is to design laminates with on-demand debonding capabilities, allowing for the separate recycling of individual film layers [30]. A more unconventional method is compatibilization, which involves the use of chemical substances to enhance the mechanical compatibility of various materials within the multi-layer structures during the mechanical recycling process. This approach enables the recycling of all layers within a single stream without the need for separation [31]. The most common route is to replace the multi-material films with mechanically recyclable mono-material films. By definition, a mono-material film contains less than 10 wt% foreign materials [32]. Foreign materials include barrier layers, adhesive layers, and printing layers. Therefore, minimizing the thickness of each of these layers is crucial for improving recyclability. Mono-material films achieve gas barrier properties through the application of thin barrier layers, typically applied via physical vapor deposition or wet chemical coating.

The composite barrier lacquers described in this thesis offer a promising solution for reducing the thickness of the barrier layer. The incorporation of impermeable fillers into barrier layers significantly enhances their gas barrier properties. In the realm of food packaging, reducing the permeation coefficient for oxygen or water vapor yields two distinct benefits. First, achieving a more effective barrier with the same layer thickness can extend the shelf life of packaged food.

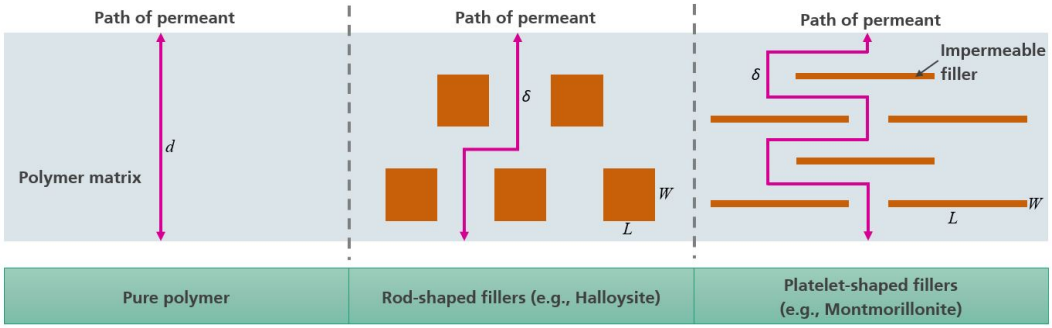

Figure 1.4.: Schematic drawing of the permeation path through a pure polymer film and composite polymer films with halloysites or montmorillonites (adapted from Nielsen [33]).

Second, improved barrier properties enable the thinning of the barrier layer without compromising performance. This reduction in layer thickness decreases the proportion of foreign material in the mono-material film, thereby enhancing its recyclability.

1.3. Composite barrier lacquers for mono-material applications

Polymers are rarely used in their pure form for technical applications; instead, they are typically modified with fillers or additives, such as calcium carbonate, glass beads, talc, antioxidants, and lubricants [34]. These modifications may enhance processability, adjust mechanical properties, alter appearance, improve conductivity, reduce flammability, or lower production costs [35].

When two or more distinct materials are combined to form a composite, the individual components remain separate and retain their unique properties in the final structure [36]. This characteristic distinguishes composites from homogeneous mixtures or solutions. Ideally, composites synergistically integrate the advantageous properties of the polymer matrix with those of the fillers, leading to significant improvements in mechanical strength [37], heat resistance [38], fire redundancy [39], or barrier properties. The smaller the filler particles are, the larger their interface with the polymer is at a constant mixing ratio. The mixing ratio by weight is defined as the ratio of filler weight to polymer weight.

The filler size, the homogeneous distribution of the filler, and the interaction between the polymer matrix and the filler all play a critical role in determining the properties of composite materials [40]. A notable type of composite used in gas barrier applications consists of a polymer matrix integrated with impermeable

fillers. When platelet-shaped fillers are uniformly distributed and aligned parallel to the direction of permeation, they effectively extend the diffusion path of the permeant, thereby reducing the permeation coefficient (Figure 1.4). This phenomenon is called the tortuous path effect. In the following sections, composite barrier layers are explained step by step.

1.3.1. Gas permeation through composites

In 1967, Nielsen [33] initiated research on the simulation of diffusion through composites, with a fundamental analytical approach for the determination of the gas barrier properties of composite layers. Over the years, this approach has been refined and adapted to accommodate advances in the field. Zid et al. [41], in their review, provide a comprehensive overview of the chronological development of transport mechanism modeling in composite layers, tracing the progression from Nielsen's initial two-dimensional (2D) analytical calculations to three-dimensional (3D) numerical simulation techniques, such as the finite element method.

In the present thesis, geometric models based on Nielsen's approach have been employed to calculate the improvement of barrier properties of polymers through the incorporation of silicate particles. These geometric models rely exclusively on parameters — such as particle size, concentration, and orientation — for calculations, while disregarding factors like chemical modifications in the polymer matrix, or polymer/filler interactions. Several assumptions underpin these calculations. First, the particles are assumed to be entirely impermeable to the permeating gas, thereby extending the diffusion path that can be quantified. Additionally, the particles are presumed to be free of agglomeration and homogeneously distributed within the polymer matrix. In the initial analysis, it is further assumed that the particles are oriented parallel to the surface and perpendicular to the direction of gas permeation.

The tortuous path is mathematically described by the tortuosity factor τ

$$\tau = \frac{\delta}{d} \tag{1.11}$$

defined by the quotient of the thickness of the polymer layer d and the distance a permeant migrates through the film δ. The permeability is reduced, not only because of an increase in the tortuosity factor but also because a portion of the cross-sectional area is occupied by fillers rather than polymer, as indicated by

the filler volume fraction ϕ_F. Thus, a first approximation in the form of

$$\frac{P_\mathrm{F}}{P_\mathrm{u}} = \frac{1-\phi_\mathrm{F}}{\tau} \tag{1.12}$$

is used, where P_F and P_u are the permeability coefficients of the filled and unfilled polymer. Since this analysis is two-dimensional, it is further assumed that the area fraction of the polymer in each cross section equals the volume fraction of the polymer in the composite. Figure 1.4 illustrates the path a molecule must take to get through the film, and an averaging process yields

$$\tau = 1 + \left(\frac{L}{2W}\right) \cdot \phi_\mathrm{F} \tag{1.13}$$

for the tortuosity factor. Within this expression the quotient of longest extension of the filler L (either length or width) and the shortest extension of the filler W (thickness) is included, which is called the aspect ratio α [42].

$$\alpha = \frac{L}{W} \tag{1.14}$$

Integrating Eq.1.13 in Eq.1.12 leads to

$$\frac{P_\mathrm{F}}{P_\mathrm{u}} = \frac{1-\phi_\mathrm{F}}{1 + \left(\frac{L}{2W}\right) \cdot \phi_\mathrm{F}} \tag{1.15}$$

the Nielsen equation for effective permeability. Troeh et al. [43] showed that squaring the tortuosity factor in the Nielsen equation leads to better agreement between experimental and theoretical values, a finding later confirmed by Lape et al. [44] and by Shen and Chen [45]. Therefore, the equation used in this investigation for modeling the permeability of composites in [46] was

$$\frac{P_\mathrm{F}}{P_\mathrm{u}} = \frac{1-\phi_\mathrm{F}}{\left(1 + \left(\frac{L}{2W}\right) \cdot \phi_\mathrm{F}\right)^2} \quad . \tag{1.16}$$

Since one assumption of the Nielsen approach is the parallel orientation of the fillers in the composite layer, Bharadwaj [47] proposed incorporating an orientation parameter Υ to enable more accurate modeling.

$$\Upsilon = \frac{1}{2} \cdot \left(3 \cdot \cos^2 \zeta - 1\right) \tag{1.17}$$

Here ζ is the average angle between the particle plane and the substrate surface, and it accounts for deviations from the idealized parallel alignment of fillers

assumed in Nielsen's original model. The tortuosity factor adjusted for particle orientation τ_{orient} is then

$$\tau_{\text{orient}} = 1 + \frac{L}{2W} \cdot \phi_{\text{F}} \cdot \frac{2}{3} \cdot \left(\Upsilon + \frac{1}{2}\right) \tag{1.18}$$

and the finally modified Nielsen equation used for modeling in [48] is

$$\frac{P_{\text{F}}}{P_{\text{u}}} = \frac{1 - \phi_{\text{F}}}{\left(1 + \frac{L}{2W} \cdot \phi_{\text{F}} \cdot \frac{2}{3} \cdot \left(\Upsilon + \frac{1}{2}\right)\right)^2} \quad . \tag{1.19}$$

The barrier improvement factor (BIF) quantifies the degree of improvement and is defined as the ratio of the permeability of the unfilled polymer to the permeability of the composite.

$$BIF = \frac{P_{\text{u}}}{P_{\text{F}}} \tag{1.20}$$

The unfilled polymer, referred to as the polymer matrix, is the medium into which the fillers are integrated; it is described in the next section.

1.3.2. Polymer matrix

Gas barrier lacquers

A lacquer is a liquid coating material applied in thin layers to substrates, forming continuous, solid coatings via chemical or physical processes [49, 50]. In principle, any polymer that can be converted into a liquid state or applied as a dispersion may serve as a lacquer. Some monomers and polymers (e.g., UV-curable two-component polyacrylates [51]) intrinsically exist in a liquid state (solvent-free) at room temperature, while others require transformation into a liquid form via dissolution (solutions) or via dispersion of small polymer particles (dispersions) [52]. Gas barrier lacquers represent a specific class of lacquers characterized by their high resistance to gas permeation, including oxygen, water vapor, or other gases. Representative polymers for such applications include polyamides, polyacrylates, polyurethanes, polyvinylidene chloride, ethylene vinyl alcohol, polycarboxylic acids, polypropylene, and polyvinyl alcohol [53–56]. In the present thesis, the term "lacquer" refers to the liquid material, while "coating" designates the resulting dried layer.

While each type of lacquer offers distinct advantages and disadvantages in specific applications, generally one type of lacquer will be preferable to another. Solvent-free lacquers represent an exception, as they are rarely used compared

to water-based or solvent-based lacquers [57]. The primary advantage of solvent-free lacquers is that drying occurs through a chemical reaction, resulting in a cross-linked structure that imparts a high level of temperature and chemical stability to the cured coating layer [58]. However, their limited availability for specialized applications, along with their typically high viscosity (>500 mPa s), necessitates the use of specialized coating equipment [59].

Lacquers based on organic solvents offer several benefits, including a low evaporation temperature, rapid evaporation rates compared to water, straightforward manufacturing processes, and ease of application and control of the coating layer [60]. Common solvents used in these lacquers include ethyl acetate, ethanol, methyl ethyl ketone, and acetone. Additionally, solvent-based lacquers generally exhibit greater resistance to high temperature, chemicals, and water compared to their water-based counterparts. The primary drawback of solvent-based lacquers lies in the environmental and safety risks associated with solvent evaporation. First, the release of volatile organic compounds (VOCs) into the atmosphere poses a significant explosion hazard, necessitating extensive protective measures to safeguard personnel and equipment. Second, solvents can enter wastewater systems via cleaning processes and industrial effluents. Due to their low biodegradability, they accumulate in water bodies, leading to contamination, and requiring complex and costly treatment methods. Consequently, solvent recovery is often economically unviable, making solvent-based lacquers both environmentally and financially disadvantageous in industrial applications [61].

Water-based lacquers, on the other hand, are considered to have a lower environmental impact and pose a lower toxicity risk to on-site workers [62]. However, they also have disadvantages, among them, the limited range of polymers that can be stably dissolved or dispersed in water. Additionally, water-based lacquers require higher drying temperatures (typically 60 to 120 °C) compared to solvent-based lacquers (20 to 80 °C). In terms of drying time, solvent-based lacquers typically dry within 20 to 40 s for standard application thicknesses, whereas water-based systems require longer drying times, ranging from 40 to 60 s [50]. Advances in water-based lacquer technology have significantly mitigated many of these limitations, leading to a substantial increase in demand for these lacquers [63]. During the state-of-the-art research phase and the experimental investigations for this thesis, the focus was placed on water-based lacquers.

Difference between lacquer solutions and dispersions

Lacquer solutions are homogeneous mixtures of two or more components, in which one component, the polymer (solute), is fully dissolved in another (solvent). In this system, the interactions between the solvent and the solute break the polymer down to its molecular level, dispersing the polymer molecules uniformly throughout the solvent. As a result, the size of the solute can be measured on a molecular scale (<1 nm), and the system consists of a single phase [64]. The dissolved polymer molecules are not visible and do not scatter light, as they fall below the threshold for the Tyndall effect [65]. Furthermore, the dissolved polymer cannot be separated from the solvent by filtration or size-exclusion methods [56]. The solubility of the polymer in the solvent is limited by the saturation point, beyond which the polymer will precipitate. With an increase in solid content, the solution is initially diluted, then becomes more concentrated, and finally reaches a saturated state. If the polymer content exceeds the saturation point, precipitation occurs [66].
In contrast, dispersions consist of polymer particles suspended in a continuous solvent phase. Unlike solutions, the two phases in a dispersion are immiscible, resulting in a biphasic system [64]. When light passes through a dispersion, the suspended particles scatter the light, making the beam visible (Tyndall effect) [65]. In addition, the polymer particles in a dispersion can be separated from the solvent by filtration or other size-based separation methods [67].
In both lacquer solutions and dispersions, a hydration shell forms around the polymer molecules or particles when dispersed in water. However, when the solid content exceeds the saturation point, the polymer particles cannot form individual hydration shells, and the lacquer transitions from a liquid to a paste-like consistency [68]. Because the surface-to-volume ratio is higher in a solution, the saturation point is reached more quickly than in a dispersion. Consequently, lacquer solutions typically contain lower percentages of solid content (up to 25 wt%) compared to dispersions, which may contain up to 80 wt% solid content [69].

1.3.3. Inorganic filler

Incorporating impermeable fillers can significantly improve the gas barrier properties of lacquers. A key characteristic of these fillers is their shape, which may be spherical, fibrous (stick-like), or platelet-like. In general, fillers are classified into two main categories: organic and inorganic. Among inorganic fillers, a further distinction is made between phyllosilicates and other types.

Fibrillated nanocellulose and cellulose nanocrystals are examples of organic fillers. These materials are increasingly being used due to their natural origin, which aligns with the growing demand for sustainable, biodegradable, and compostable materials [70]. The hydroxy groups on nanocellulose enable chemical interactions through hydrogen bonding with the polar groups of polymer matrices. However, since nanocellulose typically occurs as needles or fibrils, its effective cross-sectional shape is nearly spherical, resulting in an aspect ratio close to 1. Consequently, composites containing organic fillers generally exhibit only modest improvements in gas barrier properties compared to those incorporating platelet-shaped fillers [71, 72]. Nevertheless, the incorporation of nanocellulose into polymers can significantly enhance mechanical properties, such as tensile strength [73].

Phyllosilicates are the inorganic fillers most commonly used for enhancing the gas barrier properties of polymers due to their platelet-like structure [74, 75]. Examples include montmorillonite (MMT), vermiculite, kaolinite, and hectorite — all of which belong to the phyllosilicate class. Although these materials differ in chemical composition and crystal structure, they share a common feature: hydration, with water or hydroxy groups attached to their surfaces. These groups facilitate hydrogen bonding, with polar functional groups in the polymer matrix. An exception is halloysite, which, unlike the typical platelets, occurs as nanotubes [76].

Other inorganic fillers that have facilitated gas barrier improvements when incorporated into polymer matrices include silicon dioxide nanoparticles [77], titanium dioxide nanoparticles [78], aluminum oxide [79], and carbon nanotubes [80]. However, their use is relatively rare compared to phyllosilicates due to several disadvantages, such as higher cost, limited natural abundance, non-biodegradability, lower aspect ratios, and reduced compatibility with most polymers.

In recent years, graphene and graphene oxide composites have attracted increasing attention because of their unique electrical, mechanical, and thermal properties [81, 82]. Graphene, in particular, offers a similar or even higher aspect ratio (500 to 1000 [83]) compared to phyllosilicates, and its hydrophobic nature makes it particularly effective for enhancing the water vapor barrier of polymer composites [84]. Despite these advantages, the widespread use of graphene as a filler is hindered by challenges in large-scale production, the difficulty of achieving stable dispersions in water or solvents, and the limits on graphene's ability to interact with most polymers.

Among the phyllosilicate fillers, MMT is the most commonly used due to its natural abundance, low cost, environmental compatibility, high surface area,

good water absorption, and significant swelling ability in water [85]. Like all phyllosilicates, MMT is hydrophilic, which facilitates its dispersion in water and interaction with polar functional groups. To ensure compatibility with non-polar polymers, MMT is typically organically modified, for instance, through the addition of ammonium cations or salts [86, 87]. Organically modified MMT is commonly referred to in the literature as O-MMT. The widespread use of MMT as an impermeable filler is well-documented in reviews by Kalendova et al.[88], Cui et al.[74], and Rovera et al.[75]. Since MMT is utilized in the present work, its structure, swelling behavior, and exfoliation are discussed in more detail below.

Structure of montmorillonite

Montmorillonite (MMT) belongs to the smectite group, which comprises a variety of swelling phyllosilicates characterized by a three-layered structure [89]. As illustrated in Figure 1.5, MMT's structural unit consists of an alumina octahedral sheet sandwiched between two layers of silica tetrahedra, forming what is commonly referred to as a 2:1 structure [90]. The interlayer spacing, or layer height, measures approximately 9.6 Å, while the lateral dimensions of the layers (length and width) range from 100 to 1000 nm. The structural units are held together by van der Waals forces and electrostatic interactions, forming stacks of primary platelets. Macroscopically, MMT appears as a combination of individual platelet stacks and agglomerates of such stacks. For optimal barrier properties — specifically, the greatest possible tortuosity of the diffusion path — it is desirable to separate these agglomerates and stacks into individual MMT platelets within the composite material. This separation process begins with the swelling of MMT in water, followed by the displacement of the platelets from one another in a process known as exfoliation [91]. Achieving efficient, rapid, and homogeneous exfoliation of MMT in water remains a considerable challenge, which this thesis seeks to address.

During the formation of MMT, isomorphous substitution occurs within its crystal structure. Specifically, Si^{4+} ions in the tetrahedral sheet are partially replaced by Al^{3+} ions, while some Al^{3+} ions in the octahedral sheet are substituted by Fe^{2+}, Fe^{3+}, or Mg^{2+} ions [93]. The degree and type of substitution determine the negative charge on the surface of the silicate platelets. A higher proportion of Al^{3+} ions replacing Si^{4+} ions in the tetrahedral sheet leads to a greater negative charge on the platelet surface, and similarly, substitution of Al^{3+} with lower-valency cations in the octahedral sheets increases the negative charge. The

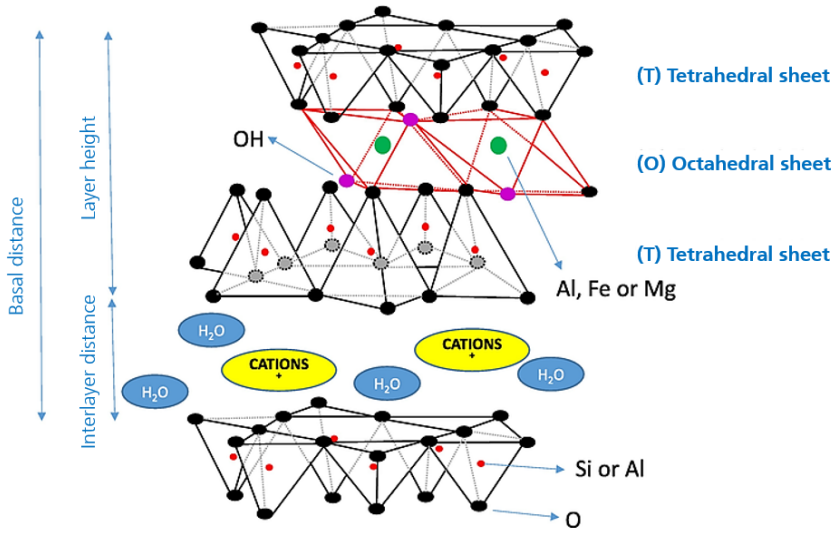

Figure 1.5.: Schematic representation of the layered MMT structure, comprising one octrahedral and two tetrahedral sheets (adapted from Nascimento [92])

charge at the edges of MMT platelets is pH dependent. Below a pH of 6.5, the platelet edges are positively charged, whereas above this pH, they become negatively charged [94]. The interlayer distance between two negatively charged platelets ranges from 9 to 14 Å. The negative charge is balanced by interlayer cations, which are naturally present as Ca^{2+}, Mg^{2+}, K^{+}, Al^{3+}, and Na^{+} [95]. These cations exhibit high hydration energy, facilitating water absorption into the interlayer spaces and leading to swelling of the phyllosilicate [96].

Swelling of montmorillonite

Upon contact with water, the interlayer cations in MMT form hydration shells, which initiates the swelling process (Figure 1.6) [97]. At first, water molecules entering the interlayer region create approximately four hydration layers around each cation [98]. In these initial layers, water molecules are likely arranged in a hexagonal network due to hydrogen bonding with the oxygen atoms of the MMT structure [99]. This process, referred to as crystalline swelling, characterizes the early stages of MMT swelling, during which the interlayer distance increases from its initial value (9 to 14 Å) to approximately 20 Å, corresponding to an absorbed water content of 0.5 $\frac{\mathrm{g\,(H_2O)}}{\mathrm{g\,(MMT)}}$ at 99 %RH. When MMT is brought into direct contact with liquid water, the water uptake increases significantly to approximately 10 $\frac{\mathrm{g\,(H_2O)}}{\mathrm{g\,(MMT)}}$, leading to a twentyfold increase in volume. This stage, which follows crystalline swelling, is known as osmotic swelling or the second swelling region.

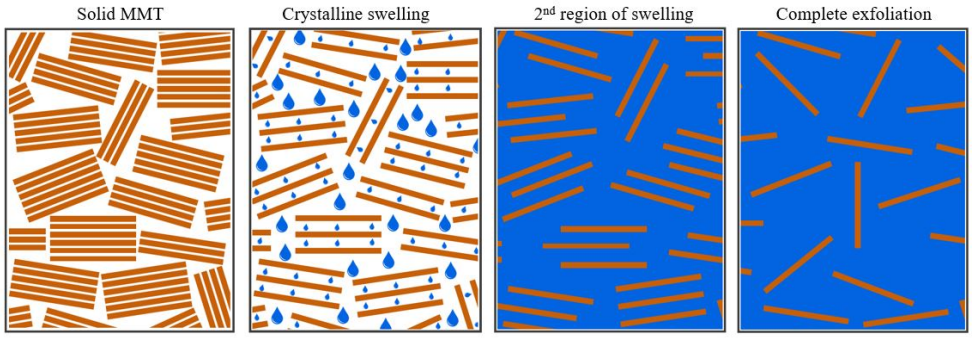

Figure 1.6.: Different stages of montmorillonite in water, from solid to exfoliated.

Further water uptake transforms the MMT into a thixotropic gel, then a sol, and ultimately a pourable dispersion, representing the third stage of water absorption [100]. Not only the interlayer cations contribute hydrophilic properties, but MMT itself also exhibits these properties, displaying a strong affinity for water molecules. This affinity results in the formation of hydration shells around the MMT particles [101] with a thickness typically on the nanometer scale [102].

Exfoliation of montmorillonite

The term exfoliation refers to the overcoming of the van der Waals and electrostatic forces that hold the structural cells within an MMT stack together, whereby these stacks are separated into individual platelets (Figure 1.6). The degree of exfoliation — defined as the extent to which stacks are separated into individual platelets — plays a critical role in the barrier performance of the resulting composite. As exfoliation progresses, the aspect ratio of the MMT agglomerates and stacks, which is initially close to 1, increases. Achieving complete exfoliation of MMT stacks into individual platelets is widely regarded as the most difficult challenge in producing polymer/MMT composites. The exfoliation behavior of MMT depends on several factors, including the source of the MMT, the exfoliation medium, and the specific methods and conditions applied during the process [91]. For large agglomerates (sizes exceeding 1 µm), the contribution of hydration shells is negligible due to the low surface-to-volume ratio. However, as exfoliation proceeds, the surface area increases substantially, enabling the adsorption of more water molecules. Consequently, the degree of exfoliation directly influences the amount of MMT that can be dispersed in water. A higher degree of exfoliation, corresponding to a larger surface-to-volume ratio, requires a lower concentration of MMT to achieve a stable dispersion. Most scientific studies report that a homogeneous dispersion of MMT in water is achievable only at concentrations below 10 wt% [103–107]. Beyond this threshold, the limited

availability of water molecules prevents the formation of hydration shells around all particles, resulting in the formation of pasty dispersions.

1.3.4. Silicate-based composites

Mixing a polymer lacquer with a silicate dispersion results in a silicate-based composite lacquer. The fabrication process is described in this section and compared to alternative methods for producing silicate-based composites. For MMT dispersions, several key parameters affect the final composite properties, including the particle size, type of interlayer ions, chemical modifications, dispersion pH, surface energy, dispersion method, and solid content. Similarly, critical factors for the liquid polymer component include the polymer type, medium (e.g., solvent-free systems, dispersions, or solutions), pH, molecular weight, surface energy, solid content, and any chemical modifications. In addition to producing detailed analyses — such as those addressing specific mixing ratios based on solid content — it is equally important to identify and evaluate overarching trends within these systems. This holistic approach provides a comprehensive understanding of the interrelationships between the material properties and the fabrication process, and ultimately guides the development of silicate-based composite lacquers.

Fabrication of silicate-based composites

Three primary methods are used to fabricate composites based on silicate platelets: melt intercalation, in-situ polymerization, and solution intercalation (Figure 1.7). In in-situ polymerization, phyllosilicates are first swollen in a liquid monomer or monomer solution. The monomers penetrate the interlayer spaces of the silicate, and polymerization is subsequently initiated using radiation, heat, or chemical initiators. This process generates polymer chains within the silicate interlayers, which can promote delamination [109].
Melt intercalation involves mixing the polymer and silicate platelets in the solid state, followed by heating the mixture above the polymer's softening point. If the silicate surface is compatible with the polymer chains, the polymer penetrates the interlayer spaces. Strong shear forces generated during extrusion further facilitate polymer intercalation and disaggregation of silicate particles. This method is particularly attractive for industrial applications, as it can be implemented using standard compounding equipment. However, hydrophilic silicate particles require surface modification with surfactants to achieve compatibility with hydrophobic polymer matrices, such as PP or PE [110]. Additionally, the high

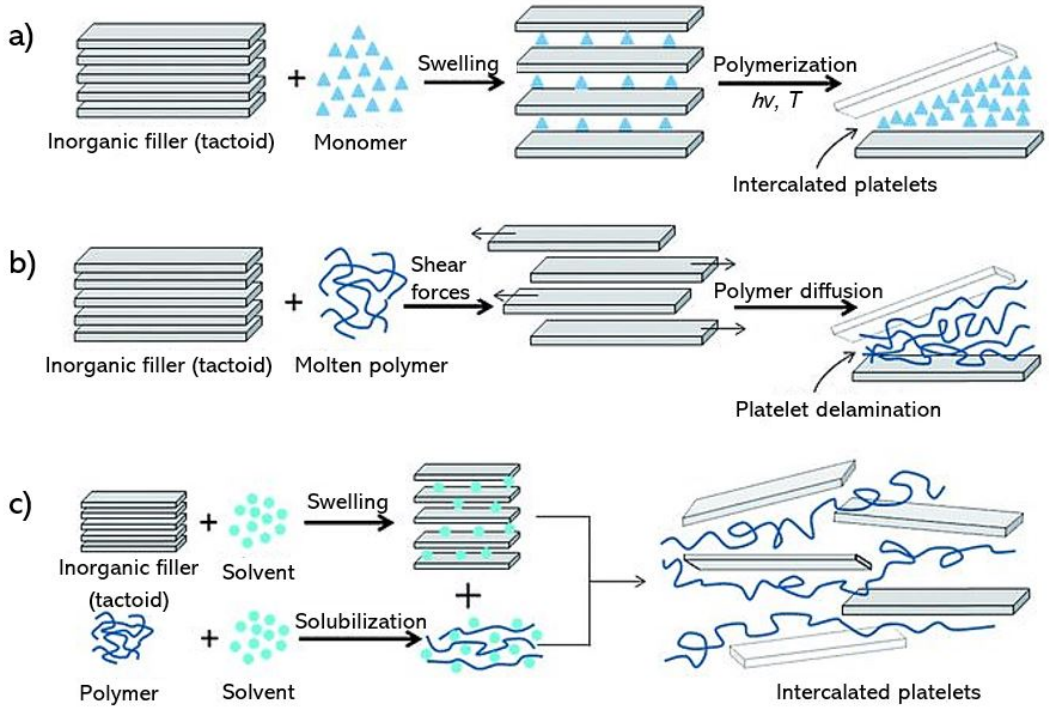

Figure 1.7.: Illustration of (a) in-situ polymerization, (b) melt intercalation, (c) solution intercalation (adapted from Uysal-Unalan et al. [108]).

viscosity of the polymer melt poses a significant challenge, as viscosity increases exponentially with silicate content, limiting the amount of silicate that can be incorporated while maintaining processability [18, 111, 112].

In solution intercalation, silicates are first dispersed in a solvent (e.g, water), where they swell and form a dispersion. This dispersion is then mixed with a polymer solution or dispersion that uses the same solvent. Once the solvent evaporates, the composite material remains. However, this method is limited by compatibility issues with the used solvents, which restricts the range of applicable materials [113].

An alternative fabrication approach, not depicted in Figure 1.7, is layer-by-layer (LbL) assembly. In this technique, alternating layers of polymer and silicate are deposited to create high-barrier stacks. While LbL assembly offers exceptional barrier properties, it faces considerable challenges related to material adhesion and is economically unfeasible due to the complexity and labor-intensive nature of the process [114–116].

Key parameters influencing composite properties

There are four major parameters that affect the macroscopic properties of the composite [35]:

- Aspect ratio of the filler particles
- Homogeneity of the filler dispersion
- Filler orientation within the coating layer and homogeneous distribution within the coating layer
- Interactions inbetween polymer chains, filler particles, and between polymer and filler

The aspect ratio of filler particles (Eq.1.14) significantly impacts two primary properties of barrier composites: the barrier potential and composite lacquer viscosity. A higher aspect ratio enhances the barrier potential, as fewer particles are required to completely cover the permeation surface, thereby maximizing the diffusion path [117–119]. However, high-aspect-ratio fillers tend to increase viscosity substantially, even at low filler contents [120]. To ensure processability, lacquers containing high-aspect-ratio fillers must have either a low total solid content or a reduced filler concentration. Consequently, achieving an optimal balance between high barrier performance and moderate viscosity is critical for practical applications.

The quality of filler dispersion determines the ability of particles to be distributed homogeneously, exfoliated (i.e., individually separated), and equidistantly arranged within the polymer matrix. Poor dispersion, characterized by agglomeration or accumulation in specific regions, reduces homogeneity and adversely affects the barrier performance. Agglomerated particles do not effectively extend the diffusion path, resulting in gas barrier properties that are lower than theoretically achievable.

Filler orientation within a composite is influenced by the fabrication process, filler morphology, and characteristics of the polymer matrix. During film production, shear forces — such as those generated during extrusion — tend to align platelet-shaped particles along the direction of shear [18, 111, 112]. Similarly, in liquid composite coating processes using laboratory-scale techniques (e.g., k-bar coating, doctor blade application, spin coating), particles typically align parallel to the shear direction. To optimize gas barrier properties, a parallel alignment of particles in the composite layer is ideal, as illustrated schematically in Figure 1.4. Conversely, for applications requiring increased ductility or fracture toughness, a heterogeneous particle orientation may be preferred [121, 122].

In two-material systems, interactions between the polymer and filler help to stabilize the mixture. If the interactions between polymer particles or between filler particles are energetically favored over polymer/filler interactions, the mixture

may become unstable and non-homogeneous, leading to de-mixing and the formation of agglomerates [123]. Typically, polymer/filler interactions involve van der Waals attractions [124]. However, if fillers possess hydroxyl groups, such as in the case of MMT, hydrogen bonding can also occur, further influencing the stability and dispersion of the mixture [35]. In both polymer dispersions and polymer solutions, dissolved polymer strands or dispersed spherical polymer beads are surrounded by hydration shells. When mixed with an MMT dispersion, the MMT particles compete with the polymer particles for water molecules to maintain their hydration shells. As the total solid content increases, a critical threshold is reached at which there are insufficient water molecules to maintain hydration shells around all polymer particles and MMT platelets. At this point, agglomeration occurs at the microscopic level, and the mixture transitions from a flowable state to a paste-like consistency. This behavior underscores the importance of balancing hydration dynamics and solid content during composite formulation.

Silicate composites based on polyvinyl alcohol

Polyvinyl alcohol (PVA) is the most commonly used polymer matrix for silicate-based composites. This is due to its intrinsic properties, including excellent oxygen barrier performance, chemical resistance, processability, non-toxicity, non-carcinogenicity, biodegradability, and affordability. Additionally, its hydrophilic nature facilitates hydrogen bond formation with the silanol groups (-Si-OH) of MMT. This interaction enables MMT and other phyllosilicates to act as crosslinkers for hydrophilic polymers, thereby enhancing the composite's structural integrity and performance [125, 126]. Table 1.1 provides an overview of silicate-based composite coatings with PVA as the polymer matrix, highlighting their properties and applications.

A notable observation from the reviewed studies is that the total solid content typically remains below 2 wt%, with the exception of the work by Nyflött et al., who employed a lacquer with 13 wt%. Low solid content has several implications for the coating process. To achieve a desired dry-coating layer thickness, either multiple coats must be applied [118, 129, 131, 133, 136, 137], or a thick liquid film must undergo prolonged drying times, often exceeding 30 min [127, 130, 134, 135]. In some cases, low solid content results in very thin dry films, with measurements as low as 150 nm [135]. The drying duration should be evaluated under realistic industrial conditions, such as those encountered in roll-to-roll (R2R) coating processes. For instance, a combination of a web speed of 150 m/min and

Table 1.1.: List of published studies on silicate-based composite gas barrier coatings with a polymer matrix of polyvinyl alcohol.

Author	Lacquer	MMT exfoliation	coating technique	substrate (thickness)	oxygen permeability ($\frac{cm^3\ (STP)\ \mu m}{m^2\ d\ bar}$)	explanation for barrier improvement
Grunlan et al. [127]	PVA and MMT with 4:1 mixing ratio; total solid content of 1.5 wt%; modified with 1 wt% iactonic acid	Stirring in hot polymer solution for 4 to 8 h followed by 24 h stirring at RT and 24 h rolling	k-bar coating	PET (50.8 µm)	0.03 (23 °C/55 %RH) BIF of 21 compared to unfilled PVA	Addition of silicate particles disrupts polymer crystallinity and occupies polymers' hydroxy groups, but the benefit of the tortuous path effect outweighs these adverse factors
Nyflött et al. [128]	PVA and kaolin (modified with NaPAA) with 8:5 mixing ratio; total solid content of 13 wt%; adjusted to pH 7.3 with NaOH	Stirring in water (undefined duration), then mixing with PVA solution (undefined duration)	k-bar coating	PET (23 µm)	0.70 (23 °C/50 %RH) BIF of 1.7 compared to unfilled PVA	Tortuous path effect introduced by polymer crystallinity and kaolin platelets traps oxygen molecules; elongated lag time for thicker coating layers
Ding et al. [129]	PVA and MMT with 1:1 mixing ratio; total solid content of 1.5 wt%; cross-linked with glutaraldehyde	Stirring in water (undefined duration) followed by 30 min ultrasonication, then mixing with polymer solution and 30 min ultrasonication	4x dip coating	PET (24 µm)	0.07 (23 °C/0 %RH) BIF of 127 compared to unfilled PVA	High level of orientation and very dense packaging of MMT are the reason for outstanding barrier performance
Tsurko et al. [118]	PVA and synthesized silicate (fluorohectorite) with 1:1 mixing ratio; total solid content of 0.25 wt%	Osmotic swelling in deionized water (undefined duration), then shaking with PVA solution over night	100 to 1000x spray coating	PET (36 µm)	4.05×10^{-4} (23 °C/50 %RH) BIF of 489 compared to unfilled PVA	Incorporation of large aspect ratio particles reduces oxygen permeation due to tortuous path effect
Song et al. [130]	PVA and MMT with 1:1 mixing ratio; total solid content of 2 wt%	Dispersion in deionized water and rolling over night, then mixing with PVA solution for 5 min	solution casting	PET (179 µm)	0.002 (23 °C/0 %RH) BIF of 149 compared to unfilled PVA	Oxygen molecules follow a tortuous path forced by silicate platelets; better platelet alignment increases tortuosity
Ben Dhieb et al. [131]	PVA and MMT separately coated with 0.5 wt% solid content	Dispersion in DI water (undefined duration)	30x blade	PET (16 µm)	0.20 (23 °C/0 %RH) BIF of 24 compared to unfilled PVA	Silicate loading enhances tortuosity in the film; high density of hydroxy groups in PVA and MMT leads to strong hydrogen bonding and therefore to a reduction of free volume in the coating, which reduces permeability

Author	Lacquer	MMT exfoliation	coating technique	substrate (thickness)	oxygen permeability ($\frac{cm^3\,(STP)\,\mu m}{m^2\,d\,bar}$)	explanation for barrier improvement
Dabbaghianamiri et al. [132]	PVA and MMT separately coated with 0.3 and 0.45 wt% solid content, respectively	Dispersion in deionized water (undefined duration), then 30 min ultrasonication	12x inkjet printing	PET (110 µm)	0.90 (23 °C/0 %RH) BIF of 2760 compared to PVA layer with similar thickness	Highly ordered and oriented MMT leading to elongation of tortuous path; combined with constrained polymer effect induced by interaction of silicate and polymer
Meng et al. [133]	PVA and MMT with 1:2 mixing ratio; total solid content of 1.5 wt%	Stirring in distilled water for 12 h, then 2 h cooled ultrasonication, after mixing with polymer again 1 h ultrasonication	9x dip coating	PET (50 µm)	6.00 (23 °C/0 %RH) no reference for unfilled PVA given	Reducing the space among deposited silicate layers improves oxygen barrier due to compact shielding; lower amount of little cracks
LaChance et al. [134]	PVA and MMT with 1:1 mixing ratio; total solid content of 1.5 wt%; crosslinked with glutaraldehyde	Stirring in deionzed water (undefined duration), then stirring with PVA solution (undefined duration), last ultrasonication of mixture (undefined duration)	blade coating	PET (25.4 µm)	0.03 (23 °C/0 %RH) no reference for unfilled PVA given	High orientation level and dense packing orientation level; dense packing of MMT nanosheets creates tortuous path for oxygen diffusion
LaChance et al. [135]	PVA and MMT with 1:1 mixing ratio; total solid content of 1.5 wt%	Stirring in deionzed water (undefined duration), then stirring with PVA solution (undefined duration), last ultrasonication of mixture (undefined duration)	spin coating	PET (25.4 µm)	0.43 (23 °C/0 %RH) no reference for unfilled PVA given	High orientation level and dense packing orientation level; dense packing of MMT nanosheets creates tortuous path for oxygen diffusion
Yue et al. [136]	PVA and MMT with 1:1 mixing ratio; total solid content of 1.5 wt%; crosslinked with glutaraldehyde and HCL	1 h stirring in water, then 1 h ultrasonication, after mixing with PVA solution stirring for 1 h followed by short ultrasonication, supernatant after 3 d used for coating	4x dip coating	PPC-P (122 µm)	0.26 (23 °C/0 %RH) BIF of 60 compared to unfilled PVA	High concentration of well-oriented MMT nanosheets with high aspect ratio leads to tortuous pathway for permeating oxygen molecules
Zou et al. [137]	PVA and MMT with 1:1 mixing ratio; total solid content of 1.5 wt%; crosslinked with glutaraldehyde	Stirring in deionized water over night, then mixing with PVA solution, followed by stirring for 4 h, then 30 min ultrasonication of mixture	2x dip coating	PET (?)	0.15 (23 °C/0 %RH) no reference for unfilled PVA given	Large amount of highly-oriented MMT in PVA contributes to thicker and denser composite coating layers

a dryer-path of 50 m corresponds to a drying time of 20 s [138]. A key objective in the development of silicate-based composite coatings with PVA is to increase the solid content to a level that allows the desired film thickness to be achieved in a single coating step, while maintaining a drying time of less than one minute. It is noteworthy that the dispersion of MMT in water, which is expected to yield optimal exfoliation, often requires prolonged durations exceeding 12 h in many published studies [118, 127, 130, 133, 136, 137]. In some cases, researchers have attempted to accelerate exfoliation using ultrasonic treatment, both prior to and following the mixture with PVA [129, 132–137]. However, several publications place little or no emphasis on the preparation of silicate dispersions, despite exfoliation being a critical step that significantly impacts the overall performance of the composite [128, 131]. Consequently, an important objective in the development of new composite lacquers is to establish a short, reproducible method for dispersing MMT particles in water and achieving a consistent degree of exfoliation.

PVA is known for its excellent oxygen barrier properties, with reported values ranging from 1 to 6 $\frac{\mathrm{cm^3\,(STP)\,\mu m}}{\mathrm{m^2\,d\,bar}}$ [127, 128, 139, 140]. The incorporation of silicate particles can significantly enhance this barrier performance, a finding consistently demonstrated in the studies on free-standing PVA films and composite coatings [35, 141–146]. In many cases, the improvement in barrier properties is primarily attributed to the tortuous path effect [118, 128–130, 136]. Other investigations emphasize factors such as the orientation of the barrier particles [134, 135] or the increased density of the coating [133–135, 137]. However, the role of interactions between PVA and MMT, particularly the contribution of hydrogen bonding to enhanced barrier performance, is addressed only occasionally in the literature. Addressing this challenge raises the first scientific question: How do the exfoliation process and the mixing ratio affect the gas barrier performance of a PVA/MMT composite layer?

Silicate composites based on alternative polymer matrices

In addition to PVA, which is the most commonly used polymer matrix for silicate-based composites, other polymers are also employed as matrix materials. The selection of alternative polymer matrices is driven by several factors. From a basic research perspective, it is important to identify alternatives to PVA [158], to develop fully bio-based composites as replacements for fossil-based materials [159], and to explore the impact of differences in the properties of commonly used polymers when identical fillers are considered [160]. From an application

Table 1.2.: List of published studies on silicate-based composite gas barrier coatings with alternative polymer matrices than PVA.

Author	Lacquer	coating technique	oxygen permeability ($\frac{cm^3\,(STP)\,\mu m}{m^2\,d\,bar}$)	Water vapor permeability ($\frac{g\,mm}{m^2\,d}$)	explanation for barrier improvement
Osman et al. [117]	Epoxy resin with organo-MMT with a mixing ratio of 19:1 and a total solid content of 10 wt%	k-bar	585 (23 °C/0 %RH) BIF of 2.6 compared to coating with unfilled epoxy resin	4.6 (23 °C/100 %RH) BIF of 1.7 compared to coating with unfilled epoxy resin	Exfoliated MMT built the permeation barrier; creation of tortuous pathway
Lai et al. [147]	Polyacrylate latex with MMT with a mixing ratio of 32:1 and a total solid content of 10 wt%	k-bar	2.9 (?/?) BIF of 1.2 compared to coating with unfilled polyacrylate	13.5 (?/?) BIF of 2.5 compared to coating with unfilled polyacrylate	MMT particles lead to tortuous path; high dispersion quality
Nazarenko et al. [148]	Polystyrene mixed with organo-MMT with a mixing ratio of 10:3 and a radical initiator of 2,2-azobis (isobutyronitrile)	fsf (compression molded)	4×10^4 (25 °C/0 %RH) BIF of 3.1 compared to unfilled polystyrene	Not measured	Tortuous path theory; the better the interaction of polymer matrix with the silicate, the better the gas barrier
Yuan et al. [149]	Polyurethane with organo-MMT with a mixing ratio of 13:1 and a total solid content of 25 wt%	k-bar	9.3×10^3 (23 °C/0 %RH) BIF of 4.4 compared to unfilled polyurethane	Not measured	High dispersion quality leads to high gas barrier
Herrera-Alonso et al. [150]	Co-polymer of methyl methacrylate and butyl methacrylate with MMT with a mixing ratio of 19:1 and a total solid content of 10 wt%	fsf	0.259 (25 °C/0 %RH) BIF of 3.25 compared to unfilled co-polymer coating	Not measured	High level of exfoliation and dispersion quality
Introzzi et al. [151]	Pullulan with MMT with a mixing ratio of 3:1 and a total solid content of 3 wt%	k-bar	11.7 (23 °C/70 %RH) BIF of 9.8 compared to unfilled pullulan	Not measured	Tortuous path theory; re-agglomeration of MMT particles leads to reduced gas barrier compared to calculated value

Author	Lacquer	coating technique	oxygen permeability ($\frac{cm^3\ (STP)\ \mu m}{m^2\ d\ bar}$)	Water vapor permeability ($\frac{g\ mm}{m^2\ d}$)	explanation for barrier improvement
Möller et al. [152]	UV-curable polyurethane with synthetic hectorite with a mixing ratio of 3:1 and a total solid content of 4 wt%	k-bar	13.1 (23 °C/50 %RH) BIF of 312 compared to unfilled polyurethane coating	Not measured	Tortuous path theory; theory assumes no change in matrix permeability due to fillers and does not consider changes in free volume at the interfaces
Wu et al. [153]	Oxidized cellulose nanofibrils with MMT with a mixing ratio of 1:1 and a total solid content of 1 wt%	fsf (poured in Petri dish)	0.5 (23 °C/50 %RH) BIF of 4 compared to unfilled cellulose nanofibrils	Not measured	MMT forms multiwalls, hindering oxygen permeation and closing nanosized pores
Kochumalayil et al. [154]	Xyloglucan with MMT with a mixing ratio of 4:1 and a total solid content of 5 wt%	k-bar (R2R)	0.05 (23 °C/50 %RH) BIF of 9 compared to unfilled Xyloglucan coating	Not measured	Tortuous path effect; permeation values in good accordance with Nielsen model
Malucelli et al. [155]	Acrylic latex mixed with organo-MMT with a mixing ratio of 19:1 and a total solid content of 43 wt%	k-bar	0.29 (25 °C/0 %RH) BIF of 1.2 compared to unfilled acrylic coating	Not measured	Increase of tortuosity of diffusion path
Agarwal et al. [156]	Nylon6 with MMT with a mixing ratio of 19:1 and a total solid content of 20 wt% in formic acid	spin coating	12.5 (?/?) BIF of 2.8 compared to unfilled Nylon6 coating	8.4 (?/?) BIF of 1.8 compared to unfilled Nylon6 coating	No explanation
Lim et al. [157]	Polyacrylic acid with MMT with a mixing ratio of 100:1 and a total solid content of 10 wt%	k-bar	4.37 (25 °C/50 %RH) BIF of 10 compared to unfilled PAA coating	No barrier improvement achieved for PAA with integration of MMT	Tortuous pathway formed by dispersed MMT particles

perspective, alternatives should be sought, to enhance specific properties that PVA may not offer. These include improved sealability at moderate temperatures (<150 °C), compatibility with extrusion processes, stable gas barrier performance at high humidity levels (>60 %RH), and increased buckling resistance of the barrier layer [161–163].

Table 1.2 presents a selection of silicate-based composites with enhanced gas barrier properties that use polymer matrices other than PVA. Despite employing less common polymer matrices, hydrophilic polymers such as acrylates, nylon-6, polyurethanes, polyethylene glycol, and various biopolymers are predominantly combined with MMT. The hydrophilicity of these polymers provides two main advantages: first, hydrophilic polymers form hydration shells, which improve the dispersion of MMT in water without compromising the dispersion quality; and second, their hydrophilicity facilitates the formation of hydrogen bonds between the filler and the matrix, potentially enhancing the composite's structural integrity and barrier performance.

An analysis of the BIF reveals that PVA-based composites generally exhibit higher BIFs. To better understand the influence of polymer-matrix interactions on gas barrier performance, a key research objective is to mix different polymers with the same MMT particles and investigate the resulting composite's gas barrier properties.

Compared to PVA composites, those with alternative polymer matrices typically have a lower MMT-to-polymer mixing ratio. Additionally, the total solid content of the lacquers tends to be higher in these composites. The mixing ratio and total solid content are opposing factors in the development of barrier lacquers [164]. A higher concentration of silicates in the composite generally improves the gas barrier potential; however, it also increases the viscosity. When the lacquer's viscosity exceeds 100 mPa s at the shear rate applied during the coating process, it becomes difficult to apply. Therefore, the challenge lies in balancing these two parameters, by using either lacquers with low total solid content and high MMT concentration, or those with a high total solid content and a low MMT concentration. To facilitate a meaningful comparison of composites with different polymer matrices, the goal should be to maintain a constant mixing ratio between the polymer and MMT.

The form of the lacquer — whether a dispersion or a solution — also influences both the mixing ratio and the total solid content [165]. Dispersions can typically be processed with higher solid contents due to their lower viscosity and the reduced impact of MMT on viscosity. This is attributed to the generally weaker interaction between MMT and the polymer in dispersions compared to solutions.

To further investigate the role of MMT/polymer interactions in the liquid phase, both dispersions and solutions with identical MMT contents could be mixed and analyzed for their interaction effects.

Many studies on gas barrier coatings primarily focus on oxygen and water vapor permeation, as these are the most critical properties for applications such as food packaging [74]. Some studies have also investigated the barrier properties for other gases, such as CO_2 [87, 145], helium [150, 166–169], hydrogen [168, 169], and nitrogen [167, 170]. Because these permeants differ in size and polarity, different factors are likely to influence their permeation through silicate-based composites. To better understand the mechanisms of gas permeation and optimize composite formulations, a key objective is to test the gas barrier performance of the same composite against different gases. This approach can help identify which composite properties most significantly affect the permeation of specific gases and to what extent.

In addition to composites with hydrophilic polymers, studies have also examined the gas barrier properties of composites with hydrophobic polymers, such as PP [111, 112, 166, 167, 171]. For these composites, melt intercalation is the preferred fabrication method. In this process, MMT is dispersed in molten PP, and the composite is extruded rather than coated [74]. Compared to coating a flexible film with a composite barrier lacquer, extrusion offers the advantage of requiring only a single manufacturing step to produce the gas barrier film. However, one limitation of this method is that only small amounts (<10 wt%) of MMT can be incorporated into the PP, as higher MMT concentrations rapidly increase the melt viscosity, rendering the material difficult to process. As with the composites shown in Table 1.2, the low MMT content in extruded composites is the primary reason for their relatively low BIFs. The main advantage of extruded composite films lies in the enhancement of their mechanical properties, with gas barrier improvement being a secondary benefit. Although it may seem counterintuitive to combine hydrophobic, relatively inert PP with MMT particles — given that polymer/MMT interactions can significantly improve gas barrier properties — this approach provides an opportunity to adjust the mixing ratio and increase the MMT content, thereby enabling a comparison of mixing ratios similar to those used with hydrophilic polymers. Given these considerations, the following scientific question arises when comparing PVA-based composites with those based on other polymers: To what extent do polymer/MMT interactions influence the gas barrier performance for gases of different polarity and size?

1.3.5. Coating processes for barrier lacquers

Various methods are employed to apply lacquers onto flexible films, resulting in thin-film coatings. In contrast to evaporation techniques such as physical vapor deposition (PVD), lacquer coating is a solution-based process [172]. In this process, a lacquer is uniformly applied to a substrate, and then dried. A key distinction exists between sheet coating — used for small film sections in laboratory settings — and R2R coating, which is more suitable for industrial-scale production [138, 173]. Sheet coating enables rapid application of different lacquers onto prepared sheets during the development phase, whereas R2R coating facilitates the automatic coating of large volumes of film material in a relatively short time. The main coating techniques include spin coating, dip coating, slot-die coating, k-bar coating, spray coating, and gravure coating [174]. These techniques are generally categorized based on their suitability for laboratory-scale or R2R applications, with some techniques adaptable to both scales.
During the coating process, precise control over the quantity of lacquer applied to the substrate is critical. This control, referred to as metering, directly determines the coating weight [175]. Coating techniques can be classified as either self-metered or pre-metered, depending on how the coating weight is regulated. In a self-metered coating process, the coating weight is determined by the intrinsic properties of the lacquer, the substrate, and the applicator. Key factors influencing this process include lacquer viscosity, flow behavior, application technique, coating speed, and the interactions between the surface energies of the lacquer and substrate, and other variables. Due to the interplay of these factors, the exact coating weight must be evaluated for each specific set of parameters. In contrast, a pre-metered coating process precisely defines the coating weight by controlling the lacquer flow rate. In this case, the device supplying the lacquer, such as a pump, directly regulates the coating weight, independent of the application technique itself [176].

Coating techniques for composite barrier lacquers

Spin coating. In spin coating, the lacquer is deposited at the center of a substrate that is then rapidly rotated on a flat surface. The centrifugal force spreads the lacquer evenly, and the resulting film thickness is influenced by factors such as lacquer viscosity, surface tension, and rotational speed. This self-metered process can produce uniform films ranging from nanometers to microns, using a wide variety of solutions. Due to the air flow generated during spinning, external heat may not be necessary for drying. Spin coating is cost-effective and well

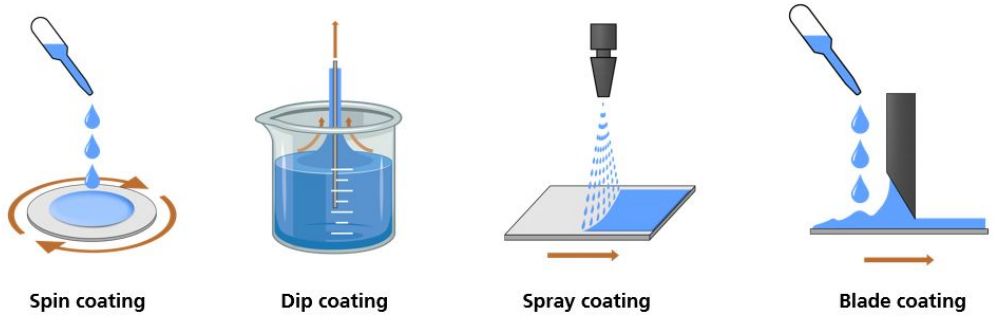

Figure 1.8.: Schematic drawing of four coating techniques: spin coating, dip coating, spray coating, and blade coating. The lacquer is shown in blue and the coating direction is indicated by the orange arrows (adapted from Kwon et al. [174]).

suited for small batches and individual films in thin-film research. However, its batch-based nature makes it unsuitable for large-scale production, and it tends to generate significant waste, as excess solution is spun off [177].

Dip coating. In dip coating, the substrate is immersed in a lacquer solution and then withdrawn at a controlled rate. The thickness of the wet film depends on the withdrawal speed, ambient air flow, and lacquer viscosity; thus, dip coating is classified as a self-metered technique. After withdrawal, the substrate is dried either at ambient temperature or in an oven to accelerate drying. This method is simple and versatile, allowing for the adjustment of film thickness by varying key parameters, and ensuring the uniform coating of both sides of the substrate. However, dip coating typically requires a large amount of lacquer, leading to substantial waste, and the wet film is sensitive during drying, often necessitating cleanroom conditions or fume hoods to prevent contamination [174].

Spray coating. Spray coating atomizes the lacquer using a stream of pressurized gas, breaking it into fine droplets that are uniformly deposited onto the substrate to form a wet film. The final film thickness is determined by surface tension, lacquer viscosity, gas flow properties, nozzle characteristics, wetting behavior, solid content, coating distance, and application speed. As a pre-metered coating technique, spray coating is well-suited for producing thin films, although thicker films can be achieved by creating multiple layers. The method is scalable for both laboratory and industrial applications and generates relatively low levels of waste. However, optimizing the lacquer formulation and nozzle settings to achieve a uniform spray pattern that yields a homogeneous dry film remains a key challenge [178].

Blade coating. In blade coating, the lacquer is applied in front of a blade that is positioned at a small distance from the substrate. As the substrate or the

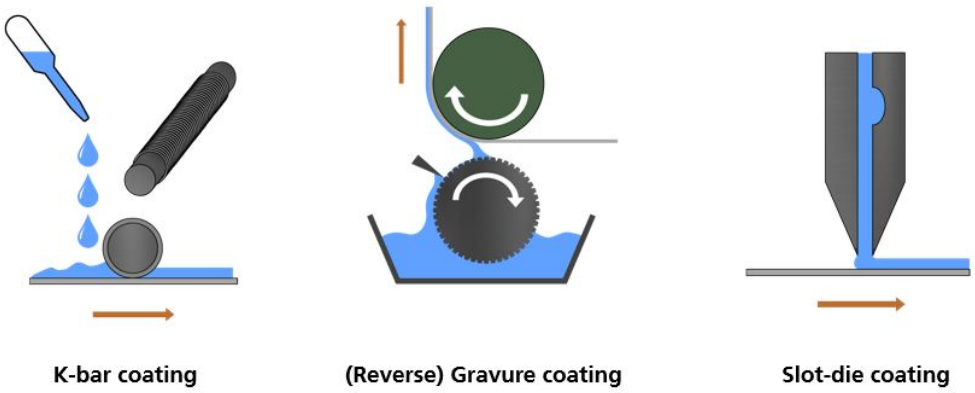

Figure 1.9.: Schematic drawing of three coating techniques: k-bar coating, reverse gravure coating, and slot-die coating. The lacquer is shown in blue and the coating direction is indicated by the orange arrows (adapted from Kwon et al. [174])

blade moves, the lacquer is evenly spread over the surface. The film thickness is controlled by the distance between the blade and the substrate, the lacquer viscosity, and the coating speed, making this a self-metered process. Blade coating is versatile, applicable for a wide range of viscosities and substrates (both rigid and flexible), and it is efficient for large-scale production, with lower levels of waste compared to dip and spin coating. However, achieving very thin films (less than 10 µm) can be challenging, and contamination of the lacquer or the surrounding environment may lead to streaks in the wet film [179].

K-bar coating. The K-bar coating technique is similar to blade coating and is also a self-metered process. In this method, a lacquer is applied in front of a bar wrapped with a precision wire of a specific diameter. As the bar is drawn across the substrate, the lacquer is metered through the gaps between the wire windings, resulting in a consistent coating. Key process parameters include the type of bar, the wire diameter, the applied pressure, the coating speed, and the properties of the lacquer, such as viscosity and solid content. Although K-bar coating allows quick changes in the bars and can accommodate a range of coating thicknesses, a drawback is that the wire pattern can sometimes be transferred onto the lacquer layer, particularly if the lacquer has a high viscosity. Additionally, the scaling up of the process is limited by the rate at which the lacquer fills the gaps via capillary action [180].

Gravure coating. Gravure coating employs an engraved gravure roll that rotates in a reservoir of lacquer. The lacquer fills the engraved cells on the roll, and when the roll contacts the substrate, the lacquer is transferred to form a liq-

uid film. As a self-metered process, gravure coating is widely used in large-scale production due to its ability to produce precise and uniform films at high speeds [138]. It can handle a broad range of lacquers, from low to high viscosity. However, similar to K-bar coating, there is a risk of transferring the cell pattern onto the film when using highly viscous lacquers. Additionally, adjusting the coating thickness can be time-consuming, often requiring modification of the lacquer's solid content or a change in the gravure roll. Exposure of the lacquer reservoir to ambient air may lead to solvent evaporation, altering the solid content and consistency of the coating [181].

Slot-die coating. In slot-die coating, the lacquer is pumped through a die at a defined flow rate while the substrate moves relative to the die head, making this a pre-metered process. Critical parameters, such as flow rate, die opening length, substrate (web) speed, lacquer viscosity, and solid content must be finely adjusted to optimize film uniformity and stability. Slot-die coating is versatile and efficient, capable of processing both high- and low-viscosity lacquers and accommodating a wide range of film thicknesses. It minimizes waste since nearly all the pumped lacquer is used. The technique is applicable in both laboratory-scale sheet coating and industrial-scale R2R processes. However, its complexity, due to the numerous parameters that must be controlled, requires substantial expertise to achieve defect-free coatings, and the intricate flow physics can make troubleshooting challenging. Additionally, the need to clean the die means this coating technique can be more labor-intensive than others compared to other coating techniques [182].

Coating with composite lacquers

The coating process is a critical factor in the performance of a gas barrier lacquer, as the lacquer properties must be aligned with the specific coating technique used [183]. For example, the flow characteristics, viscosity, and solid content of the lacquer influence the final appearance of the dry coating layer, which is determined by the chosen coating technique. For composite lacquers optimized for gas barriers, an additional factor comes into play: the tortuous path effect. This effect is most pronounced when platelet-shaped particles are aligned parallel to the substrate surface and perpendicular to the direction of gas permeation. The degree of alignment and particle distribution in the barrier layer is influenced by various factors, including the coating method used.

Tables 1.1 and 1.2, which list MMT-based gas barrier coatings, indicate that all coatings were applied on a laboratory scale. The techniques employed include

spin coating, dip coating, k-bar coating, injection printing, spray coating, blade coating, and solution casting. In other reviews of studies involving composite barrier coatings, such as those by Uysal-Unalan et al. [108], Joshi et al. [184], and Rovera et al. [75] there is likewise no mention of R2R coatings. Transitioning from laboratory-scale to industrial-scale R2R coating involves adapting the lacquer formulation to the specific requirements of the R2R process — a challenge that can be as difficult as the initial lacquer development itself. To the author's knowledge, there have been no studies on R2R coating of silicate-based composite barrier lacquers. This gap in the literature leads to the following scientific question: What modifications to a composite barrier lacquer are necessary in order to scale up from laboratory-scale coating to roll-to-roll coating?

1.4. Scientific questions and aim of the thesis

Numerous studies have focused on enhancing the gas barrier properties of polymers by incorporating platelet-shaped silicate particles. However, drawing generalizable conclusions remains challenging, as each polymer/silicate combination behaves differently. It is essential to elucidate the gas permeation mechanisms through these composites and to understand how various parameters influence their performance. Therefore, this thesis aims to address the following scientific questions:

1. **How do the exfoliation process and the mixing ratio affect the gas barrier performance of a PVA/MMT composite layer?**
   The exfoliation of MMT in water is typically achieved via mixing and ultrasonication. Theoretically, the highest gas barrier values are reached when the composite contains a maximum amount of silicate particles. In Section 3.1, the preparation of a PVA/MMT gas barrier lacquer formulation is described. This includes both a comparison of two mechanical mixing methods, using a high-shear mixer and a planetary ball mill to disperse MMT in water, and the identification of the optimum mixing ratio of PVA and MMT.
   The incorporation of impermeable MMT particles into the PVA polymer matrix extends the diffusion path for gas molecules, resulting in a lower permeation coefficient. Measurements of the oxygen barrier at various temperatures not only yield the permeation coefficient for the composites but also enable the determination of the activation energy for permeation. The

combined analysis of these parameters facilitates a deeper understanding of how silicate incorporation modifies the polymer matrix structure and affects gas barrier performance.

2. **To what extent do polymer/MMT interactions influence the gas barrier performance for gases of different polarity and size?**
   The permeation mechanism is affected by both the size and the polarity of the gas molecules. Helium, hydrogen, and oxygen differ in their kinetic diameters, while water vapor, being polar, introduces additional complexities, such as condensation behavior and solubility mechanisms. In Section 3.2, the gas barrier properties against these four permeants are evaluated for silicate-based composites formulated with different polymer matrices (e.g., PVA, acrylate and PP). This investigation focuses on how the interactions between the polymer and MMT — mediated by factors such as hydrogen bonding — affect the overall barrier performance for gases with varying physicochemical characteristics.

3. **What modifications to a composite barrier lacquer are necessary in order to scale up from laboratory-scale coating to roll-to-roll coating?**
   For industrial applications, it is crucial that the lacquer formulation is compatible with standard R2R coating technologies. Key parameters, such as lacquer viscosity, shear thinning behavior, solid content (which directly influences drying time), and the tendency for re-agglomeration of silicate particles become particularly important during the R2R process. In Section 3.3, the modifications required to adapt PVA/MMT composite lacquers for R2R coating via slot die or gravure techniques are discussed, ensuring that the high gas barrier performance is maintained at an industrial scale.

The overarching aim of this thesis is to address the key challenges in the development and application of composite lacquers, and to attain a comprehensive understanding of the interplay between material properties, processing conditions, and gas permeation in silicate-based composite barrier lacquers.

2. Materials and Methods

Materials

All materials utilized in this investigation are commercially available and are described in detail in the respective references [46, 48, 185]. The polymer lacquers employed as components of the composite barrier lacquers are all water-based formulations. These lacquers are provided either as dispersions (polyacrylic dispersion and polypropylene dispersion) or solutions (polycarboxylic solution and polyvinyl alcohol solution). The silicate particles used as fillers include rod-shaped halloysite and platelet-shaped montmorillonite, both utilized in their unmodified, as-purchased form. PET and BoPP polymer films were selected as substrate materials for the composite barrier lacquers. PET was chosen due to its high surface energy ($44\,\frac{\mathrm{mN}}{\mathrm{m}}$[186]) compared to BoPP ($24\,\frac{\mathrm{mN}}{\mathrm{m}}$) and its lower surface roughness, which make it an optimal reference surface material [187, 188]. The PET film, with a thickness of 23 µm, also exhibits lower water vapor permeability ($8.4\,\frac{\mathrm{g}}{\mathrm{m^2\,d}}$) than the 30 µm BoPP film ($4.9\,\frac{\mathrm{g}}{\mathrm{m^2\,d}}$), allowing for a more precise identification of water vapor barrier improvements at identical coating thicknesses. BoPP was included as a substrate material because the current trend in food packaging favors mono-polypropylene (mono-PP) flexible packaging [189]. Additionally, PP exhibits low barrier properties against oxygen and other non-polar gases, which facilitates the assessment of permeability enhancements for such gases.

Methods

Size determination of silicate particles

Determining the size of the silicate particles is an essential step in the subsequent analysis of the composite barrier layers. First, it is necessary to confirm the particles' shape, that is, halloysites are rods and MMT are platelets. In the case of halloysites, the rod shape is confirmed by analyzing scanning electron microscope (SEM) images of the coating surface as described in [46]. In the case

of MMT, the platelet shape is determined by combining two measurement methods. Theoretically, a single particle must be isolated and its lateral expansion in all three dimensions should be determined by one measuring principle, but this is not possible in practice. Therefore, the particle size is determined in two steps. First, the radius of gyration is determined by a combination of asymmetrical flow field-flow fractionation (AF4) and multi-angle laser light-scattering spectrometry (MALLS), as described in [46]. Since the particles are randomly oriented during laser light-scattering measurement, the results of AF4/MALLS describe the expansion in two dimensions as a random coil, that is, the length and width of the particle. To determine the thickness of the platelets, cross sections of the coated films are prepared by Ar^+ beam milling, and the thickness is measured by SEM as described in [46] and [185].

Viscosity measurement of lacquers

The viscosity of the lacquer is a parameter of particular importance in the processing of the lacquer. MMT dispersions exhibit a shear-thinning behavior, which is transferred to the composite barrier lacquers upon mixing with the polymer lacquers [190]. Consequently, it is essential to determine the viscosity at the particular shear rate encountered during the coating process. The procedures for viscosity determination and the calculation of the shear rate during coating are described in detail in [185] and [48].

Measurement of permeability coefficients

For this thesis, the gas permeation of hydrogen [48], helium [46, 48], oxygen [46, 48, 185] and water vapor [48] was measured following the methods described in the respective references. In all cases, the permeance through a coated film Q_{total} was measured with the coated side facing the measurement chamber that contained the permeant. To allow for comparison of coating layers irrespective of the substrate or any additional layers (i.e., polycarbonate stabilization plate during hydrogen permeation measurements), the permeance of the coating layer Q_{coating} was separated from that of the substrate $Q_{\text{substrate}}$ (and the plate Q_{plate}) by solving Eq.2.1.

$$\frac{1}{Q_{\text{total}}} = \frac{1}{Q_{\text{coating}}} + \frac{1}{Q_{\text{substrate}}} \left(+ \frac{1}{Q_{\text{plate}}} \right) \tag{2.1}$$

To obtain the permeability coefficient of the coating layer P_{coating}, the permeance of the coating layer was normalized to a layer thickness d of 1 µm according to

Eq.2.2.

$$P_{\text{coating}} = Q_{\text{coating}} \cdot d \tag{2.2}$$

Here, the permeability coefficient is expressed in units of $\frac{\text{cm}^3\,(\text{STP})\,\mu\text{m}}{\text{m}^2\,\text{d}\,\text{bar}}$ for hydrogen, helium, and oxygen and in $\frac{\text{g}\,\mu\text{m}}{\text{m}^2\,\text{d}}$ for water vapor. To quantify the improvement in barrier performance due to the integration of silicate particles compared to plain polymer coatings, the barrier improvement factor BIF is calculated via Eq.1.20. Furthermore, measuring the permeance at different temperatures enables the determination of the activation energy for permeation using an Arrhenius approach. The temperature dependence of the permeability coefficient is given by

$$P_{\text{coating}}(T) = P_0 \cdot e^{-\frac{E_\text{A}}{RT}} \tag{2.3}$$

where $P_{\text{coating}}(T)$ is the permeability coefficient at the temperature T, P_0 is the pre-exponential factor, and R is the universal gas constant. The activation energy for permeation has been measured for oxygen[46, 48] and hydrogen[48].

Surface energy measurement

In this investigation, the surface energy of the (pre-treated) substrates and the dried coating layers was determined using the sessile drop method. For the polymer lacquers in their liquid state, for the MMT dispersion, and for their mixtures, the pendant drop method was employed. The underlying principles of these techniques are described in [185] and [48]. The measured surface energies of the substrates and liquid lacquers were used to predict the wetting behavior on the substrate surfaces. Moreover, evaluating the surface energy of both the liquid lacquer components and their mixtures, as well as that of the dried coating layers, provides insight into possible interactions between the polymer and silicate.

Measurement of coating layer thickness

The permeance is inversely proportional to the coating thickness, meaning that thinner layers exhibit higher permeance. Therefore, accurately determining the thickness of the barrier layer is essential for normalizing the permeance values needed to calculate the permeability coefficient. The coating layer thickness was determined either via SEM cross-sectional images with the SEM software [46] or with a precision thickness gauge [48, 185].

Roughness measurement

The surface roughness of the coating layer was measured as described in [185]. This parameter provides a qualitative indication of the degree of particle agglomeration within the coating, as higher roughness values typically correspond to a greater presence of agglomerates.

X-ray diffraction measurement and pole figures

X-ray diffraction (XRD) was employed to characterize the amorphous and crystalline domains within the composite coating layer. During all measurements, the XRD analysis was performed on the coated side of the film using a Cu-K_α radiation ($\lambda = 1.541\,84\,\text{Å}$) source as described in [46] and [48].
The pole figure measurements were conducted at a fixed 2θ angle of 6°, corresponding to the (001) lattice plane of MMT, following the procedures detailed in [185] and [48]. These pole figures enable the determination of the orientation distribution of MMT platelets in the dried coating layer, which is critical for calculating the barrier improvement achieved through particle alignment, as shown in Eq. 1.19.

Fourier transform infrared spectroscopy

Fourier transform infrared (FTIR) spectroscopy is a physical analysis technique in which molecules are stimulated by infrared radiation to probe their vibrational modes [191]. In this investigation, FTIR spectroscopy was utilized to identify interactions between the polymer matrix and the silicate particles. All measurements were performed using the attenuated total reflectance (ATR) method. In this approach, the coated side of the film is brought into contact with a diamond crystal. Given that the penetration depth in polymer coating layers ranges from several hundred nanometers to a few microns, the majority of the spectral information is derived from the coating layer itself, without significant interference from the substrate [192, 193]. Detailed measurement procedures are described in [46] and [48].

Calculation of barrier improvement attributable to filler integration

The permeability coefficient was calculated according to Eq.1.16 in Section 3.1, which does not consider particle orientation, and according to Eq.1.19, which

incorporates a parameter for particle orientation. These calculated values represent the theoretical potential for barrier improvement achievable with various particle shapes and sizes. If the experimental results fall below this theoretical potential, it may indicate that the coating process or sample preparation requires optimization. Conversely, if the experimental values exceed the theoretical predictions, this suggests that, in addition to the geometric factors, beneficial chemical or structural modifications have been induced in the polymer matrix, thereby enhancing the gas barrier properties. However, evaluating these outcomes is challenging because the opposing effects of these factors may cancel each other out. Consequently, it is essential to employ multiple analytical methods to draw robust and reliable conclusions.

3. Results

3.1. Nanocomposite Coatings Based on Polyvinyl Alcohol and Montmorillonite for High-Barrier Food Packaging

by Stefan Schiessl, Esra Kucukpinar, Stéphane Cros, Oliver Miesbauer, Horst-Christian Langowski, and Peter Eisner [46]

In the food packaging sector, there is a steady demand for flexible packaging with high barrier properties. Polyvinyl alcohol (PVA) layers, known for their excellent oxygen barrier performance, can be further improved by integrating impermeable platelet-shaped silicates. The integration of such particles extends the diffusion path for permeant molecules — a phenomenon known as the tortuous path effect — which in turn reduces the permeation coefficient of the composite layer compared to that of the pure polymer. Mathematical models, such as Nielsen's model, can be used to predict the potential improvement in barrier performance.

To investigate the correlation between calculated and measured permeation coefficients, PP films were coated with both pure PVA and PVA-based composite coatings. These coatings were subjected to permeation measurements conducted at different temperatures to determine the activation energy for the permeation. Two types of silicate particles were selected: stick-shaped halloysite and platelet-shaped montmorillonite (MMT). These particles were incorporated into the PVA matrix at mixing ratios of 7, 30, and 47 vol%. For particle dispersion in water, two methods were compared: a laboratory-scale disperser (Ultra-Turrax®) and a planetary ball mill. The permeating gases used were oxygen and helium.

It was shown that the permeation coefficient of a composite layer can be approximated if the particle geometry, the mixing ratio, and the permeability coefficient of the pure polymer are known, provided that the particles are well-dispersed and free of agglomerates. In particular, the dispersion of the particles with a ball mill resulted in composites free of agglomerates, without breaking the sili-

cate platelets or changing their size. The calculation of the permeation coefficient implies that barrier performance improves with increasing particle content; however, an optimum was experimentally identified at 30 vol%. At higher particle loadings, the polymer matrix can no longer be closed, leading to macroscopic defects in the coating. Notably, the activation energy for permeation decreased upon the incorporation of silicate particles, in comparison with pure PVA. Despite this decrease, the overall permeation coefficient was reduced by a factor of 17 for helium and 12 for oxygen at 30 vol% particle content. The results imply that the permeation process through the composite requires less energy than through pure PVA, indicating that permeation may preferentially occur at the polymer/silicate interfaces (i.e., in weak-boundary areas). Moreover, although the activation energy is reduced, the dominant factor in lowering the permeation coefficient is the extension of the diffusion path via the tortuous path effect, which outweighs the influence of the decreased activation energy.

Author contribution: Stefan Schiessl developed the study's concept and design and wrote the manuscript under the supervision of Esra Kucukpinar and Peter Eisner. Oliver Miesbauer and Horst-Christian Langowski contributed to the permeation models. Stéphane Cros performed the helium permeation measurement. Esra Kucukpinar, Peter Eisner, and Horst-Christian Langowski revised the manuscript.

3.2. Mechanisms of permeation of helium, hydrogen, oxygen, and water vapor through silicate-based composite barrier coating layers

by Stefan Schiessl, Esra Kucukpinar, René Schwiddessen, Horst-Christian Langowski, and Peter Eisner [48]

The incorporation of montmorillonite (MMT) into polymer layers can substantially enhance the gas barrier properties of the polymer. Due to the compatibility of the hydroxy groups and the interaction via hydrogen bonding, PVA is a matrix material commonly used in combination with MMT. However, PVA is not universally applicable, particularly in moisture-sensitive environments, which underscores the need to evaluate the compatibility of MMT with alternative matrix materials. This investigation focused on the properties that are decisive for the barrier performance of a composite coating layer and the influences on the permeation mechanisms.
In this study, composite barrier lacquers were prepared using MMT and various polymer matrix materials. Specifically, two water-based dispersions (polypropylene and polyacrylate) and two water-based solutions (polycarboxylic acid and polyvinyl alcohol) were utilized. The polymers were mixed with MMT at mixing ratios of 3:1 and 1:1, and both the composites and the pure polymer were coated onto PET films. The barrier properties of the resulting coatings were then measured against helium, hydrogen, oxygen, and water vapor.
The addition of MMT to the aqueous polymer lacquers increased their viscosity. The resulting composite lacquers showed pronounced shear thinning behavior, particularly for those based on polycarboxylic acid and PVA, which, according to FTIR spectral peak shifts, also interact chemically with MMT. In contrast, no significant interaction was observed for polypropylene and polyacrylate matrices. The measured permeability coefficients correlated with the permeant size, with helium (the smallest species) showing the highest permeability, followed by hydrogen and oxygen. The barrier improvement factors, on the other hand, were found to be highest for the smallest permeant and vice versa. For a composite coating layer made of PVA and MMT, improvement factors of 49, 41, and 26 were found for helium, hydrogen, and oxygen, in comparison to pure PVA. Pole figure analysis was employed to assess the alignment of MMT platelets within the composite layers. The results indicated that composites formulated from solution-based matrices achieved the most highly parallel alignment, likely due

to reduced steric hindrance, which facilitates the orientation of MMT platelets. This alignment parameter was incorporated into the calculation of the permeability coefficients for the composite coatings. The deviation between the calculated and experimental permeability values increased as the permeant size decreased. The deviation further suggests that, in addition to elongating the diffusion path (the tortuous path effect), the incorporation of MMT induces beneficial structural changes in the polymer matrix — such as modifications of its crystallinity — that enhance barrier performance. For water vapor, the permeation mechanism differed from that of non-polar gases. Given MMT's hydrophilic character, water molecules tend to accumulate within MMT particles and, when MMT particles are in contact with each other, water molecules move from particle to particle. This phenomenon, referred to as the polar path effect, underlines the distinct behavior of water vapor permeation compared to other gases.

Author contribution: Stefan Schiessl developed the concept and design of the study and prepared the manuscript under the supervision of Esra Kucukpinar and Peter Eisner. René Schwiddessen supervised the pole figure measurements and assisted with their interpretation. Esra Kucukpinar, Peter Eisner, and Horst-Christian Langowski revised the manuscript.

3.3. A Comparative Study on the Roll-to-Roll Processing of a Silicate-Polyvinyl Alcohol Composite Barrier Lacquer Using Slot-Die and Reverse Gravure Coating Techniques

by Stefan Schiessl, Esra Kucukpinar, Horst-Christian Langowski, and Peter Eisner [185]

Numerous studies have reported improvements in the gas barrier properties of polyvinyl alcohol (PVA) by incorporating silicate platelets, either in free-standing films, or as components in lacquers. However, most investigations have been confined to laboratory-scale (sheet-based) coatings, and the roll-to-roll (R2R) coating of such composite formulations has not been thoroughly examined. The transition from laboratory-scale to R2R-scale coating presents challenges that are as difficult as those encountered during lacquer development, as the process is influenced by the coating technique, the coating speed, the drying conditions, and the lacquer's rheological properties.

In this study, R2R coating of PVA-based composite lacquers containing 50 wt% montmorillonite (MMT) was performed using two techniques: reverse gravure and slot-die coating. The reverse gravure process is inherently self-metered, with the final dry layer thickness being determined by factors such as the gravure roll design, the lacquer viscosity, the solid content, and the interplay between the surface energies of the lacquer and the substrate. In contrast, the slot-die process is pre-metered, allowing the final dry layer thickness to be adjusted by controlling the volumetric flow rate through the die. Within each coating technique, experimental setups were varied to subject the lacquers to different shear rates. For reverse gravure coating, different gravure rolls were used, thereby altering the gap between the roll and the substrate. For slot-die coating, various opening widths were employed. Lacquers with solid contents of 3, 6, and 9 wt% were tested, corresponding to increasing viscosities.

For both coating technologies, an optimal parameter set was identified that yielded low permeability coefficients of 0.14 and 0.12 $\frac{\mathrm{cm^3\,(STP)\,\mu m}}{\mathrm{m^2\,d\,bar}}$ for slot-die and reverse gravure coatings, respectively. These values are comparable to those previously achieved at the laboratory scale. In the case of reverse gravure coating, a highly viscous lacquer (70 mPa s) with a high solid content (9 wt%) proved advantageous, likely because the high shear rate inherent in the self-metered process

helps to disperse and prevent the transfer of agglomerates to the liquid layer, while the higher viscosity aids film formation. Conversely, for slot-die coating, a lower viscosity lacquer (3.2 mPa s) with a lower solid content (3 wt%) was preferable; in this pre-metered process, any agglomerates formed are transferred to the liquid layer, so a lower solid content minimizes the risk of re-agglomeration. These observations were corroborated by surface morphology analyses. Reverse-gravure-coated samples exhibited homogeneously smooth surfaces, whereas slot-die-coated samples showed increased surface roughness with increasing solid content. Pole figure measurements revealed no significant differences in the orientation of the MMT platelets among the various coatings; in all cases, the platelets were predominantly aligned parallel to the film surface. Achieving these results required careful adjustment of the lacquer parameters, in accordance with the specific coating technology.

Author contribution: Stefan Schiessl developed the concept and design of the study and drafted the manuscript under the supervision of Esra Kucukpinar and Peter Eisner. Noemie Rivollier performed the measurement of the pole figures and assisted with their analyses. Esra Kucukpinar, Peter Eisner, and Horst-Christian Langowski revised the manuscript.

4. Discussion

Recyclable mono-material laminates require a thin barrier layer, which cannot be produced using conventional barrier lacquers. The lack of a simple and efficient method for producing gas barrier composite lacquers with the necessary protective properties has resulted in limited industrial interest and a lack of expertise in roll-to-roll coating of these materials.

This thesis proposes incorporating silicate particles into polymeric lacquers to enhance gas barrier performance. By mechanically exfoliating MMT particles in a ball mill, it is possible to produce lacquers with a higher total solid content through a straightforward process. This allows for the application of coating layers with sufficient dry film thickness in a single step, even at roll-to-roll scale. It is well known that integrating silicate particles into polymeric lacquers can substantially improve their barrier properties. Modifying silicates for integration into various polymer matrices further enhances performance, as these fillers create tortuous pathways that increase the diffusion distance for gas molecules, reducing permeability. While the application of multiple coatings has demonstrated exceptional barrier performance, knowledge of the underlying mechanisms, optimal compositions and particle shapes, and of scalable industrial processing methods is still insufficient. Furthermore, the most efficient dispersion techniques have not been determined conclusively. Although laboratory-scale formulations have shown promise, their adaptation for roll-to-roll industrial processes has not been sufficiently explored before now.

The aim of this thesis was to deepen the understanding of gas permeation mechanisms in composites, specifically focusing on how molecular size affects permeability. A straightforward method for calculating potential barrier improvements was developed, enabling the prediction of barrier values, therefore reducing the number of experiments and facilitating comparisons between experimental and calculated values. In the thesis effective MMT dispersion techniques to achieve optimal barrier performance were investigated, and the impact of polymer/filler interactions was analyzed. Key factors influencing the transition from laboratory to R2R scale were assessed. These findings revealed that using a ball mill is the most effective method for mechanically exfoliating MMT particles in water, elim-

inating the need for ultrasonic treatment or particle modification. Furthermore, the investigation also demonstrated that MMT-based composite coatings could be applied using slot-die and reverse gravure processes without performance loss. Finally, the investigation highlighted that stronger interactions between polymer and filler lead to higher improvement factors, with gas permeation occurring along the particles in weak boundary areas between the MMT particles and the polymer matrix.

The knowledge gained from this research has significant implications. It enables the development of recyclable, high-barrier flexible packaging mono-materials, reducing dependence on non-recyclable multi-layer plastic films. Additionally, it provides enhanced methods for scaling up the production of composite coatings. The results also contribute to improved food preservation by minimizing oxygen permeation. Beyond food packaging, these findings support the development of high-performance barrier coatings for applications in home- and personal-care packaging, and for the encapsulation of flexible electronics; these coatings offer improved protection against gas and moisture infiltration. Ultimately, by optimizing coating processes, this investigation lays the groundwork for more sustainable packaging solutions across various industries.

4.1. Development of a composite gas barrier lacquer

This section addresses the first scientific question: How do the exfoliation process and the mixing ratio affect the gas barrier performance of a PVA/MMT composite layer? Since the aim was to systematically answer this question, it was deconstructed into its key aspects: one subsection focuses on the exfoliation method, another on the mixing ratio, and a third on barrier performance. The final subsection, which compares calculated and experimental permeation coefficients, serves as a transition to the next scientific question, which concerns polymer/filler interactions.

In summary, the findings indicate that a higher degree of MMT exfoliation enhances the gas barrier properties of a composite coating. Regarding the mixing ratio, an increased MMT content improves gas barrier performance; however, there is a critical threshold beyond which no further enhancement occurs. Exceeding this limit prevents the formation of coherent polymer regions, thereby compromising the barrier function. This threshold depends on the properties,

such as appearance (dispersion or solution) and polarity, of the polymer matrix used.

Dispersion and exfoliation via ball milling

The process scheme outlined in Table 1.1 describes the conventional approach for mixing PVA and MMT to form a composite barrier lacquer. Typically, MMT is first dispersed in water by manual stirring or mechanical mixing, followed by ultrasonication of the dispersion. The dispersion is then mixed with the PVA solution, and in some cases, an additional ultrasonication of the mixture finalizes the lacquer. As ultrasonic treatment is an additional, time-consuming and costly process step, an attempt has been made to eliminate this step in the production of composite lacquers.

As demonstrated in Section 3.1, the dispersion and exfoliation of MMT particles can be achieved in a single step using a planetary ball mill. Additionally, it was shown that PVA granules can be directly dissolved in the MMT dispersion, as MMT remains stable at the elevated temperatures (>80 °C) required for PVA dissolution. By dissolving PVA directly in the MMT dispersion, the conventional five-step process (dispersion of MMT, ultrasonication of MMT dispersion, dissolution of PVA, mixing of PVA solution and MMT dispersion, ultrasonication of the mixture) is reduced to two steps (dispersion of MMT via ball milling and dissolution of PVA in the MMT dispersion). This reduction of process steps not only decreases production time but also minimizes costs and lowers the risk of processing errors, provided that the performance achieved in the end remains uncompromised.

The oxygen permeation coefficient achieved with a lacquer produced using this simplified two-step process within 2 h was 0.12 $\frac{\mathrm{cm^3\,(STP)\,\mu m}}{\mathrm{m^2\,d\,bar}}$. Compared to other single-pass PVA/MMT composite barrier coatings, this value ranks in the mid-range (Table 1.1). For instance, Grunlan et al. [127] achieved a lower permeability coefficient (0.03 $\frac{\mathrm{cm^3\,(STP)\,\mu m}}{\mathrm{m^2\,d\,bar}}$) but required more than 52 h for production, while Song et al. [130] reported an even lower permeability coefficient (0.002 $\frac{\mathrm{cm^3\,(STP)\,\mu m}}{\mathrm{m^2\,d\,bar}}$) with a production time exceeding 17 h. In contrast, Nyflött et al. [128] (0.70 $\frac{\mathrm{cm^3\,(STP)\,\mu m}}{\mathrm{m^2\,d\,bar}}$) and LaChance et al. [135] (0.43 $\frac{\mathrm{cm^3\,(STP)\,\mu m}}{\mathrm{m^2\,d\,bar}}$) achieved higher permeability coefficients despite utilizing more extensive processing steps.

At first glance, the use of ball milling for MMT exfoliation may seem counterintuitive, as the impact of the milling media could potentially fracture the MMT platelets, thereby reducing their aspect ratio and diminishing their contribution to the barrier improvement. In their review on the fabrication of polymer

nanocomposites via ball milling, Delogu et al. [194] highlighted that this method is typically used to homogeneously reduce the size of inorganic particles such as iron, titanium dioxide, or silicon dioxide before blending them with polymers (e.g., PE, PP, polyester, polyamide), to enhance flame retardancy or mechanical properties, or reduce polymer content. However, Valera-Zaragoza et al. [195] demonstrated that with careful selection of process parameters (ball size, ball material, rotational speed, and type of mill), there exists a processing window in which the applied energy promotes MMT exfoliation without breaking the platelets. They quantified this optimal energy range as 6.6 to 13.2 $\frac{\mathrm{J}}{\mathrm{g}}$. The planetary ball mill setup used in Section 3.1 operates at 9.1 $\frac{\mathrm{J}}{\mathrm{g}}$, calculated according to Garcia et al. [196] (Section A.4), which falls within this energy range identified for effective exfoliation without fragmentation.

In comparison, the average energy input for the laboratory-scale disperser was determined to be 4.0 $\frac{\mathrm{J}}{\mathrm{g}}$, as numerically evaluated for an identical mixer by Pacek et al. [197]. However, while planetary ball milling provides homogeneous shear distribution, mixing with a laboratory-scale disperser is inherently heterogeneous. The shear rate is highest in a small volume (5 % of the volume in the beaker used) directly between the rotor and stator, where localized energy input can reach up to 80 $\frac{\mathrm{J}}{\mathrm{g}}$; energy decreases exponentially with increasing distance from this high-shear zone. Consequently, MMT dispersed using the laboratory-scale disperser exhibits a bimodal size distribution: exfoliated and slightly fragmented platelets ($\sim$340 nm) that have passed through the high-shear zone, and non-exfoliated MMT stacks ($\sim$2960 nm) that have not been subjected to sufficient shear.

In contrast, the uniform shear environment of the planetary ball mill results in a single particle size distribution ($\sim$494 nm), which is slightly larger due to the lower peak energy input but remains consistent across the dispersion. Bari et al. [198] demonstrated that for a layer-by-layer coating of an MMT dispersion with epoxy resin, dispersions prepared using ball milling led to superior water vapor barrier performance (0.03 $\frac{\mathrm{g}}{\mathrm{m^2\,d}}$), compared to those prepared by mixing with laboratory-scale disperser (0.31 $\frac{\mathrm{g}}{\mathrm{m^2\,d}}$). Section 3.1 outlines the specific milling parameters necessary to achieve optimal dispersion and exfoliation of MMT in water, enabling high oxygen barrier performance in PVA/MMT coatings without the need for ultrasonication or extensive processing steps.

The primary determinant of barrier performance in composite coatings is the absence of particle agglomerates. In this context an agglomerate is a non-exfoliated MMT stack with a thickness of more than 100 nm or a width of more than 1000 nm; the negative influence of the barrier increases with increasing agglomerate size, synonymous with an increasing number of agglomerated MMT platelets.

The use of a planetary ball mill not only simplifies the process and reduces production time but also ensures a composite layer free of agglomerates.

Mixing ratio, particle aspect ratio, and viscosity

When the MMT dispersion is being mixed with the polymer, the quality of the mixture at a given mixing ratio depends on both the type of MMT particles and the polymer used [199]. The modeling presented in Section 1.3.1 predicts that increasing the particle content improves gas barrier performance; however, as shown in Section 3.1, this improvement only holds to a certain point. For the materials used in this investigation, a 50 wt% MMT content (equivalent to 30 vol%) was found to be best. Beyond a critical threshold — typically between 50 and 66 wt% MMT content — the barrier performance declines because the polymer content becomes too low to form coherent regions [128]. This results in areas composed solely of MMT, leading to defects such as pores in the polymer matrix and a deterioration in barrier properties, compared to the pure polymer [200].

Increasing the MMT content also raises the viscosity of the lacquer. Although MMT dispersions cause shear thinning, a balance must be maintained, because each coating technique has a maximum acceptable viscosity (generally between 1 to 200 mPa s) beyond which a homogeneous and defect-free coating cannot be achieved. This creates a trade-off: a high proportion of MMT is desirable for high gas barrier performance, yet low viscosity is required for proper coating application.

The aspect ratio of the filler is another important parameter. A high aspect ratio can significantly improve the barrier properties even at low filler contents but also causes a rapid increase in viscosity. Naturally occurring MMT has an aspect ratio ranging from 10 to 1000 [201–205], with the MMT used in this investigation exhibiting an aspect ratio of approximately 25. In contrast, synthetic silicates may reach aspect ratios of up to 20 000 [206].

Two strategies can be employed to control viscosity: changing the MMT content in the formulation or modifying the total solid content of the lacquer. As evidenced in Tables 1.1 and 1.2, the preferred strategy varies with the polymer matrix. For PVA-based composites, a near-balanced or slightly PVA-favored mixing ratio with MMT (approximately 1:1 in weight) is typical, with a relatively low total solid content (around 2.0 wt%). In contrast, composites based on alternative polymers often use a higher total solid content (>10 wt%) with a lower MMT content (e.g., a mixing ratio of 19:1 in weight is common) [117, 150,

155, 156]. In Section 3.2, these discrepancies were addressed by producing composite coatings with different polymers while maintaining a consistent mixing ratio and similar solid content. This was achieved by:

- Selecting MMT with an aspect ratio of 25, which has a less pronounced effect on viscosity than silicates with higher aspect ratios, thereby enabling a 1:1 mixing ratio for polymer matrices such as PVA, polyacrylates, and PP at a minimum solid content of 5.0 wt% suitable for single-pass coating; and
- Using appropriate water-based polymer lacquers. Notably, while MMT is typically added to PP in melt-based processes at contents below 10 wt%, a water-based PP dispersion was selected and adjusted to achieve a 1:1 mixing ratio (50 wt% MMT). Such a mixing ratio has not been reported to date.

Maintaining a constant mixing ratio and similar solid content across different polymer matrices enables a detailed evaluation of the influence of polymer/MMT interactions on gas barrier performance against various gases.
Achieving an optimal balance between performance and processability is crucial when selecting the mixing ratio and the aspect ratio. While a high MMT content and large aspect ratio enhance barrier performance, they might be limited if the coating requires highly specialized application techniques or exhibits a low solid content necessitating multiple coating layers. To ensure feasibility, lacquer development should prioritize a viscosity suitable for standard R2R coating processes while ensuring sufficient coating thickness — and thus gas barrier performance — in a single application step.

Barrier performance of composite barrier layers

In most cases, the development of a gas barrier composite is motivated by its application as a coating for polymer films in food packaging. Therefore, the barrier properties against oxygen and water vapor are commonly measured, as these are the most critical permeants in food packaging [207]. Water vapor (kinetic diameter: 2.65 Å) and oxygen (3.46 Å) differ in both molecular size and polarity — water vapor is polar, whereas oxygen is non-polar [208]. Consequently, the influence of MMT platelets on permeability is analyzed separately for each permeant, given that their permeation mechanisms differ. A novel aspect presented in Section 3.2 is the measurement of permeation for the same composite layers against helium (2.60 Å), hydrogen (2.89 Å), oxygen, and water vapor. This

comprehensive approach enables a separate evaluation of how the size of the permeant affects both the permeability and the barrier enhancement factors.
For non-polar gases, the data indicate that the permeation coefficients decrease with increasing permeant size. For example, for a PVA/MMT composite coating with a 1:1 mixing ratio, the permeation coefficients were measured as 5.1, 1.2, and 4.2×10^{-3} $\frac{\mathrm{cm^3\,(STP)\,\mu m}}{\mathrm{m^2\,d\,bar}}$ for helium, hydrogen, and oxygen, respectively. Henry et al. [209] reported for evaporated metal oxide layers on films that helium and hydrogen can more easily penetrate micro-defects than oxygen, thereby accessing more permeation paths — a phenomenon that has now been confirmed for composite layers. Consequently, the barrier improvement factors (BIFs) are greatest for the smaller permeants; for instance, for the same PVA/MMT composite coating, the BIFs with 50 wt% MMT compared to pure PVA coatings were 49, 41, and 26 for helium, hydrogen, and oxygen, respectively. This is because the likelihood of closing a permeation path increases with the incorporation of a sufficient quantity of particles. Since smaller permeants encounter a greater number of permeation paths, the improvement in barrier performance is more pronounced for them [210].
The barrier properties of a coating depend on multiple factors, including the coating technique, drying temperature, substrate type, solid content, and polymer molecular weight. Thus, to evaluate the improvement provided by the incorporation of silicate particles, it is crucial to measure the barrier performance of the pure polymer coating under identical processing conditions. The permeation coefficient of the pure polymer coating serves as the reference (P_u in Eq.1.12) for calculating the theoretical barrier potential that is attributable to the silicate particles. Notably, the improvement factors differed between Sections 3.1 and 3.2, even when the same coating formulation was used. For example, for a PVA/MMT composite with a 1:1 mixing ratio, the BIFs on BoPP were 17 and 12 for helium and oxygen, respectively, whereas on PET the BIFs were 49 and 26 for helium and oxygen, respectively. This discrepancy indicates that both the performance of the pure PVA coating and the composite barrier layer depend on the substrate. Differences in surface energy between BoPP and PET affect the interaction between the substrate and the coating [211], while variations in the mechanical properties of PP and PET, along with differences in mechanical stresses experienced after drying — due to transport, temperature fluctuations, or measurement conditions — further influence the overall barrier performance [212].
For polymer/MMT composites, the activation energy is typically determined in conjunction with kinetic analyses of polymer degradation [213–215]. However,

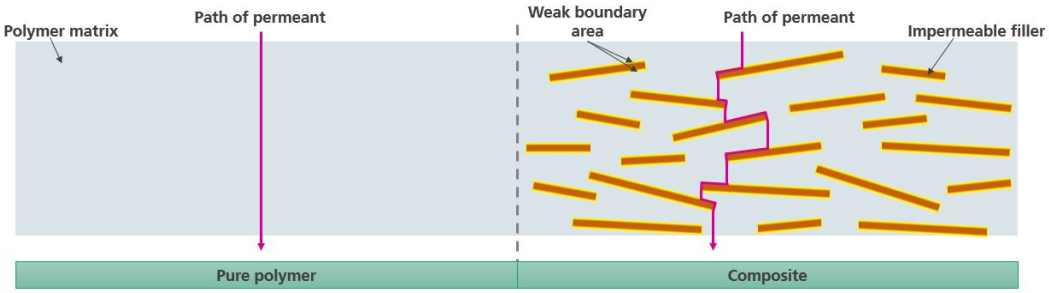

Figure 4.1.: Schematic representation of the permeation path of a permeant through a pure polymer (left) and a composite with elongated diffusion path (right), also called a tortuous path. This is a modified version of Figure 1.4, indicating the diffusion along weak boundary areas between polymer matrix and fillers marked in yellow.

an activation energy for permeation can also be obtained from Arrhenius plots by measuring the permeation rate at different temperatures. Historically, this approach has been increasingly applied to PVD-coated polymer films, but not to composite-coated films [209, 216]. In the studies summarized in Table 1.1 and Table 1.2, permeability was either measured at a single temperature, or the activation energy was not determined when multiple temperatures were used.
In the present investigation, the activation energies for hydrogen and oxygen permeation were determined, as these values provide insight into the permeation mechanism. Henry et al. [209] suggested that an unchanged or decreased activation energy in going from a pure polymer to a composite indicates that the filler acts as a simple barrier obstacle, without offering alternative low-energy pathways. A decrease in activation energy implies that less energy is required to initiate permeation — possibly due to an increase in free volume and a corresponding increase in the solubility coefficient [217]. The experimental data for PVA/MMT and polycarboxylic acid/MMT composites (Sections 3.1 and 3.2) show that the overall permeation coefficient decreases significantly with the addition of MMT. This observation implies that the reduction in the diffusion coefficient, resulting from the tortuous path effect, has a greater effect than any increase in the solubility coefficient. In other words, while diffusion may occur preferentially in regions of larger free volume along the MMT particles (weak boundary areas), the net effect of MMT incorporation is a substantial reduction in gas permeation.
As a result of these findings, the schematic representation of the tortuous path effect presented in Figure 1.4 has been refined and is now depicted in Figure 4.1.

Comparison of experimentally determined and calculated permeability coefficients

Numerous studies have modeled the gas barrier performance of composite coatings, as summarized in reviews by Zid et al. [41] and Idris et al. [119]. These models vary in complexity and approach — ranging from simple analytical models (used in this investigation) to more advanced numerical simulations. In simple models, a reliable estimate of the composite barrier value can be obtained by specifying the particle length, thickness, and volume fraction. However, despite the relative simplicity of these calculations, only a few studies have applied them to PVA-based composite layers (e.g., Dabbaghianamiri et al. [132]) and to composite layers based on other polymers (e.g., Kochumalayil et al. [154], Herrera-Alonso et al. [150], and Nazarenko et al. [148]).

This investigation demonstrates the advantages of directly comparing measured permeation coefficients with calculated values. While the models (e.g., Eq.1.12) predict that barrier performance improves continuously with increasing filler content, experimental results (Section 3.1) reveal a maximum filler content — for example, a 50 wt% MMT load in a PVA/MMT composite — beyond which further addition of MMT degrades the barrier. This maximum is not predicted by purely geometric calculations but has been observed in several studies (e.g., Zhang et al. [145], Spoilaric et al. [142], and Yue et al. [136]). Notably, the calculation indicates that the improvement approaches the maximum exponentially, suggesting that even a small amount of MMT significantly enhances the barrier until the maximum is reached. This finding is particularly relevant for applications with conflicting requirements — for instance, stretchable barrier layers, where maximum barrier properties require a high filler content, while flexibility demands a low amount of filler. In such cases, the calculations can expedite finding a compromise between barrier performance and mechanical properties.

Once the optimum mixing ratio is determined experimentally, the model provides an estimate of the maximum barrier improvement (i.e., the barrier potential) achievable through the integration of impermeable fillers. In the present investigation, calculations were performed using Eq.1.16 (which does not consider particle orientation) and Eq.1.19 (which incorporates particle orientation). If the measured gas barrier performance falls short of the calculated value, this suggests that the filler particles may not be dispersed homogeneously, that agglomerates have formed, or that defects are present in the composite layer. Conversely, if the experimental barrier performance exceeds the calculated predictions, this implies that, beyond modifying geometric factors, filler integration has induced

additional beneficial changes in the polymer matrix (e.g., a reduction in free volume or an increase in crystallinity), further enhancing the barrier.
An illustrative example is provided by the permeation mechanism of water vapor. For a PVA/MMT composite with a 1:1 mixing ratio, the measured water vapor permeability was 2.8 $\frac{\mathrm{g\,mm}}{\mathrm{m^2\,d}}$, while the model predicted only 0.29 $\frac{\mathrm{g\,mm}}{\mathrm{m^2\,d}}$. This significant discrepancy is observed consistently for water vapor, whereas for non-polar gases (helium, hydrogen, and oxygen), the integration of MMT leads to improved barrier performance. The deviation for water vapor is thus not attributable to agglomeration or defects, but rather indicates that the permeation mechanism for water vapor — dominated by the polar path effect (Section 3.2) — differs from that of non-polar gases (the tortuous path effect). The polar path effect describes the interaction of water molecules with hydrophilic components, that is, MMT, which leads to increased diffusion along polar domains within the material [218].
In summary, the combined evaluation of experimental data and theoretical models not only validates the effectiveness of the composite design but also highlights additional mechanisms at play in the polymer matrix that contribute to the overall gas barrier performance.

4.2. Effect of interactions between polymer and MMT on gas permeation

This section addresses the second scientific question: To what extent do polymer/MMT interactions influence the gas barrier performance for gases of different polarity and size? To answer this question, the first step is to identify suitable measurement techniques for assessing polymer/MMT interactions in both liquid and solid states. Viscosity and surface energy analysis proved effective in evaluating interaction potential in the liquid state and are discussed in the first subsection. For the dried composite layer, FTIR spectroscopy was used to directly assess chemical interactions, while XRD was employed to examine the influence of silicate on the polymer's crystallinity, as presented in the subsequent subsection.
The results indicate that stronger polymer/MMT interactions lead to lower absolute permeation coefficients and more pronounced barrier improvements. For non-polar gases, smaller gas kinetic diameters correlate with greater sensitivity to these interactions. In contrast, polar water vapor follows a distinct permeation mechanism and remains nearly unaffected by polymer/MMT interactions.

As described in Section 1.3.4, several approaches were used to study the interaction between the silicate and the polymer. For example, Grunlan et al. [127] inferred a high degree of MMT dispersion — and thus strong interaction — from fine lines observed in TEM images, an assumption supported by an increase in the glass transition temperature with increasing MMT concentration. Similarly, Lim et al. [157] deduced from the disappearance of the MMT (001) peak in the XRD pattern of the composite that MMT is completely exfoliated in the lacquer and that its dispersion is maintained in the dry state by interactions with polyacrylic acid. There have been no reports of investigations of polymer/MMT interaction in the liquid state.
In some studies, the interaction between silicate and PVA is invoked to explain observed phenomena without direct measurement [118, 129, 131, 132, 135, 137], whereas other studies on composite barrier coatings do not address the interaction between components at all [128, 133, 136, 156].

Determination of polymer/silicate interactions via liquid lacquer analysis

It has been shown that measuring the surface energy of the liquid components — the MMT dispersion and the polymeric lacquer — can provide an indication of potential interactions in the dried composite layer. In state-of-the-art adhesion studies, the surface energies of an adhesive and a substrate are compared; high adhesion is more likely when their overall values or the ratios of their dispersive and polar components are similar [219–221]. This approach is also well established for carbon or glass fiber reinforced composites, where determining the surface energy of both the fiber and the matrix helps to identify high-performance fiber pairings and effective pre-treatments [222, 223]. A similar method has now been extended to the liquid components of a composite lacquer.
First, the surface energy of the MMT dispersion ($68\,\frac{\mathrm{mN}}{\mathrm{m}}$) is compared to that of the polymer lacquer. For example, the PVA solution exhibits a surface energy of $64\,\frac{\mathrm{mN}}{\mathrm{m}}$, whereas the polyacrylic dispersion shows a value of $37\,\frac{\mathrm{mN}}{\mathrm{m}}$. The standard pendant drop method is used to measure the total surface energy of liquids, although it does not separate the dispersive and polar fractions. To obtain this division — less established for liquids than for solids — a modified sessile drop method is employed, in which the liquid is placed on a known, purely dispersive substrate. This method requires that the lacquers have a sufficiently low viscosity to form a drop. The polar fractions obtained are $27\,\frac{\mathrm{mN}}{\mathrm{m}}$ for the MMT

dispersion, 21 $\frac{\mathrm{mN}}{\mathrm{m}}$ for the PVA solution, and 6.4 $\frac{\mathrm{mN}}{\mathrm{m}}$ for the polyacrylic dispersion. In the cases examined, the similarity between the PVA solution and the MMT dispersion with respect to both the total surface energy and the polar fraction suggests a strong potential for interaction, whereas the polyacrylic dispersion is distinctly different. Similar trends were observed for other polymer matrices, indicating that greater similarity in these surface energy parameters correlates with stronger polymer/silicate interactions. Thus, surface energy measurements provide a rapid and effective means of estimating the potential interactions between the composite components.

Another useful parameter for assessing these interactions is the viscosity of the liquid lacquer. The polymer lacquers — whether used as solutions or dispersions — exhibit Newtonian behavior, while the MMT dispersion displays shear-thinning characteristics. The degree of shear thinning in the composite lacquer is indicative of the extent of interaction between the components in the liquid state. For instance, when subjected to shear rates ranging from 10 to 1000 $\frac{1}{\mathrm{s}}$, the viscosity of a 5 wt% MMT dispersion decreases by 75 % (from 52.5 to 13.1 mPa s). Under the same shear conditions, composite lacquers with a 5 wt% solid content and 50 wt% MMT show a viscosity reduction of 90 % (from 261 to 26.5 mPa s) for a PVA-based composite and 66 % (from 24.3 to 8.26 mPa s) for a polyacrylic-based composite. Thus, for equivalent MMT and total solid contents, the PVA-based lacquer exhibits more pronounced shear thinning than the polyacrylic-based lacquer, which suggests stronger interactions. In practice, viscosity measurements are routinely used to select appropriate coating techniques and parameters; here, the extent of shear thinning serves as an additional indicator of potential polymer/silicate interactions.

In summary, the combined analysis of surface energy and viscosity in the liquid state offers a quick and practical method for estimating the potential interactions between the polymer and MMT. This approach enables early-stage modifications of the lacquer formulation — such as altering the polymer matrix or adjusting the MMT characteristics — to optimize the final barrier performance of the composite coating.

Determination of polymer/silicate interactions via solid coating analysis

While the analysis of liquid components provides an indication of potential interactions, the critical factor determining the coating's performance is the interaction between the polymer and MMT in the dried composite. Notably, the

methods for assessing these interactions have not been standardized, as evidenced by the varied approaches in Tables 1.1 and 1.2. Here, two methods are proposed that could serve as standards in the future: FTIR spectroscopy to directly identify chemical interactions, and X-ray diffraction (XRD) to detect filler-induced changes in polymer crystallinity.

FTIR spectroscopy can reveal the formation of hydrogen bonds between the polymer and MMT. For example, the -OH stretching band of the Al–OH bond in the MMT octahedral layer, observed at 3624 $\frac{1}{\text{cm}}$, should remain unchanged when no interaction occurs, since this layer is shielded by the tetrahedral layers. In contrast, the Si–O stretching bands in the tetrahedral layer, typically observed as a double peak at 1031 and 1008 $\frac{1}{\text{cm}}$, shift to higher wavenumbers (blue shift) when hydrogen bonds form between the Si–O groups and a polymer functional group. In the case of PVA, the polymer's –OH stretching band at 1085 $\frac{1}{\text{cm}}$ shifts to lower wavenumbers (red shift) upon interaction. Conversely, if a functional group capable of hydrogen bonding — such as the C–O stretching band in a polyacrylic dispersion at 1164 $\frac{1}{\text{cm}}$ — remains unchanged, this indicates no significant interaction.

The penetration depth of the IR radiation (up to 1 µm) ensures that the measurement predominantly reflects the coating layer without substrate interference [193]. Additionally, according to Ito et al. [224], at least 1 vol% of the material should be in the boundary region to yield a reliable FTIR interaction analysis. A composite with 50 wt% MMT, and even a minimal interaction distance of 1 nm, yields a boundary volume of 2.4 vol%, as calculated in Section A.4. These weak boundary areas are schematically illustrated in Figure 4.1. Because FTIR measurements require only a small portion of the coated film to be placed on the ATR crystal and take approximately 2 min, this method is both rapid and effective for identifying hydrogen-bonding interactions. In this investigation, composite coatings of PVA/MMT and polycarboxylic acid/MMT that exhibited clear FTIR shifts also consistently demonstrated the highest gas barrier improvement factors.

In addition to chemical interaction, the crystallinity of the polymer matrix significantly influences the gas barrier [140]. An increase in crystallinity generally extends the diffusion path, as diffusion through amorphous regions is energetically less demanding. However, there are conflicting reports in the literature on the effect of MMT on polymer crystallinity. Some studies show a decrease in crystallinity due to interference with crystalline domain formation [128, 225], while others report an increase, attributing it to MMT particles acting as nucleation sites [226–228].

In the present thesis, MMT integration increased the crystallinity of PVA, polyacrylate, and polycarboxylic acid matrices, whereas no significant change was observed in PP-based coatings. Evaluating crystallinity in conjunction with other analytical methods is essential. For example, if the gas barrier for a particular gas improves beyond theoretical predictions, this may be due to increased crystallinity reducing free volume and the sorption coefficient. Similarly, a decrease in activation energy for permeation accompanied by improved barrier performance may indicate that an increased number of grain boundaries, resulting from higher crystallinity, is facilitating diffusion with lower activation energy, even if the overall permeation coefficient reflects the extended diffusion path.
Thus, the measurement of crystallinity, alongside FTIR analyses, is a crucial component in understanding the complex interplay of interactions that occur in composite barrier coatings.

4.3. Processability of composite barrier lacquers at roll-to-roll scale

This section addresses the third scientific question: What modifications to a composite barrier lacquer are necessary in order to scale up from laboratory-scale coating to roll-to-roll coating? To explore this question, the first step is to assess the impact of coating viscosity on different application techniques. Previous studies on dispersion technology have demonstrated that particle agglomeration significantly affects barrier performance, and thus, further analysis of this phenomenon is necessary. The first subsection examines viscosity and agglomeration effects, while the second focuses on methods for measuring particle orientation and its influence on barrier properties.
In summary, modifying the composite lacquer is essential for scaling up from laboratory to industrial production. While low-viscosity formulations ($<10\,\mathrm{mPa\,s}$) are optimal for slot-die coating, high-viscosity formulations ($>70\,\mathrm{mPa\,s}$) are more suitable for reverse gravure printing.

Effect of viscosity and agglomerates

Most research on MMT-based composite coatings has been conducted at laboratory scale using techniques such as k-bar coating, spin coating, dip coating, inkjet printing, or blade coating (Tables 1.1 and 1.2). However, for industrial applications, it is essential to develop composite barrier lacquers that can be coated

on a large scale using roll-to-roll (R2R) processes. Section 3.3 presents the first detailed investigation to date of R2R coating for these composite lacquers.
The influence of viscosity on the gas barrier performance of the final composite coating layer is critical. In laboratory-scale batch processes, factors such as shear thinning over time or solvent evaporation are less significant, and the coating process can be rapidly optimized. In contrast, R2R coating requires that the lacquer properties be precisely matched to the continuous process, which can run for several hours. With a constant MMT/polymer mixing ratio being maintained, it became clear that the viscosity — adjusted by solid content — is a key parameter for both reverse gravure and slot-die coating.
The detrimental effect of MMT agglomerates on barrier performance, already noted in Section 4.1, was confirmed in the R2R experiments. Agglomerates may arise from insufficient exfoliation during lacquer production or from re-agglomeration during manufacturing, coating, or drying. For a PVA/MMT composite coating with a 1:1 mixing ratio, the following tendencies were observed:

- Slot-Die Coating: A low viscosity, achieved with a low solid content (approximately 3 wt%), is advantageous because it minimizes the formation of agglomerates. In the pre-metered slot-die process, all of the delivered lacquer — including any agglomerates — is transferred to the substrate. However, the low solid content can be compensated for by adjusting the flow rate to achieve the desired dry film thickness.

- Reverse Gravure Coating: This self-metered process requires a higher solid content (approximately 9 wt%) to produce a sufficiently thick film in a single pass. Although a higher solid content increases viscosity and the likelihood of agglomerate formation, two factors mitigate this effect: first, not all the lacquer in the reservoir is transferred to the substrate, which allows agglomerates to remain in the reservoir; and second, the higher shear rates during reverse gravure coating can break up agglomerates.

For a PVA/MMT composite lacquer with 1:1 mixing ratio, low permeation coefficients of 0.14 and 0.12 $\frac{\mathrm{cm^3\,(STP)\,\mu m}}{\mathrm{m^2\,d\,bar}}$ were achieved with slot-die and reverse gravure coating, respectively. These values are in the same range as the 0.12 $\frac{\mathrm{cm^3\,(STP)\,\mu m}}{\mathrm{m^2\,d\,bar}}$ achieved for the same lacquer at the laboratory scale with k-bar coating. Hence, the successful translation of composite barrier coatings from laboratory-scale experiments to industrial-scale processes was demonstrated.

Montmorillonite orientation in composite barrier layers

It is generally assumed that an orientation as parallel as possible to the coating direction — that is, perpendicular to the permeation direction — is advantageous for achieving an effective gas barrier [35, 47]. In this investigation, pole figure measurements consistently yielded orientation angles of less than 20°, regardless of the lacquer formulation or coating technique. This result can be attributed to the low viscosity (below 100 mPa s) of all lacquer formulations at the shear rates employed during coating. Specifically, the shear rates ranged from 208 to 1190 $\frac{1}{s}$ for slot-die coating, from 1000 to 4000 $\frac{1}{s}$ for reverse gravure coating, and from 222 to 667 $\frac{1}{s}$ for k-bar coating. Low viscosity facilitates the free movement and alignment of MMT particles during the coating process, whereas higher viscosity impedes particle orientation [148].

This principle is further illustrated by the contrasting behavior observed in melt intercalation processes. For instance, Zhu et al. [229] reported that a composite of 100 parts PP and 5 parts MMT, with a melt viscosity exceeding 10 000 mPa s at a shear rate of 1000 $\frac{1}{s}$, resulted in a heterogeneous orientation of the MMT particles, which, in turn, increased the Young's modulus rather than enhancing the gas barrier. Consequently, silicate-based composite lacquer formulations should aim for the lowest possible viscosity to promote parallel particle orientation during coating.

In addition to viscosity, the relative influence on the gas barrier of silicate orientation versus silicate content was examined. For a fixed orientation angle (10°), the calculated tortuosity factors according to Eq. 1.18 for composites with 25 and 50 wt% silicate were 2.17 and 3.81, respectively. Within composites containing 25 wt% silicate, the tortuosity factor varied from 2.20 to 1.50 over an orientation range of 0 to 40°, but only from 2.20 to 2.06 within 0 to 20°. Given that the MMT orientation in the coatings was consistently below 20°, it can be concluded that, within this range, orientation exerts a relatively minor influence on the gas barrier, compared to the silicate content.

In summary, while the orientation of MMT particles remains an important factor influencing gas barrier performance, maintaining a low viscosity in water-based composite lacquers ensures sufficient orientation across various coating techniques. Therefore, optimizing the gas barrier is more effectively achieved by adjusting the silicate content or refining the lacquer manufacturing process than by further modifying particle orientation via the coating process.

4.4. Economic feasibility and industrial implementation

This thesis demonstrated that incorporating platelet-shaped montmorillonite (MMT) into polymer lacquers significantly enhances gas barrier properties via the tortuous path effect. The developed composite lacquers achieved high barrier performance in a single coating step, reducing process complexity in comparison to multi-layer coatings. Laboratory-scale development was successfully translated to an industrially viable process through roll-to-roll (R2R) application using reverse gravure and slot-die techniques.

From an economic perspective, the coating systems that were developed offer significant advantages over conventional barrier solutions. Other composite lacquers often require multiple applications to achieve high barrier properties, increasing production complexity and costs. In contrast, the composite lacquers developed in the frame of this thesis achieve the desired barrier performance with a single coating step, reducing process steps, energy consumption, and material costs. The required amount of PVA is also significantly lower than in standard barrier layers, leading to reduced consumption of ethyl acetate, a costly fossil-based polymer. Additionally, silicates are naturally abundant and cost-effective, and they do not interfere with biodegradability, making them a more sustainable alternative to traditional high-barrier layers produced via PVD processes. The latter are expensive due to their vacuum deposition requirements and the specialized equipment needed for their production, whereas the coating systems developed in this thesis provide a flexible, cost-efficient alternative with rapid substrate adaptability. Because PVD machines are very expensive and the process is complex, only a few manufacturers in Europe have chosen to engage in this type of production. Users of packaging systems based on the PVD-processed films will be dependent on those manufacturers. Composite coatings can be applied using standard coating techniques, which are already available on many film converters or can be developed and brought into production with moderate investment costs. This also enables smaller companies to use these coatings. The composite lacquer has already been successfully tested on PP, PE, PET, and paper, consistently demonstrating outstanding barrier properties.

A crucial aspect of industrial implementation is scalability. While the production of the silicate dispersion was initially carried out using a laboratory ball mill, preliminary tests confirmed that an equivalent exfoliation level can be achieved with rotational ball mills, enabling a seamless transition to large-scale produc-

tion. Furthermore, the process remains cost-effective, as no energy-intensive treatments, such as ultrasonic dispersion or chemical modification of the particles, are required. Compared to complex multi-layer coatings or PVD processes, the overall process remains economically viable and resource-efficient.

Despite these advantages, several challenges must be addressed for industrial implementation. In practical applications, these coated films serve as one layer within laminate structures rather than stand-alone packaging materials. A typical laminate consists of a substrate film, a barrier coating, an adhesive layer, and a sealing film. Beyond gas barrier performance, other critical properties — such as buckling resistance and interlayer adhesion — are essential for packaging applications. Previous studies have shown that bucking resistance decreases with increasing MMT concentration and coating thickness [230]. Furthermore, composite coatings generally exhibit lower adhesion compared to pure polymer coatings [231]. These findings highlight the need for a carefully balanced optimization among coating thickness, viscosity, gas barrier performance, adhesion, and mechanical properties in practical applications.

Another potential challenge is the accumulation of silicate particles during the recycling process. If the barrier layer is not completely removed during mechanical recycling — particularly if it is embedded within a laminate — silicate particles may be compounded into the recycled polymer film. Over multiple recycling cycles, this accumulation could negatively impact material properties, which would necessitate further investigation into its long-term effects.

Additionally, the water vapor barrier properties of the coatings that were developed still require optimization. While the gas barrier performance against non-polar gases already achieves excellent values, further improvements could be realized by combining hydrophilic and hydrophobic platelet-shaped particles (e.g. graphene) to minimize water vapor permeation while maintaining non-polar gas impermeability.

For the packaging industry, these findings offer valuable insights into sustainable material development. Precise knowledge of barrier requirements is crucial, especially in food packaging, where aluminum-based multi-layer materials have traditionally been used. Since aluminum provides an almost perfect barrier, gas barrier considerations were often overlooked. However, this investigation indicates that carefully designed mono-material solutions can provide sufficient barrier performance while maintaining recyclability — representing a significant step toward sustainable packaging solutions.

Beyond packaging, the results highlight the broader potential of composite barrier coatings. The key innovation lies not only in the development of a novel

lacquer but in the conceptual approach to combining fillers with polymer matrices. By adjusting parameters such as the polymer matrix, total solid content, and mixing ratio, the composite lacquer can be tailored to specific industrial requirements.

In addition, preliminary tests suggest that the principles established for MMT-based composite coatings can be extended to synthetic hectorite-based systems [206]. Due to their higher aspect ratio, synthetic hectorites could potentially provide substantial barrier improvements. However, processing these materials remains challenging. In high-performance applications, such as hydrogen barriers under high pressure conditions — where MMT-based coatings have already shown promise — the use of synthetic hectorites may offer new opportunities for further optimization and enhanced performance.

One particularly promising development would be the creation of a sprayable lacquer with excellent hydrogen barrier properties. Its sprayability would make it suitable for 3D components such as tanks, pipes, or technical parts, where conventional barrier coatings face limitations. Such applications could expand the scope of barrier coatings beyond flexible packaging into fields such as hydrogen distribution and storage and high-performance engineering materials.

In summary, this thesis demonstrates that silicate-based composite lacquers provide both economic and ecological advantages while enabling new industrial applications. The combination of scalability and high barrier performance makes this technology a forward-thinking solution for sustainable materials within a resource-efficient circular economy.

Bibliography

1. Stern, S. A. & Frisch, H. L. The selective permeation of gases through polymers. *Annual Review of Materials Science* **11,** 523–550 (1981).
2. Pinnau, I., Wijmans, J. G., Blume, I., Kuroda, T. & Peinemann, K. V. Gas permeation through composite membranes. *Journal of Membrane Science* **37,** 81–88. ISSN: 0376-7388 (1988).
3. Arora, A. & Padua, G. Review: Nanocomposites in Food Packaging. *Journal of Food Science* **75,** R43–R49 (2010).
4. Manceau, M., Rivaton, A., Gardette, J.-L., Guillerez, S. & Lemaître, N. The mechanism of photo- and thermooxidation of poly(3-hexylthiophene) (P3HT) reconsidered. *Polymer Degradation and Stability* **94,** 898–907. ISSN: 0141-3910 (2009).
5. Choi, K. *et al.* Reduced Water Vapor Transmission Rate of Graphene Gas Barrier Films for Flexible Organic Field-Effect Transistors. *ACS Nano* **9.** PMID: 25988910, 5818–5824 (2015).
6. Muthukumar, M. *et al.* The development of fuel cell electric vehicles – A review. *Materials Today: Proceedings* **45.** International Conference on Advances in Materials Research - 2019, 1181–1187. ISSN: 2214-7853 (2021).
7. Langowski, H.-C. in *Plastic Packaging* 297–347 (John Wiley & Sons, Ltd, 2008). ISBN: 9783527621422.
8. Klopffer, M. & Flaconneche, B. Transport properties of gases in polymers: bibliographic review. *Oil & Gas Science and Technology* **56,** 223–244 (2001).
9. George, S. C. & Thomas, S. Transport phenomena through polymeric systems. *Progress in Polymer Science* **26,** 985–1017. ISSN: 0079-6700 (2001).
10. Park, G. S. in *Synthetic Membranes: Science, Engineering and Applications* (eds Bungay, P. M., Lonsdale, H. K. & de Pinho, M. N.) 57–107 (Springer Netherlands, Dordrecht, 1986). ISBN: 978-94-009-4712-2.

11. De Angelis, M. G. in *Encyclopedia of Membranes* (eds Drioli, E. & Giorno, L.) 1–5 (Springer Berlin Heidelberg, Berlin, Heidelberg, 2015). ISBN: 978-3-642-40872-4.

12. Rogers, C. E. in *Polymer Permeability* (ed Comyn, J.) 11–73 (Springer Netherlands, Dordrecht, 1985). ISBN: 978-94-009-4858-7.

13. Mahdi, N., Ibrahim, S. & Alsalhy, Q. Modeling and simulation of pervaporation (PV) separation for alcohol dehydration. *Heliyon* **9,** e13713 (Feb. 2023).

14. Müller-Plathe, F. Permeation of polymers — a computational approach. *Acta Polymerica* **45,** 259–293 (1994).

15. Barrer, R. M. *Diffusion in and through solids* ISBN: 5883795331 (University Press, 1941).

16. Teck Kim, Y., Min, B. & Won Kim, K. in *Innovations in Food Packaging (Second Edition)* (ed Han, J. H.) Second Edition, 13–35 (Academic Press, San Diego, 2014). ISBN: 978-0-12-394601-0.

17. Tajeddin, B. & Arabkhedri, M. in *Polymer Science and Innovative Applications* (eds AlMaadeed, M. A. A., Ponnamma, D. & Carignano, M. A.) 525–543 (Elsevier, 2020). ISBN: 978-0-12-816808-0.

18. Siracusa, V. in *Antimicrobial Food Packaging* (ed Barros-Velázquez, J.) 95–106 (Academic Press, San Diego, 2016). ISBN: 978-0-12-800723-5.

19. Song, Y., Tzeng, P. & Grunlan, J. C. Super Oxygen and Improved Water Vapor Barrier of Polypropylene Film with Polyelectrolyte Multilayer Nanocoatings. *Macromolecular Rapid Communications* **37,** 963–968 (2016).

20. Akelah, A. in *Functionalized Polymeric Materials in Agriculture and the Food Industry* 293–347 (Springer US, 2013). ISBN: 978-1-4614-7061-8.

21. Amberg-Schwab, S. in *Handbook of Sol-Gel Science and Technology: Processing, Characterization and Applications* (eds Klein, L., Aparicio, M. & Jitianu, A.) 3295–3315 (Springer International Publishing, Cham, 2018). ISBN: 978-3-319-32101-1.

22. Logothetidis, S. *et al.* Ultra high barrier materials for encapsulation of flexible organic electronics. *The European Physical Journal - Applied Physics* **51.** 33203, 33203. ISSN: 1286-0042 (2010).

23. Kiese, S., Kücükpinar, E., Miesbauer, O. & Langowski, H.-C. Time-dependent water vapor permeation through multilayer barrier films: Empirical versus theoretical results. *Thin Solid Films* **672,** 199–205. ISSN: 0040-6090 (2019).

24. Commission, E. *Proposal for a REGULATION OF THE EUROPEAN PARLIAMENT AND OF THE COUNCIL on packaging and packaging waste, amending Regulation (EU) 2019/1020 and Directive (EU) 2019/904, and repealing Directive 94/62/EC* COM/2022/677 final. Nov. 2022. `https://eur-lex.europa.eu/legal-content/EN/TXT/?uri=CELEX%3A52022-PC0677`.

25. Nonclercq, A. *Mapping flexible packaging in a Circular Economy [F.I.A.C.E]* Final Report. Oct. 2016. `https://kidv.nl/mapping-flexible-packaging-in-a-circular-economy-1`.

26. Schmidt, J., Grau, L., Auer, M., Maletz, R. & Woidasky, J. Multilayer Packaging in a Circular Economy. *Polymers* **14.** ISSN: 2073-4360 (2022).

27. De Mello Soares, C. T., Ek, M., Östmark, E., Gällstedt, M. & Karlsson, S. Recycling of multi-material multilayer plastic packaging: Current trends and future scenarios. *Resources, Conservation and Recycling* **176,** 105905. ISSN: 0921-3449 (2022).

28. Arends, D., Schlummer, M. & Mäurer, A. Removal of inorganic colour pigments from acrylonitrile butadiene styrene by dissolution-based recycling. *Journal of Material Cycles and Waste Management* **14,** 85–93. ISSN: 1611-8227 (2012).

29. Ragaert, K., Delva, L. & Van Geem, K. Mechanical and chemical recycling of solid plastic waste. *Waste Management* **69,** 24–58. ISSN: 0956-053X (2017).

30. Mulcahy, K., Kilpatrick, A., Harper, G., Walton, A. & Abbott, A. Debondable adhesives and their use in recycling. *Green Chemistry* **24,** 36–61. ISSN: 1463-9262 (Jan. 2022).

31. Mostafapoor, F. *et al.* in *Compatibilization of Polymer Blends* 349–371 (Elsevier, 2020). ISBN: 978-0-12-816006-0.

32. Circular Economy for Flexible Packaging (CEFLEX). *Designing for a Circular Economy (D4ACE)* Sept. 2024. `https://guidelines.ceflex.eu/guidelines/`.

33. Nielsen, L. E. Models for the Permeability of Filled Polymer Systems. *Journal of Macromolecular Science: Part A - Chemistry* **1,** 929–942 (1967).

34. Lau, O.-W. & Wong, S.-K. Contamination in food from packaging material. *Journal of Chromatography A* **882,** 255–270. ISSN: 0021-9673 (2000).

35. Sapalidis, A. A., Katsaros, F. K. & Kanellopoulos, N. K. PVA/montmorillonite nanocomposites: development and properties. *Nanocomposites and polymers with analytical methods,* 29–50 (2011).

36. Matthews, F. L. & Rawlings, R. D. in *Composite Materials* (eds Matthews, F. & Rawlings, R.) 1–28 (Woodhead Publishing, 1999). ISBN: 978-1-85573-473-9.

37. Giannelis, E. P. Polymer-layered silicate nanocomposites: synthesis, properties and applications. *Applied organometallic chemistry* **12,** 675–680. `https://cir.nii.ac.jp/crid/1571135650797160704` (1998).

38. Gilman, J. W. Flammability and thermal stability studies of polymer layered-silicate (clay) nanocomposites. *Applied Clay Science* **15,** 31–49. ISSN: 0169-1317 (1999).

39. Morgan, A. B. Flame retarded polymer layered silicate nanocomposites: a review of commercial and open literature systems. *Polymers for Advanced Technologies* **17,** 206–217 (2006).

40. Samal, S. Effect of shape and size of filler particle on the aggregation and sedimentation behavior of the polymer composite. *Powder Technology* **366,** 43–51. ISSN: 0032-5910 (2020).

41. Zid, S., Zinet, M. & Espuche, E. Modeling diffusion mass transport in multiphase polymer systems for gas barrier applications: A review. *Journal of Polymer Science Part B: Polymer Physics* **56,** 621–639 (2018).

42. Lu, C. & Mai, Y.-W. Influence of Aspect Ratio on Barrier Properties of Polymer-Clay Nanocomposites. *Physical Review Letters* **95,** 088303 (8 2005).

43. Troeh, F. R., Jabro, J. D. & Kirkham, D. Gaseous diffusion equations for porous materials. *Geoderma* **27,** 239–253. ISSN: 0016-7061 (1982).

44. Lape, N. K., Nuxoll, E. E. & Cussler, E. Polydisperse flakes in barrier films. *Journal of Membrane Science* **236,** 29–37. ISSN: 0376-7388 (2004).

45. Shen, L. & Chen, Z. Critical review of the impact of tortuosity on diffusion. *Chemical Engineering Science* **62,** 3748–3755 (2007).

46. Schiessl, S. *et al.* Nanocomposite Coatings Based on Polyvinyl Alcohol and Montmorillonite for High-Barrier Food Packaging. *Frontiers in nutrition* **9,** 790157. ISSN: 2296-861X (2022).

47. Bharadwaj, R. K. Modeling the Barrier Properties of Polymer-Layered Silicate Nanocomposites. *Macromolecules* **34,** 9189–9192 (2001).

48. Schiessl, S., Kucukpinar, E., Schwiddessen, R., Langowski, H.-C. & Eisner, P. Mechanisms of permeation of helium, hydrogen, oxygen, and water vapor through silicate-based composite barrier coating layers. *Surface and Coatings Technology* **483,** 130800. ISSN: 0257-8972 (2024).

49. Kittel, H. *Verarbeitung von Lacken und Beschichtungsstoffen Lehrbuch der Lacke und Beschichtungen* **9.** ISBN: 978-3-7776-1120-4 (2004).

50. Webster, D. C. & Ryntz, R. A. in *Handbook of Industrial Chemistry and Biotechnology* (eds Kent, J. A., Bommaraju, T. V. & Barnicki, S. D.) 805–822 (Springer International Publishing, Cham, 2017). ISBN: 978-3-319-52287-6.

51. Calvez, I., Davoudi, S., Szczepanski, C. R. & Landry, V. Low-gloss UV-curable coatings: Light mechanisms, formulations and processes — A review. *Progress in Organic Coatings* **171,** 107039. ISSN: 0300-9440 (2022).

52. Rawlins, J. W. & Mendon, S. K. in *Polymer Grafting and Crosslinking* 273–318 (John Wiley & Sons, Ltd, 2008). ISBN: 9780470414811.

53. Lange, J. & Wyser, Y. Recent innovations in barrier technologies for plastic packaging—a review. *Packaging Technology and Science* **16,** 149–158 (2003).

54. Fereydoon, M. & Ebnesajjad, S. in *Plastic Films in Food Packaging: Materials, Technology and Applications* 71–92 (Elsevier, 2012).

55. Balgude, D. & Sabnis, A. S. CNSL: an environment friendly alternative for the modern coating industry. *Journal of Coatings Technology and Research* **11,** 169–183. ISSN: 1935-3804 (2014).

56. Friedman, M. Barrier Polymers: Review of Materials, Technologies, and Trends. *Scientific Israel: Technological Advantages* **17** (2015).

57. Todorova, D., Dimitrov, K. & Herzog, M. Solvent free UV curable coating for paper protection. *Sustainable Chemistry and Pharmacy* **24,** 100543. ISSN: 2352-5541 (2021).

58. Wegmann, A. Chemical resistance of waterborne epoxy/amine coatings. *Progress in Organic Coatings* **32,** 231–239. ISSN: 0300-9440 (1997).

59. in. *Paints, Coatings and Solvents* (eds Stoye, D. & Freitag, W.) 11–100 (John Wiley & Sons, Ltd, 1998). ISBN: 9783527611867.

60. Bustillo Revuelta, M. in *Construction Materials: Geology, Production and Applications* 587–602 (Springer International Publishing, Cham, 2021). ISBN: 978-3-030-65207-4.

61. Reed, K. G. in *Surface Coatings: Volume 1 Raw Materials and Their Usage* 356–408 (Springer Netherlands, Dordrecht, 1993). ISBN: 978-94-011-1220-8.

62. Akhter, P., Arshad, A. & Hussain, M. A review on environmental impacts of paints and strategies for producing eco-friendly-paints. *International Journal of Environmental Science and Technology* **22,** 555–578. ISSN: 1735-2630 (2025).

63. Akkerman, J. *et al. Resins for Water-borne Coatings* ISBN: 9783748605249 (Vincentz Network, Hannover, Germany, 2021).

64. Müller, B. & Schackmann, M. *Coatings formulation* (Vincentz Network Hannover, Germany, 2011).

65. Chen, H. *et al.* In Situ Preparation of Mechanically Enhanced Hydrogel via Dispersion Polymerization in Aqueous Solution. *Macromolecular Rapid Communications* **42,** 2100028 (2021).

66. Flory, P. J. Thermodynamics of High Polymer Solutions. *The Journal of Chemical Physics* **10,** 51–61. ISSN: 0021-9606 (1942).

67. Mendel, J. in *Nanostructure Science and Technology: R&D Status and Trends in Nanoparticles, Nanostructured Materials, and Nanodevices* 35–47 (Springer Netherlands, Dordrecht, 1999). ISBN: 978-94-015-9185-0.

68. Pissis, P. & Kyritsis, A. Hydration studies in polymer hydrogels. *Journal of Polymer Science Part B: Polymer Physics* **51,** 159–175 (2013).

69. Francis, L. & Roberts, C. in *Materials Processing* Publisher Copyright: © 2016 Elsevier Inc. All rights reserved., 415–512 (Elsevier, Jan. 2016). ISBN: 9780123851338.

70. Rovera, C. *et al.* Enzymatic Hydrolysis in the Green Production of Bacterial Cellulose Nanocrystals. *ACS Sustainable Chemistry & Engineering* **6,** 7725–7734 (2018).

71. Wang, J. *et al.* Moisture and Oxygen Barrier Properties of Cellulose Nanomaterial-Based Films. *ACS Sustainable Chemistry & Engineering* **6,** 49–70 (2018).

72. Wu, Y. *et al.* Advanced nanocellulose-based gas barrier materials: Present status and prospects. *Chemosphere* **286,** 131891. ISSN: 0045-6535 (2022).

73. Gan, P. G., Sam, S. T., Abdullah, M. F. b. & Omar, M. F. Thermal properties of nanocellulose-reinforced composites: A review. *Journal of Applied Polymer Science* **137,** 48544 (2020).

74. Cui, Y., Kumar, S., Rao Kona, B. & van Houcke, D. Gas barrier properties of polymer/clay nanocomposites. *RSC Advances* **5,** 63669–63690 (78 2015).

75. Rovera, C., Ghaani, M. & Farris, S. Nano-inspired oxygen barrier coatings for food packaging applications: An overview. *Trends in Food Science & Technology* **97,** 210–220 (2020).

76. Strunz Karl Hugo und Tennyson, C. *Mineralogische Tabellen* (Akademische Verlagsgesellschaft Geest & Portig KG, 1982).

77. Vladimirov, V., Betchev, C., Vassiliou, A., Papageorgiou, G. & Bikiaris, D. Dynamic mechanical and morphological studies of isotactic polypropylene/fumed silica nanocomposites with enhanced gas barrier properties. *Composites Science and Technology* **66,** 2935–2944. ISSN: 0266-3538 (2006).

78. Zoppi, R., das Neves, S. & Nunes, S. Hybrid films of poly(ethylene oxide-b-amide-6) containing sol–gel silicon or titanium oxide as inorganic fillers: effect of morphology and mechanical properties on gas permeability. *Polymer* **41,** 5461–5470. ISSN: 0032-3861 (2000).

79. Dameron, A. A. *et al.* Gas Diffusion Barriers on Polymers Using Multilayers Fabricated by Al2O3 and Rapid SiO2 Atomic Layer Deposition. *The Journal of Physical Chemistry C* **112,** 4573–4580 (2008).

80. Ali, A., Yusoh, K. & Hasany, S. F. Synthesis and Physicochemical Behaviour of Polyurethane-Multiwalled Carbon Nanotubes Nanocomposites Based on Renewable Castor Oil Polyols. *Journal of Nanomaterials* **2014,** 564384 (2014).

81. Berean, K. J. *et al.* Enhanced Gas Permeation through Graphene Nanocomposites. *The Journal of Physical Chemistry C* **119,** 13700–13712 (2015).

82. Cui, Y., Kundalwal, S. & Kumar, S. Gas barrier performance of graphene/polymer nanocomposites. *Carbon* **98,** 313–333. ISSN: 0008-6223 (2016).

83. Gao, Y., Picot, O. T., Bilotti, E. & Peijs, T. Influence of filler size on the properties of poly(lactic acid) (PLA)/graphene nanoplatelet (GNP) nanocomposites. *European Polymer Journal* **86,** 117–131. ISSN: 0014-3057 (2017).

84. Leenaerts, O., Partoens, B. & Peeters, F. M. Water on graphene: Hydrophobicity and dipole moment using density functional theory. *Physical Review B* **79,** 235440 (23 2009).

85. Sinha Ray, S. & Okamoto, M. Polymer/layered silicate nanocomposites: a review from preparation to processing. *Progress in Polymer Science* **28,** 1539–1641. ISSN: 0079-6700 (2003).

86. Picard, E., Espuche, E. & Fulchiron, R. Effect of an organo-modified montmorillonite on PLA crystallization and gas barrier properties. *Applied Clay Science* **53,** 58–65. ISSN: 0169-1317 (2011).

87. Xie, L. *et al.* Preparation and Performance of High-Barrier Low Density Polyethylene/Organic Montmorillonite Nanocomposite. *Polymer-Plastics Technology and Engineering* **51,** 1251–1257 (2012).

88. Kalendova, A., Merinska, D., Gerard, J. F. & Slouf, M. Polymer/clay nanocomposites and their gas barrier properties. *Polymer Composites* **34,** 1418–1424 (2013).

89. Klockmann, F., Ramdohr, P. & Strunz, H. *Lehrbuch der Mineralogie* ISBN: 9783432829869 (Thieme, Stuttgart, 1978).

90. Zhou, C., Tong, D. & Yu, W. in *Nanomaterials from Clay Minerals* (eds Wang, A. & Wang, W.) 335–364 (Elsevier, 2019). ISBN: 978-0-12-814533-3.

91. Zhu, T. T. *et al.* Exfoliation of montmorillonite and related properties of clay/polymer nanocomposites. *Applied Clay Science* **169,** 48–66. ISSN: 0169-1317 (2019).

92. Do Nascimento, G. M. in *Clay and Clay Minerals* (ed Nascimento, G. M. D.) chap. 1 (IntechOpen, Rijeka, 2021).

93. Schoonheydt, R. A. & Johnston, C. T. The surface properties of clay minerals. **11** (eds Brigatti, M. F. & Mottana, A.) (2011).

94. Tombácz, E. & Szekeres, M. Colloidal behavior of aqueous montmorillonite suspensions: the specific role of pH in the presence of indifferent electrolytes. *Applied Clay Science* **27,** 75–94. ISSN: 0169-1317 (2004).

95. Borchardt, G. in *Minerals in Soil Environments* 675–727 (John Wiley & Sons, Ltd, 1989). ISBN: 9780891188605.

96. Schoonheydt, R. & Johnston, C. in *Handbook of Clay Science* (eds Bergaya, F. & Lagaly, G.) 139–172 (Elsevier, 2013).

97. Hendricks, S. B., Nelson, R. & Alexander, L. T. Hydration mechanism of the clay mineral montmorillonite saturated with various Cations. *Journal of the American Chemical Society* **62,** 1457–1464 (1940).

98. Clark, G. L., Grim, R. E. & Bradley, W. F. A Study of the Behavior of Montmorillonite upon Wetting. *Zeitschrift für Kristallographie - Crystalline Materials* **97,** 216–222 (1937).

99. White, W. A. Water Sorption Properties of Homoionic Montmorillonite. *Clays and Clay Minerals* **3,** 186–204. ISSN: 1552-8367 (1954).

100. Norrish, K. The swelling of montmorillonite. *Discussions of the Faraday Society* **18,** 120–134 (1954).

101. Murima, D., Pfukwa, H., Tiggelman, I., Hartmann, P. C. & Pasch, H. Novel Polymer Clay-Based Nanocomposites: Films with Remarkable Optical and Water Vapor Barrier Properties. *Macromolecular Materials and Engineering* **301,** 836–845 (2016).

102. Min, F., Peng, C. & Liu, L. Investigation on hydration layers of fine clay mineral particles in different electrolyte aqueous solutions. *Powder Technology* **283,** 368–372. ISSN: 0032-5910 (2015).

103. Yürüdü, C. *et al.* Preparation and characterization of PVA/OMMT composites. *Journal of Applied Polymer Science* **102,** 2315–2323 (2006).

104. Günister, E., Pestreli, D., Ünlü, C. H., Atıcı, O. & Güngör, N. Synthesis and characterization of chitosan-MMT biocomposite systems. *Carbohydrate Polymers* **67,** 358–365. ISSN: 0144-8617 (2007).

105. Diaconu, G., Paulis, M. & Leiza, J. R. Towards the synthesis of high solids content waterborne poly(methyl methacrylate-co-butyl acrylate)/ montmorillonite nanocomposites. *Polymer* **49,** 2444–2454. ISSN: 0032-3861 (2008).

106. Reading, M. & Vaughan, A. S. *Dispersion and Rheology of Poly(ethylene oxide) / MMT Nanocomposites* in *2008 Annual Report Conference on Electrical Insulation and Dielectric Phenomena* (2008), 37–40.

107. Majdzadeh-Ardakani, K., Lofgren, E. A. & Jabarin, S. A. The effect of particle size distribution on the dispersion of nanoclays in poly(ethylene terephthalate)/clay nanocomposites. *Journal of Reinforced Plastics and Composites* **33,** 358–368 (2014).

108. Uysal-Unalan, I., Cerri, G., Marcuzzo, E., Cozzolino, C. A. & Farris, S. Nanocomposite films and coatings using inorganic nanobuilding blocks (NBB): current applications and future opportunities in the food packaging sector. *RSC Advances* **4,** 29393–29428 (56 2014).

109. Zhou, X.-P., Xie, X.-L., Yu, Z.-Z. & Mai, Y.-W. Intercalated structure of polypropylene/in situ polymerization-modified talc composites via melt compounding. *Polymer* **48,** 3555–3564. ISSN: 0032-3861 (2007).

110. Shen, Z., Simon, G. P. & Cheng, Y.-B. Comparison of solution intercalation and melt intercalation of polymer–clay nanocomposites. *Polymer* **43,** 4251–4260. ISSN: 0032-3861 (2002).

111. Zehetmeyer, G., Soares, R. M. D., Brandelli, A., Mauler, R. S. & Oliveira, R. V. B. Evaluation of polypropylene/montmorillonite nanocomposites as food packaging material. *Polymer Bulletin* **68,** 2199–2217. ISSN: 1436-2449 (2012).

112. Kong, J., Li, Z., Cao, Z., Han, C. & Dong, L. The excellent gas barrier properties and unique mechanical properties of poly(propylene carbonate)/ organo-montmorillonite nanocomposites. *Polymer Bulletin* **74,** 5065–5082. ISSN: 1436-2449 (2017).

113. Li, Y. *et al.* Properties of Poly(Lactic Acid)/ Organo-Montmorillonite Nanocomposites Prepared by Solution Intercalation. *Journal of Macromolecular Science, Part B* **52,** 1041–1055 (2013).

114. Priolo, M. A., Holder, K. M., Gamboa, D. & Grunlan, J. C. Influence of Clay Concentration on the Gas Barrier of Clay–Polymer Nanobrick Wall Thin Film Assemblies. *Langmuir* **27,** 12106–12114 (2011).

115. Hagen, D. A., Saucier, L. & Grunlan, J. C. Controlling Effective Aspect Ratio and Packing of Clay with pH for Improved Gas Barrier in Nanobrick Wall Thin Films. *ACS Applied Materials & Interfaces* **6,** 22914–22919 (2014).

116. Kim, S., Byeon, C. C. & Kim, S. Y. Electrochemical Response of Clay/Polyelectrolyte Composite Barrier Coatings. *Coatings* **10.** ISSN: 2079-6412 (2020).

117. Osman, M. A., Mittal, V., Morbidelli, M. & Suter, U. W. Epoxy-Layered Silicate Nanocomposites and Their Gas Permeation Properties. *Macromolecules* **37,** 7250–7257 (2004).

118. Tsurko, E. S. *et al.* Can high oxygen and water vapor barrier nanocomposite coatings be obtained with a waterborne formulation? *Journal of Membrane Science* **540,** 212–218. ISSN: 0376-7388 (2017).

119. Idris, A., Muntean, A. & Mesic, B. A review on predictive tortuosity models for composite films in gas barrier applications. *Journal of Coatings Technology and Research* **19,** 699–716. ISSN: 1935-3804 (2022).

120. Cassagnau, P. Linear viscoelasticity and dynamics of suspensions and molten polymers filled with nanoparticles of different aspect ratios. *Polymer* **54,** 4762–4775. ISSN: 0032-3861 (2013).

121. Galgali, G., Agarwal, S. & Lele, A. Effect of clay orientation on the tensile modulus of polypropylene–nanoclay composites. *Polymer* **45,** 6059–6069. ISSN: 0032-3861 (2004).

122. Weon, J.-I. & Sue, H.-J. Effects of clay orientation and aspect ratio on mechanical behavior of nylon-6 nanocomposite. *Polymer* **46.** Polymer Blends, Composites and Hybrid Polymeric Materials, 6325–6334. ISSN: 0032-3861 (2005).

123. Edwards, D. C. Polymer-filler interactions in rubber reinforcement. *Journal of Materials Science* **25,** 4175–4185. ISSN: 1573-4803 (1990).

124. Hooper, J. B. & Schweizer, K. S. Theory of Phase Separation in Polymer Nanocomposites. *Macromolecules* **39,** 5133–5142 (2006).

125. Silva, F. E. F., Di-Medeiros, M. C. B., Batista, K. A. & Fernandes, K. F. PVA/Polysaccharides Blended Films: Mechanical Properties. *Journal of Materials* **2013,** 413578 (2013).

126. Karimi, A. & Wan Daud, W. M. A. Comparison the properties of PVA/Na^+-MMT nanocomposite hydrogels prepared by physical and physicochemical crosslinking. *Polymer Composites* **37,** 897–906 (2016).

127. Grunlan, J. C., Grigorian, A., Hamilton, C. B. & Mehrabi, A. R. Effect of clay concentration on the oxygen permeability and optical properties of a modified poly(vinyl alcohol). *Journal of Applied Polymer Science* **93,** 1102–1109 (2004).

128. Åsa Nyflött *et al.* Influence of kaolin addition on the dynamics of oxygen mass transport in polyvinyl alcohol dispersion coatings. *Nordic Pulp & Paper Research Journal* **30,** 385–392 (2015).

129. Ding, F. *et al.* Biomimetic nanocoatings with exceptional mechanical, barrier, and flame-retardant properties from large-scale one-step coassembly. *Science Advances* **3,** 1701212 (2017).

130. Song, Y., Gerringer, J., Qin, S. & Grunlan, J. C. High Oxygen Barrier Thin Film from Aqueous Polymer/Clay Slurry. *Industrial & Engineering Chemistry Research* **57,** 6904–6909 (2018).

131. Ben Dhieb, F., Tabatabaei, S. H., Mighri, F. & Ajji, A. Comparison of Crosslinking Efficiency in Dip and Roll-Deposited Coatings on Their Oxygen Barrier. *ACS Omega* **4.** PMID: 31592139, 15772–15779 (2019).

132. Dabbaghianamiri, M., Duraia, E.-S. M. & Beall, G. W. Self-assembled Montmorillonite clay-poly vinyl alcohol nanocomposite as a safe and efficient gas barrier. *Results in Materials* **7,** 100101. ISSN: 2590-048X (2020).

133. Meng, X. *et al.* Fabrication of transparent clay-polymer hybrid coatings on PET film to enhance flame retardancy and oxygen barrier properties. *Progress in Organic Coatings* **147,** 105788. ISSN: 0300-9440 (2020).

134. LaChance, A. M. *et al.* Doctor-Blade-Assisted Casting for Forming Thin Composite Coatings of Montmorillonite and Poly(vinyl alcohol). *Industrial & Engineering Chemistry Research* **61,** 3766–3774 (2022).

135. LaChance, A. M. *et al.* Spin Coating for Forming Thin Composite Coatings of Montmorillonite and Poly(vinyl alcohol). *Industrial & Engineering Chemistry Research* **61,** 4168–4177 (2022).

136. Yue, S. *et al.* Polyvinyl Alcohol/Montmorillonite Nanocomposite Coated Biodegradable Films With Outstanding Barrier Properties. *ES Materials & Manufacturing* **20,** 834. ISSN: 2576-9898 (2023).

137. Zou, T. *et al.* Polyethylene Terephthalate Composite Films with Enhanced Flame Retardancy and Gas Barrier Properties via Self-Assembly Nanocoating. *Nanomaterials* **13.** ISSN: 2079-4991 (2023).

138. Park, J., Shin, K. & Lee, C. Roll-to-Roll Coating Technology and Its Applications: A Review. *International Journal of Precision Engineering and Manufacturing* **17,** 537–550. ISSN: 2005-4602 (2016).

139. Wang, H. *et al.* Kinetics and functional effectiveness of nisin loaded antimicrobial packaging film based on chitosan/poly(vinyl alcohol). *Carbohydrate Polymers* **127,** 64–71 (2015).

140. Maes, C. *et al.* Recent Updates on the Barrier Properties of Ethylene Vinyl Alcohol Copolymer (EVOH): A Review. *Polymer Reviews* **58,** 209–246 (2018).

141. Gaume, J. *et al.* Optimization of PVA clay nanocomposite for ultra-barrier multilayer encapsulation of organic solar cells. *Solar Energy Materials and Solar Cells* **99.** 9th International Meeting on Electrochromism, 240–249. ISSN: 0927-0248 (2012).

142. Spoljaric, S. *et al.* Nanofibrillated cellulose, poly(vinyl alcohol), montmorillonite clay hybrid nanocomposites with superior barrier and thermomechanical properties. *Polymer Composites* **35,** 1117–1131 (2014).

143. Johansson, C. & Clegg, F. Hydrophobically modified poly(vinyl alcohol) and bentonite nanocomposites thereof: Barrier, mechanical, and aesthetic properties. *Journal of Applied Polymer Science* **132** (2015).

144. Chen, C. *et al.* Effects of montmorillonite on the properties of cross-linked poly(vinyl alcohol)/boric acid films. *Progress in Organic Coatings* **112,** 66–74. ISSN: 0300-9440 (2017).

145. Zhang, L. *et al.* Sodium lactate loaded chitosan-polyvinyl alcohol/montmorillonite composite film towards active food packaging. *Innovative Food Science & Emerging Technologies* **42,** 101–108. ISSN: 1466-8564 (2017).

146. Zamanian, M. *et al.* Barrier Properties of PVA/TiO2/MMT Mixed-Matrix Membranes for Food Packaging. *Journal of Polymers and the Environment* **29,** 1396–1411. ISSN: 1572-8919 (2021).

147. Lai, M.-C. *et al.* Advanced environmentally friendly anticorrosive materials prepared from water-based polyacrylate/Na+-MMT clay nanocomposite latexes. *European Polymer Journal* **43,** 4219–4228. ISSN: 0014-3057 (2007).

148. Nazarenko, S., Meneghetti, P., Julmon, P., Olson, B. G. & Qutubuddin, S. Gas barrier of polystyrene montmorillonite clay nanocomposites: Effect of mineral layer aggregation. *Journal of Polymer Science Part B: Polymer Physics* **45,** 1733–1753 (2007).

149. Yuan, G.-L. *et al.* Nanocomposites of urethane and montmorillonite clay in emulsion: In situ preparation and characterization. *Journal of Applied Polymer Science* **114,** 1964–1969 (2009).

150. Herrera-Alonso, J. M., Sedláková, Z. & Marand, E. Gas transport properties of polyacrylate/clay nanocomposites prepared via emulsion polymerization. *Journal of Membrane Science* **363,** 48–56. ISSN: 0376-7388 (2010).

151. Introzzi, L. *et al.* Ultrasound-Assisted Pullulan/Montmorillonite Bionanocomposite Coating with High Oxygen Barrier Properties. *Langmuir* **28.** PMID: 22765289, 11206–11214 (2012).

152. Möller, M. W. *et al.* UV-cured, flexible, and transparent nanocomposite coating with remarkable oxygen barrier. *Advanced materials (Deerfield Beach, Fla.)* **24,** 2142—2147. ISSN: 0935-9648 (2012).

153. Wu, C.-N., Saito, T., Fujisawa, S., Fukuzumi, H. & Isogai, A. Ultrastrong and High Gas-Barrier Nanocellulose/Clay-Layered Composites. *Biomacromolecules* **13.** PMID: 22568705, 1927–1932 (2012).

154. Kochumalayil, J. J. *et al.* Bioinspired and Highly Oriented Clay Nanocomposites with a Xyloglucan Biopolymer Matrix: Extending the Range of Mechanical and Barrier Properties. *Biomacromolecules* **14.** PMID: 23198819, 84–91 (2013).

155. Malucelli, G., Alongi, J., Gioffredi, E. & Lazzari, M. Thermal, rheological, and barrier properties of waterborne acrylic nanocomposite coatings based on boehmite or organo-modified montmorillonite. *Journal of Thermal Analysis and Calorimetry* **111,** 1303–1310. ISSN: 1572-8943 (2013).

156. Agarwal, A., Raheja, A., Natarajan, T. & Chandra, T. Effect of electrospun montmorillonite-nylon 6 nanofibrous membrane coated packaging on potato chips and bread. *Innovative Food Science & Emerging Technologies* **26,** 424–430. ISSN: 1466-8564 (2014).

157. Lim, J. W., Lim, W. S., Lee, M. H. & Park, H. J. Barrier and structural properties of polyethylene terephthalate film coated with poly(acrylic acid)/montmorillonite nanocomposites. *Packaging Technology and Science* **34,** 141–150 (2021).

158. Barbato, A., Apicella, A., Malvano, F., Scarfato, P. & Incarnato, L. High-Barrier, Biodegradable Films with Polyvinyl Alcohol/Polylactic Acid + Wax Double Coatings: Influence of Relative Humidity on Transport Properties and Suitability for Modified Atmosphere Packaging Applications. *Polymers* **15.** ISSN: 2073-4360 (2023).

159. Kunam, P. K., Ramakanth, D., Akhila, K. & Gaikwad, K. K. Bio-based materials for barrier coatings on paper packaging. *Biomass Conversion and Biorefinery* **14,** 12637–12652. ISSN: 2190-6823 (2024).

160. Bee, S.-L., Abdullah, M., Bee, S.-T., Sin, L. T. & Rahmat, A. Polymer nanocomposites based on silylated-montmorillonite: A review. *Progress in Polymer Science* **85,** 57–82. ISSN: 0079-6700 (2018).

161. Tai, J., Chen, K., Yang, F. & Yang, R. Heat-sealing properties of soy protein isolate/polyvinyl alcohol film made compatible by glycerol. *Journal of Applied Polymer Science* **131** (2014).

162. Kim, J. M. *et al.* Influence of Food with High Moisture Content on Oxygen Barrier Property of Polyvinyl Alcohol (PVA)/Vermiculite Nanocomposite Coated Multilayer Packaging Film. *Journal of Food Science* **83,** 349–357 (2018).

163. Niinivaara, E., Desmaisons, J., Dufresne, A., Bras, J. & Cranston, E. D. Film thickness limits of a buckling-based method to determine mechanical properties of polymer coatings. *Journal of Colloid and Interface Science* **582,** 227–235. ISSN: 0021-9797 (2021).

164. Schneider, M., Claverie, J., Graillat, C. & McKenna, T. F. High solids content emulsions. I. A study of the influence of the particle size distribution and polymer concentration on viscosity. *Journal of Applied Polymer Science* **84,** 1878–1896 (2002).

165. Kunnen, J. General viscosity-composition relationship for dispersions, solutions and binary liquid systems. *Rheologica Acta* **23,** 424–434. ISSN: 1435-1528 (1984).

166. Dumont, M.-J., Reyna-Valencia, A., Emond, J.-P. & Bousmina, M. Barrier properties of polypropylene/organoclay nanocomposites. *Journal of Applied Polymer Science* **103,** 618–625 (2007).

167. Villaluenga, J. *et al.* Gas transport properties of polypropylene/clay composite membranes. *European Polymer Journal* **43,** 1132–1143. ISSN: 0014-3057 (2007).

168. Tzeng, P., Lugo, E. L., Mai, G. D., Wilhite, B. A. & Grunlan, J. C. Super Hydrogen and Helium Barrier with Polyelectolyte Nanobrick Wall Thin Film. *Macromolecular Rapid Communications* **36,** 96–101 (2015).

169. Habel, C. *et al.* Lightweight Ultra-High-Barrier Liners for Helium and Hydrogen. *ACS Nano* **14,** 7018–7024 (2020).

170. Zhang, Y., Liu, Q., Zhang, Q. & Lu, Y. Gas barrier properties of natural rubber/kaolin composites prepared by melt blending. *Applied Clay Science* **50,** 255–259. ISSN: 0169-1317 (2010).

171. Sirousazar, M., Yari, M., Achachlouei, B. F., Arsalani, J. & Mansoori, Y. Polypropylene/montmorillonite Nanocomposites for Food Packaging. *e-Polymers* **7,** 027 (2007).

172. Fotovvati, B., Namdari, N. & Dehghanghadikolaei, A. On Coating Techniques for Surface Protection: A Review. *Journal of Manufacturing and Materials Processing* **3.** ISSN: 2504-4494 (2019).

173. Fahlteich, J. *et al.* Roll-to-roll thin film coating on fluoropolymer webs – Status, challenges and applications. *Surface and Coatings Technology* **314.** Selected papers from the Society of Vacuum Coaters 59th Annual Technical Conference, 160–168. ISSN: 0257-8972 (2017).

174. Kwon, O. *et al.* Fabrication Techniques for Graphene Oxide-Based Molecular Separation Membranes: Towards Industrial Application. *Nanomaterials* **11.** ISSN: 2079-4991 (2021).

175. Lightfoot, E. J. & Cohen, E. D. in *Roll-to-Roll Manufacturing* 19–63 (John Wiley & Sons, Ltd, 2018). ISBN: 9781119163824.

176. Kistler, S. F. & Schweizer, P. M. in *Liquid Film Coating: Scientific principles and their technological implications* (eds Kistler, S. F. & Schweizer, P. M.) 3–15 (Springer Netherlands, Dordrecht, 1997). ISBN: 978-94-011-5342-3.

177. Pasquarelli, R. M., Ginley, D. S. & O'Hayre, R. Solution processing of transparent conductors: from flask to film. *Chemical Society reviews* **40,** 5406–5441. ISSN: 0306-0012 (2011).

178. Bauer, M., Duerkop, A. & Baeumner, A. J. Critical review of polymer and hydrogel deposition methods for optical and electrochemical bioanalytical sensors correlated to the sensor's applicability in real samples. *Analytical and Bioanalytical Chemistry* **415,** 83–95. ISSN: 1618-2650 (2023).

179. Zhang, X. *et al.* Development and application of blade-coating technique in organic solar cells. *Nano Research* **16,** 11571–11588. ISSN: 1998-0000 (2023).

180. Kannan, A. *et al.* Wire rod coating process of gas diffusion layers fabrication for proton exchange membrane fuel cells. *Journal of Power Sources* **178,** 231–237. ISSN: 0378-7753 (2008).

181. Durst, F. & Wagner, H.-G. in *Liquid Film Coating* 401–426 (Springer Science+Business Media Dordrecht, 2012). ISBN: 978-94-010-6246-6.

182. Ding, X., Liu, J. & Harris, T. A. L. A review of the operating limits in slot die coating processes. *AIChE Journal* **62,** 2508–2524 (2016).

183. Madaeni, S., Badieh, M. M. S. & Vatanpour, V. Effect of coating method on gas separation by PDMS/PES membrane. *Polymer Engineering & Science* **53,** 1878–1885 (2013).

184. Joshi, M., Adak, B. & Butola, B. Polyurethane nanocomposite based gas barrier films, membranes and coatings: A review on synthesis, characterization and potential applications. *Progress in Materials Science* **97,** 230–282. ISSN: 0079-6425 (2018).

185. Schiessl, S., Kucukpinar, E., Rivollier, N., Langowski, H.-C. & Eisner, P. A Comparative Study on the Roll-to-Roll Processing of a Silicate–Polyvinyl Alcohol Composite Barrier Lacquer Using Slot-Die and Reverse Gravure Coating Techniques. *Polymers* **15.** ISSN: 2073-4360 (2023).

186. Lindner, M., Rodler, N., Jesdinszki, M., Schmid, M. & Sängerlaub, S. Surface energy of corona treated PP, PE and PET films, its alteration as function of storage time and the effect of various corona dosages on their bond strength after lamination. *Journal of Applied Polymer Science* **135,** 45842 (2018).

187. Struller, C., Kelly, P. & Copeland, N. Aluminum oxide barrier coatings on polymer films for food packaging applications. *Surface and Coatings Technology* **241.** Selected Papers from the Society of Vacuum Coaters 56th Annual Technical Conference - SVC TechCon 2013, 130–137. ISSN: 0257-8972 (2014).

188. Navaneetha Pandiyaraj, K., Selvarajan, V., Deshmukh, R. & Gao, C. Adhesive properties of polypropylene (PP) and polyethylene terephthalate (PET) film surfaces treated by DC glow discharge plasma. *Vacuum* **83,** 332–339. ISSN: 0042-207X (2008).

189. Guerritore, M. *et al.* Recyclable-by-design mono-material flexible packaging with high barrier properties realized through graphene hybrid coatings. *Resources, Conservation and Recycling* **179,** 106126. ISSN: 0921-3449 (2022).

190. Shi, H., Jiang, G., Shi, H. & Luo, S. Study on Morphology and Rheological Property of Organoclay Dispersions in Soybean Oil Fatty Acid Ethyl Ester over a Wide Temperature Range. *ACS Omega* **5.** PMID: 32039321, 1851–1861 (2020).

191. Huang, Y., Ma, X., Wang, X. & Liang, X. Determination of the interaction using FTIR within the composite gel polymer electrolyte. *Journal of Molecular Structure* **1031,** 30–37. ISSN: 0022-2860 (2013).

192. Kane, S. R., Ashby, P. D. & Pruitt, L. A. ATR-FTIR as a thickness measurement technique for hydrated polymer-on-polymer coatings. *Journal of Biomedical Materials Research Part B: Applied Biomaterials* **91B,** 613–620 (2009).

193. Laroche, G., Fitremann, J. & Gherardi, N. FTIR-ATR spectroscopy in thin film studies: The importance of sampling depth and deposition substrate. *Applied Surface Science* **273,** 632–637. ISSN: 0169-4332 (2013).

194. Delogu, F., Gorrasi, G. & Sorrentino, A. Fabrication of polymer nanocomposites via ball milling: Present status and future perspectives. *Progress in Materials Science* **86,** 75–126. ISSN: 0079-6425 (2017).

195. Valera-Zaragoza, M. *et al.* Controlled modification of sodium montmorillonite clay by a planetary ball-mill as a versatile tool to tune its properties. *Advanced Powder Technology* **32,** 591–599. ISSN: 0921-8831 (2021).

196. Martinez-Garcia, A. *et al.* Effect of ball to powder ratio on the mechanosynthesis of Re_2C and its compressibility. *Journal of Alloys and Compounds* **810,** 151867. ISSN: 0925-8388 (2019).

197. Pacek, A, Baker, M & Utomo, A. Characterisation of flow pattern in a rotor stator high shear mixer. *Proc. Eur. Congr. Chem. Eng* **1,** 16–20 (2007).

198. Rafiqul Bari, G. A., Park, S., Shakila Parveen, A., Lee, S. & Kim, H. High barrier performance of the multilayer film based on epoxy and montmorillonite. *Progress in Organic Coatings* **126,** 1–7. ISSN: 0300-9440 (2019).

199. Giannakas, A. E. & Leontiou, A. A. in *Composites Materials for Food Packaging* 1–71 (John Wiley & Sons, Ltd, 2018). ISBN: 9781119160243.

200. Moldrup, P., Olesen, T., Komatsu, T., Schjønning, P. & Rolston, D. Tortuosity, Diffusivity, and Permeability in the Soil Liquid and Gaseous Phases. *Soil Science Society of America Journal* **65,** 613–623 (2001).

201. Giannelis, E. P. Polymer Layered Silicate Nanocomposites. *Advanced Materials* **8,** 29–35 (1996).

202. Hatzikiriakos, S. G., Rathod, N. & Muliawan, E. B. The effect of nanoclays on the processibility of polyolefins. *Polymer Engineering & Science* **45,** 1098–1107 (2005).

203. Weber, C., Heuser, M. & Stanjek, H. A collection of aspect ratios of common clay minerals determined from conductometric titrations. *Clay Minerals* **49,** 495–498 (2014).

204. Wakai, M. & Almenar, E. Effect of the presence of montmorillonite on the solubility of whey protein isolate films in food model systems with different compositions and pH. *Food Hydrocolloids* **43,** 612–621 (2015).

205. Chen, L. *et al.* Correlation of aspect ratio of montmorillonite nanosheets with the colloidal properties in aqueous solutions. *Results in Physics* **15,** 102526 (2019).

206. Stöter, M. *et al.* Nanoplatelets of Sodium Hectorite Showing Aspect Ratios of ≈ 20 000 and Superior Purity. *Langmuir* **29.** PMID: 23286394, 1280–1285 (2013).

207. Pasquier, E. *et al.* Multilayers of Renewable Nanostructured Materials with High Oxygen and Water Vapor Barriers for Food Packaging. *ACS Applied Materials & Interfaces* **14,** 30236–30245 (2022).

208. Woodard & Curran, Inc. in *Industrial Waste Treatment Handbook (Second Edition)* (ed Woodard & Curran, Inc.) Second Edition, 149–334 (Butterworth-Heinemann, Burlington, 2006). ISBN: 978-0-7506-7963-3.

209. Henry, B. *et al. Gas permeation studies of metal oxide/polymer composite films* in *Proceedings of the annual technical conference-society of vacuum coaters* (2002), 514–518.

210. Ogasawara, T., Ishida, Y., Ishikawa, T., Aoki, T. & Ogura, T. Helium gas permeability of montmorillonite/epoxy nanocomposites. *Composites Part A: Applied Science and Manufacturing* **37.** The 11th US–Japan Conference on Composite Materials, 2236–2240. ISSN: 1359-835X (2006).

211. Wang, X., Pei, Y. & Ma, Y. The effect of microstructure at interface between coating and substrate on damping capacity of coating systems. *Applied Surface Science* **282,** 60–66. ISSN: 0169-4332 (2013).

212. Seidl, W., Bartosik, M., Kolozsvári, S., Bolvardi, H. & Mayrhofer, P. Influence of coating thickness and substrate on stresses and mechanical properties of (Ti,Al,Ta)N/(Al,Cr)N multilayers. *Surface and Coatings Technology* **347,** 92–98. ISSN: 0257-8972 (2018).

213. Wan, C., Tian, G., Cui, N., Zhang, Y. & Zhang, Y. Processing thermal stability and degradation kinetics of poly(vinyl chloride)/montmorillonite composites. *Journal of Applied Polymer Science* **92,** 1521–1526 (2004).

214. Leszczyńska, A., Njuguna, J., Pielichowski, K. & Banerjee, J. Polymer/ montmorillonite nanocomposites with improved thermal properties: Part II. Thermal stability of montmorillonite nanocomposites based on different polymeric matrixes. *Thermochimica Acta* **454,** 1–22. ISSN: 0040-6031 (2007).

215. Zheng, W., Beeler, M., Claus, J. & Xu, X. Poly(lactic acid)/montmorillonite blown films: Crystallization, mechanics, and permeation. *Journal of Applied Polymer Science* **134,** 45260 (2017).

216. Roberts, A. *et al.* Gas permeation in silicon-oxide/polymer (SiO_x/PET) barrier films: role of the oxide lattice, nano-defects and macro-defects. *Journal of Membrane Science* **208,** 75–88. ISSN: 0376-7388 (2002).

217. Feng, X. & Huang, R. Y. Estimation of activation energy for permeation in pervaporation processes. *Journal of Membrane Science* **118,** 127–131. ISSN: 0376-7388 (1996).

218. Sankaran, K., Manoharan, P., S, S. R. & Chattopadhyay, S. A brief insight into the prediction of water vapor transmissibility in highly impermeable hybrid nanocomposites based on bromobutyl/epichlorohydrin rubber blends. *Open Chemistry* **16,** 1207–1213 (2018).

219. Dillingham, R. G. & Oakley, B. R. Surface Energy and Adhesion in Composite–Composite Adhesive Bonds. *The Journal of Adhesion* **82,** 407–426 (2006).

220. Ochoa-Putman, C. & Vaidya, U. K. Mechanisms of interfacial adhesion in metal–polymer composites – Effect of chemical treatment. *Composites Part A: Applied Science and Manufacturing* **42,** 906–915. ISSN: 1359-835X (2011).

221. Encinas, N. *et al.* Surface modification of aircraft used composites for adhesive bonding. *International Journal of Adhesion and Adhesives* **50,** 157–163. ISSN: 0143-7496 (2014).

222. Ulkem, I. & Schreiber, H. The role of interactions at interfaces of glass-fiber reinforced composites. *Composite Interfaces* **2,** 253–263 (1994).

223. Ma, Q., Gu, Y., Li, M., Wang, S. & Zhang, Z. Effects of surface treating methods of high-strength carbon fibers on interfacial properties of epoxy resin matrix composite. *Applied Surface Science* **379,** 199–205. ISSN: 0169-4332 (2016).

224. Ito, Y. & Nakashima, S. Water distribution in low-grade siliceous metamorphic rocks by micro-FTIR and its relation to grain size: a case from the Kanto Mountain region, Japan. *Chemical Geology* **189,** 1–18. ISSN: 0009-2541 (2002).

225. Aktzi, N., Nir, Y., Wang, D., Narkis, M. & Siegmann, A. EVOH/clay nanocomposites produced by melt processing. *Polymer Composites* **22,** 710–720 (2001).

226. Cabedo, L., Giménez, E., Lagaron, J. M., Gavara, R. & Saura, J. J. Development of EVOH-kaolinite nanocomposites. *Polymer* **45,** 5233–5238 (2004).

227. López-Rubio, A. in *Multifunctional and Nanoreinforced Polymers for Food Packaging* (ed Lagarón, J.-M.) 261–284 (Woodhead Publishing, 2011). ISBN: 978-1-84569-738-9.

228. Gaidukov, S., Danilenko, I. & Gaidukova, G. Characterization of Strong and Crystalline Polyvinyl Alcohol/Montmorillonite Films Prepared by Layer-by-Layer Deposition Method. *International Journal of Polymer Science* **2015,** 1–8 (2015).

229. Zhu, S., Chen, J., Zuo, Y., Li, H. & Cao, Y. Montmorillonite/polypropylene nanocomposites: Mechanical properties, crystallization and rheological behaviors. *Applied Clay Science* **52,** 171–178. ISSN: 0169-1317 (2011).

230. Zainal Abedin, N. H., Schiessl, S. & Langowski, H.-C. Buckling Resistance and Its Effect on the Gas Barrier of Composite Coating Layers Based on Polyvinyl Alcohol and Montmorillonite. *Coatings* **14.** ISSN: 2079-6412 (2024).

231. Mirzamohammadi, S., Eslami-Farsani, R. & Ebrahimnezhad-Khaljiri, H. The Effect of Hybridizing Natural Fibers and Adding Montmorillonite Nanoparticles on the Impact and Bending Properties of Eco-Friendly Metal/Composite Laminates. *Advanced Engineering Materials* **25,** 2201791 (2023).

A. Appendix

frontiers in Nutrition

ORIGINAL RESEARCH
published: 07 March 2022
doi: 10.3389/fnut.2022.790157

Nanocomposite Coatings Based on Polyvinyl Alcohol and Montmorillonite for High-Barrier Food Packaging

Stefan Schiessl[1,2]*, *Esra Kucukpinar*[2], *Stéphane Cros*[3], *Oliver Miesbauer*[1], *Horst-Christian Langowski*[1,2] *and Peter Eisner*[1,2,4]

[1] TUM School of Life Sciences, Technical University of Munich, Freising, Germany, [2] Fraunhofer Gesellschaft FhG, Fraunhofer Institute for Process Engineering and Packaging IVV, Freising, Germany, [3] Département Des Technologies Solaires, Université Crenoble Alpes, Commissariat àl'énergieatomique et aux énergies alternatives, Le Bourget-du-Lac, France, [4] Steinbeis-Hochschule, Faculty of Technology and Engineering, Dresden, Germany

OPEN ACCESS

Edited by:
Coralia Garcia,
Keimyung University, South Korea

Reviewed by:
Javier Solorza,
Instituto Politécnico Nacional (IPN), Mexico
Catherine Joly,
Université Claude Bernard Lyon 1, France
Helena Pardo Minetti,
UdelaR, Uruguay

***Correspondence:**
Stefan Schiessl
stefan.schiessl@ivv.fraunhofer.de

Specialty section:
This article was submitted to Nutrition and Food Science Technology, a section of the journal Frontiers in Nutrition

Received: 06 October 2021
Accepted: 24 January 2022
Published: 07 March 2022

Citation:
Schiessl S, Kucukpinar E, Cros S, Miesbauer O, Langowski HC and Eisner P (2022) Nanocomposite Coatings Based on Polyvinyl Alcohol and Montmorillonite for High-Barrier Food Packaging. Front. Nutr. 9:790157. doi: 10.3389/fnut.2022.790157

Materials with high barrier properties against oxygen are required for the packaging of many sensitive foods. Since commodity polymers lack these properties, additional barrier materials are used in plastic-based barrier packaging. These are usually more expensive than commodity polymers and, in higher fractions, also make recycling more difficult. Current developments, therefore, aim at barrier layers that are as thin as possible but retain the barrier properties. One approach is to incorporate nanoparticles into these layers. In this study, the barrier properties of nanocomposite coatings, consisting of unmodified polyvinyl alcohol (PVA), and dispersed stick-shaped halloysite (Hal) or platelet-shaped montmorillonite (MMT) silicate nanoparticles, were investigated. The PVA was dissolved in aqueous nanoparticle dispersions, which were prepared by mechanical shearing, to produce the so-called "nanolacquer." Nanolacquers with nanoparticle concentrations of 7, 30, and 47 vol% with respect to PVA were applied in a single process step with *k*-bar on a polypropylene substrate film. The integration of 30 vol% platelet-shaped MMT enhances the barrier performance in comparison to pure PVA by a factor of 12 and 17 for oxygen and helium, respectively. Scanning electron microscopy (SEM) shows a homogeneous distribution and a parallel alignment of the nanoparticles within the coated layer. An increase in the crystallinity of PVA was observed due to the nanoparticle integration as demonstrated by *x*-ray diffraction (XRD) measurements. The investigation by Fourier transform infrared (FTIR) spectroscopy and the activation energy of the permeation coefficient indicate an interaction between the nanoparticles and the PVA. The theoretically calculated values for barrier enhancement accord well with the experimental values, which emphasizes that the gas barrier improvement for oxygen and helium is mainly dominated by the tortuous path effect.

Keywords: barrier coating, montmorillonite, halloysite, tortuous path, polyvinyl alcohol, nanocomposite, helium permeability, oxygen permeability

1. INTRODUCTION

Some sensitive foods are described by consumers as sensory impaired already at an oxygen intake of less than 1 $\frac{mg}{kg}$ (1). For such products, packaging materials with oxygen permeability down to 0.1 $\frac{cm^3\,(STP)}{m^2\,d\,bar}$ are needed to ensure a sufficiently long shelf life (2). If one wants to achieve high barrier properties, lightweight, and good recyclability for the corresponding packaging at the same time, different solutions are available. The most common are polymer barrier layers made of polyvinyl alcohol (PVA).

These PVA barrier layers are targeted to be as thin as possible without having to sacrifice the barrier properties, because of two main reasons. First, the cost of PVA can be about three to five times higher than for polyolefins that are typically used in flexible packaging applications. Second, the PVA interferes with the recycling of polyolefins. Since the incorporation of platelet-shaped nanoparticles has already shown a significant improvement in many polymers, especially in the oxygen barrier properties (3), this approach was also pursued in this study.

Polyvinyl alcohol provides one of the lowest gas permeability among polymers (4). Its excellent oxygen (O_2) barrier property is - in addition to its flexibility, transparency, toughness, non-toxicity, water solubility, and chemical resistance—the reason why it is a standard polymer for high-barrier food packaging (5, 6). Due to the sensitivity of its oxygen barrier performance toward the high humidity levels, PVA layers are commonly used behind a polypropylene or a polyethylene layer in typical multilayered flexible packaging applications.

The measured oxygen transmission rate is highly dependent on the degree of hydrolysis, the molecular weight, the curing, the measuring conditions, and above all the composition. PVA compositions with an ethylene content of less than 10 %, which are still water soluble, are called PVA in the literature, instead of the more accurate abbreviation EVOH, for ethylene vinyl alcohol co-polymer. The reason, therefore, is that nearly all PVA coatings contain at least a small amount of ethylene, to reduce the melting point of the PVA and increase the temperature gap between the melting point and the decomposition temperature for easier processing of the PVA (7, 8).

Hence, the oxygen permeability coefficients for PVA reported in the literature vary significantly. A summary of several approaches and the corresponding values is given in **Table 1**. While one of the lowest values, 0.3 $\frac{cm^3\,(STP)\,1\,\mu m}{m^2\,d\,bar}$, was obtained by Tsurko et al. (9) with 100 to 1,000 times spray coating of PVA on PET, leading to a dry film thickness of 700 nm, values of higher than 100 $\frac{cm^3\,(STP)\,1\,\mu m}{m^2\,d\,bar}$ are reported for free-standing films (10–13). But apart from these, a typical value for one time coating on flexible films, which was reported as 1 to 6 $\frac{cm^3\,(STP)\,1\,\mu m}{m^2\,d\,bar}$, has been set as a comparative value within this study (14–18).

By the integration of nanoparticles, the abovementioned properties have been enhanced. Coatings with nanocomposite materials provide, e.g., enhancements in antimicrobial, self-healing, flame retardant and barrier properties (19, 20). The oxygen barrier improvement for PVA as a polymer matrix, due to the addition of platelet-shaped silicates, has already been widely studied (see **Table 1**).

TABLE 1 | Overview of oxygen permeability values P_{O_2} for PVA and PVA in combination with silicate nanoparticles described in Section 1.

	P_{O_2} $\frac{cm^3\,(STP)\,1\,\mu m}{m^2\,d\,bar}$	Approach	Source
PVA	0.300	700 nm dry coating layer thickness on PET substrate film, coated with spray coating (100 to 1000 times)	(9)
	1.00	6 µm dry coating layer thickness on PET substrate film, coated with k-bar	(14)
	1.20	4.4 µm dry coating layer thickness on PET substrate film, coated with k-bar	(15)
	4.30	2 µm dry coating layer thickness on PET substrate film, coated with k-bar	(18)
	135	free standing film with 30 µm dry thickness poured in Petri dish and de-formed	(12)
	238	free standing film with 140 µm dry thickness purred in Petri dish and de-formed	(13)
	358	free standing film with 60 µm dry thickness coated with k-bar on glass and peeled off	(11)
PVA in combination with nanoparticles	0.001	synthesized silicate particles with high aspect ratio mixed with PVA and spray coated (100 to 1000 times) on PET	(9)
	0.002	slurry of PVA and MMT poured onto PET sitting in a Petri dish	(26)
	0.010	mixture of MMT, Laponite, and PVA coated 5 times *via* dip coating of PET	(25)
	0.025	modification of PVA with vinyl acetate and iactonic acid and mixing with MMT, coated with k-bar on PET	(14)
	0.200	30 layers in summary, alternating PVA and MMT dispersion coated with k-bar on PET	(23)
	0.800	12 layers in summary, alternating PVA and MMT dispersion coated *via* ink-jetting on PET	(24)

One of the approaches is the development and synthesis of silicate particles, which are nearly impermeable for molecular species, with the highest possible aspect ratio. The aspect ratio is the ratio of the longest and the shortest dimension of a particle. The higher this ratio is, the better is the barrier that can be achieved (21, 22) synthesized, e.g., silicate nanoparticles with an aspect ratio of up to 20,000 (length of 20 µm and width of 1 nm). Nanocomposites with these particles provided one of the lowest published permeability coefficients with 0.001 $\frac{cm^3\,(STP)\,1\,\mu m}{m^2\,d\,bar}$ at 23°C and 50 % RH for a 100 to 1,000 times spray coating on PET by Tsurko et al. (9).

Another approach is a layer-by-layer application of PVA and montmorillonite (MMT) layers. Ben Dhieb et al. (23) reached an oxygen permeability coefficient of 0.2 $\frac{cm^3\,(STP)\,1\,\mu m}{m^2\,d\,bar}$ at 25°C and

0 % RH by an alternating structure of 15 PVA and 15 MMT layers, using a doctor blade coating process. Dabbaghianamiri et al. (24) used an inkjet printing process to produce 6 bilayers. The final value was 0.8 $\frac{cm^3\,(STP)\,1\,\mu m}{m^2\,d\,bar}$ at 23°C and 40 % RH.

One practical approach, for the preparation of PVA-based nanocomposite coatings, focuses on using commercially available clay particles and PVA lacquers, and only a single-layer coating on the respective substrate. For mixtures of PVA with increasing ratios of kaolin (phyllosilicate like MMT with a slightly different structure), Nyflätt et al. (12) did not observe any improvement on the barrier properties of the coatings on PET at a thickness of 1.8 µm. Meng et al. (25) did not find a barrier improvement due to MMT integration for one-time dip-coated PET films. The films have been dipped in PVA and a nanocomposite lacquer of PVA and MMT at a mixing ratio of 1:2. The dry coating layer thickness was 0.8 µm.

In these studies using commercially available clay particles and PVA, some further investigations were still required; for example, Meng et al. (25) mixed MMT with laponite and PVA in equal parts and increased the number of layers to five, leading to a total dry coating layer thickness of 4.0 µm and an oxygen permeability coefficient of 0.01 $\frac{cm^3\,(STP)\,1\,\mu m}{m^2\,d\,bar}$ at 23°C and 0 % RH. Grunlan et al. (14) mixed PVA with vinyl acetate and iactonic acid to get a terpolymer with an intrinsically high oxygen permeability coefficient of 0.5 $\frac{cm^3\,(STP)\,1\,\mu m}{m^2\,d\,bar}$ at 23°C and 55 % RH. This value could be decreased by a factor of 20 by mixing with 20 wt% MMT particles. A high oxygen permeability coefficient of 0.002 $\frac{cm^3\,(STP)\,1\,\mu m}{m^2\,d\,bar}$ at 23°C and 0 % RH was reached by Song et al. (26) with a quite simple process: They poured a slurry of PVA and 50 % MMT onto a 179 µm thick PET substrate and let it dry at room temperature for 6 h.

Although the barrier improvement of PVA coatings with silicate nanoparticles has been proven and very high oxygen barrier performance has already been reported in the literature, the usage of PVA silicate nanocomposites in the packaging industry is still rare. The reasons for this are manifold: either the synthesis of silicate particles is extensive, the number of coating layers is high, the curing time is not adjusted to industrial scale, the substrate material is not the material of interest for the food packaging industry, the barrier properties can only be achieved at low humidity, or there are currently no available green and effective exfoliation methods for the particles. Besides the economic reasons, further scientific knowledge is needed. Factors such as crystallinity, tortuosity, interactions between particles and the polymer need to be further investigated and identified (20, 27).

The aim of this study is a deeper understanding of gas permeation mechanisms in silicate nanocomposites. Therefore, several factors have been taken into account. First of all, two different permeants with different gas kinetic diameters, helium (2.6 Å) and oxygen (3.5 Å), were used (28). The bigger oxygen molecules permeate predominantly through macro-defects (> 1 nm), whereas the permeation of helium is mostly determined by the permeation through nano-defects (< 1 nm) (29–31).

To gain a better understanding of the tortuosity effect, two differently shaped silicate nanoparticles were selected: a stick-shaped Halloysite (Hal), and a platelet-shaped MMT. MMT is a 2:1 type, meaning two SiO-tetrahedra layers flank a central AlO-octahedra layer. Hal is a 1:1 type, like kaolin, but rolled to a nanotube with the SiO-tetrahedra layer outside and the AlO-octahedra layer inside (32).

Since the exfoliation of clay particles to nanoparticles is the crucial step during the production of a nanolacquer, because only well-exfoliated and well-dispersed nanoparticles can improve the barrier properties (20), two different mechanical dispersing techniques were used and the results were compared: a mechanical stirrer and a planetary ball mill. Compared to the typically used mechanical stirrers, the usage of ball mills in the field of nanocomposites is only starting (33). The colliding surfaces in a ball mill subject the particles to mechanical load. This mechanical load, leading to the fracturing and exfoliation, appears very homogeneously in the whole dispersion during the milling process. A mechanical stirrer, in comparison, has one rotating head that applies the shear force to the liquid, with only random direct contact with the particles (34). The resulting dispersions from the dispersing instrument and the planetary ball mill were used as the basis for the nanolacquer and the effect of the mechanical dispersing technique on agglomerations and gas barrier properties is compared.

Finally, the barrier improvement for the respective nanoparticle shape and concentration was calculated based on geometrical factors only and compared with the measured permeability values to identify whether the tortuosity or the structural changes within the PVA resin is the dominating factor for the barrier improvement.

2. MATERIALS AND METHODS

2.1. Materials

Two different types of naturally abundant clay-based silicate types were used to exfoliate nanoparticles, MMT and Hal. The MMT was purchased as CLOISITE Na^+ from BYK Additives and Instruments, Wesel, Germany. Dry ball-milling of this MMT was performed without the addition of any solvent by a proprietary process of MBN Nanomaterialia, Carbonera TV, Italy (35). The powder obtained was then agglomerated, in form of granules, by using a small amount of water, highly reducing the dustiness of the product and, thus, providing operational safety. The Hal was purchased as Hal Clay MF7 from DURTEC, Neubrandenburg, Germany. These two powder types were then mixed with water according to the procedures as described in Section 2.1.1 to obtain the feed-stock dispersion for the coating processes.

PVA, with the trade name Exceval AQ 4104, from Kuraray (Frankfurt, Germany), was the polymeric basis for the lacquers. Since the ethylene content of this material is below 10 %, it is called polyvinyl alcohol in the technical data sheet, although its real chemical composition is an atatic copolymer of ethylene and vinyl alcohol. The molecular weight of AQ 4104 is 27.000 $\frac{g}{mol}$ and the degree of hydrolysis is 98 to 99 mol% (36). The glass transition temperature, T_g, is 74.8°C, the crystallization temperature is 193.3°C, and the melting temperature is 220°C (37).

Biaxially oriented Polypropylene (BoPP) sheets (30 µm in thickness) were purchased as transparent, non-sealable (referred to as TNS) film from Taghleef Industries (San Giorgio, Italy).

To assure a suitable and repeatable wetting, the substrate was pretreated with a modified polyethylenimine (PEI) primer, ORGATIX WS-680A from Matsumoto Fine Chemical Co. (Chiba, Japan). The modification is a crosslinking with a water soluble titanate compound. The primer provides a solid content of 9 % in weight (38).

2.1.1. Preparation of Nanoparticle Dispersion

To exfoliate the clay particles to nanoparticle size, two devices, both providing high mechanical shearing, were used; a high-performance mechanical stirrer (T 25B ULTRA-TURRAX®, IKA Labortechnik, Staufen, Germany) and a planetary ball mill (PULVERISETTE 6, FRITSCH, Idar-Oberstein, Germany). Four different types of aqueous nanoparticle dispersions, each at a solid content of 5 wt%, were produced using either the MMT or Hal powders, each by using one of the two dispersing processes. These four dispersion types are defined as MMT dispersion-UT, MMT dispersion-BM, Hal dispersion-UT, and Hal dispersion-BM. UT and BM are the abbreviations used for ULTRA-TURRAX® and planetary ball mill processes, respectively. The preliminary trials of the authors have shown that, as the nanoparticle concentration increases, the gas barrier performance also increases. On the other hand, if the solid content is increased above 5 wt%, the dispersion becomes pasty. The solid content of 5 wt% was chosen in this study due to the fact that it is the highest possible amount at which the viscosity of the material still allows a homogeneous mixture in PVA as discussed in Section 2.1.4. Based on this, 190 ml of water and 10 g of nanoparticles were mixed for 1 min at 1.000 rpm in a laboratory glass bottle with the ULTRA-TURRAX® (UT). For the exfoliation with the planetary ball mill (BM), 190 ml of water and 10 g of nanoparticles were put in a zirconium oxide cup together with 500 g of zirconium oxide balls (each ball 3 mm in diameter) and rotated at 400 rpm for 1 h. Several exfoliation times for UT and BM have been tested for both processes and further increase of this parameter did not lead to different results, as well as a change of rotation time (UT and BM) and ball size (only BM), therefore, this is not shown in this manuscript.

2.1.2. Fabrication of Nanolacquer

To produce the so-called "nanolacquer," 4 g of PVA granulate were added to the nanoparticle dispersions and slightly diluted with water to obtain the nanoparticle to PVA mixing ratios of 1:6, 1:1, and 2:1 in weight (refer to **Table 2**). This represents the minimum, medium, and high volume fractions of 7, 30, and 47% for the silicate particles calculated with the densities of 2.86 $\frac{g}{cm^3}$ and 1.22 $\frac{g}{cm^3}$ for MMT and for pure PVA, respectively (36, 39). To start the dissolving process of PVA, the mixture was stirred in a closed beaker with a magnetic stirrer for 30 min at 400 rpm. Subsequently, the mixing rate was reduced to 150 rpm and heated up to 90°C for 120 min until the PVA was dissolved completely. This lacquer was then cooled down to room temperature under constant shearing at 150 rpm and degassed in a pressure tank for about 2 h.

TABLE 2 | Nanolacquer formulations using two types of exfoliated nanoparticles (NP) of two different processes, in PVA polymer, each at three different NP:PVA ratios in weight.

Sample code	Mixing ratio (NP : PVA)	NP weight (g)	PVA weight* (g)	Total solid content (wt%)
PVA-ref	0:1	-	8.0	8.0
MMT-UT-30	1:1	4.0	4.0	8.0
MMT-UT-7	1:6	0.7	4.0	4.7
MMT-UT-47	2:1	8.0	4.0	7.3
MMT-BM-30	1:1	4.0	4.0	8.0
MMT-BM-7	1:6	0.7	4.0	4.7
MMT-BM-47	2:1	8.0	4.0	7.3
Hal-UT-30	1:1	4.0	4.0	8.0
Hal-UT-7	1:6	0.7	4.0	4.7
Hal-UT-47	2:1	8.0	4.0	7.3
Hal-BM-30	1:1	4.0	4.0	8.0
Hal-BM-7	1:6	0.7	4.0	4.7
Hal-BM-47	2:1	8.0	4.0	7.3

**For these series of tests, the PVA weight in the final nanolacquer was kept constant.*

2.1.3. Pretreatment of Substrate Film

As described in Section 2.1 the PEI primer, ORGATIX WS-680A, was used to pretreat the substrate chemically. An amount of 30 ml primer was mixed with 970 ml of ethanol (>99.7 %, ethanol absolute, VWR CHEMICALS, Darmstadt, Germany), leading to a solid content of 0.3 wt%. The mixture was applied using a reverse gravure coating process (JWS Maschinenfabrik GmbH, Sinsheim, Germany) at the Fraunhofer-IVV at a web-speed of 4 m/min, and dried at 80°C for 50 s. The theoretical dry layer thickness has been calculated based on the density of 0.789 $\frac{g}{cm^3}$, and with the given solid content of 0.3 wt% for this formulation. It has given a dry layer thickness value of 16.6 nm. The surface energy after pretreatment was measured to be more than 44 $\frac{mN}{m}$ by means of test inks (Teststifte PINK, arcotest, Mönsheim, Germany, according to DIN ISO 8296) (40). This is sufficiently high for the wettability of PVA-based nanolacquers in comparison to untreated PP with 30 $\frac{mN}{m}$. After the roll-to-roll pretreatment with PEI primer, the BoPP film was cut into A4 sized sheets for coatings as described in Section 2.1.4.

2.1.4. Coating of Substrate With Nanolacquer

The pure PVA and the nanolacquer formulations shown in **Table 2** were used to coat the chemically pretreated BoPP substrate. The coatings were applied by a lab-coating unit CUF 5 (Sumet Messtechnik, Denklingen, Germany) with an actuation speed of 30 $\frac{mm}{s}$ and a contact pressure of 30 N. The coating was performed using the k-bar providing a wet layer thickness of 33 µm. The drying process took place directly after the application of the wet lacquer at 80°C in a built-in convective dryer for 2 min.

2.1.5. Preparation of Nanocomposite Free-Standing Films

For the X-ray diffraction (XRD) measurements, free-standing films of pure PVA and nanocomposites were produced, since the BoPP signal was overlapping with the signals of PVA and silicate particles. Therefore, the aforementioned lacquers were coated on a polytetrafluoroethylene (PTFE) film after corona pretreatment according to the procedure in Section 2.1.4, but with several repetitions until a dry layer thickness of 15 µm is reached for each formulation. After 1 week, the coating layers were peeled from the PTFE. A minimum thickness of 15 µm was necessary since the films cannot be handled below this thickness.

2.2. Methods

2.2.1. Asymmetrical Flow Field-Flow Fractionation (AF4)

The particles were separated according to size by means of AF4 measurements with the AF2000 MT Series mid temperature (Postnova Analytics, Landsberg am Lech, Germany). The system is equipped with a 350 µm channel and a cellulose membrane (cut-off: 5 kDa, Postnova Analytics). The channel was constantly maintained at 40°C. Ultrapure water with a conductivity of $<0.055\,\frac{\mu S}{cm}$ was prepared in-house using a TKA GenPure ultrapure water system (TKA Wasseraufbereitungssysteme GmbH, Niederelbert, Germany) and used as flowing liquid for the AF4. The channel flows were controlled by AF2000 Control Program software (Postnova Analytics). Aqueous MMT dispersions were injected into the channel at a flow of 0.2 ml/min with a focus flow of 1.3 ml/min. During the injection time of 8 min, and an additional transition time of 1 min, the cross-flow was kept constant at 1.0 ml/min. After transition, the cross-flow was eliminated within 25 min using a parabolic flow profile (power gradient of 0.2). The main channel flow was kept constant at 0.5 ml/min during the entire run. Sample amounts of 50 µl were injected with a PN5300 series autosampler (Postnova Analytics).

2.2.2. Multi-Angle Laser Light-Scattering Spectrometry (MALLS)

A 21-angle MALLS detector PN3621 (Postnova Analytics) was used for the determination of MMT particle size, controlled by AF2000 Control Program software (Postnova Analytics) (41). The size of the eluting particles was calculated as the radius of gyration r_g using a random coil fit. The calculated r_g was converted into a geometrical radius r_{geo} using the equation developed by Andersson et al. (42).

$$r_g^2 = 0.6 \cdot r_{geo}^2. \tag{1}$$

The particle extension in length L and thickness T, assuming that the MMT particles are symmetric, is calculated as

$$2 \cdot r_{geo} = L = T. \tag{2}$$

The detector was directly coupled to the AF4 system as discussed in Section 2.2.1 and was operated at $\lambda = 532$ nm and 25 mW laser power.

2.2.3. Measurement of Oxygen Permeability

The oxygen permeability, Q_{total}, for coated substrates was measured according to the DIN 53380-3 standard with the oxygen-specific carrier gas method (43). The measurements were carried out with an OX-TRAN 2/21 OTR Analyzer (AMETEK MOCON, Minneapolis, USA) at 23°C and 50 % RH, and afterward also at 23, 25, 30, 35, and 40°C and 0 % RH. If the respective transmission rate was constant for at least 10 h, the measurement was stopped assuming that the steady state was established. A 2-fold determination for all coatings was carried out. The activation energy of the permeation coefficient E_A was determined *via* an Arrhenius plot

$$P = P_0 \cdot e^{-\frac{E_A}{RT}} \tag{3}$$

by measuring the permeability coefficient P at the aforementioned five temperatures at 0 % RH (44). The oxygen permeability of the deposited nanocomposite layer, Q_{NC}, was calculated using the following equation

$$\frac{1}{Q_{total}} = \frac{1}{Q_{Subs}} + \frac{1}{Q_{NC}}. \tag{4}$$

In Equation (4), Q_{Subs} is the oxygen permeability of the BoPP substrate, and Q_{total} is the total permeability of the coated BoPP substrate. Since the permeability strongly depends on the layer thickness d, the permeability values were converted to the corresponding permeability coefficients P according to Equation (5) (45).

$$P = Q \cdot d. \tag{5}$$

A common way to compare the different modifications for gas barrier improvement is the calculation of the barrier improvement factor, *BIF*. As shown in Equation (6), the *BIF* is calculated from the ratio of the permeation coefficient of the pure PVA P_{PVA} and that of the nanocomposite P_{NC}.

$$BIF = \frac{P_{PVA}}{P_{NC}} \tag{6}$$

2.2.4. Measurement of Helium Permeability

The helium permeability was measured with a permeameter QHV-4 (Vinci Technologies, Nanterre, France) using a patented protocol (46, 47). In this measurement device, a mass spectrometer detects an ion current proportional to the permeating rate of the gas. The measurement is performed at 38°C and 0 % RH. First, a helium calibrated leak is measured, then the baseline, and finally, the helium transmission rate of the sample. The measurement is automatically stopped in the steady state considering a geometrical criterion. The use of helium gas allows reducing the measurement time, which is in the range of 1 h considering the full procedure (47).

2.2.5. Comparison of Experimentally Measured Permeability Values of Filled Polymer Systems With Values Calculated Based on Theoretical Models

The Nielsen model was used in order to calculate the permeability coefficients and compare these with the experimentally measured

values (48). It is a purely geometrical model assuming that the nanoparticles are impermeable for the permeating gas and, therefore, increase the diffusion path length, called tortuous path, as shown in **Figure 1**. It is assumed in this model that all particles are homogeneously dispersed and fully exfoliated with no agglomeration in the polymer layer and all oriented parallel to the surface, which means perpendicular to the effective direction of permeation. Although the permeation process through a filled polymer is an extremely complex phenomenon, the model allows—with some assumptions—the appraisal of the permeation blocking potential of nanoparticles based on the geometrical factors. These factors are the particle length L, the particle width W, and the volume ratio of the nanoparticle (filler) ϕ_F. The tortuosity τ is defined as (49).

$$\tau = \frac{\delta}{d} \tag{7}$$

where δ is the distance a molecule must travel to get through the film, i.e., the diffusion path length, and d is the unit length (thickness) of the film. According to this model, δ_{theo} is calculated *via* Equation (8), based on the particle size and volume ratio of the filler (48).

$$\delta_{theo} = \left(1 + \frac{L}{2W} \cdot \phi_F\right) \cdot d. \tag{8}$$

The empirical relation to evaluating δ is based on the measured values for the permeability of the filled (P_{NC}) and the unfilled (P_{PVA}) polymer (49).

$$\delta_{emp} = \sqrt{\frac{P_{PVA}}{P_{NC}} \cdot (1 - \phi_F) \cdot d^2}. \tag{9}$$

The two values δ_{theo} and δ_{emp}, based on the particle geometry and the measured values for permeability, respectively, were compared. By knowing the values for L, W, and ϕ_F, it is also possible to calculate the potential improvement for a known permeability value of PVA without filler according to Equation (10).

$$P_{NC} = \frac{1 - \phi_F}{\left(1 + \frac{L}{2W} \cdot \phi_F\right)^2} \cdot P_{PVA} \tag{10}$$

FIGURE 1 | 2D model for the path of a diffusing molecule through a polymer filled with either impermeable sticks (Hal) or impermeable platelets (MMT), redrawn from (48).

2.2.6. Scanning Electron Microscopy (SEM) Imaging of Barrier Films

The SEM images were captured with a JSM-7200F (JEOL, Akishima, Japan) at a high vacuum (2e−4 Pa). All samples were sputtered with a gold layer using a Hummer JR (Technics, Alexandria VA, USA), to reduce electrical charging of the non-conductive polymer samples. A solid state detector (SSD), detecting backscattered electrons, was used im combination with the JEOL-SEM software. The coated films were placed between Si wafers and cross-sections were prepared by Ar^+ beam milling with a cross-section polisher (IB-19530CP, JEOL, Japan).

2.2.7. X-ray Diffraction

The X-ray powder diffraction (XRD) data were collected with a Seifert 3003 TT diffractometer (XRD Eigenmann GmbH, Schnaittach-Hormersdorf, Germany) using Cu-K_α radiation (λ = 1.54184 Å) equipped with a METEOR 1D linear detector in Bragg-Brentano geometry.

2.2.8. Fourier Transform Infrared (FTIR) Spectroscopy

The FTIR spectra were measured with a Frontier™ FTIR spectrometer L1280034 and analyzed with the PerkinElmer Spectrum IR, Version 10.6.1 software, both supplied by PerkinElmer (Shelton CT, USA). A golden gate setup was used to fix the coated films with the coated side to the diamante crystal for the ATR (attenuated total reflectance) measuring mode. A total number of 16 scans with a resolution of 4 $\frac{1}{cm}$ were recorded within a wavenumber range of 4.000 to 600 $\frac{1}{cm}$. All spectra were baseline corrected.

3. RESULTS AND DISCUSSION

3.1. Particle Size Distribution and Aspect Ratio

Since the isolation and a simultaneous rotation of a single silicate platelet or a tube, in order to be able to measure the extension in three dimensions, is unfeasible, the size estimation of the nanoparticles was executed in two steps. To determine L and T (x- and y-direction), the exfoliated MMT in dispersion was analyzed using AF4/MALLS. To measure the extension in the z-direction (W), SEM images of cross-sections of the coatings were analyzed. The assumption for this is that the degree of exfoliation of the nanoparticles is not effected during the mixing process of the dispersion with PVA (20).

Figure 2 shows the size distribution of silicate platelets dispersed in water as a function of r_{geo} calculated using Equation (1). The particle radius is then transferred to particle size L (=T) by Equation (2). For the dispersion with BM, 90 % of the particles are smaller than 1,000 nm, which is represented by the cumulative curve. The average value for particle size for this dispersion technique was around 494 nm. The dispersion with the UT, on the other hand, showed two peaks, 90 % of the particles were smaller than 3.000 nm with two appearing sizes at 340 and 2,960 nm. The particles bigger than 2.000 nm, originated from agglomerates of silicate platelets that were not exfoliated sufficiently. Nevertheless, the average value for L (=T) of the exfoliated particles was found to be 340 and 494 nm

prepared by UT and BM, respectively. The particles were not broken while dispersing with BM, despite the countless crushes with the ZrO balls. Using the AF4 technique, it is possible to determine the particle size, if the particles appear as spheres, but since they are platelets, cross-section images were analyzed to determine their width. **Figure 3A** shows a cross-section image of MMT-BM coating. In this illustration the MMT platelets appear to be white, since the electron density of silicates is higher than it is for PVA due the heavier Al, Si, and Mg atoms. The thickness of these white lines indicates the W of the platelets and a value of 25 nm was measured for both MMT-BM and MMT-UT (not shown here) samples. Hence, the aspect ratio (L/W) of the MMT particles was calculated as 14 and 20 for dispersions prepared by UT- and BM-processes, respectively. These values are at the lower end of a range from 10 to 1,000, reported for the aspect ratio of MMT containing clay particles (50–54). The variations in L, T, and W, leading to this broad range, are due to the differences in natural abundance in clay minerals, as well as the different preparation methods. Whereas high barriers are normally reached with high aspect ratios (48, 49, 55), nanolacquers with these particles are limited in viscosity, total solid content, and mixing ratio (54). That means an increased size in the aspect ratio always goes along with an increase in viscosity of the nanolacquer. The viscosity, however, can only be as high as the coating technique allows. Additionally, a higher aspect ratio requires more water molecules to be part of the hydration shell, which is necessary for a stable dispersion. Therefore, less water molecules are available to dissolve the polymer, which results either in a lower total solid content of the lacquer or in a limitation in the mixing ratio (56). The parameters of aspect ratio, mixing ratio, total solid content, and viscosity, need to meet the requirement of the coating technique and intended number of coatings and coating layer thickness. The nanoparticles with aspect ratios of 14 and 20, used in this study, allow exactly this sufficient solid content and mixing ratio for the coating within one process step with the k-bar coating technique.

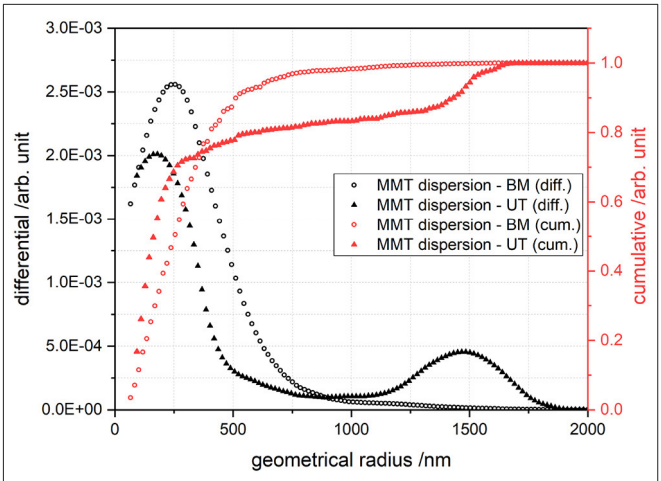

FIGURE 2 | Representative measurement of particle size distribution, assuming spherical shaped particles, for MMT in aqueous dispersion mixed with ULTRA-TURRAX® and planetary ball mill.

It was not possible to perform the size measurement for Hal with the AF4 technique, since the Hal particles were sedimenting too fast in an aqueous dispersion. Therefore, only SEM images were used to determine the L and W of the Hal sticks. As shown in the top view image in **Figure 4**, a value of 150 nm for both extensions of L and W, which represent the diameter in the stick-shaped geometry of Hal, was used for aspect ratio calculation. This accords with reported values for the outer diameter of Hal nanotubes (50 to 200 nm) (57, 58). The aspect ratio in 2D, as defined by Nielsen (48) is, therefore, found to be 1 for Hal particles.

3.2. Oxygen Permeability

Figure 5A shows the experimentally determined values for the oxygen permeability coefficients, P_{O_2}, only for the coating layers, calculated according to Equations (4) and (5). The transmission rate of the BoPP substrate film was found to be 1.250 $\frac{cm^3\,(STP)}{m^2\,d\,bar}$. The dry coating layer thicknesses were (1.0 ± 0.2) µm for the

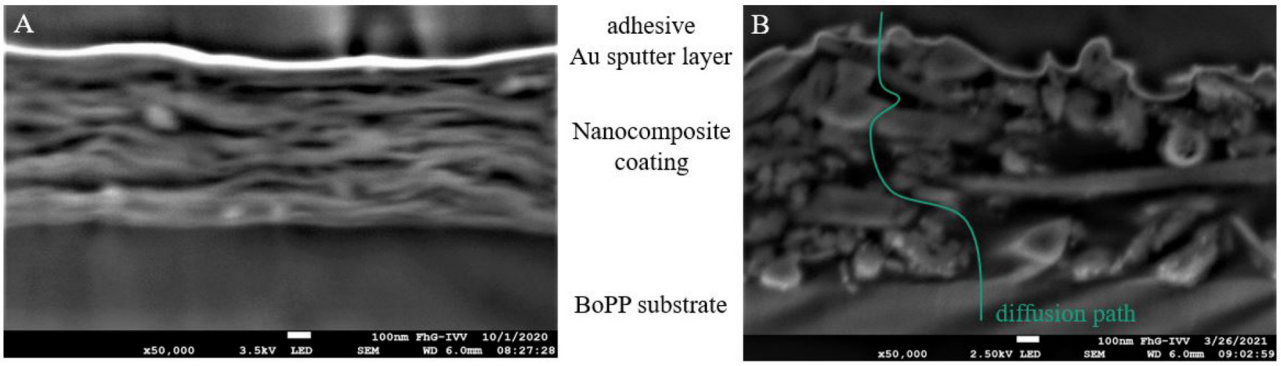

FIGURE 3 | Scanning electron microscopy (SEM) images of cross-sections prepared by Ar polishing of nanocomposite coatings with MMT-BM-30 **(A)** and Hal-BM-30 **(B)** with a magnification of 50.000; from bottom to top the layers are the BoPP substrate, the nanocomposite coating, the sputtered gold layer, and the top layer is the adhesive used to bond it to the Si wafer; in the nanocomposite layers the white areas are the nanoparticles and the black areas are PVA; for the Hal-containing sample **(B)** diffusion paths, meaning an end-to-end line with no particles, perpendicular to the coating, can be found (one example shown in green), whereas for the MMT-containing sample the diffusion path in this 2D image is always blocked by MMT platelets.

layers with 30 and 47 vol% and (0.6 ± 0.1) µm for the layers with 7 vol% of nanoparticles. The PVA-ref sample provided a dry coating layer thickness of (1.0 ± 0.2) µm.

The oxygen permeability coefficient of PVA depends on various parameters. Values of 1 to 6 $\frac{cm^3\,(STP)\,1\,\mu m}{m^2\,d\,bar}$ are reported in the literature for coatings comparable to those in this study (14–18). The measured value of 1.4 $\frac{cm^3\,(STP)\,1\,\mu m}{m^2\,d\,bar}$ in this study is within that range. Since PVA resin composition and type, the coating method, and the conditions used during coating and drying of pure PVA were kept similar to those used for the coatings with nanolacquer, the measured oxygen permeability coefficient for pure PVA, $P_{O_2|PVA}$, was used in Equation (6) to calculate the BIF_{O_2}. The highest barrier improvement factor has been achieved with the medium volume concentration of 30 vol% silicate, followed by the lowest volume concentration of 7 vol%. At the highest volume concentration of 47 vol%, no barrier improvement was obtained. The addition of only 7 vol% platelet-shaped MMT particles already led to an improvement of $P_{O_2|NC}$ to 0.55 and 0.36 $\frac{cm^3\,(STP)\,1\,\mu m}{m^2\,d\,bar}$ for MMT dispersed *via* UT and BM, respectively. The BIF_{O_2} values are, therefore, 3.9 and 4.4. A further increase in the volume ratio of MMT to 30 vol% led to a further decrease in the permeability to 0.21 and 0.12 $\frac{cm^3\,(STP)\,1\,\mu m}{m^2\,d\,bar}$ for UT and BM dispersion, respectively. These are the lowest $P_{O_2|NC}$ values achieved in this study, which is also represented by the relatively high BIF_{O_2} values of 6.8 for UT and 12 for BM dispersed samples. However, further increasing the amount of MMT did not constantly lead to an improvement: for instance, at a concentration of 47 vol% MMT, a strong increase in $P_{O_2|NC}$ compared to pure PVA was reached. The $P_{O_2|NC}$ was measured as 76 $\frac{cm^3\,(STP)\,1\,\mu m}{m^2\,d\,bar}$ for MMT-UT-47 and 50 $\frac{cm^3\,(STP)\,1\,\mu m}{m^2\,d\,bar}$ for MMT-BM-47. Apparently, there is no coherent structure anymore with this high filler concentration. The values are not shown in the diagram.

Looking at the BIF_{O_2} values more closely, it is noticeable that they do not differ significantly between the UT and BM dispersion techniques at a volume fraction of 7 %. However, at a volume fraction of 30 %, the BIF_{O_2} is higher for BM than for UT dispersed samples (refer to **Table 3**). The higher the solid content of a dispersion, the more difficult it is to distribute the agglomerates completely, during dispersal. The BM process provides, in comparison to the UT process, a more homogeneous shearing, since the whole dispersion is equally in contact with the milling zirconium oxide balls (33), whereas the UT has a rotational mixing head, which is located in the middle of the dispersion during mixing (34). This study has found that at a high concentration of 30 vol%, this uniformity of distribution can

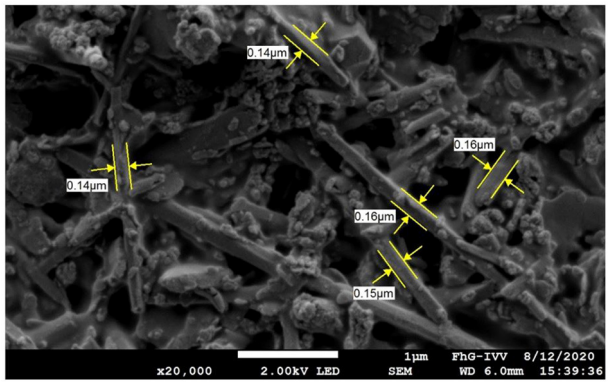

FIGURE 4 | Top-down SEM image with a magnification of 20.000 of the Hal-BM-47 coating; the sticks are Hal particles, whose size *L* (=*W*) is measured; the lumps next to the sticks are PVA; at a filler ratio of 47 vol% there is no coherent structure anymore.

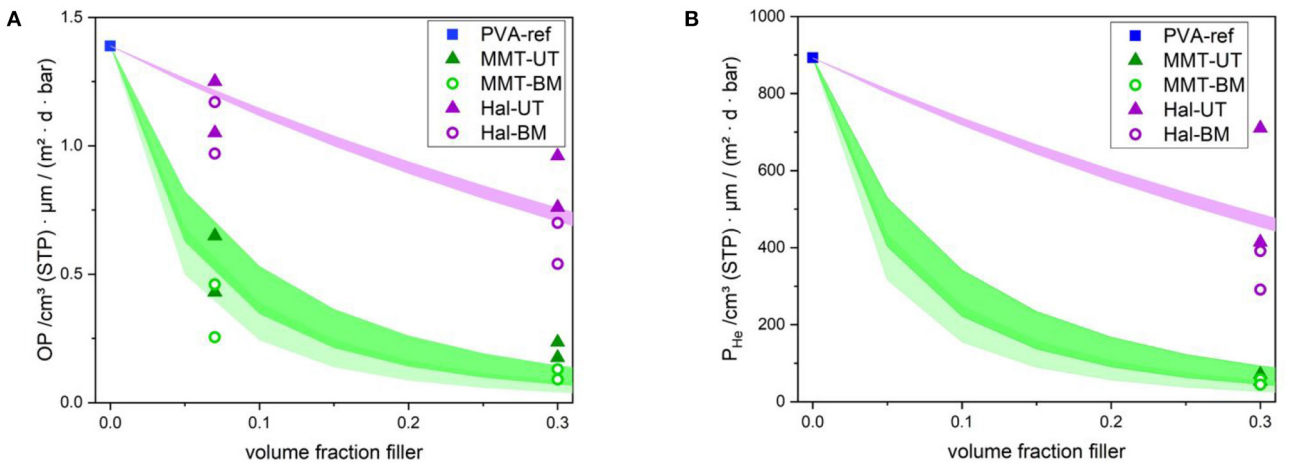

FIGURE 5 | Calculated and measured oxygen **(A)** and helium **(B)** permeability values as a function of the nanoparticle concentration in volume. A 2-fold measurement for PVA, MMT-UT, MMT-BM, Hal-UT, and Hal-BM was executed, where both values for each sample are shown. The areas marked in color represent the calculated values for permeability coefficients of nanocomposites according to Equation (10). The particle size ranges used for MMT-UT were 320–360 nm for particle length and 20–30 nm for particle width (■ MMT-UT). The size ranges used for MMT-BM were 474–514 nm for particle length and 20–30 nm for particle width (■ MMT-BM). The size ranges used for Hal were 140–160 nm for tube diameter (■ Hal, independent dispersion technique).

TABLE 3 | The aspect ratio of nanoparticles, gas barrier improvement factors of nanocomposites for helium and oxygen, and comparison of molecule travel distance, δ is given.

	Aspect ratio	Helium				Oxygen			
Sample code	L/W	BIF_{He}	δ_{theo} µm	δ_{emp} µm	Difference %	BIF_{O_2}	δ_{theo} µm	δ_{emp} µm	Difference %
n	**5**	**2**	**5**	**2**		**2**	**5**	**2**	
MMT-UT-30	14 ± 2.7	14 ± 3.0	2.7 ± 0.8	2.9 ± 0.7	7.0	6.8 ± 2.3	2.7 ± 0.8	2.0 ± 0.6	26
MMT-BM-30	20 ± 4.0	17 ± 2.0	3.6 ± 0.8	3.1 ± 0.8	14	12 ± 3.0	3.6 ± 0.8	2.6 ± 0.7	28
Hal-UT-30	1.0 ± 0.1	1.6 ± 0.3	1.0 ± 0.1	0.9 ± 0.2	n.a.*	1.6 ± 0.3	1.0 ± 0.3	1.0 ± 0.3	n.a.*
Hal-BM-30	1.0 ± 0.1	2.9 ± 0.8	1.0 ± 0.1	1.3 ± 0.4	n.a.*	2.2 ± 0.8	1.0 ± 0.1	1.1 ± 0.5	n.a.*

The values are given with SD for the number of measured specimens n per sample.
**No tortuous path effect for Hal.*

be sustained better by BM dispersion technique (refer to Section 3.1). The present agglomerates after UT dispersion technique, on the one hand, disturb the parallel alignment of the exfoliated platelets sterically and, on the other hand, the agglomerated platelets do not contribute to the elongation of diffusion path. These reasons, together with the slightly smaller particle size after UT dispersion, cause the lower BIF_{O_2} for UT dispersed samples at 30 vol%.

As expected, the BIF_{O_2} values for platelet-shaped particles were found to be remarkably higher than for stick-shaped ones. The addition of 7 vol% Hal led to a slight improvement, resulting in an oxygen permeability coefficient of 1.1 and 1.2 $\frac{cm^3\,(STP)\,1\,\mu m}{m^2\,d\,bar}$ for UT and BM, respectively, compared to 1.4 $\frac{cm^3\,(STP)\,1\,\mu m}{m^2\,d\,bar}$ for pure PVA. The lowest permeability values reached by the addition of Hal were achieved for a filler ratio of 30 vol% and were 0.87 and 0.63 $\frac{cm^3\,(STP)\,1\,\mu m}{m^2\,d\,bar}$ for UT and BM dispersion technique, respectively. Similar to the platelet-shaped particles, a further increase of the volume fraction above 30 vol% led to a reduction in barrier properties.

In general, the effects of the mixing ratio and the dispersion technique on the gas barrier enhancement for both particles types, MMT and Hal, were found to be similar. The highest barrier was achieved for a mixing ratio of 30 vol% and the BM dispersion technique led to the higher barrier performance, due to the reduced amount of agglomerations.

The reason for not having a high barrier improvement with Hal, refer to **Table 3**, was that there is not really a tortuous path created by the integration of sticks. As shown in the cross-section image of the coating, **Figure 3B**, the sticks only acted as small obstacles but did not really build up a closed layer with an elongation of the permeation path. The alignment and homogeneous distribution of the platelet-shaped particles, which is an assumption of the Nielsen model, is demonstrated in the cross-section SEM image in **Figure 3A**. The MMT particles, indicated by the white lines, are oriented parallel to the surface and provide a tortuous path. This SEM image indicates the tortuous path effect for the 30 vol% MMT nanocomposite prepared by the BM dispersion technique, as it was also shown schematically in **Figure 1**.

Based on this, further investigations were performed with the samples containing 30 vol% nanoparticles, due to their higher BIF_{O_2} values.

3.3. Helium Permeability

Roberts et al. (29) proposed a model for permeation through oxide layers (e.g. AlO_x) coated via physical vapor deposition. Within this model, defects or pinholes in the oxide layer with a size of $\geq$1 nm are defined as macro-defects, and defects or pinholes with a size of 0.35 to 1 nm are defined as nano-defects. This model has been transferred to the permeation in nanocomposites. In this study that is about the investigation of nanocomposites the expression "defect" does not describe a pinhole in a very thin oxide layer, but an inhomogeneity in the coated layer, e.g. a not parallel aligned particle or an agglomeration that disturbs the homogeneous distribution of the particles. The defect does not necessarily be an air-filled hole, as it can also be described as a free volume with no inorganic particle, but with polymer.

It is known that small molecules, such as water, permeate predominantly through nano-sized defects (30, 31). However, water molecules form hydrogen bonds with the side groups of PVA and disrupt the intermolecular hydrogen bonds among the PVA chains (59, 60). Hence, helium, being an inert gas, was chosen as the small permeating molecule. On the other hand, it is known that for oxygen, the permeation mechanism is dominated by macro-sized defects, i.e., regions where there is no inorganic material (29, 31). Therefore, helium (2.6 Å) and oxygen (3.5 Å), with two different gas kinetic diameters, were compared in terms of their permeability in the nanocomposites, in order to distinguish the dominating structural effects on the gas permeation (28).

The measured permeability coefficients for helium, P_{He}, are shown in **Figure 5B**. The $P_{He|PVA}$ for pure PVA was 892 $\frac{cm^3\,(STP)\,1\,\mu m}{m^2\,d\,bar}$, which is close to the value of 765 $\frac{cm^3\,(STP)\,1\,\mu m}{m^2\,d\,bar}$ measured by Carstens and Ehart (61). The integration of 30 vol% MMT particles reduces the P_{He} down to 62 and 51 $\frac{cm^3\,(STP)\,1\,\mu m}{m^2\,d\,bar}$ for UT and BM dispersion techniques, respectively. There is no significant difference between the barrier performance of the samples prepared by UT and BM dispersion techniques,

where the BIF_{He} was calculated as 14 and 17, respectively. An integration of stick-shaped Hal particles, however, only led to a slight helium barrier improvement. The BIF_{He} is found to be 1.6 and 2.9 with the corresponding $P_{He|NC}$ values of 565 and 341 $\frac{cm^3\,(STP)\,1\,\mu m}{m^2\,d\,bar}$ for UT and BM dispersion, respectively.

Unlike the oxygen permeation, for the helium permeation, there was no significant difference between the BIF_{He} values of MMT-UT-30 and MMT-BM-30 formulations (refer to also **Table 3**). This might be due to the fact that an agglomeration essentially affects the macro-structure of a coating layer but only slightly affects the nano-structure. Wang et al. (62) showed that agglomerations of MMT particles lead to a reduced oxygen barrier performance because of poor inter-facial compatibility. That means an agglomeration disturbs the homogeneous distribution and alignment of the platelets in the layer. This disturbance might lead to additional free volumes or areas with no inorganic particle and adversely oriented particles (63, 64). The macro-sized defects enable the oxygen to permeate, why the UT-dispersed sample only provided a BIF_{O_2} of 6.8 for oxygen. The BM-dispersed sample, however, provided a BIF_{O_2} of 12, since there were fewer disturbances of the particle alignment due to fewer agglomerations as a result of the high shear ball milling process as shown in **Figure 6** and by the size measurement results in Section 3.1.

Similar to the oxygen permeation, the Hal-containing nanocomposites did not provide a barrier improvement for helium.

3.4. Crystallinity and Intermolecular Interactions

Unlike the permeation through an oxide layer or the coating with simple barrier lacquer, a nanocomposite is a two-material system, meaning the components can interact and affect each other. To evaluate this interaction between PVA and nanoparticles, XRD and FTIR measurements have been performed, and the activation energy of the permeation coefficient was determined.

X-ray powder diffraction measurements were performed for pure MMT, pure Hal, free-standing PVA film, and free-standing nanocomposite films to evaluate the effect of clay particles on the crystallinity of PVA. The diffraction pattern is shown in **Figure 7**. The pure PVA appeared with the typical peak shape of a semicrystalline material, which stresses a high amount of amorphous ratio with only a small reflection at 19.4° and a broad maximum called a hump. The nanocomposite also appeared with the peak shape of a semicrystalline material, but with a larger quantity of crystalline phase indicated by the larger reflection at 19.4° (65). The reflection at 19.4°, which corresponds to the $10\bar{1}$ reflection, is present for both, pure PVA and nanocomposite, and is typical for crystalline atactic PVA (66, 67). The diffraction pattern of pure MMT provides a reflection at 19.8°, which is quite close to this atactic reflection. However, the other reflections of MMT, which were in good accordance with previously reported ones (68), at 22.1, 26.4, 28.2, 35.6, 54.3, and 62.0°, were not observed in the nanocomposite curve, which indicates that PVA is the dominating part in the nanocomposite's diffraction pattern. The same is valid for the Hal-containing sample (69). To estimate the degree of crystallinity of one sample, the ratio between the amorphous hump and crystalline peak within one curve is examined. For the nanocomposites, the percentage of the crystalline peak is higher than for the PVA film. Hence, the addition of clay particles to the PVA solution seemed to increase the crystallinity of the PVA matrix.

In the literature, there is no clear trend discernible when it comes to the effect of nanoparticle integration on polymer crystallinity. There are some publications claiming that the crystallinity decreases (12, 70), whereas other authors report that the crystalline fraction increases (71–73). The decrease in crystallinity is explained by a disturbance of crystalline regions in PVA by clay particles. On the contrary, the clay particles may act as crystallization nuclei, which would lead to an increase in the number of crystalline regions, and therefore, the total crystallinity. Zhu et al. (74) showed that the influence on the crystalline appearance of nanocomposites is highly dependent on the curing conditions and, therefore, the crystallization kinetics. Consequently, the measurements in this study were performed with the pure PVA and nanolacquer using the same coating and curing conditions for both, to see the influence of clay particles on crystallinity and intermolecular interactions. An increase in matrix crystallinity leads to an improvement of the gas barrier of the polymer (4, 17). Since the crystallinity of Hal-containing samples has increased in the same order of magnitude, as the MMT-containing samples (refer to **Figure 7**), the higher $BIF_{He|O_2}$ is mainly based on the geometrical factor, i.e., the tortuous path effect. The very slight increase of the barrier properties of Hal-containing samples, however, might be based on the increase in crystallinity.

The activation energy for the permeation coefficient measured for pure PVA was found to be higher than the values measured for all nanocomposites, and there was no significant difference among themselves as shown in **Figure 8**.

The highest activation energy with 54 $\frac{kJ}{mol}$ was measured for pure PVA coatings, which fits quite well with the value measured by Zhang et al. (75). With the integration of 30 vol% silicate nanoparticles, the activation energy decreased down to 47 $\frac{kJ}{mol}$ for the nanocomposites, being very similar to each other regardless of the mixing method and the particle shape. This reduction in the activation energy values of the nanocomposite in comparison to pure PVA was expected to be due to the weakening of the intermolecular hydrogen bonds of the PVA chains. As proven by the following FTIR investigation, the silicate particles interact with the PVA matrix, probably *via* hydrogen bonds. If some hydroxy groups of a PVA chain are interacting with an adjacent silicate particle, these hydroxy groups are not part of the intermolecular cohesion of the PVA matrix anymore. This share of hydroxy groups in the adjacency of particles and PVA chains leads to weak boundary areas where the diffusion might take place more easily, as for example proposed by Bhunia et al. (76).

The intermolecular interaction between PVA and MMT nanoparticles was determined by means of FTIR measurements

(see **Figure 9**). This interaction involves hydrogen bonds between the hydroxy groups of PVA and the terminal oxygen atoms of the Si-tetrahedra. In MMT-BM-30, this was indicated by a shift of the C-O stretching mode of PVA from 1092 $\frac{1}{cm}$ to 1065 $\frac{1}{cm}$ and a shift of the Si-O stretching mode of MMT from 1027 $\frac{1}{cm}$ to 1040 $\frac{1}{cm}$ and 1009 $\frac{1}{cm}$ to 1018 $\frac{1}{cm}$, respectively (77, 78). Since the positions of the C-H stretching vibration (2941 and 2808 $\frac{1}{cm}$) and the C-H deformation (1375 $\frac{1}{cm}$) peaks, originating from the PP substrate film, retained their positions for all three measurements, a peak shift of mentioned peaks from PVA and MMT was present and not a shift of the whole curve (79, 80). The combined peak of C-O and Si-O stretching modes with signals at 1065, 1040, and 1018 $\frac{1}{cm}$ indicated this interaction between PVA and MMT, as well as the broadband in the region from 3600 to 3000 $\frac{1}{cm}$, which corresponds to the O-H groups involved in hydrogen bonds (71). It might be expected that the Si interactions with the PVA hydroxy groups reduce the inter-chain hydrogen bonds of PVA, which may, in turn, lead to cavity sizes within the PVA matrix being affected, thereby resulting in additional permeation paths for gas molecules.

In summary, the mixing of the MMT nanoparticles in a PVA polymer changed the crystallinity of the polymer and, on the other hand, caused the hydrogen bond to weaken, both seeming to have an opposing effect on the final gas permeability of the PVA matrix. Although no difference in these parameters was found for Hal and MMT particles, the MMT-containing samples showed a significantly higher BIF for both gases, suggesting that the tortuous path effect is the dominating factor for diffusion.

3.5. Comparison of Measured and Calculated Values for Gas Permeability and Diffusion Path Length

The permeation model for filled polymer systems developed by Nielsen is mainly based on particle geometry and particle

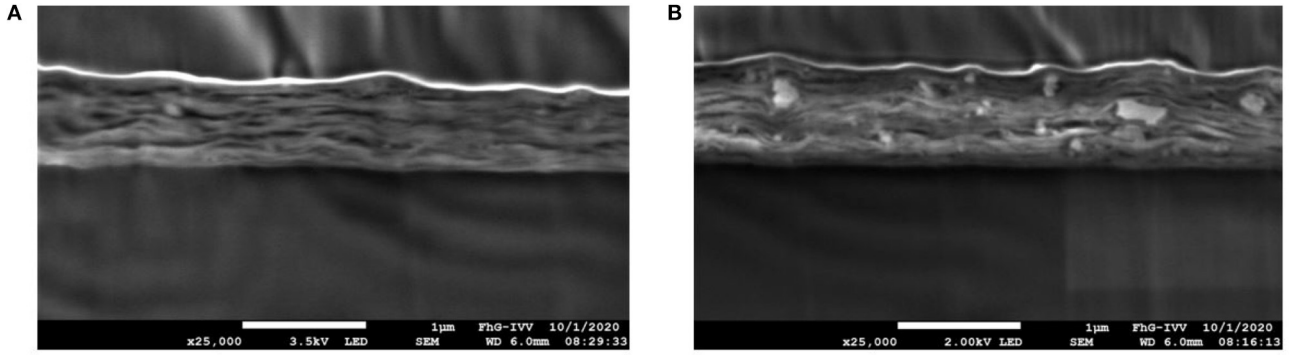

FIGURE 6 | Scanning electron microscopy images of cross-sections with a magnification of 25.000 prepared by Ar polishing of MMT-containing samples dispersed with a planetary ball mill **(A)** and ULTRA-TURRAX® **(B)**; from bottom to top the layers are the BoPP substrate, the nanocomposite, the sputtered gold layer, and the adhesive to bond the Si wafer; for the BM-dispersed sample **(A)**, there are nearly no agglomerations in the layer, whereas for the UT-dispersed samples **(B)**, some agglomerations are present, which lead to disturbances in the homogeneity of the layer.

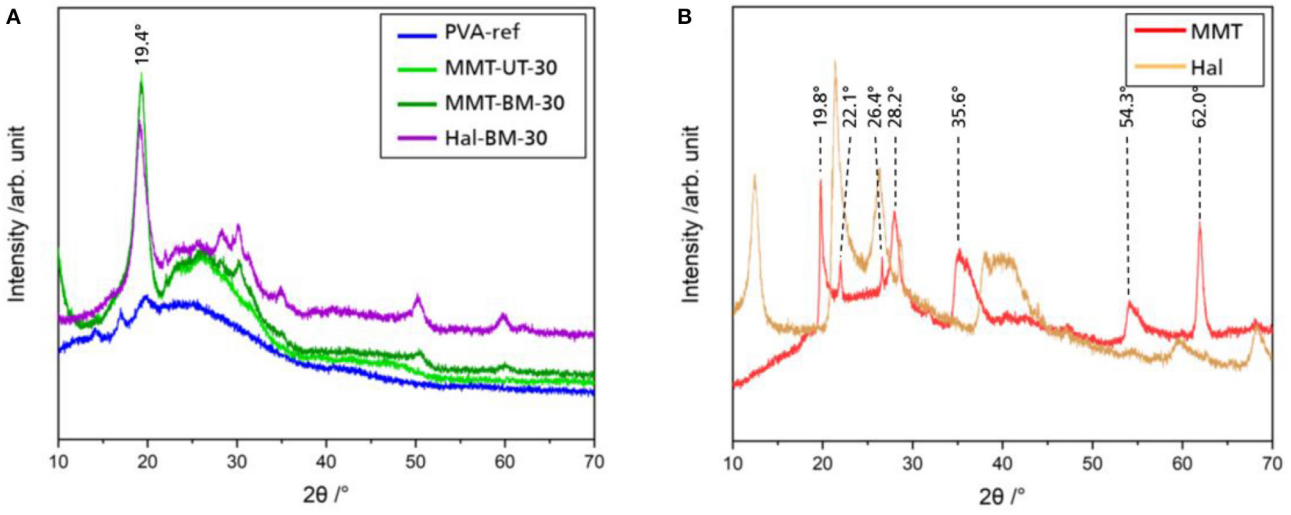

FIGURE 7 | X-ray diffraction (XRD) pattern of free-standing films of PVA, MMT, and Hal nanocomposites **(A)** and of pure MMT and Hal **(B)** as a function of a 2Θ range of 10 to 70°.

concentration (48). That means, if the particle length L, the particle width W, and the amount of particles ϕ_F in a coating layer with thickness d are known, the permeability coefficient of a nanocomposite coating, P_{NC}, can be calculated in comparison to its pure polymer matrix. In this study, this pure polymer matrix is PVA, having the permeability coefficient P_{PVA}. Factors that are not considered in Nielsen's model are structural changes in the polymeric matrix of the nanocomposite induced by the nanoparticles possibly affecting its final gas permeability. The interaction of the PVA with silicate nanoparticles, leading to changes in PVA crystallinity and weakening of the intermolecular hydrogen bonds of the PVA, could have an effect on the gas permeability of the polymer within the nanocomposite. As suggested by Haghighi et al. (81), this limits the cohesion forces within the PVA and consequently decreases the degree of crosslinking. The possible effects of nanoparticles on these factors are discussed in Section 3.4.

The gas-blocking potential of the nanoparticles, calculated by Equation (10), is shown by the colored areas in **Figure 5**. The calculations are performed using the minimum and the maximum aspect ratio values for each concentration and are plotted; accordingly, the colored areas represent the regions in-between. The parameters used for the calculation of permeability coefficients for the respective dispersion technique, UT or BM, and the particle shape, Hal or BM, are listed in **Table 4**. The green and violet areas indicate the possible barrier improvement starting from pure PVA with 0 % filler up to a volume fraction of 30 %. The shape of these areas is found to be similar for both gases, helium and oxygen. For both particle shapes, platelets and sticks, the calculation provides an area due to the deviations in the parameters used; L and W.

The calculated values fit quite well with the experimentally measured values for permeability coefficients. This is valid for both dispersion techniques and both particle shapes, indicating that the permeation process is dominated by the factors L, W, and ϕ_F. Only in the case of oxygen permeation in the nanocomposite, with a volume filler fraction of 30 %, the difference between the experimental and calculated values is slightly higher. This can be due to the matrix changes, as discussed in more detail when comparing δ values.

Table 3 shows the values calculated for δ_{theo} and δ_{emp} using Equations (8) and (9), respectively, for 30 vol% samples. The values for δ_{theo} and δ_{emp} are compared using the measured dry layer thickness of the coating, which is (1.0 ± 0.2) µm for all the 30 vol% samples for both helium and oxygen. For a coating

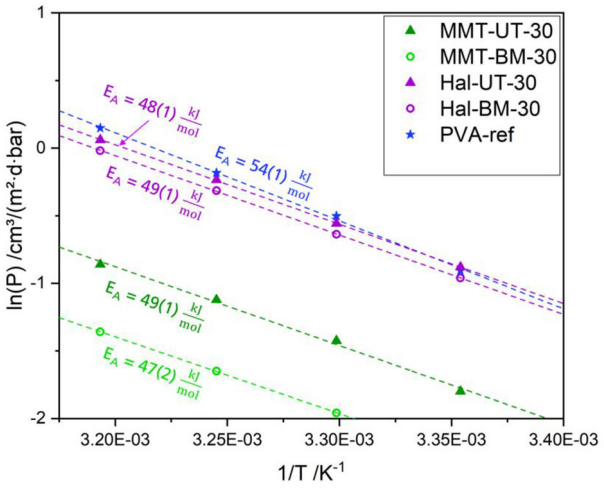

FIGURE 8 | Arrhenius plots for determining activation energy of oxygen permeation of PVA-ref, MMT-UT-30, MMT-BM-30, Hal-UT-30, and Hal-BM-30. The given values for the activation energy are calculated according to Equation (3) with SD for a 2-fold measurement.

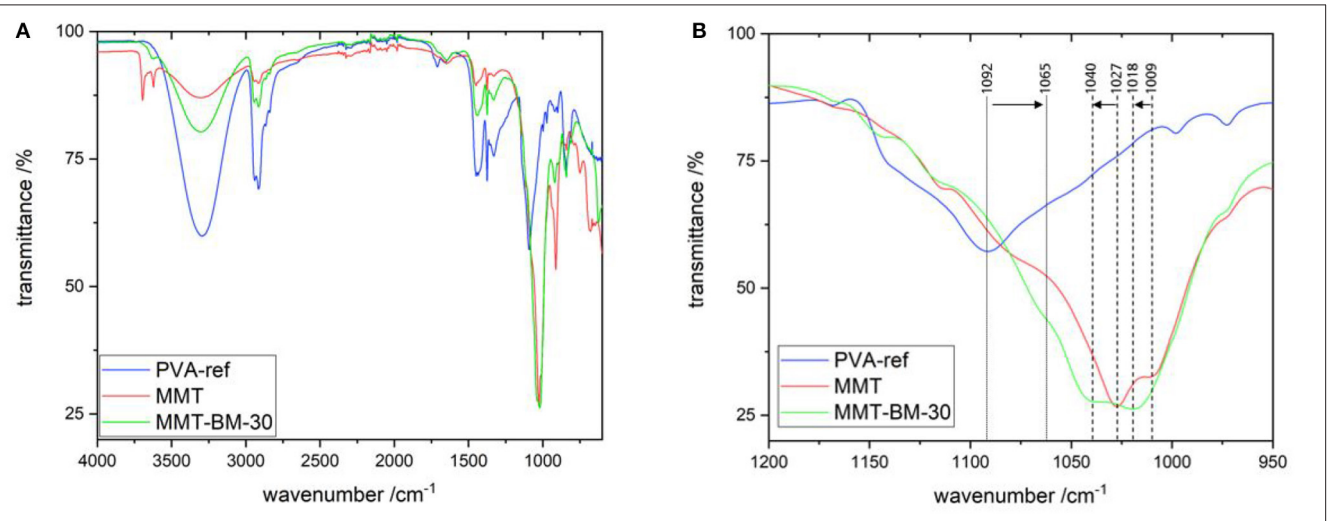

FIGURE 9 | Fourier transform infrared (FTIR) spectra, **(A)** measured in the range from 500 to 4000 1/cm for PVA, pure MMT, and MMT-BM-30. **(B)** Shows a magnification of the fingerprint region and indicates the shift of the C-O (1092 to 1065 1/cm) and the Si-O (1027 to 1040 1/cm and 1009 to 1018 1/cm) stretching mode of PVA and MMT, respectively. MMT-UT-30 provides similar curve as of MMT-BM-30 and is not shown in the figure.

TABLE 4 | Parameters used for calculating P_{NC}, δ_{theo}, and δ_{emp} for oxygen and helium according to the Nielsen model Equations (8) and (9).

	Length	Width	Filler ratio	Coating thickness	Permeability coefficients of pure PVA	
	L	W	ϕ_F	d	$P_{O_2\|PVA}$	$P_{He\|PVA}$
	nm	nm		µm	$\frac{cm^3\ (STP)\ 1\ µm}{m^2\ d\ bar}$	$\frac{cm^3\ (STP)\ 1\ µm}{m^2\ d\ bar}$
n	5	5		5	2	2
MMT-UT-30	340*	25 ± 5	0 to 0.5	1.0 ± 0.2	1.4 ± 0.2	892 ± 47
MMT-BM-30	494 *	25 ± 5				
Hal-UT-30	150 ± 10	150 ± 10				
Hal-BM-30	150 ± 10	150 ± 10				

The values are given with SD for the number of measured specimens n per sample.
Representative measurement with AF4/MALLS, refer to **Figure 2.*

without nanoparticles, this dry layer thickness would be equal to the distance a molecule must travel. Both δ values for Hal-containing nanocomposites are found to be at 1 µm, similar to the dry coating layer thickness, verifying that stick-shaped particles do not provide a tortuous path effect in this configuration. The slight, but not outstanding, BIF_{He} (1.6 to 2.9) and BIF_{O_2} (1.6 to 2.2) of the two samples, Hal-UT-30 and Hal-BM-30, were not mainly the result of the tortuous path effect but were possibly due to the slight structural changes of PVA with nanoparticles, and Hal particles acting as obstacles within the PVA.

The calculated δ values for MMT-containing nanocomposites are found to be higher than for Hal-containing ones. The $\delta_{emp|He}$ values of 2.9 and 3.1 µm for UT and BM dispersed samples, respectively, fit well with the values for $\delta_{theo|He}$. This indicates that the distance a helium molecule must travel is elongated by a factor of around 3 when 30 vol% MMT are included in the nanocomposite. Similar behavior has also been observed for oxygen permeation. However, the values for $\delta_{emp|O_2}$ are, being 2.0 and 2.6 µm for UT and BM dispersed samples, respectively, found to be slightly smaller than for helium permeation. In this study, the elongation of the travel distance for oxygen is by a factor of 2 for UT and a factor of 2.6 for BM nanocomposites.

It might be that the nanoparticles lead to a change in the permeability coefficient of the PVA matrix within the nanocomposite, P_{PVA}, due to an increase in the crystallinity, or weakening of the hydrogen bonds within the polymer matrix, or the interaction of the Si with the hydroxy groups of PVA (refer to Section 3.4). Since the difference between $\delta_{theo|O_2}$ and $\delta_{emp|O_2}$ is higher for oxygen (refer to **Table 3**), this change in P_{PVA} seems to affect mainly the bigger oxygen molecule and indicates additional oxygen permeation pathways within the nanocomposite.

4. CONCLUSIONS

This manuscript adds additional knowledge to the field of permeation mechanisms in nanocomposites. The main investigated factors are the effect of particle shape (sticks and platelets) on the tortuous path, the effect of the size of the permeating molecule (helium and oxygen), the effect of the polymer crystallinity on the permeability, and the comparison of calculated and measured permeability coefficients.

The permeability coefficients have demonstrated a barrier improvement factor of 17 for helium and 12 for oxygen, from the integration of 30 vol% platelet-shaped silicate particles dispersed with BM. For this particular nanocomposite, this corresponds to an elongation of the molecule travel distance by a factor of 3.1 for helium and a factor of 2.6 for oxygen. The preparation method for nanoparticles with a planetary ball mill has outperformed the method with ULTRA-TURRAX®, especially for oxygen.

There was no relevant barrier improvement measured for the nanocomposites with stick-shaped nanoparticles, neither for helium nor for oxygen. The molecule travel distance was not increased in comparison to the layer thickness of the nanocomposite because of their low aspect ratio.

The conformity of theoretical permeation values with the empirical ones affirmed the interpretation of the particle shapes' results. The permeation of the chosen gas molecules is affected by the geometrical factors, mainly the tortuous path effect.

The Nielsen model does not consider the structural effects of the nanoparticles on the PVA matrix. On the other hand, the XRD values showed an increase in the crystallinity of PVA due to the incorporation of nanoparticles. However, the FTIR investigation and the determination of the activation energy for permeation have shown an interaction between the silicate nanoparticles and the PVA polymer chains, which might lead to weaker boundary areas, with additional permeation pathways. These two contrary trends seem to oppose each other, which leads to good conformity of δ_{theo} and δ_{emp}, especially for helium molecules.

Since the average value of δ_{emp} tends to be slightly lower than the value of δ_{theo}, mainly for oxygen at 30 vol% MMT, and the weak boundary areas are present and not advantageous for permeation, there is still potential to improve the barrier performance, e.g., by an improvement of the chemical interaction of particles and polymer matrix by functional grafting of the particles. Another potential for investigation is the optimization of the aspect ratio. A one time coating step with a certain amount of solid content and a sufficient mixing ratio of polymer

and particle should still be possible but with the highest aspect ratio of a commercially available particle. The integration of thin nanocomposite coatings, at layer thicknesses of 1 µm, will bring new insights for the production of recyclable flexible food packaging materials.

DATA AVAILABILITY STATEMENT

The raw data supporting the conclusions of this article will be made available by the authors, without undue reservation.

AUTHOR CONTRIBUTIONS

SS, EK, and PE contributed to conception and design of the study. OM and H-CL contributed especially to the permeation models and the described comparison of calculated and measured permeation values. SC performed the helium permeation measurement and contributed to the permeation discussion of oxygen and helium. All authors contributed to manuscript revision, read, and approved the submitted version.

FUNDING

This study has received support from the BarriFlex project (IGF Nr. 235 EBG), funded by the Federal Ministry of Economic Affairs and Energy (BMWi) within the funding body Industrielle Gemeinschaftsforschung (IGF) *via* Arbeitsgemeinschaft industrieller Forschungsvereinigungen e.V. (AiF).

ACKNOWLEDGMENTS

The authors sincerely thank Dr. Joachim Schomburg from Durtec GmbH, Dr. Uwe Bölz from HPX Polymers GmbH, and Dr. Samuel Michel from Kuraray Europe GmbH, who provided the samples and were open for discussion. Dr. Philip Netzsch from University Augsburg is acknowledged for the XRD measurements.

REFERENCES

1. Heiss R. *Verpackung von Lebensmitteln - Anwendung der wissenschaftlichen Grundlagen in der Praxis.* Heidelberg: Springer-Verlag (1980).
2. Langowski HC. *Shelf Life of Packed Food and Packaging Functionality*. in *Food Packaging Materials*. CRC Press (2017). p. 11–66.
3. Mittal V. *Barrier Properties of Polymer Clay Nanocomposites.* Nova Science Publishers Inc. (2010).
4. Mokwena KK, Tang J. Ethylene vinyl alcohol: a review of barrier properties for packaging shelf stable foods. *Crit Rev Food Sci Nutr.* (2012) 52:640–50. doi: 10.1080/10408398.2010.504903
5. Li HZ, Chen SC, Wang YZ. Preparation and characterization of nanocomposites of polyvinyl alcohol/cellulose nanowhiskers/chitosan. *Composites Sci. Technol.* (2015) 115:60–5. doi: 10.1016/j.compscitech.2015.05.004
6. Shankar S, Rhim JW. Polymer Nanocomposites for Food Packaging Applications. In: *Functional and Physical Properties of Polymer Nanocomposites.* John Wiley & Sons, Ltd. (2016). p. 29–55.
7. Kit KM, Schultz JM, Gohil RM. Morphology and barrier properties of oriented blends of poly(ethylene terephthalate) and poly(ethylene 2,6-naphthalate) with poly(ethylene-co-vinyl alcohol). *Poly Eng Sci.* (1995) 35:680–92. doi: 10.1002/pen.760350808
8. Jang J, Dong KL. Plasticizer effect on the melting and crystallization behavior of polyvinyl alcohol. *Polymer.* (2003) 44:8139–46. doi: 10.1016/j.polymer.2003.10.015
9. Tsurko ES, Feicht P, Habel C, Schilling T, Daab M, Rosenfeldt S, et al. Can high oxygen and water vapor barrier nanocomposite coatings be obtained with a waterborne formulation? *J Membr Sci.* (2017) 540:212–8. doi: 10.1016/j.memsci.2017.06.051
10. Gaume J, Taviot-Gueho C, Cros S, Rivaton A, Therias S, Gardette JL. Optimization of PVA clay nanocomposite for ultra-barrier multilayer encapsulation of organic solar cells. *Solar Energy Mater Solar Cells.* (2012) 99:240–9. doi: 10.1016/j.solmat.2011.12.005
11. Lim M, Kwon H, Kim D, Seo J, Han H, Khan S. Highly-enhanced water resistant and oxygen barrier properties of cross-linked poly(vinyl alcohol) hybrid films for packaging applications. *Progr Org Coatings.* (2015) 85:68–75. doi: 10.1016/j.porgcoat.2015.03.005
12. Nyflött, Moons E, Bonnerup C, Carlsson G, Järnström L, Lestelius M. The influence of clay orientation and crystallinity on oxygen permeation in dispersion barrier coatings. *Appl Clay Sci.* (2016) 126:17–24. doi: 10.1016/j.clay.2016.02.029
13. Woo J, Kim NH, Kim S, Park OK, Lee J. Effects of the addition of boric acid on the physical properties of MXene/polyvinyl alcohol (PVA) nanocomposite. *Composites Part B Eng.* (2020) 199:108–205. doi: 10.1016/j.compositesb.2020.108205
14. Grunlan JC, Grigorian A, Hamilton CB, Mehrabi AR. Effect of clay concentration on the oxygen permeability and optical properties of a modified poly(vinyl alcohol). *J Appl Polym Sci.* (2004) 93:1102–9. doi: 10.1002/app.20564
15. Nyflätt s, Axrup L, Carlsson G, Jänström L, Lestelius M, Moons E, et al. Influence of kaolin addition on the dynamics of oxygen mass transport in polyvinyl alcohol dispersion coatings. *Nordic Pulp Paper Res J.* (2015) 30:385–92. doi: 10.3183/npprj-2015-30-03-p385-392
16. Wang H, Zhang R, Zhang H, Jiang S, Liu H, Sun M, et al. Kinetics and functional effectiveness of nisin loaded antimicrobial packaging film based on chitosan/poly(vinyl alcohol). *Carbohydrate Polym.* (2015) 127:64–71. doi: 10.1016/j.carbpol.2015.03.058
17. Maes C, Luyten W, Herremans G, Peeters R, Carleer R, Buntinx M. Recent updates on the barrier properties of ethylene vinyl alcohol Copolymer (EVOH): a review. *Polym Rev.* (2018) 58:209–46. doi: 10.1080/15583724.2017.1394323
18. You J, Oh B, Jin HJ, Yun YS. Improvement in barrier properties using a large lateral size of exfoliated graphene oxide. *Macromol Res.* (2020) 28:1–5. doi: 10.1007/s13233-020-8089-x
19. Müller K, Bugnicourt E, Latorre M, Jorda Beneyto M, Echegoyen Y, Lagaron JM, et al. Review on the Processing and Properties of Polymer Nanocomposites and Nanocoatings and Their Applications in the Packaging, Automotive and Solar Energy Fields. *Nanomaterials.* (2017) 7:1–47. doi: 10.3390/nano7040074
20. Zhu TT, Zhou CH, Kabwe FB, Wu QQ, Li CS, Zhang JR. Exfoliation of montmorillonite and related properties of clay/polymer nanocomposites. *Appl Clay Sci.* (2019) 169:48–66. doi: 10.1016/j.clay.2018.12.006
21. Gusev AA, and Lusti HR. Rational design of nanocomposites for barrier applications. *Adv Mater.* (2001) 13:1641–3. doi: 10.1002/1521-4095(200111)13:21<1641::AID-ADMA1641>3.0.CO;2-P
22. Stöter M, Kunz DA, Schmidt M, Hirsemann D, Kalo H, Putz B, et al. Nanoplatelets of sodium hectorite showing aspect ratios of 20000 and superior purity *Langmuir* (2013) 29:1280–5. doi: 10.1021/la304453h
23. Ben Dhieb F, Tabatabaei SH, Mighri F, Ajji A. Comparison of crosslinking efficiency in dip and roll-deposited coatings on their oxygen barrier. *ACS Omega.* (2019) 4:15772–9. doi: 10.1021/acsomega.9b00950

24. Dabbaghianamiri M, shazly M Duraia E, Beall GW. Self-assembled montmorillonite clay-poly vinyl alcohol nanocomposite as a safe and efficient gas barrier. *Results Mater.* (2020) 7:100101. doi: 10.1016/j.rinma.2020.100101
25. Meng X, Qi P, Sun J, Li H, Zhang S, Liu X, et al. Fabrication of transparent clay-polymer hybrid coatings on PET film to enhance flame retardancy and oxygen barrier properties. *Progr Org Coatings.* (2020) 147:105788. doi: 10.1016/j.porgcoat.2020.105788
26. Song Y, Gerringer J, Qin S, Grunlan JC. High oxygen barrier thin film from aqueous polymer/clay slurry. *Ind Eng Chem Res.* (2018) 57:6904–09. doi: 10.1021/acs.iecr.8b01077
27. Vasile C. Polymeric nanocomposites and nanocoatings for food packaging: a review. *Materials.* (2018) 11:18–34. doi: 10.3390/ma11101834
28. Mehio N, Dai S, Jiang De. Quantum mechanical basis for kinetic diameters of small gaseous molecules. *J Phys Chem A.* (2014) 118:1150–4. doi: 10.1021/jp412588f
29. Roberts AP, Henry BM, Sutton AP, Grovenor CRM, Briggs GAD, Miyamoto T, et al. Gas permeation in silicon-oxide/polymer (SiO_x/PET) barrier films: role of the oxide lattice, nano-defects and macro-defects. *J Membrane Sci.* (2002) 208:75–88. doi: 10.1016/S0376-7388(02)00178-3
30. Müller-Meskamp L, Fahlteich J, Krebs FC. 10. In: *Barrier Technology and Applications.* John Wiley and Sons (2012). p. 269–329.
31. Kiese S, Kücükpinar E, Miesbauer O, Langowski HC. The influence of temperature on the intrinsic transport properties of water in inorganic and polymeric coatings. *Thin Solid Films.* (2021) 717:138476. doi: 10.1016/j.tsf.2020.138476
32. Edelman CH, Favejee JCL. On the crystal structure of montmorillonite and halloysite. *Zeitschrift für Kristallographie - Crystalline Mater.* (1940) 102:1–6.
33. Delogu F, Gorrasi G, Sorrentino A. Fabrication of polymer nanocomposites via ball milling: present status and future perspectives. *Progr Mater Sci.* (2017) 86:75–126. doi: 10.1016/j.pmatsci.2017.01.003
34. Baláž P. Applied mechanochemistry. In: *Mechanochemistry in Nanoscience and Minerals Engineering.* Berlin: Springer (2008). p. 297–405.
35. Bugnicourt E, Brzoska N, Kucukpinar E, Philippe S, Forlin E, Bianchin A, et al. Dispersion and performance of a nanoclay/whey protein isolate coating upon its upscaling as a novel ready-to-use formulation for packaging converters. *Polymers.* (2019) 11:1410. doi: 10.3390/polym11091410
36. Kuraray Europe GmbH. *Kuraray Poval & Exceval.* (2021). Technical Data Sheet.
37. Mao L, Xie J, Wu H, Liu Y. Mussel-inspired approach to constructing dual network coated layered clay for enhanced barrier and antibacterial properties of poly (vinyl alcohol) nanocomposites. *Polymers.* (2020) 12:1–15. doi: 10.3390/polym12092093
38. Matsumoto Fine Chemical Co Ltd. *Anchor Coating Agent ORGATIX WS-680A.* (2013). Technical Data Sheet.
39. BYK Additives & Instruments. *Cloisite* Na^+. (2013). Technical Data Sheet.
40. DIN Deutsches Institut für Normung e V . *Plastics - Film and Sheeting - Determination of Wetting Tension [Norm].* (2008). DIN ISO 8296.
41. Podzimek S. Light scattering, size exclusion chromatography and asymmetric flow field flow fractionation. In: *Asymmetric Flow Field Flow Fractionation.* John Wiley and Sons (2011). p. 259–305.
42. Andersson M, Wittgren B, Wahlund KG. Accuracy in multiangle light scattering measurements for molar mass and radius estimations. model calculations and experiments. *Anal Chem.* (2003) 75:4279–91.
43. DIN Deutsches Institut für Normung e V . *Determining the Gas Transmission Rate of Plastic Film, Sheeting and Mouldings by the Carrier Gas Method [Norm].* (1998). DIN 53380-3.
44. Brandrup J, Immergut EH, Grulke EA. Polymer handbook. *No. Bd. 2 in Polymer Handbook.* New York, NY; Chichester; Weinheim; Brisbane; Singapore; Toronto, ON: John Wiley & Sons, INC. (2004).
45. Barrer RM. Diffusion in and through solids. *J Phys Chem.* (1942) 533–4. doi: 10.1021/j150418a018
46. Firon M, Cros S, Trouslard P. *Method and Device for Measurement of Permeation.* (2007). U.S. Patent US2007186622.
47. Morlier A, Cros S, Garandet JP, Alberola N. Structural properties of ultraviolet cured polysilazane gas barrier layers on polymer substrates. *Thin Solid Films.* (2014) 550:85–9. doi: 10.1016/j.tsf.2013.10.140
48. Nielsen LE. Models for the permeability of filled polymer systems. *J Macromol Sci Part A Chem.* (1967) 1:929–42. doi: 10.1080/10601326708053745
49. Shen L, Chen Z. Critical review of the impact of tortuosity on diffusion. *Chem Eng Sci.* (2007) 62:3748–55. doi: 10.1016/J.CES.2007.03.041
50. Giannelis EP. Polymer layered silicate nanocomposites. *Adv Mater.* (1996) 8:29–35.
51. Hatzikiriakos SG, Rathod N, Muliawan EB. The effect of nanoclays on the processibility of polyolefins. *Poly Eng Sci.* (2005) 45:1098–107. doi: 10.1002/pen.20388
52. Weber C, Heuser M, Stanjek H. A collection of aspect ratios of common clay minerals determined from conductometric titrations. *Clay Minerals.* (2014) 49:495–8. doi: 10.1180/claymin.2014.049.3.10
53. Wakai M, Almenar E. Effect of the presence of montmorillonite on the solubility of whey protein isolate films in food model systems with different compositions and pH. *Food Hydrocolloids.* (2015) 43:612–21. doi: 10.1016/j.foodhyd.2014.07.022
54. Chen L, Zhao Y, Chen T, Bai H, Zhang T, Li H, et al. Correlation of aspect ratio of montmorillonite nanosheets with the colloidal properties in aqueous solutions. *Results Phys.* (2019) 15:102526. doi: 10.1016/j.rinp.2019.102526
55. Lu C, Mai YW. Influence of aspect ratio on barrier properties of polymer-clay nanocomposites. *Phys Rev Lett.* (2005) 95:088303. doi: 10.1103/PhysRevLett.95.088303
56. Zhao Y, Yi H, Jia F, Li H, Peng C, Song S. A novel method for determining the thickness of hydration shells on nanosheets: a case of montmorillonite in water. *Powder Technol.* (2017) 306:74–9. doi: 10.1016/j.powtec.2016.10.045
57. Lecouvet B, Horion J, D'Haese C, Bailly C, Nysten B. Elastic modulus of halloysite nanotubes. *Nanotechnology.* (2013) 24:105704. doi: 10.1088/0957-4484/24/10/105704
58. Makaremi M, Pasbakhsh P, Cavallaro G, Lazzara G, Aw YK, Lee SM, et al. Effect of morphology and size of halloysite nanotubes on functional pectin bionanocomposites for food packaging applications. *ACS Appl Mater Interfaces.* (2017) 9:17476–88. doi: 10.1021/acsami.7b04297
59. Aucejo S, Marco C, Gavara R. Water effect on the morphology of EVOH copolymers. *J Appl Polym Sci.* (1999) 74:1201–6.
60. Kucukpinar E, Doruker P. Effect of absorbed water on oxygen transport in EVOH matrices. a molecular dynamics study. *Polymer.* (2004) 45:3555–64. doi: 10.1016/j.polymer.2004.03.024
61. Carstens DHW, Ehart EP. Permeability of deuterium and helium in poly(vinyl alcohol). *J Appl Polymer Sci.* (1984) 29:261–8.
62. Wang H, Zhang H, Niu B, Jiang S, Cheng J, Jiang S. Structure and properties of the poly(vinyl alcohol-co-ethylene)/montmorillonite-phosphorylated soybean protein isolate barrier film. *RSC Adv.* (2016) 6:29294–302. doi: 10.1039/C6RA03158G
63. Oades JM, Waters AG. Aggregate hierarchy in soils. *Soil Res.* (1991) 29:815–28.
64. Fityus S, Buzzi O. The place of expansive clays in the framework of unsaturated soil mechanics. *Appl Clay Sci.* (2009) 43:150–5. doi: 10.1016/j.clay.2008.08.005
65. Abhilash V, Rajender N, Suresh K. Chapter 14 - X-ray diffraction spectroscopy of polymer nanocomposites. In: Thomas S, Rouxel D, Ponnamma D, editors. *Spectroscopy of Polymer Nanocomposites.* Amsterdam; Boston, MA; Heidelberg; London; New York, NY; Oxford; Paris; San Diego, CA; San Francisco, CA; Singapore; Sydney, NSW; Tokyo: William Andrew Publishing (2016). p. 410–51.
66. Lagarón JM, Giménez E, Saura JJ, Gavara R. Phase morphology, crystallinity and mechanical properties of binary blends of high barrier ethylene–vinyl alcohol copolymer and amorphous polyamide and a polyamide-containing ionomer. *Polymer.* (2001) 42:7381–94. doi: 10.1016/S0032-3861(01)00204-X
67. Ricciardi R, Auriemma F, De Rosa C, Lauprêtre F. X-ray diffraction analysis of poly(vinyl alcohol) hydrogels, obtained by freezing and thawing techniques. *Macromolecules.* (2004) 37:1921–27. doi: 10.1021/ma035663q
68. Viani A, Gualtieri AF, Artioli G. The nature of disorder in montmorillonite by simulation of X-ray powder patterns. *Am Mineral.* (2002) 87:966–75. doi: 10.2138/am-2002-0720

69. Drits VA, Sakharov BA, Hillier S. Phase and structural features of tubular halloysite (7 Å). *Clay Minerals*. (2018) 53:691–720. doi: 10.1180/clm.2018.57
70. Aktzi N, Nir Y, Wang D, Narkis M, Siegmann A. EVOH/clay nanocomposites produced by melt processing. *Polym Composites*. (2001) 22:710–20. doi: 10.1002/pc.10573
71. Gaidukov S, Danilenko I, Gaidukova G. Characterization of strong and crystalline polyvinyl alcohol/montmorillonite films prepared by layer-by-layer deposition method. *Int J Polym Sci*. (2015) 2015:1–8. doi: 10.1155/2015/123469
72. Cabedo L, Giménez E, Lagaron JM, Gavara R, Saura JJ. Development of EVOH-kaolinite nanocomposites. *Polymer*. (2004) 45:5233–8. doi: 10.1016/j.polymer.2004.05.018
73. López-Rubio A. 10 - Ethylene-vinyl alcohol (EVOH) copolymers. In: Lagarón JM, editor. *Multifunctional and Nanoreinforced Polymers for Food Packaging*. Oxford; Cambridge; Philadelphia, PA; New Delhi: Woodhead Publishing, (2011). p. 261–84.
74. Zhu BD, Zhang JY, Lin CH, Chen HL, Wang J. Nonisothermal crystallization kinetics of ethylene vinyl alcohol copolymer with poly(oxypropylene)diamine intercalated montmorrilonite. *J Macromol Sci Part B*. (2018) 57:333–47. doi: 10.1080/00222348.2018.1460971
75. Zhang Z, Britt IJ, Tung MA. Permeation of oxygen and water vapor through EVOH films as influenced by relative humidity. *J Appl Polym Sci*. (2001) 82:1866–72. doi: 10.1002/app.2030
76. Bhunia K, Dhawan S, Sablani SS. Modeling the oxygen diffusion of nanocomposite-based food packaging films. *J Food Sci*. (2012) 77:29–38. doi: 10.1111/j.1750-3841.2012.02768.x
77. López-Rubio A, Lagarón JM, Hernández-Muñoz P, Almenar E, Catalá R, Gavara R, et al. Effect of high pressure treatments on the properties of EVOH-based food packaging materials. *Innov Food Sci Emerg Technol*. (2005) 6:51–8. doi: 10.1016/j.ifset.2004.09.002
78. Manoratne C, Rajapakse R, Dissanayake L. Ionic conductivity of poly(ethylene oxide) (PEO)-montmorillonite (MMT) nanocomposites prepared by intercalation from aqueous medium. *Int J Electrochem Sci*. (2006) 1:32–46. doi: 10.5930/issn.1452-3981
79. Pandey K, Pitman A. FTIR studies of the changes in wood chemistry following decay by brown-rot and white-rot fungi. *Int Biodeterioration Biodegradation*. (2003) 10:151–60. doi: 10.1016/S0964-8305(03)00052-0
80. Lu W, Lu C, Hu J, Wu J, Zhou Q. Effects of the blending time on the properties and non-isothermal crystallization behavior of PA6/EVOH blends. *Polym Eng Sci*. (2021) 61:1719–31. doi: 10.1002/pen.25695
81. Haghighi H, Leugoue SK, Pfeifer F, Siesler HW, Licciardello F, Fava P, et al. Development of antimicrobial films based on chitosan-polyvinyl alcohol blend enriched with ethyl lauroyl arginate (LAE) for food packaging applications. *Food Hydrocolloids*. (2020) 100:105419. doi: 10.1016/j.foodhyd.2019.105419

Conflict of Interest: The authors declare that the research was conducted in the absence of any commercial or financial relationships that could be construed as a potential conflict of interest.

Publisher's Note: All claims expressed in this article are solely those of the authors and do not necessarily represent those of their affiliated organizations, or those of the publisher, the editors and the reviewers. Any product that may be evaluated in this article, or claim that may be made by its manufacturer, is not guaranteed or endorsed by the publisher.

polymers

MDPI

Article

A Comparative Study on the Roll-to-Roll Processing of a Silicate–Polyvinyl Alcohol Composite Barrier Lacquer Using Slot-Die and Reverse Gravure Coating Techniques

Stefan Schiessl [1,2,*], Esra Kucukpinar [2], Noémie Rivollier [3,4], Horst-Christian Langowski [2] and Peter Eisner [1,2,5]

1 TUM School of Life Sciences Weihenstephan, Technical University of Munich, Alte Akademie 8, 85354 Freising, Germany
2 Fraunhofer Institute for Process Engineering and Packaging IVV, Materials Development Giggenhauser Strasse 35, 85354 Freising, Germany
3 Centre Technique Industriel de la Plasturgie (CT-IPC), 2 Rue Pierre et Marie Curie, 01100 Bellignat, France
4 Institut für Geologische Wissenschaften, Freie Universität Berlin, Kaiserswerther Str. 16, 14195 Berlin, Germany
5 Steinbeis-Hochschule, System- und Bioverfahrenstechnik, Ernst-Augustin-Straße 15, 12489 Berlin, Germany
* Correspondence: stefan.schiessl@ivv.fraunhofer.de

Abstract: The integration of platelet-shaped montmorillonite particles to improve the oxygen barrier of polyvinyl-alcohol-based barrier layers is state-of-the-art, but research on roll-to-roll coatings of such composite barrier lacquers has not been widely published. In this study, two different coating techniques, slot-die and reverse gravure, were used on a roll-to-roll scale to apply barrier lacquers comprising polyvinyl alcohol and montmorillonite. The lacquers were analyzed regarding viscosity at certain shear rates and surface energy and the dried coating layers regarding oxygen barrier, surface morphology, and particle orientation. Low permeability coefficients delivering a high oxygen barrier of 0.14 and 0.12 $\frac{cm^3\,(STP)\,1\,\mu m}{m^2\,d\,bar}$ were achieved for the coating layers with slot-die and reverse gravure coating, respectively. It turned out that the properties of the barrier lacquer need to be adjusted to the coating technique to achieve high oxygen barrier performance. By tailoring the barrier lacquer formulation, the orientation of the platelet-shaped montmorillonite particles can be achieved using both techniques. A low solid content of down to 3 wt% is preferable for the premetered slot-die coating, because it results in low agglomeration quantity in the coating layer. A high solid content of up to 9 wt% is preferable for the self-metered reverse gravure coating to assure a homogeneously coated layer.

Keywords: barrier lacquer; reverse gravure; oxygen permeability; montmorillonite; slot-die; polyvinyl alcohol; flexible packaging

Citation: Schiessl, S.; Kucukpinar, E.; Rivollier, N.; Langowski, H.-C.; Eisner, P. A Comparative Study on the Roll-to-Roll Processing of a Silicate–Polyvinyl Alcohol Composite Barrier Lacquer Using Slot-Die and Reverse Gravure Coating Techniques. *Polymers* **2023**, *15*, 2761. https://doi.org/10.3390/polym15132761

Academic Editors: Verónica San Miguel Arnanz and Juan Pedro Fernández Blázquez

Received: 23 May 2023
Revised: 12 June 2023
Accepted: 13 June 2023
Published: 21 June 2023

1. Introduction

Polyvinyl alcohol (PVA) is a widely applied and commonly used layer in flexible films intended for food packaging. It is chosen because it provides barrier properties against oxygen, biocompatibility, and biodegradability, as well as nontoxicity and easy film formation [1]. However, the availability of essential raw materials for production of PVA is limited [2]. The availability issue mainly concerns acetic acid, which is a precursor of vinyl acetate [3]. Of course, the global supply shortage causes prices to increase, e.g., in Europe by more than 100 % from 2021 to 2022 [4,5]. Therefore, there is a strong interest in replacing PVA [6], producing it from biomass [7], reducing its amount [8] in gas barrier films, or reducing its content in packaging film in general.

In order to prevent the gas barrier deterioration of the packaging film due to the reduction in PVA content, nanoparticles can be added to keep the barrier performance at the same level despite reduced coating layer thickness. Numerous investigations have

demonstrated that the barrier performance of PVA coatings can be improved by the addition of platelet-shaped silicate particles such as montmorillonite (MMT) [9–14]. These publications are restricted to sheet coatings at the lab scale. The transition between lab-scale and roll-to-roll scale applications is as challenging as the development of the coating material itself [15]. The limiting factors include (among others) the coating technique, the coating speed, the drying conditions, and the rheological properties of the lacquer [16,17]. Only a few publications have discussed the roll-to-roll coating of such silicate-based composite materials. Koppolu et al. [18] reported the roll-to-roll coating of microfibrillated cellulose or cellulose nanocrystals with the slot-die coating technique. In order to achieve an effective barrier using such cellulose-based coatings, they can be alternately coated with MMT dispersions to form a layer-by-layer structure, but this is then offset by the inefficiency of multiple coatings [19]. One potential layer-by-layer approach was also reported by Ben Dhieb et al. [11] for PVA and MMT dispersions, where blade coating was introduced as alternative coating technique to dip coating, but it was not performed on a roll-to-roll line. They achieved a low permeability coefficient of 0.2 $\frac{cm^3\,(STP)\,1\,\mu m}{m^2\,d\,bar}$ and delivered a high oxygen barrier for 30 alternating layers coated with a doctor blade. Another feasible approach was introduced by LaChance et al. [20]. They demonstrated a one-time doctor-blade coating of a nanocomposite lacquer, also comprising PVA and MMT with an oxygen permeability of 2.1 $\frac{cm^3\,(STP)\,1\,\mu m}{m^2\,d\,bar}$.

One possible field of application for these barrier lacquers is food packaging. Therefore, the barrier performance of the coating layer is compared with common barrier concepts in this application field, e.g., AlO_x- or SiO_x-deposited films or films with metallization [21,22]. Polypropylene films can reach permeation rates of down to 0.3 $\frac{cm^3\,(STP)}{m^2\,d\,bar}$ with SiO_x deposition [23], down to 0.7 $\frac{cm^3\,(STP)}{m^2\,d\,bar}$ with AlO_x deposition [24], and down to 0.5 $\frac{cm^3\,(STP)}{m^2\,d\,bar}$ with metallization with aluminum [25]. Many of these barrier materials are used in laminate structures. Although packaging materials of only 12 to 20 µm are required to be vacuum-coated, the final packaging products may well be considerably thicker as they end up as a laminate. To ensure ease of handling for downstream processes and thus maintain the best barrier performance, most vacuum-coated barrier films are laminated [26].

As an alternative to these coatings in vacuum, this study presents a barrier lacquer that can be coated at atmospheric pressure. For this purpose, the aim is to investigate the roll-to-roll coating of a composite barrier lacquer comprising PVA and MMT using the slot-die or reverse gravure technique for the first time in detail to the author's knowledge. The question to answer is how these two application techniques affect the layer homogeneity, surface morphology, agglomerate formation, and gas barrier performance. Therefore, a lacquer previously developed by Schiessl et al. [14] was prepared at three different solid contents of 3, 6, and 9 wt% in order to modify viscosities. The prepared lacquers were applied by means of a semiautomated roll-to-roll coating machine using two different coating techniques: slot-die and reverse gravure. The effect of the shear rate on the coating material was taken into consideration in addition to the lacquer viscosity and solid content effects. As a result, two different ceramic gravure rolls, with quadrangular and trihelical geometry, and two different shim thicknesses (gap openings) during the slot-die coating were used for each lacquer. This approach enabled investigations of various coating process windows with different parameter sets of lacquer viscosity and shear rate for both of the application techniques presented. The flexible films comprising a dried barrier layer were characterized in terms of surface roughness, orientation of MMT particles, and oxygen permeability coefficients of the coating layers. Based on the present research, a parameter set leading to low permeability coefficients delivering a high oxygen barrier was generated for every coating technique.

2. Materials and Methods

2.1. Materials

The platelet-shaped MMT particles (CLOISITE Na^+ from BYK Additives and Instruments, Wesel, Germany) were dispersed using a planetary ball mill (PULVERISETTE 6, FRITSCH, Idar-Oberstein, Germany) and mixed with PVA (Exceval AQ-4104 from Kuraray, Frankfurt, Germany) at a mixing ratio of 1:1 by weight as reported by Schiessl et al. [14]. In contrast to the latter procedure, mixing and heating of the barrier lacquers were performed in a heatable blender (Thermomix TM5 from Vorwerk, Wuppertal, Germany) with a capacity of 2 L. The total solid content c_{solid} of the barrier lacquers was primarily adjusted to 9 wt% and subsequently diluted to 6 and 3 wt% with demineralized water using the same blender. The samples of the liquid barrier lacquers (BL) were labeled as BL-3, BL-6, and BL-9. A lower limit of 3 wt% solid content was chosen to provide a stable coating layer at the same drying conditions as the other coatings. The upper limit was set to 9 wt%, because, given their excessive viscosity, it was not possible to homogeneously coat lacquers having a higher solid content.

Biaxially oriented polypropylene (BoPP) was used as a substrate on rolls with a width of 300 mm and several hundred meters in length. BoPP was purchased as transparent, nonsealable film with a thickness of 30 µm (TNS from Taghleef Industries, San Giorgio, Italy). The BoPP film had a unit weight of 27.3 $\frac{g}{m^2}$, and in machine direction, a tensile strength of 150 MPa and an elongation at break of 140 %.

2.2. Coating Processes

2.2.1. Slot-Die Coating

The slot-die (SD) technique, shown in Figure 1, is a premetered process, i.e., the amount of liquid applied to the web per unit area is precisely adjusted by the volume flow [27]. The coatings were applied using a T-shaped manifold half circle slot-die (FMP Technology, Erlangen, Germany). The slot-die width W was 260 mm, and the gap length L in the slot-die was 45 mm. The shim thickness S was adjustable by using different shim plates from 100 to 500 µm. The wet coating layer thickness t_{wet} needed to achieve a defined dry layer thickness t_{dry} is calculated by

$$t_{wet} = \frac{t_{dry}}{c_{solid}} \quad (1)$$

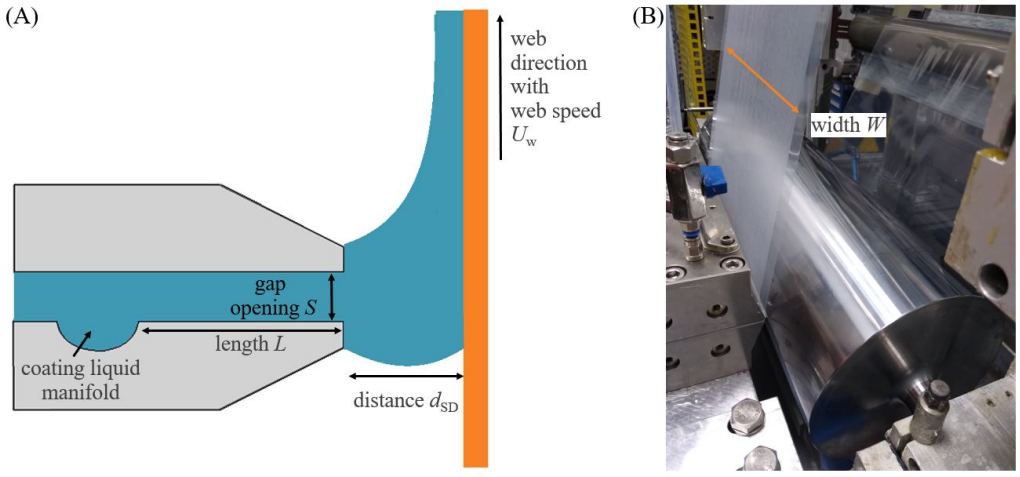

Figure 1. (**A**) Schematic drawing of the slot-die coating process illustrating the parameters of gap length L, shim thickness S, and distance from die to web d_{SD}. (**B**) Picture of slot-die coating illustrating the coating width W.

The dry coating layer thickness was adjusted to 1.5 µm for all coatings using the slot-die, thus leading to the wet layer thicknesses listed in Table 1 for all parameter sets. A total

of six different coating parameter sets, labeled as SD-500-9, SD-300-9, SD-300-6, SD-200-6, SD-200-3, and SD-100-3, were used to coat the BoPP. The volume flow $\dot{Q}$ dispensed by alternately pumping syringe pumps (Base 120 with two Nemesys S syringes, CETONI, Korbussen, Germany) required to achieve a wet layer thickness at a given web speed U_w of 5 $\frac{m}{min}$ is calculated by

$$\dot{Q} = t_{wet} \cdot U_w \cdot W \quad (2)$$

as listed in Table 1. Before reaching the slot-die, the barrier lacquer was pumped through a polymeric filter with a mesh size of 100 µm. Regarding the shear rates $\dot{\gamma}$ during the coating with slot-die, there are two important locations to consider, the shear rate within the die $\dot{\gamma}_{in}$ and the shear rate directly before reaching the web $\dot{\gamma}_{SD}$. A plane Couette flow develops in the slot-die, and the shear rate is calculated by

$$\dot{\gamma}_{in} = \frac{6 \cdot \dot{Q}}{W \cdot S^2} \quad (3)$$

according to Durst et al. [28]. The shear rate in the slot-die must be calculated to obtain the present viscosity η in the die, which in turn is needed to calculate the pressure loss Δp in the slot-die [29].

$$\Delta p = \frac{12 \cdot \eta \cdot L \cdot \dot{Q}}{S^3 \cdot W} \quad (4)$$

Table 1. Parameter sets used for coatings with slot-die (S: shim thickness, c_{solid}: total solid content, t_{wet}: wet layer thickness, $\dot{Q}$: volume flow, $\dot{\gamma}_{in}$: shear rate, η: viscosity, and Δp: pressure loss).

	S	c_{solid}	t_{wet}	$\dot{Q}$	$\dot{\gamma}_{in}$	η	Δp
Sample Code	**µm**	**wt%**	**µm**	$\frac{mL}{min}$	$\frac{1}{s}$	**mPa s**	**bar**
SD-500-9	500	9	17	21.7	33.3	336	0.020
SD-300-9	300	9	17	21.7	92.6	201	0.056
SD-300-6	300	6	25	32.5	139	16.5	0.007
SD-200-6	200	6	25	32.5	313	14.7	0.021
SD-200-3	200	3	50	65.0	625	2.99	0.008
SD-100-3	100	3	50	65.0	2500	2.83	0.064

A specific dynamic pressure in the slot-die is necessary for the coating liquid to be distributed homogeneously over the entire die [27]. The resulting pressure loss should be as low as possible for energy and safety reasons (bursting of hoses), and it was below a set value of 0.4 bar in any case, as shown in Table 1.

The slot-die was operated in bead mode for each coating, meaning that the distance d_{SD} between web and die was 2 to 5 times higher than t_{wet} [30]. Since the gap flow was already fully developed after a development length of less than 1 µm, the shear rate before touching the web was

$$\dot{\gamma}_{SD} = \frac{U_w}{d_{SD}} \quad (5)$$

when using the setup and coating fluids described [28,31,32]. The development length describes the length that is needed for a liquid to build up a constant flow without turbulence in a certain environment. Turbulent flow within the slot-die gap takes place for only several hundred nanometers after the liquid manifold. The subsequent flow can be described as fully developed.

2.2.2. Reverse Gravure Coating

The reverse gravure (RG) coating, as shown in Figure 2, was performed on two different gravure rolls. One of them was a ceramic gravure roll with quadrangular geometry (RG-q) with 65 µm in depth with a theoretical coating volume of 25 $\frac{mL}{m^2}$ made by UNGRICHT (Moenchengladbach, Germany). The second was a ceramic gravure roll with a 45° trihelical

geometry (RG-t) and 40 $\frac{\text{lines}}{\text{cm}}$, leading to a theoretical coating volume of 45 $\frac{\text{mL}}{\text{m}^2}$ made by JWS (Sinsheim, Germany). In comparison with the slot-die coating technique, coating with reverse gravure is understood to be a self-metered process, which means that the wet layer thickness depends mainly on the gravure roll type but also on the solid content and flow behavior of the lacquer, the web speed, the surface energy of substrate and of the lacquer, and the interactions of these parameters with each other [27]. Barrier lacquers with a solid content of 3, 6, and 9 wt%, respectively, were coated using the two gravure rolls, leading to six different coating parameter sets with the sample codes RG-q-3, RG-q-6, RG-q-9, RG-t-3, RG-t-6, and RG-t-9. The coating width was 270 mm, and the web speed was similar to that of the slot-die coating 5 $\frac{\text{m}}{\text{min}}$. The speed of the gravure roll U_g was set to 7 $\frac{\text{m}}{\text{min}}$ for all the parameter sets. Given that the development lengths for a fully developed flow are similar in both coating methods, the shear rate on the barrier lacquer before touching the web was calculated in a manner similar to the slot-die coating process. Therefore, a constant shear rate in both gaps, between die and web and between gravure roll and web d_{RG}, is present [28,31].

$$\dot{\gamma}_{RG} = \frac{U_w + U_g}{d_{RG}} \tag{6}$$

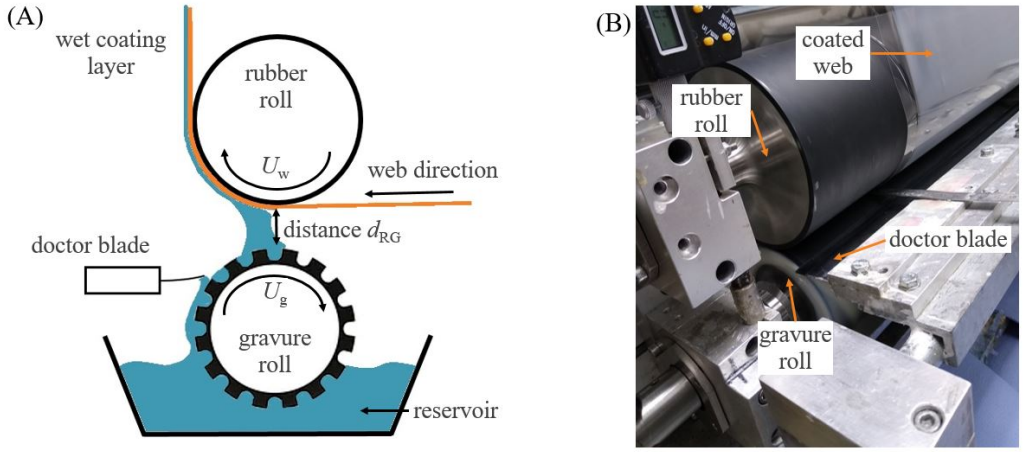

Figure 2. (**A**) Schematic drawing of reverse gravure coating process with delineated roll directions U_w and U_g representing the speed of substrate (web) and gravure roll, respectively. The distance between gravure roll and substrate is d_{RG} (adapted with permission from Shim [33], 2023, Elsevier). (**B**) Picture of reverse gravure coating process with quadrangular gravure roll.

2.2.3. Roll-to-Roll Machine Adjustments and Curing

The slot-die and reverse gravure coating techniques are inherent to a semiautomated roll-to-roll coating machine. The BoPP substrate was placed in the unwinding station and passes consecutively through the corona pretreatment station, the coating station, the curing station, and the rewinding station, consecutively. During this process, the web tension at the unwinding station was always a little lower than the tension adjusted at the rewinding station due to the friction losses at several intervening rolls. The roll-to-roll coating line used was designed such that the coated side of the substrate never makes contact with a roll. The web tension for the BoPP substrate was at the rewinding station 30 N and at the unwinding station 20 N.

The substrate was physically pretreated using a corona discharge station (CLNE from SOFTAL electronic, Hamburg, Germany) to ensure a homogeneous wetting with lacquer. The plasma dose was adjusted to 4.8 $\frac{\text{kJ}}{\text{m}^2}$ for the pretreatment of BoPP in order to achieve a surface energy sufficient for wetting with aqueous barrier lacquers. In this context, "sufficient" means that the surface energy was measured to be more than 36 $\frac{\text{mJ}}{\text{m}^2}$ by means of test inks (Teststifte PINK, arcotest, Moensheim, Germany, according to DIN ISO 8296 [34]). This is required for wetting with water-based coating liquids [35]. The

curing was performed with a convection oven directly after the coating station. The curing conditions were 60 °C, applied for 50 s. At least 50 m of film length was coated with every parameter set.

2.3. Methods

2.3.1. Thickness Measurement

The thickness of the coating layer was measured using a precision thickness gauge (Hanatek FT3 from Rhopoint Instruments, Beyhill on Sea, UK). The resolution was 0.1 µm, the thickness was measured at five random spots on the coated sample, and an average value was then reported.

2.3.2. Oxygen Permeability

The oxygen permeation rates of the coated films were measured according to the DIN 53380-3 standard with the oxygen-specific carrier gas method [36]. The measurements were performed using an OX-TRAN 2/21 OTR Analyzer (AMETEK MOCON, Minneapolis, MN, USA) at 23 °C and 50 %RH. If the respective permeation rate was constant for at least 10 h, then a steady state was assumed to have been achieved, and the measurement was then stopped. Duplicate determination was performed for all of the coatings, and the values were reported at standard deviation. After measuring the oxygen permeation rate of the coated film, the permeability coefficient of the coating layer was calculated using the measured total permeation rate of the coated substrate and the permeation rate of uncoated BoPP, which is 1250 $\frac{cm^3\,(STP)}{m^2\,d\,bar}$. In this context, the value of the permeability coefficient is expressed as normalized to a material thickness of 1 µm, as described by Langowski [37].

2.3.3. Surface Energy Measurement

The surface energy of the substrate–air interface was determined according to DIN EN ISO 19404-2 [38] via the sessile drop method with a DSA 100 from Kruess (Hamburg, Germany). For this purpose, at least five drops of three different liquids, water, ethylene glycol, and diiodomethane, were placed on the surface, and the contact angle was measured at equilibrium. At least two liquids with known polar and dispersive energy components are needed to calculate the polar and dispersive components of the surface energy using the Owens–Wendt–Rabel–Kaelble (OWRK) evaluation method [39].

The surface energy of the lacquer–air interface was measured according to DIN EN ISO 1904-3 [40] via the pendent drop method using the same device.

2.3.4. Distance Measurement during Coating Processes

The values for d_{SD} and d_{RG} were measured in a similar way. First, the slot-die or the gravure roll were brought in contact with the substrate. This position was set as the zero point. The distance was then increased stepwise until reaching the final position for the respective parameter set and measured with a high-precision sensor head, GT2-H12K, from Keyence (Neu-Isenburg, Germany). The resolution was 10 µm.

2.3.5. Viscosity Measurement

The rheological measurements were performed using a modular compact rheometer 302 from Anton Paar (Graz, Austria) equipped with a cone–plate set-up with a 50 mm diameter, an angle of 0.995°, and a preadjusted gap size of 100 µm. Since shear force is permanently applied in one direction during both of the coating processes used in the present study, the viscosity measurements were performed with a rotating plate. The shear sweep measurements of the lacquers produced were performed at room temperature, i.e., 23 °C, from 10 to 10,000 $\frac{1}{s}$ with a logarithmically increasing step size limited to 30 measuring points.

2.3.6. Roughness Measurement

The roughness was measured via direct mechanical contact over the surface with a Hommel Tester W55 from Hommelwerke (Villingen-Schwenningen, Germany). For each sample, 5 lines with a length of 4.5 mm were measured parallel (MD) and perpendicular (TD) to the coating direction, and the roughness is given as an arithmetic mean value (R_a) of these 5 measurements, respectively.

2.3.7. Scanning Electron Microscopy (SEM)

The SEM images were captured with a JSM-7200F (JEOL, Akishima, Japan) at high vacuum (2×10^{-4} Pa). All samples were sputtered with a gold layer using a Hummer JR sputter coater (Technics, Alexandria VA, USA) in order to reduce electrical charging of the nonconductive polymer samples. A solid-state detector (SSD), which detected backscattered electrons, was used in combination with the JEOL-SEM software Ver. 7.1.0.9. To perform a cross-section image, the coated substrate was placed between copper tapes with electrically conductive adhesive, and cross-cuts were prepared by Ar^+ beam milling with a cross-section polisher (JEOL, Akishima, Japan).

2.3.8. Pole Figures

Pole figures were measured using a PANalytical MRD X-ray diffractometer (Almelo, The Netherlands) equipped with a Eulerian cradle employing two-axis scans along ϕ and χ. Measurements were performed at a fixed 2θ angle of 6°, corresponding to the 2θ angle position of the lattice plane (002) studied. To plot pole figures, the intensity distribution was measured along the ϕ axis from 0 to 360° at sample tilts χ from 0 to 85°, with an increment of 5° each.

3. Results and Discussion

3.1. Oxygen Permeability

The coating thicknesses required to normalize the oxygen transmission rate and obtain the oxygen permeability coefficient are shown in Table 2. As expected, the thickness values for the premetered slot-die coating technique were all close to the target of 1.5 µm.

Table 2. Dry coating layer thickness measured for the various coating techniques and parameter sets. These values are used to normalize the permeation rate to calculate the permeability coefficients.

Self-Metered Reverse Gravure Coating		Premetered Slot-Die Coating	
	µm		µm
RG-t-9	1.9 ± 0.1	SD-500-9	1.6 ± 0.1
RG-t-6	1.3 ± 0.1	SD-300-9	1.6 ± 0.2
RG-t-3	0.5 ± 0.2	SD-300-6	1.6 ± 0.1
RG-q-9	1.0 ± 0.1	SD-200-6	1.5 ± 0.1
RG-q-6	0.3 ± 0.2	SD-200-3	1.5 ± 0.1
RG-q-3	0.1 ± 0.1	SD-100-3	1.4 ± 0.1

The coating layer thicknesses for the self-metered reverse gravure technique were difficult to adjust because of the dependency of the wet layer thickness on various parameters, as described in Section 2.2.2. Indeed, the higher the solid content, the thicker the coating layer. This relationship was valid for both gravure roll geometries. The thickness of the coatings with the trihelical gravure roll is measured as 1.9 µm, 1.3 µm, and 0.5 µm for the solid contents of 9, 6, and 3 wt%, respectively. Generally, the coating thicknesses achieved with the quadrangular gravure roll were found to be lower due to the lower theoretical coating volume of 25 $\frac{mL}{m^2}$ compared with the trihelical gravure roll with 45 $\frac{mL}{m^2}$. The coating layer thickness for RG-q-9 was 1.0 µm. For the barrier lacquers with lower solid contents of 3 and 6 wt%, the thicknesses with quadrangular gravure roll were found to be 0.1 and 0.3 µm. This corresponds to a wet layer thickness of only 3.3 and 5.0 µm, respectively. There

are limits below which a stable film can no longer be formed, which is then reflected in very poor barrier properties. It was not possible to transfer more material to the substrate surface using the quadrangular gravure roll at these low solid contents.

Figure 3 shows the oxygen permeability coefficients of the barrier lacquers investigated. The previously reported permeability coefficient of this barrier lacquer obtained with a k-bar coating on BoPP sheets by Schiessl et al. [14] was 0.12 $\frac{cm^3\,(STP)\,1\,\mu m}{m^2\,d\,bar}$ at a total solid content of 8 wt%. Similar values were achieved in this study. The lowest value with reverse gravure was 0.12 $\frac{cm^3\,(STP)\,1\,\mu m}{m^2\,d\,bar}$ for RG-t-9, indicating the trihelical gravure roll and a solid content of 9 wt%. In the case of the slot-die coatings, the lowest value was 0.14 $\frac{cm^3\,(STP)\,1\,\mu m}{m^2\,d\,bar}$ for SD-200-3, indicating a shim thickness of 200 µm and a solid content of 3 wt%.

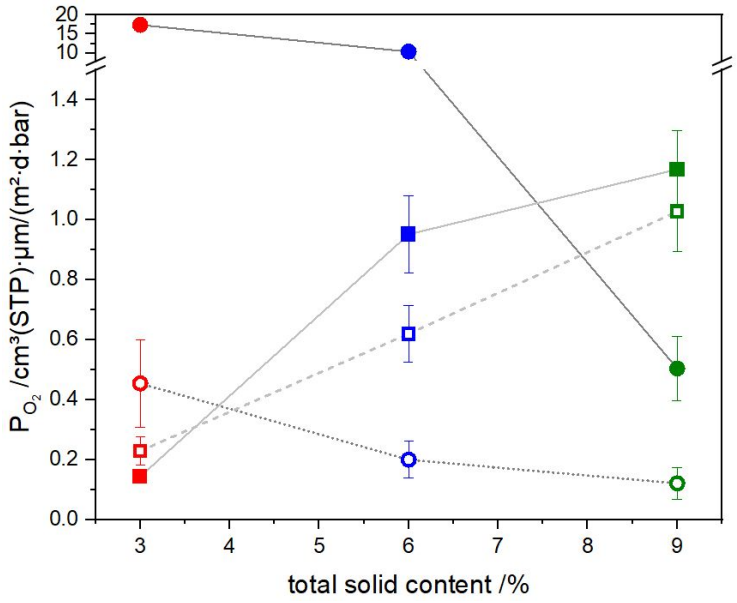

Figure 3. Oxygen permeability coefficients for the coating layers depending on the solid content of the barrier lacquer: The colors red, blue, and green represent the solid content of the barrier lacquers of 3, 6, and 9 wt%, respectively. The square symbols represent the slot-die coating, and the circle symbols represent the reverse gravure coating. A filled symbol represents the higher shear rate within a solid content, i.e., the quadrangular roll in the reverse gravure technique and the thin shims in the slot-die (300 µm for 9 wt%, 200 µm for 6 wt%, and 100 µm for 3 wt%). The empty symbol represents the lower shear rate within a solid content, i.e., the trihelical roll in the reverse gravure technique and the thick shims in the slot-die (500 µm for 9 wt%, 300 µm for 6 wt%, and 200 µm for 3 wt%).

The barrier performance of the slot-die-coated samples decreases by increasing the solid content, whereas the converse is true for the reverse-gravure-coated samples. Using slot-die coating, the permeability coefficients for BL-9 are similar, with values of 1.0 and 1.2 $\frac{cm^3\,(STP)\,1\,\mu m}{m^2\,d\,bar}$, regardless of shear rate. Within the BL-6, the stronger sheared sample provides a permeability coefficient of 0.95 $\frac{cm^3\,(STP)\,1\,\mu m}{m^2\,d\,bar}$ and the less sheared sample one of 0.62 $\frac{cm^3\,(STP)\,1\,\mu m}{m^2\,d\,bar}$. For the BL-3, the low permeability coefficient of 0.23 $\frac{cm^3\,(STP)\,1\,\mu m}{m^2\,d\,bar}$ is provided by the less sheared sample and the lowest value of 0.14 $\frac{cm^3\,(STP)\,1\,\mu m}{m^2\,d\,bar}$ by the stronger sheared sample. Given that this does not represent a trend, it appears that the shear rate has little influence on the oxygen barrier performance of the coating layer. The main influencing factor during slot-die coating is the solid content and the properties accompanied with it.

The permeability coefficients for the samples coated with trihelical gravure roll, which are less sheared than the ones coated with quadrangular gravure roll, decrease from 0.45 to 0.12 $\frac{cm^3\,(STP)\,1\,\mu m}{m^2\,d\,bar}$ as the solid content increases from 3 to 9 wt%. The lowest permeability coefficient, reached using the quadrangular gravure roll, was 0.50 $\frac{cm^3\,(STP)\,1\,\mu m}{m^2\,d\,bar}$ at a solid

content of 9 wt%. The barrier improvements reached with the quadrangular gravure roll at 3 and 6 wt% were much lower than those achieved using the trihelical gravure roll, which may have been due to the insufficient amount of material transferred, as shown in Table 2.

Samples RG-t-9, RG-t-6, RG-t-3, RG-q-9, SD-200-3, and SD-100-3, which were obtained using 6 different parameter sets, provided oxygen permeability coefficients below 0.5 $\frac{cm^3\,(STP)\,1\,\mu m}{m^2\,d\,bar}$ on BoPP. The reasons for the differences among the 12 measured samples are discussed in the next sections.

3.2. Surface Energy of the Barrier Lacquers and Substrate

The surface energies of the barrier lacquers with various solid contents are shown in Table 3. In comparison with the surface energy of pure water with 72 $\frac{mJ}{m^2}$ [41], the surface energy of the barrier lacquers decreases to 62 $\frac{mJ}{m^2}$ after mixing water with PVA and MMT. All three barrier lacquers exhibited nearly the same surface energy. It was shown by Chen et al. [42] that an increasing amount of MMT in an aqueous dispersion leads to an increase in surface energy. On the other hand, Nagarkar and Patel [43] found out that an increasing amount of PVA in an aqueous dispersion leads to a decrease in surface energy. The variation in total solid content in this study did not affect the surface energy. This outcome may have been due to the combination of PVA and MMT effects in the formulation used having counteracted one another.

Table 3. Surface energy of BoPP before and after corona pretreatment measured using the sessile drop method giving the corresponding dispersive and polar components and surface energy measured with the pendant drop method of barrier lacquers with solid contents of 3, 6, and 9 wt%. The subdivision in dispersive and polar components is not applicable (N/A) with the pendant drop method.

	Total ($\frac{mJ}{m^2}$)	**Dispersive ($\frac{mJ}{m^2}$)**	**Polar ($\frac{mJ}{m^2}$)**
BoPP (untreated)	24.1 ± 0.2	24.0 ± 0.2	0.08 ± 0.01
BoPP (pretreated)	37.0 ± 0.4	30.1 ± 0.3	6.94 ± 0.12
BL-3	61.7 ± 0.2	N/A	N/A
BL-6	62.3 ± 0.2	N/A	N/A
BL-9	61.5 ± 0.7	N/A	N/A

One of the major requirements for a strong bond between a barrier lacquer and a polymeric substrate is that the liquid lacquer completely covers the substrate surface during the coating process, i.e., wettability [44]. If a lacquer does not wet, defects such as islands will appear during the coating process, even before curing of the lacquer, which leads to degradation of the functional properties. A high level of wettability can be achieved if the total surface energy of the coating formulation is lower than the total surface energy of the substrate [45]. The surface energy of untreated BoPP with 24 $\frac{mJ}{m^2}$ was found to be too low in comparison with the surface energy of the barrier lacquers. After corona pretreatment, however, the surface energy increased to 37 $\frac{mJ}{m^2}$, mainly due to the significant increase in the polar component by 6.8 $\frac{mJ}{m^2}$. This increase was in agreement with values previously reported by Lindner et al. [46] and Aydemir et al. [35]. Although the total surface energy of BoPP after the corona pretreatment was still lower than the surface energy of the barrier lacquers, it was possible to spread the barrier lacquers spontaneously on the substrate surface by means of slot-die and reverse gravure coating. It was discovered that the viscosity of the barrier lacquer formulations, the wet coating layer thickness, and the coating parameters have additional influences on the layer coating performance, as was demonstrated by previous research [35,45,47,48].

The foregoing findings enable conclusions to be made about the oxygen barrier performance of the barrier lacquers (Section 3.1). If the BL-3 is, e.g., coated at a certain wet layer thickness, in the case of SD-200-3 with 50 µm, then the substrate will be wetted completely. Otherwise, a barrier value of 0.14 $\frac{cm^3\,(STP)\,1\,\mu m}{m^2\,d\,bar}$ for slot-die coating would not have been

measured. However, if the BL-3 is coated too thinly, as was the case for quadrangular gravure roll with only 3.3 µm, then a few uncoated areas may remain. This would explain why the permeability coefficient, which is independent of the coating layer thickness, was much higher for the same lacquer in sample RG-q-3 comprising 17 $\frac{cm^3\,(STP)\,1\,\mu m}{m^2\,d\,bar}$. Therefore, the explanation is that the resulting force from the surface energy mismatch needed to form an island is higher than the gravitational force that holds the lacquer in place. Barrier lacquer BL-6, which had a similarly thin coating of 5.0 µm as BL-3 but a higher viscosity (see Section 3.4), also provided a high permeability coefficient of 10 $\frac{cm^3\,(STP)\,1\,\mu m}{m^2\,d\,bar}$ for the RG-q-6 sample. This result demonstrates that the combination of viscosity, wet coating layer thickness, and surface energy needs to be sufficient to wet the substrate homogeneously.

3.3. Shear Rates during Coating Process

Figure 4A illustrates the shear rates during the two coating processes as a function of the distances between slot-die and web or between gravure roll and web. The shear rates to which the lacquer is subjected during both coating techniques are calculated according to Equations (5) and (6), respectively.

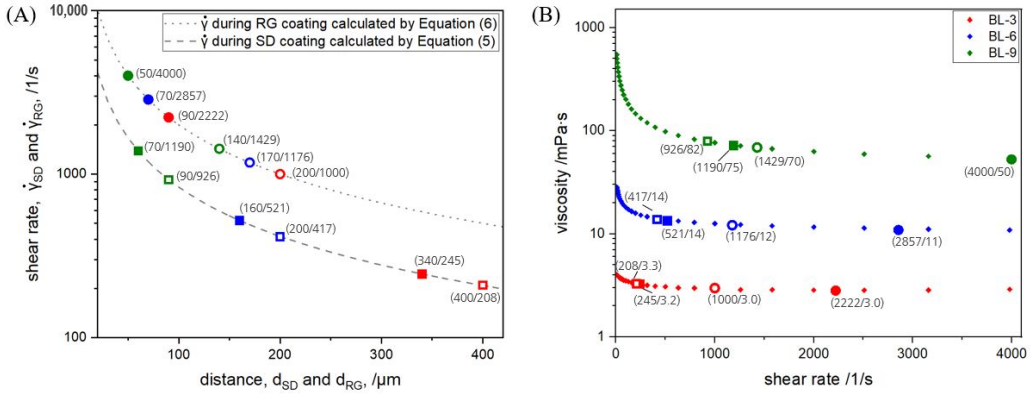

Figure 4. (**A**) The calculated shear rate during slot-die and reverse gravure coating plotted as a function of the measured distance between the slot-die and substrate d_{SD} or between gravure roll and substrate d_{RG}, respectively. (**B**) The viscosity of the barrier lacquers depending on the shear rate. The colors red, blue, and green represent the solid content of the barrier lacquers of 3, 6, and 9 wt%, respectively. The square symbol represents the slot-die coating and the circle symbol the reverse gravure coating. A filled symbol represents the higher shear rate within one solid content and the empty symbol the lower shear rate. The highlighted dots show the exact shear rates that the lacquers were subjected to during coating with the corresponding numerical values in (x/y) form.

The difference between reverse gravure and slot-die coating in terms of shear rate is best described using an example, i.e., BL-9. Sample BL-9 was sheared at 1190 and 926 $\frac{1}{s}$ and distances of 70 and 90 µm, respectively, during the slot-die process but at 4000 and 1429 $\frac{1}{s}$ and distances of 50 and 140 µm during the reverse gravure process. Within the slot-die coating, BL-9 was sheared at 925 $\frac{1}{s}$ for a shim of 300 µm but at 1190 $\frac{1}{s}$ for a shim of 500 µm. Within the parameter set of the thicker shims, as indicated by the filled symbols in Figure 4A, the shear rate decreased from 1190 to 245 $\frac{1}{s}$ due to the distance increasing from 70 to 340 µm for solid content decreasing from 9 to 3 wt%. The shear rates during the slot-die process were lower than those occurring during the reverse gravure process. Within the slot-die process, it was found that the shear rate decreased with a decreasing shim thickness (increasing distance between die and web) within one solid content or with a decreasing solid content. The distances, d_{SD} and d_{RG}, were adjusted in a way to provide the best coating picture and were measured for every coating parameter set. In this context, a good coating picture means a wet coating layer without any ribbings, striations, voids, or other inhomogeneities. The highest possible distance providing a good coating picture is preferred for the barrier lacquers, as was demonstrated by Creel et al. [49] for

polymer electrolyte fuel cell cathode ink. Bhamidipati et al. [50] showed that the potential for air entrainment is higher for higher viscosity and that it can be reduced by reducing the distance from die to web. This finding was applied within this study, since an air entrainment would lead to the aforementioned inhomogeneity and needs to be avoided. Even if entrained bubbles in the liquid coating layer are not visible during coating, they still result in an inhomogeneous appearance after drying. This is due to the fact that the thermal expansion coefficient of gases is three times higher than that of solids, and the encapsulated bubbles almost burst open during drying [51]. The viscosity of BL-9 was higher than that of BL-3 (see Section 3.4), for which reason the distance was lower for BL-9.

In the case of reverse gravure coatings, the distance for the quadrangular gravure roll extended from 50 to 90 µm and led to shear rates from 4000 to 2222 $\frac{1}{s}$ for decreasing solid content. The distance range for the trihelical gravure roll was from 140 to 200 µm, resulting in shear rates from 1429 to 1000 $\frac{1}{s}$. The distance increased with an increasing coating volume, which led to a lower shear rate. Within one roll geometry, the distance for the lacquer with higher solid content is lower because of two reasons. Firstly, it is similar to the slot-die coating, i.e., the higher the viscosity, the higher the risk of air entrainment with increasing distance. Secondly, since the surface energy of the lacquers was quite similar (see Table 3), the only varying parameter in the law of capillary rise is the density, and the density for lacquers with higher solid content was higher, so the capillary rise is lower [52].

3.4. Viscosity of Barrier Lacquers

Figure 4B shows the viscosity of the barrier lacquers prepared at three different solid contents as a function of shear rate. The shear rates applied on the barrier lacquers during the coating processes (Figure 4A) are marked on the diagram.

Sample BL-9 exhibited a shear-thinning behavior, as quantified by a viscosity reduction from 550 mPa s at a shear rate range of 10 $\frac{1}{s}$ to 50 mPa s at a shear rate of 4000 $\frac{1}{s}$. The viscosity reduction for BL-6 and BL-3 lasted from 28 to 11 mPa s and from 4.0 to 3.0 mPa s for the same shear rate range, respectively. At a shear rate of 4000 $\frac{1}{s}$, the viscosity increased from 3.0 to 50 mPa s for an increasing solid content from 3 to 9 wt%. In both coating techniques, the parameter sets used led to a shear rate, which was in turn accompanied by a viscosity that started to become approximately constant, or at least to a viscosity not in the area of strong exponential decay at low shear rates from 10 to 200 $\frac{1}{s}$.

All of the formulations provided a shear-thinning behavior similar to PVA solutions [53] and MMT dispersions [54]. Without any shear force, the PVA chains were oriented randomly in the lacquer, as were the MMT platelets. As soon as the lacquer is sheared, the chains and platelets start to orient, which results in a decrease in viscosity. This effect became increasingly pronounced with an increasing lacquer solid content, as described by, e.g., Xu et al. [55]. When the majority of chains and platelets were oriented, the viscosity no longer changed significantly. At this shear rate, when the viscosity became nearly constant, the barrier lacquers should be coated. As expected, the viscosity increased with an increasing solid content because fewer water molecules are mobile and more water molecules are part of hydration shells, either from PVOH or from MMT. For the single components of the barrier lacquers, PVA and MMT, it is also true that the viscosity increases with increasing solid content [56,57].

3.5. Roughness

Figure 5 shows the value most commonly used to describe the roughness of coated surfaces (the arithmetic mean value R_a) for the coating parameter sets. The roughness in coating direction did not differ from the perpendicular direction in either coating technique.

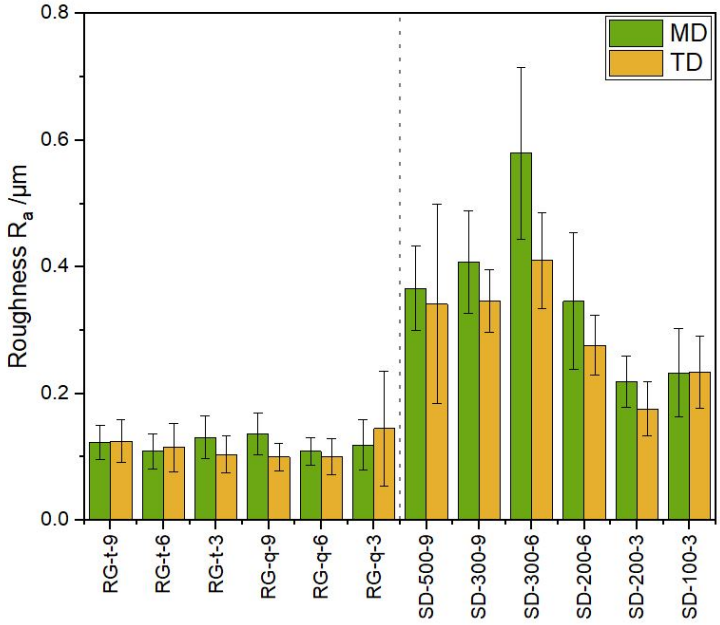

Figure 5. Arithmetic mean values for the roughness of the coated BoPP substrate measured parallel (MD) and perpendicular (TD) to the coating direction.

Regarding reverse gravure coating, the roughness values were all within a range of 0.10 to 0.14 µm. In comparison, slot-die coated samples varied from 0.18 to 0.58 µm, with SD-200-3 being the smoothest at 0.18 µm and SD-300-6 being the roughest at 0.58 µm. Counterintuitively, the roughness values of the reverse-gravure-coated samples were all below the roughness values measured for the slot-die-coated samples. Since the roughness values were similar in the two different gravure geometries and all of the solid contents measured, it can be concluded that the gravure roll type had no direct influence on the roughness for the setups and barrier lacquers used. This outcome stands in contrast to the finding by Voigt et al. [58] for gravure coatings of similar viscous polythiophene but with a different gravure geometry and setup.

The roughness is, among others things, determined by agglomerations on the surface of the coating. Figure 6 shows a comparison of the surface structure of two samples, SD-300-6 and RG-t-9. The surface of the sample SD-300-6 consists of several particles (whitish regions). These particles are MMT agglomerations. Since MMT contains heavier atoms in terms of atomic number compared with PVA, MMT appears brighter in the SEM image. Three reasons can be identified for why the potential for agglomerations during slot-die coating was higher than during reverse gravure coating.

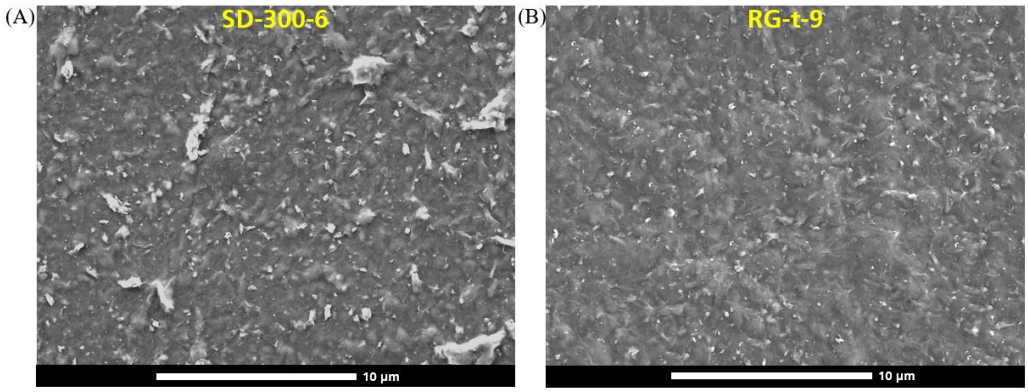

Figure 6. Top view SEM image of the coated substrate with a magnification of 5000: (**A**) SD-300-6 (**B**) RG-t-9.

Since the slot-die coating technique is premetered, any agglomeration formed during lacquer production which is smaller than the filter (mesh size 100 µm) ends up in the coating layer. Additionally, during the slot-die coating process, there are some zones that act as dead volume within the die, for example, in the coating liquid manifold or on the very edges of the die gap. Spontaneously formed agglomerations at these zones also enter the coating. Finally, the agglomerations formed during slot-die coating face lower shear rates within the range of 1190 to 208 $\frac{1}{s}$ than those applied during reverse gravure coating (Figure 4).

In the reverse gravure process, on the other hand, agglomerations formed during barrier lacquer production are not completely transferred to the substrate and also remain in the reservoir. Moreover, the agglomerations transferred by the gravure roll are actually sheared at a higher shear rate of 4000 to 1000 $\frac{1}{s}$ (Figure 4) and reduced in size before coating, or they are blocked via the doctor blade and returned to the reservoir. It was demonstrated earlier with regard to this barrier lacquer that a larger agglomeration quantity results in a lower barrier potential of the barrier lacquer [14], and this phenomenon was further confirmed by the roll-to-roll coatings using two coating techniques.

3.6. Orientation of Montmorillonite Particles in Dry Coating Layer

The commonly held opinion is that the orientation of the platelet-shaped MMT particles has a decisive influence on barrier performance [59]. Therefore, the orientation of the MMT particles in the roll-to-roll-coated samples was investigated via two methods: quantitatively with a pole figure measurement of the (002) lattice plane of MMT and qualitatively with a cross-section SEM image.

Figure 7 shows two pole figures of the (002) lattice plane, measured for a representative slot-die- and reverse-gravure-coated sample. Samples SD-200-3 and RG-t-9 were chosen by virtue of their low permeability coefficient, thereby delivering high oxygen barrier performance (see Section 3.1). The (002) lattice plane describes the parallel plane of an MMT platelet, where the reflection takes place on the next parallel plate. Hence, this lattice plane is used to observe the swelling and separation of the platelets, as well as their orientation [60]. Both pole figures exhibited a high intensity for χ angles from −10 to 10°, as indicated by the red coloring in the center, which corresponds to the (002) tilt angle to the substrate surface. This result revealed that the majority of the particles were oriented more or less parallel to the surface, with a maximum tilt of 10°. Both samples exhibit a diffraction halo for χ from 10 to 30°, as indicated by the color range from yellow to bright blue. This implies that a minority of MMT platelets provides larger tilts than 10°. Based on the pole figure results, it appears that the coating techniques investigated had similar influence on the orientation, since the MMT orientation was comparable. The shear was strong enough to align the particles during both coating processes. On this basis, it can be concluded that complete wetting without defects and a lowest possible amount of agglomerations is required for a high barrier. This is the most reliably achieved for this lacquer in the reverse gravure process, as long as the minimum amount of lacquer is transferred (see Section 3.1).

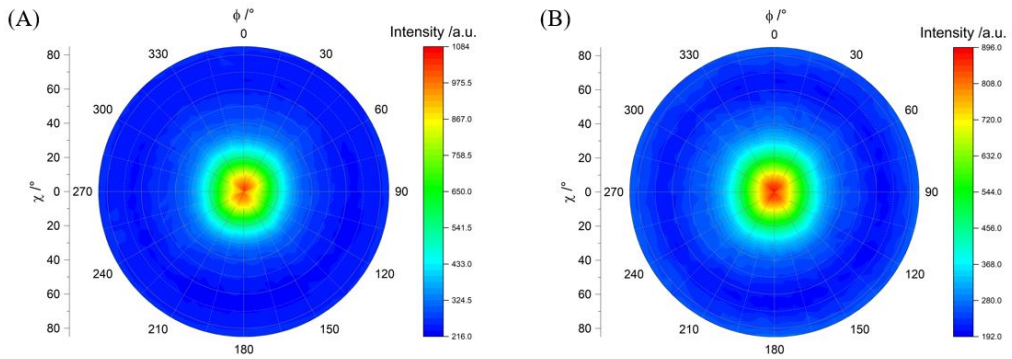

Figure 7. Pole figures of the (002) lattice plane of MMT determined for barrier lacquer coating on (**A**) SD-200-3 and (**B**) RG-t-9.

The SEM cross-section images of the same sample pair (see Figure 8) reveal that the MMT particles are oriented horizontally with respect to the substrate surface, because a dominating direction of the bright lines is recognizable from left to right, i.e., parallel to the surface. However, regions having certain tilt angles are also present, especially around agglomerations, e.g., in SD-200-3. It is important to keep in mind that a cross-section image only represents a small partial section of the whole sample. Therefore, the quantitative measurement with pole figure is more reliable for orientation investigation, because an average of a larger area is evaluated. The cross-section images confirm the findings described in Section 3.5, i.e., that the number of agglomerations is higher in slot-die-coated samples than in reverse-gravure-coated samples. Additionally, the cross-section image demonstrates that the agglomerations are not necessarily located on the surface but also within the layer.

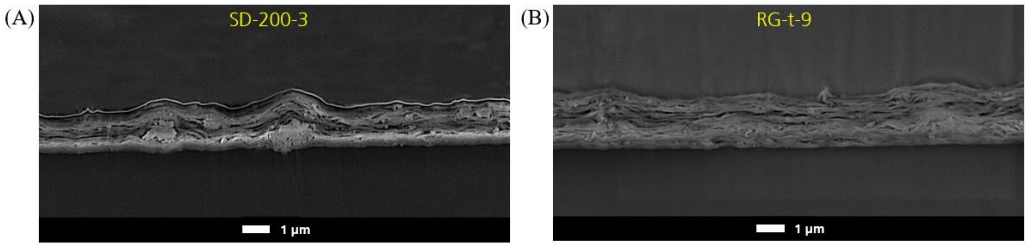

Figure 8. SEM image of cross-sections prepared by Ar polishing with a magnification of 15,000: (**A**) SD-200-3 and (**B**) RG-t-9.

During slot-die coating, the lowest permeation coefficient of 0.14 $\frac{cm^3\,(STP)\,1\,\mu m}{m^2\,d\,bar}$ was obtained for the lacquer with the lowest solid content, BL-3. This lacquer also contained the lowest number of agglomerations, as shown by the roughness measurement in Section 3.5. The higher the solid content, the higher the potential for an agglomeration to build up during lacquer production or within the dead volumes during coating process. An agglomeration disturbs the parallel orientation of platelets to the surface, and the platelets that are agglomerated no longer contribute to the tortuous path effect anymore. Therefore, a low solid content is preferable during the slot-die process in order to minimize the number of agglomerations.

Given that the reverse gravure process is self-metered, another parameter becomes important, i.e., the layer thickness. As shown in Section 3.1, a specific layer thickness at which a completely closed layer is attained is required in order to achieve high oxygen barrier performance. If this layer thickness is reached (e.g., 0.5 µm in the case of RG-t-3), all of the permeability coefficients obtained are below 0.50 $\frac{cm^3\,(STP)\,1\,\mu m}{m^2\,d\,bar}$, regardless of the shear rate. The reverse gravure coating process does not allow big agglomerations to enter the wet coating layer at all, but the agglomerations stay at the reservoir, are blocked by the doctor blade, or are reduced in size. The main factor influencing reverse gravure coating is the (specific) layer thickness, in combination with the viscosity of the lacquer. A lacquer having a high solid content and high viscosity is preferable for the reverse gravure process with the trihelical or quadrangular roll used.

4. Conclusions

This study provides a comparison of two coating techniques, reverse gravure and slot-die, using a roll-to-roll coating line. The focus is on the effecting parameters of the oxygen barrier performance of silicate composite barrier lacquers. The main factors investigated included the effect of the solid content, the reverse gravure geometry, and the shim thickness during the slot-die coating process. The permeability coefficients obtained using twelve different parameter sets were compared with each other.

The viscosity measurements demonstrated that the barrier lacquers comprising PVA and MMT provided shear-thinning behavior. The rheological investigation also showed that the viscosity of the lacquers increases with an increasing solid content. The solid content,

however, has no influence on the surface energy of the lacquers. All barrier lacquers are measured to be similar with a value of 62 $\frac{mJ}{m^2}$. The BoPP substrate was pretreated with corona discharge to be wettable for water-based barrier lacquers. A parameter set was obtained, which enables the achievement of a high oxygen barrier with a low permeability coefficients of 0.12 and 0.14 $\frac{cm^3\,(STP)\,1\,\mu m}{m^2\,d\,bar}$ for both coating processes, reverse gravure and slot-die, respectively. While for the slot-die technique it was shown that low viscous lacquers lead to a high barrier, the opposite was shown for the reverse gravure process.

It was found that the amount of agglomeration in the cured barrier layer, in addition to a defect free coating, has the greatest effect on the barrier. The reverse gravure technique is better suited to reproducibly form a coating layer that has a smooth surface (Figure 5), contains few agglomerations (Figure 6) and, if it is ensured that the dry layer thickness is above 0.5 µm (Table 2), also shows excellent barrier properties (Figure 3). The agglomeration amount during slot-die coating is the lowest when the solid content is 3 wt%, because fewer agglomerations develop during the coating process.

In conclusion, the present research suggests parameter sets for slot-die and reverse gravure coating of a silicate-based composite comprising PVA and MMT. In addition, the findings regarding solid content, viscosity, shear rate, and roughness can also be adopted for other composite materials or coating fluids. One important finding hereby is that it is not simply possible to use the coating formulations of the laboratory scale one by one, but the coating formulation must rather be adapted to suit the roll-to-roll coating process in terms of its properties, e.g., viscosity and solid content. More specifically, for the lacquer comprising MMT and PVA, a high viscosity (70 mPa s) and high solid content (9 wt%) is preferable for the reverse gravure process, whereas a lower viscosity (3.2 mPa s) and a filtered lacquer with a low agglomeration amount and low solid content (3 wt%) is preferable for the slot-die coating technique.

In a future application, these BoPP films after coating with such a silicate composite barrier lacquer would be laminated to a PP sealing film. During the recycling process, these laminates are then shredded, easily separated, and can be recovered by type after the washing process due to the solubility of the lacquer in water.

Author Contributions: Conceptualization, S.S., E.K. and P.E.; methodology, S.S. and E.K.; validation, S.S., E.K. and N.R.; investigation, S.S., E.K. and N.R.; resources, S.S., E.K. and N.R.; writing—original draft preparation, S.S. and E.K.; writing—review and editing, E.K., H.-C.L. and P.E.; supervision, P.E.; funding acquisition, E.K. All authors have read and agreed to the published version of the manuscript.

Funding: This work has received funding from the European Union's Horizon 2020 research and innovation program under grant agreements n°862156 FlexFunction2Sustain project and n°952982 Custom-Art project.

Institutional Review Board Statement: Not applicable.

Data Availability Statement: The data presented in this study are available on request from the corresponding author. The data are not publicly available for reasons of confidentiality in the aforementioned EU projects; see section "Funding".

Conflicts of Interest: The authors declare no conflict of interest.

References

1. Panda, P.K.; Sadeghi, K.; Seo, J. Recent advances in poly (vinyl alcohol)/natural polymer based films for food packaging applications: A review. *Food Packag. Shelf Life* **2022**, *33*, 100904. [CrossRef]
2. Matthews, C.M.; Hufford, A.; Eaton, C. Texas Freeze Triggers Global Plastics Shortage. *Wall Str. J.* **2021**.
3. Hedayati, H.R.; Khorasani, M.; Ahmadi, M.; Ballard, N. Preparation of well-defined Poly(Vinyl alcohol) by hydrolysis of Poly(Vinyl acetate) synthesized by RAFT suspension polymerization. *Polymer* **2022**, *246*, 124674. [CrossRef]
4. Kuraray Co., Ltd. *EVAL^{TM} EVOH Global Price Increase*; Press Release; Kuraray America, Inc. Headquaters: Houston, TX, USA, 2021.
5. Kuraray Co., Ltd. *Price Revisions for EVOH Products EVAL^{TM}*; Press Release; Kuraray America, Inc. Headquaters: Houston, TX, USA, 2022.

6. KunststoffWeb GmbH. *Schur Flexibles: Hohe Sauerstoff-Barriere Ohne EVOH*; Press Release; KunststoffWeb GmbH: Bad Homburg, Germany, 2022.
7. Harmsen, P.F.H.; Hackmann, M.M.; Bos, H.L. Green building blocks for bio-based plastics. *Biofuels Bioprod. Biorefin.* **2014**, *8*, 306–324. [CrossRef]
8. Maes, C.; Luyten, W.; Herremans, G.; Peeters, R.; Carleer, R.; Buntinx, M. Recent Updates on the Barrier Properties of Ethylene Vinyl Alcohol Copolymer (EVOH): A Review. *Polym. Rev.* **2018**, *58*, 209–246. [CrossRef]
9. Grunlan, J.C.; Grigorian, A.; Hamilton, C.B.; Mehrabi, A. Effect of clay concentration on the oxygen permeability and optical properties of a modified poly(vinyl alcohol). *J. Appl. Polym. Sci.* **2004**, *93*, 2–9. [CrossRef]
10. Song, Y.; Gerringer, J.; Qin, S.; Grunlan, J.C. High Oxygen Barrier Thin Film from Aqueous Polymer/Clay Slurry. *Ind. Eng. Chem. Res.* **2018**, *57*, 4–9. [CrossRef]
11. Ben Dhieb, F.; Tabatabaei, S.H.; Mighri, F.; Ajji, A. Comparison of Crosslinking Efficiency in Dip and Roll-Deposited Coatings on Their Oxygen Barrier. *ACS Omega* **2019**, *4*, 772–779. [CrossRef]
12. Dabbaghianamiri, M.; Shazly M.; Duraia, E.; Beall, G.W. Self-assembled Montmorillonite clay-poly vinyl alcohol nanocomposite as a safe and efficient gas barrier. *Results Mater.* **2020**, *7*, 100101. [CrossRef]
13. Meng, X.; Qi, P.; Sun, J.; Li, H.; Zhang, S.; Liu, X.; Gu, X. Fabrication of transparent clay-polymer hybrid coatings on PET film to enhance flame retardancy and oxygen barrier properties. *Prog. Org. Coatings* **2020**, *147*, 105788. [CrossRef]
14. Schiessl, S.; Kucukpinar, E.; Cros, S.; Miesbauer, O.; Langowski, H.C.; Eisner, P. Nanocomposite Coatings Based on Polyvinyl Alcohol and Montmorillonite for High-Barrier Food Packaging. *Front. Nutr.* **2022**, *9*, 790157. [CrossRef]
15. MacDonald, W.A. Latest Advances in Substrates for Flexible Electronics. In *Large Area and Flexible Electronics*; Chapter 10; John Wiley & Sons, Ltd.: Chichester, UK, 2015; pp. 291–314. [CrossRef]
16. Brunetti, F.; Operamolla, A.; Castro-Hermosa, S.; Lucarelli, G.; Manca, V.; Farinola, G.M.; Brown, T.M. Printed Solar Cells and Energy Storage Devices on Paper Substrates. *Adv. Funct. Mater.* **2019**, *29*, 80–98. [CrossRef]
17. Bugnicourt, E.; Brzoska, N.; Kucukpinar, E.; Philippe, S.; Forlin, E.; Bianchin, A.; Schmid, M. Dispersion and Performance of a Nanoclay/Whey Protein Isolate Coating upon its Upscaling as a Novel Ready-to-Use Formulation for Packaging Converters. *Polymers* **2019**, *11*, 1410. [CrossRef] [PubMed]
18. Koppolu, R.; Lahti, J.; Abitbol, T.; Swerin, A.; Kuusipalo, J.; Toivakka, M. Continuous Processing of Nanocellulose and Polylactic Acid into Multilayer Barrier Coatings. *ACS Appl. Mater. Interfaces* **2019**, *11*, 920–927. [CrossRef] [PubMed]
19. Das, P.; Schipmann, S.; Malho, J.M.; Zhu, B.; Klemradt, U.; Walther, A. Facile Access to Large-Scale, Self-Assembled, Nacre-Inspired, High-Performance Materials with Tunable Nanoscale Periodicities. *ACS Appl. Mater. Interfaces* **2013**, *5*, 38–47. [CrossRef]
20. LaChance, A.M.; Hou, Z.; Farooqui, M.M.; Carr, S.A.; Serrano, J.M.; Odendahl, C.E.; Hurley, M.E.; Morrison, T.E.; Kubachka, J.L.; Samuels, N.T.; et al. Doctor-Blade-Assisted Casting for Forming Thin Composite Coatings of Montmorillonite and Poly(vinyl alcohol). *Ind. Eng. Chem. Res.* **2022**, *61*, 3766–3774. [CrossRef]
21. Bauer, A.S.; Tacker, M.; Uysal-Unalan, I.; Cruz, R.M.S.; Varzakas, T.; Krauter, V. Recyclability and Redesign Challenges in Multilayer Flexible Food Packaging—A Review. *Foods* **2021**, *10*, 2702. [CrossRef]
22. Unsbo, H.; Strömberg, E.; Almasi, A.M. *Increasing the Circularity of High Barrier Flexible Plastic Packaging-Results from WP1: Market Analysis*; Technical Report C739; IVL Swedish Environmental Research Institute: Stockholm, Sweden, 2023.
23. Kucukpinar, E. Enhancement of Barrier Performance of Packaging Materials by Nano-Functionalization. In Proceedings of the VVD Meets Freisinger Tage, Freising, Germany, 5–6 February 2020.
24. Türksever, C.; Kizilirmar Esmer, Z. Food Packaging Trends within Sustainable Development. In Proceedings of the 31st International Scientific-Expert Conference of Agriculture and Food Industry, İzmir, Turkey, 27–28 September 2021; p. 87.
25. Mueller, K.; Schoenweitz, C.; Langowski, H.C. Thin Laminate Films for Barrier Packaging Application-Influence of Down Gauging and Substrate Surface Properties on the Permeation Properties. *Packag. Technol. Sci.* **2012**, *25*, 137–148. [CrossRef]
26. Bishop, C.A. 2-Products Using Vacuum Deposited Coatings. In *Vacuum Deposition onto Webs, Films and Foils (Second Edition)*, 2nd ed.; William Andrew Publishing: Oxford, UK, 2011; pp. 13–51. [CrossRef]
27. Ding, X.; Liu, J.; Harris, T.A.L. A review of the operating limits in slot die coating processes. *Aiche J.* **2016**, *62*, 08–24. [CrossRef]
28. Durst, F.; Ray, S.; Ünsal, B.; Bayoumi, O.A. The Development Lengths of Laminar Pipe and Channel Flows. *J. Fluids Eng.* **2005**, *127*, 1154–1160. [CrossRef]
29. Chang, H.M.; Lee, C.C.; Liu, T.J. The Effect of Bead Vacuum on Slot Die Coating. *Int. Polym. Process.* **2009**, *24*, 157–165. [CrossRef]
30. Jakubka, F.; Heyder, M.; Machui, F.; Kaschta, J.; Eggerath, D.; Lövenich, W.; Krebs, F.C.; Brabec, C.J. Determining the coating speed limitations for organic photovoltaic inks. *Sol. Energy Mater. Sol. Cells* **2013**, *109*, 120–125. [CrossRef]
31. Durst, F.; Wagner, H.G. Liquid Film Coating. In *Liquid Film Coating*; Chapter Slot Coating 11a; Springer Science+Business Media: Dordrecht, The Netherlands, 2012; pp. 401–426. [CrossRef]
32. Röhrl, M.; Mettke, J.H.; Rosenfeldt, S.; Schmalz, H.; Mansfeld, U.; Timmins, R.L.; Habel, C.; Breu, J.; Durst, F. Shear orientation of nematic phases of clay nanosheets: Processing of barrier coatings. *J. Coatings Technol. Res.* **2022**, *19*, 487–495. [CrossRef]
33. Shim, E. Smart Textile Coatings and Laminates. In *Smart Textile Coatings and Laminates*, 2nd ed.; Chapter Coating and Laminating Processes and Techniques for Textiles; Woodhead Publishing: Cambridge, UK, 2019; pp. 11–45. [CrossRef]
34. *DIN ISO 8296*; DIN Deutsches Institut für Normung e.V. Plastics-Film and Sheeting-Determination of Wetting Tension. Japanese Industrial Standards Committee: Tokyo, Japan, 2008.

35. Aydemir, C.; Altay, B.N.; Akyol, M. Surface analysis of polymer films for wettability and ink adhesion. *Color Res. Appl.* **2021**, *46*, 489–499. [CrossRef]
36. *DIN 53380-3*; DIN Deutsches Institut für Normung e.V. Determining the Gas Transmission Rate of Plastic Film, Sheeting and Mouldings by the Carrier Gas Method. Japanese Industrial Standards Committee: Tokyo, Japan, 1998.
37. Langowski, H.C. *Food Packaging Materials*; Chapter Shelf Life of Packed Food and Packaging Functionality; CRC Press: Boca Raton, FL, USA, 2017; pp. 11–66. [CrossRef]
38. *ISO 19403-2:2017*; DIN Deutsches Institut für Normung e.V. Paints and Varnishes-Wettability-Part 2: Determination of the Surface Free Energy of Solid Surfaces by Measuring the Contact Angle. DIN-Normenausschuss Beschichtungsstoffe und Beschichtungen (NAB): Berlin, Germany, 2020.
39. Owens, D.K.; Wendt, R. Estimation of the surface free energy of polymers. *J. Appl. Polym. Sci.* **1969**, *13*, 1741–1747. [CrossRef]
40. *ISO 19403-3:2017*; DIN Deutsches Institut für Normung e.V. Paints and Varnishes-Wettability-Part 3: Determination of the Surface Tension of Liquids Using the Pendant Drop Method. DIN-Normenausschuss Beschichtungsstoffe und Beschichtungen (NAB): Berlin, Germany, 2020.
41. Vargaftik, N.B.; Volkov, B.N.; Voljak, L.D. International Tables of the Surface Tension of Water. *J. Phys. Chem. Ref. Data* **1983**, *12*, 817–820. [CrossRef]
42. Chen, T.; Zhao, Y.; Song, S. Comparison of colloidal stability of montmorillonite dispersion in aqueous NaCl solution with in alcohol-water mixture. *Powder Technol.* **2017**, *322*, 378–385. [CrossRef]
43. Nagarkar, R.; Patel, J. Polyvinyl Alcohol: A Comprehensive Study. *Acta Sci. Pharm. Sci.* **2019**, *3*, 34–44.
44. Mittal, K.L. The role of the interface in adhesion phenomena. *Polym. Eng. Sci.* **1977**, *17*, 467–473. [CrossRef]
45. Svendsen, J.R.; Kontogeorgis, G.M.; Kiil, S.; Weinell, C.E.; Grønlund, M. Adhesion between coating layers based on epoxy and silicone. *J. Colloid Interface Sci.* **2007**, *316*, 678–686. [CrossRef]
46. Lindner, M.; Rodler, N.; Jesdinszki, M.; Schmid, M.; Sängerlaub, S. Surface energy of corona treated PP, PE and PET films, its alteration as function of storage time and the effect of various corona dosages on their bond strength after lamination. *J. Appl. Polym. Sci.* **2018**, *135*, 45842. [CrossRef]
47. Prabhu, K.N.; Fernades, P.; Kumar, G. Effect of substrate surface roughness on wetting behaviour of vegetable oils. *Mater. Des.* **2009**, *30*, 297–305. [CrossRef]
48. Paz, E.; Narbón, J.J.; Abenojar, J.; Cledera, M.; del Real, J.C. Influence of Acrylic Adhesive Viscosity and Surface Roughness on the Properties of Adhesive Joint. *J. Adhes.* **2016**, *92*, 877–891. [CrossRef]
49. Creel, E.B.; Tjiptowidjojo, K.; Lee, A.J.; Livingston, K.M.; Schunk, R.P.; Bell, N.S.; Serov, A.; Wood, D.L., III. Slot-die-coating operability windows for polymer electrolyte membrane fuel cell cathode catalyst layers. *J. Colloid Interface Sci.* **2022**, *610*, 474–485. [CrossRef]
50. Bhamidipati, K.L.; Didari, S.; Bedell, P.; Harris, T.A. Wetting phenomena during processing of high-viscosity shear-thinning fluid. *J. Non-Newton. Fluid Mech.* **2011**, *166*, 723–733. [CrossRef]
51. Kornum, L.; Raaschou Nielsen, H. Surface defects in drying paint films. *Prog. Org. Coatings* **1980**, *8*, 275–324. [CrossRef]
52. Benkreira, H.; Cohu, O. Direct forward gravure coating on unsupported web. *Chem. Eng. Sci.* **1998**, *53*, 23–31. [CrossRef]
53. Gao, H.; He, J.; Yang, R.; Yang, L. Characteristic rheological features of high concentration PVA solutions in water with different degrees of polymerization. *J. Appl. Polym. Sci.* **2010**, *116*, 34–41. [CrossRef]
54. Shi, H.; Jiang, G.; Shi, H.; Luo, S. Study on Morphology and Rheological Property of Organoclay Dispersions in Soybean Oil Fatty Acid Ethyl Ester over a Wide Temperature Range. *Acs Omega* **2020**, *5*, 1851–1861. [CrossRef]
55. Xu, J.; Cheng, L.; Zhang, Z.; Zhang, L.; Xiong, C.; Huang, W.; Xie, Y.; Yang, L. Highly exfoliated montmorillonite clay reinforced thermoplastic polyurethane elastomer: In situ preparation and efficient strengthening. *Rsc Adv.* **2019**, *9*, 8184–8196. [CrossRef]
56. Cruz, N.; Peng, Y.; Farrokhpay, S.; Bradshaw, D. Interactions of clay minerals in copper–gold flotation: Part 1—Rheological properties of clay mineral suspensions in the presence of flotation reagents. *Miner. Eng.* **2013**, *50–51*, 30–37. [CrossRef]
57. Vikingsson, L.; Vinals-Guitart, A.; Valera-Martínez, A.; Riera, J.; Vidaurre, A.; Gallego Ferrer, G.; Gomez Ribelles, J.L. Local deformation in a hydrogel induced by an external magnetic field. *J. Mater. Sci.* **2016**, *51*. [CrossRef]
58. Voigt, M.M.; Guite, A.; Chung, D.Y.; Khan, R.U.A.; Campbell, A.J.; Bradley, D.D.C.; Meng, F.; Steinke, J.H.G.; Tierney, S.; McCulloch, I.; et al. Polymer Field-Effect Transistors Fabricated by the Sequential Gravure Printing of Polythiophene, Two Insulator Layers, and a Metal Ink Gate. *Adv. Funct. Mater.* **2010**, *20*, 239–246. [CrossRef]
59. Dunkerley, E.; Schmidt, D. Effects of Composition, Orientation and Temperature on the O_2 Permeability of Model Polymer/Clay Nanocomposites. *Macromolecules* **2010**, *43*, 36–44. [CrossRef]
60. Cornet, I. Expansion of the Montmorillonite Lattice on Hydration. *J. Chem. Phys.* **1950**, *18*, 623–626. [CrossRef]

Surface & Coatings Technology 483 (2024) 130800

Contents lists available at ScienceDirect

Surface & Coatings Technology

journal homepage: www.elsevier.com/locate/surfcoat

Full Length Article

Mechanisms of permeation of helium, hydrogen, oxygen, and water vapor through silicate-based composite barrier coating layers

Stefan Schiessl [a,b,*], Esra Kucukpinar [b], René Schwiddessen [c], Horst-Christian Langowski [a,b], Peter Eisner [a,b]

[a] TUM School of Life Sciences, Technical University of Munich, Alte Akademie 8, 85354 Freising, Germany
[b] Department Material Science, Fraunhofer Institute for Process Engineering and Packaging, Giggenhauser Str. 35, 85354 Freising, Germany
[c] Department of Structure and Dynamics of Energy Materials, Helmholtz-Zentrum Berlin für Materialien und Energie GmbH, Hahn-Meitner-Platz 1, 14109 Berlin, Germany

ARTICLE INFO

Keywords:
Hydrogen permeation
Helium permeation
Oxygen permeation
Barrier composite
Montmorillonite

ABSTRACT

When considering coating of flexible films for the packaging of sensitive products, a common goal is to meet all gas barrier requirements in a single process step. One way to achieve this is to improve the barrier performance of polymeric coating layers by incorporating silicate particles. In order to tailor the gas barrier performance of the coatings, understanding the permeation mechanisms through these composite coating layers is required. In this study, polyethylene terephthalate films were coated with composite lacquers comprising montmorillonite particles and a polymer matrix. The compatibility of montmorillonite with polymer matrices of polypropylene, polyacrylate, polycarboxylic acid, and polyvinyl alcohol was tested. The permeation behavior of helium, hydrogen, oxygen, and water vapor in these coatings was investigated. For a composite coating layer comprising montmorillonite and polyvinyl alcohol at a mixing ratio of 1:1 by weight, barrier improvement factors of 49, 41, and 26 compared with the pure polymer coating were found for helium, hydrogen, and oxygen, respectively. It was shown that the permeability coefficients of composite coating layers decrease with increasing permeant kinetic diameter. A comparison of calculated and measured permeability values indicated that the integration of montmorillonite leads to a tortuous permeation path and changes in the free volume and crystallinity of the polymer matrix. The permeation mechanism for water vapor turned out to be completely different from that for non-polar helium, hydrogen, and oxygen and is determined by the so-called polar path effect.

1. Introduction

Gas permeation is an important topic in several application fields. Packaging materials for foods, cosmetics, healthcare products, and pharmaceutical products are considered to provide specific gas barriers against oxygen, water vapor, and volatile compounds [1]. Organic solar cells and flexible organic field-effect transistors need to be encapsulated with high barrier films against oxygen and water vapor to ensure long-life stability, since the sensitive organic materials degrade in the presence of water or oxygen molecules [2,3]. Hydrogen storage and the associated barrier against hydrogen in mobility or energy storage applications are a long standing topic [4]. Furthermore, newly developed bioelectronic implantable systems need to be protected from harsh environment consisting of biofluids, water-based solutions, and different ions [5]. The helium barrier is rarely a direct requirement, such as when sealing hard drives, as their housings are filled with helium and sealed to reduce friction at high revolution speeds [6]. However, the helium barrier is often determined since this measurement is a rapid, reliable, and commonly used method to characterize the barrier properties of materials [7,8].

There are several technologies for creating a gas barrier on flexible films. These include vacuum processes, i.e. physical and chemical vapor deposition, and atmospheric pressure wet coating processes, i.e. coating with barrier lacquers [9,10]. Even higher gas barriers are reached by combining the aforementioned processes or by increasing the number of coating layers to a layer-by-layer (LbL) assembly [11–14]. An option

* Corresponding author at: Department Material Development, Fraunhofer Institute for Process Engineering and Packaging, Giggenhauser Str. 35, 85354 Freising, Germany.
E-mail address: stefan.schiessl@ivv.fraunhofer.de (S. Schiessl).

https://doi.org/10.1016/j.surfcoat.2024.130800
Received 19 February 2024; Received in revised form 2 April 2024; Accepted 14 April 2024
Available online 18 April 2024

that allows keeping the number of process steps low is to improve barrier coating layers by the integration of impermeable platelet-shaped particles, e.g. montmorillonite (MMT) [15–18].

Such a barrier coating is, for example, polyvinyl alcohol (PVA), which is known for its compatibility with MMT. In a previous study, the authors achieved, for example an oxygen barrier improvement factor of 12 and a helium barrier improvement factor of 17 when 50 wt% MMT with respect to the dry mass was incorporated in PVA coating layers [19]. The improvement factor (see Eq. (11) later) describes the change in permeability of a pure polymer layer on addition of impermeable particles. The addition of MMT to polypropylene (PP) is commonly performed in a melt-mixing step, which limits the amount of MMT to be mixed with PP [20]. Sirousazar et al. [21] found, for example, barrier improvement factors of 1.7 and 2.5 for oxygen and water vapor, respectively, when 10 wt% MMT was added to the PP melt. The barrier of polymer-silicate composites against hydrogen has attracted increasing interest. Conde-Wolter et al. [22] measured, for example, a hydrogen barrier improvement factor of 3.0 from 7.6×10^2 to 2.6×10^2 $\frac{cm^3\,(STP)}{m^2\,d\,bar}$, when 48 wt% carbon fibers were integrated in polycaprolactam thermoplasts and a hydrogen barrier improvement factor of 3.7 from 9.6×10^2 to 2.6×10^2 $\frac{cm^3\,(STP)}{m^2\,d\,bar}$ when 55 wt% carbon fibers are incorporated in polyphthalamide thermoplasts.

In this work, the gas barrier properties and mechanisms of permeation of helium, hydrogen, oxygen, and water vapor through composite coating layers were investigated. When investigating gas permeation through composite barrier layers, it is particularly important to examine the polarity of the permeant and lacquer, the effect of filler content, the interaction between polymer and filler, the effect of the layer thickness, and temperature and humidity at which the measurements are performed. The polymer materials were a PP dispersion, a polyacrylic dispersion (PAD), a polycarboxylic solution (PCS), and a PVA solution in the form of aqueous lacquers. Thus, two dispersions and two solutions varying in polarity were selected. These lacquers were mixed with an MMT dispersion in such a way that composite lacquers with two mixing ratios of polymer:MMT of 3:1 and 1:1 were produced. MMT was selected because of its compatibility to PVA is known to the authors [19,23]. Moreover, MMT is market-available, naturally abundant, and does not disturb recycling processes.

The surface energies of the polymer lacquers and the MMT dispersion were measured in liquid (pendant drop) and dried (sessile drop) states. The comparison of these values provides information on influences on the hydration shell of the MMT particles in the composite mixture. Viscosity measurements were performed for the pure lacquer systems and the mixed composites and the shear-thinning behaviors were compared, indicating interactions between the polymer matrix and the MMT. Fourier-transform infrared (FTIR) spectra were measured for all coating layers, and peak shifts from pure systems to composites were investigated to reveal interactions in the dried state. X-ray measurements of the coating layers were performed to determine the influence of the addition of MMT on the polymer matrix's crystallinity. Pole figures generated from the XRD data were used to evaluate the orientation of the MMT platelets in the coating layers. The barrier improvement due to MMT particles was determined for gases varying in gas kinetic diameter and polarity, i.e. helium, hydrogen, and oxygen, and polar water vapor. Since helium and the other noble gases are the only gases that permeate through polymers at moderate temperatures in atomic form, helium possesses the smallest gas kinetic diameter of 2.60 Å. Hydrogen and oxygen permeate in molecular form and have gas kinetic diameters of 2.89 and 3.46 Å, respectively. The polar water molecule has a gas kinetic diameter of 2.65 Å [24]. For hydrogen and oxygen, the barrier performance was measured at different temperatures, to calculate the activation energy for permeation via the Arrhenius approach. In addition to the measured values, the potential barrier improvement due to MMT particles was calculated according to the tortuous path theory developed by Nielsen [25]. The comparison of measured and calculated values of the permeability coefficients indicates the main influencing factors for the permeation of the respective gases through the composite coating layers.

2. Materials and methods

2.1. Materials

Four different polymer matrix materials, in the form of aqueous lacquers, were used. The first lacquer was a polypropylene dispersion (PP), Aquaseal X2257 from Paramelt (Heerhugowaard, The Netherlands), with a particle size of less than 0.7 µm. It is a milky white liquid stabilized at an alkaline pH value of 10. The second lacquer was a polyacrylic dispersion (PAD), Loctite Liofol HS 59-605 RE from Henkel (Düsseldorf, Germany), with a particle size of less than 0.3 µm. The milky white aqueous dispersion contains a solid content of 44 % and has a slightly alkaline pH value of 8 to 9. The third lacquer was an aqueous solution of modified polycarboxylic acid and a small amount of polyethylenimine (PCS), Epotal BLX 3680 X from BASF (Ludwigshafen am Rhein, Germany). The solution contains 18 wt% solid content, is slightly yellowish, and has a pH value between 8 and 10. The fourth lacquer, Exceval AQ-4104 from Kuraray (Frankfurt, Germany), is mixed from polyvinyl alcohol (PVA) granulate and demineralized water to a targeted solid content. For this study, a solid content of 15 wt% was prepared according to the previously described procedure [19]. It is a transparent solution with a slightly acidic pH value of 5 to 7. Platelet-shaped MMT particles, CLOISITE Na^+, were purchased from BYK Additives and Instruments (Wesel, Germany). Polyethylene terephthalate (PET), HOSTAPHAN®RN23, from Mitsubishi Polyester Film (Wiesbaden, Germany) was used as a transparent substrate film with a thickness of 23 µm. Polytetrafluoroethylene (PTFE) film, used to characterize the dispersive and polar parts of the lacquers' surface energy, had a thickness of 100 µm and was obtained from RCT Reichelt Chemietechnik (Heidelberg, Germany).

2.2. Sample preparation

2.2.1. Lacquer formulation

All composite lacquers were produced in a similar way. The MMT dispersion was prepared with a planetary ball mill as described by Schiessl et al. [19] with a solid content of 5 wt%. Table 1 lists the amounts of polymer lacquer, MMT dispersion, and demineralized water used to mix the lacquers. First, the MMT dispersion was weighed in a beaker together with the demineralized water and homogenized with a magnetic stirrer. Subsequently, the respective amount of polymer lacquer was added via a pipette slowly under constant stirring. The beaker was closed and the composite lacquer was stirred for 10 min. For each polymer matrix, the (diluted) polymer lacquer without MMT particles as reference (ref) and the two composite lacquers with a mixing ratio of 3:1 and 1:1 by weight of polymer solid and MMT solid were prepared. The parameters that were kept constant for all coatings were the mixing ratios and the targeted dry layer thickness of 1 to 3 µm. Some polymer lacquers had to be diluted slightly to reach the required dry layer thickness with the k-bars.

2.2.2. Sheet coating

Before coating, the PET sheets of DIN A4 size were physically pretreated via corona discharge with a dose of 2.9 $\frac{kJ}{m^2}$ applied with a table corona unit from Tigres (Marschacht, Germany) to reach a minimum surface energy of 44 $\frac{mN}{m}$. The prepared lacquers were coated on the sheets with a lab-coating unit, type CUF 5 (Sumet Messtechnik, Denklingen, Germany), using the k-bar technique. The drying was performed for 2.5 min at 90 °C. Since the total solid content of each lacquer was different, k-bars providing different wet layer thicknesses were used to end up with a dry coating thickness between 1 and 3 µm (Fig. S4-S15).

Table 1
Lacquer composition with shares of polymer lacquer, MMT dispersion, and demineralized water leading to respective total solid contents.

sample	mass (polymer lacquer) g	m (MMT dispersion) g	m (water) g	total solid content %
PP-ref	55.6	0.00	94.4	20
PP(3):MMT(1)	20.8	75.0	54.2	10
PP(1):MMT(1)	6.94	75.0	68.1	5.0
PAD-ref	68.2	0.00	81.8	20
PAD(3):MMT(1)	25.6	75.0	49.4	10
PAD(1):MMT(1)	8.52	75.0	66.5	5.0
PCS-ref	83.3	0.00	66.7	10
PCS(3):MMT(1)	31.2	37.5	81.3	5.0
PCS(1):MMT(1)	10.4	37.5	102	2.5
PVA-ref	150	0.00	0.00	15
PVA(3):MMT(1)	37.5	37.5	75.0	10
PVA(1):MMT(1)	25.0	75.0	50.0	5.0

The pure MMT dispersion was coated with an initial solid content of 5 wt% on similarly prepared PET to produce a reference layer (MMT-ref) without polymeric binder.

2.3. Methods

2.3.1. Determination of surface energies of liquid and dried lacquers

The total surface energy of the lacquers γ_l was measured according to DIN EN ISO 19403-3 [26] via the pendant drop method at 23 °C. A requirement for this method is to know the density of the test liquid. Therefore, the density was measured for each liquid using a DSA 100 hydrometer from Kruess (Hamburg, Germany).

The lacquers were placed with a drop volume of 10 to 15 µL on a nearly pure dispersive solid, PTFE, according to the sessile drop method. The contact angle between the lacquers and the PTFE surface was denoted α. The surface energy γ_s of PTFE is 15.2 $\frac{\text{mN}}{\text{m}}$, distributed as a dispersive component of 14.8 $\frac{\text{mN}}{\text{m}}$ and a polar component of 0.4 $\frac{\text{mN}}{\text{m}}$. The dispersive γ_l^d and polar γ_l^p components of the lacquers were calculated according to Eq. (1) and Eq. (2) [27].

$$\gamma_l^d = \frac{\gamma_l \gamma_s (1 + cos(\alpha))}{4\gamma_s - \gamma_l (1 + cos(\alpha))} \tag{1}$$

$$\gamma_l^p = \gamma_l - \gamma_l^d \tag{2}$$

The surface energies of the dried lacquer and of the pure MMT layer were measured according to DIN EN ISO 19403-2 [28] via the sessile drop method. For this purpose, at least five drops of three different liquids, water, ethylene glycol, and diiodomethane, were placed with a drop volume of 3 µL on the surface, and the contact angle was measured at equilibrium.

2.3.2. Fourier transform infrared (FTIR) spectroscopy

The FTIR spectra were measured with a Frontier™FTIR spectrometer L1280034 from PerkinElmer (Shelton, CT, USA) in the ATR (attenuated total reflectance) mode with a diamond crystal. All spectra were baseline corrected. PerkinElmer Spectrum IV Version 10.6.1 software was used to analyze the spectra. A total of 32 scans with a resolution of 2 $\frac{1}{\text{cm}}$ were recorded within a wavenumber range from 4000 to 600 $\frac{1}{\text{cm}}$.

2.3.3. Determination of the viscosity of the lacquer formulations

Rheological measurements were performed in a cone-plate set-up with a 50 mm diameter cone, an angle of 0.995°, and a gap size of 100 µm. The rheometer used was a modular compact rheometer 302 from Anton Paar (Graz, Austria). For each lacquer, a shear sweep measurement was performed from 3 to 3000 $\frac{1}{\text{s}}$ at room temperature (23 °C) with a logarithmically increasing step size limited to 46 measuring points. Threefold measurements were performed for all lacquers and average values with standard deviations are shown in the Figures.

2.3.4. Determination of X-ray diffraction pattern and pole figures

X-ray diffraction (XRD) data were collected with a PANalytical X'Pert Pro MDP X-ray diffractometer (Almelo, The Netherlands) using Cu-K_α radiation (λ = 1.541 84 Å) equipped with an Xe proportional counter in grazing incidence geometry (angle of incidence: 2°).

The pole figures were obtained using a PANalytical X'Pert Pro MRD X-ray diffractometer (Almelo, The Netherlands) equipped with a Eulerian cradle employing two-axis scans along ϕ (rotation) and χ (tilt). Measurements were performed at a fixed 2θ angle of 6°, corresponding to the 2θ angle position of the (001) lattice plane of MMT. To plot pole figures, the intensity distribution was measured along the sample rotation angle ϕ from 0 to 360° at sample tilts χ from −85 to 85° with an increment of 5° each. After averaging the intensity for each rotation angle, the intensity was plotted against the sample tilt χ. From this graph a numerical value describing the orientation degree of the platelet-shaped particles in the coating layer can be calculated as the integral breadth. This value is defined as the ratio of the peak area and the peak height. Taking the integral from 0 to 85° gives the average alignment angle ζ between the MMT platelets and the substrate surface. The alignment angle describes the orientation of the platelets in the coating layer.

2.3.5. Helium permeability coefficients

The helium permeance Q_{He} was measured with a QHV-4 permeameter (Vinci Technologies, Nanterre, France) using a patented protocol [29]. In this measurement device, a mass spectrometer detects an ion current proportional to the permeation rate of the gas. Duplicate determinations were performed at 23 °C and 0 %RH. First, a helium calibrated leak was measured, then the baseline, and finally the helium permeance of the samples. The measurement was completed as soon as the measured permeation rate stayed constant for at least 2 h. For reliable comparability, the helium permeability coefficient P_{meas} of the coating layers was separately calculated for each sample. Therefore, the permeance of the coating layer $Q_{\text{He}}^{\text{coating}}$ was calculated from the measured total permeance of the coated film $Q_{\text{He}}^{\text{total}}$ and the known permeance of the uncoated film $Q_{\text{He}}^{\text{film}}$ (1.3×10^3 $\frac{\text{cm}^3\,(\text{STP})}{\text{m}^2\,\text{d}\,\text{bar}}$) via Eq. (3).

$$Q_{\text{He}}^{\text{coating}} = \frac{Q_{\text{He}}^{\text{film}} \cdot Q_{\text{He}}^{\text{total}}}{Q_{\text{He}}^{\text{film}} - Q_{\text{He}}^{\text{total}}} \tag{3}$$

Then, the helium permeability coefficient P_{meas} of the coated layer was calculated from the permeance $Q_{\text{He}}^{\text{coating}}$ via multiplication with the layer thickness, here in µm. In this case, the unit for P_{meas} was $\frac{\text{cm}^3\,(\text{STP})\,1\,\mu\text{m}}{\text{m}^2\,\text{d}\,\text{bar}}$ [30].

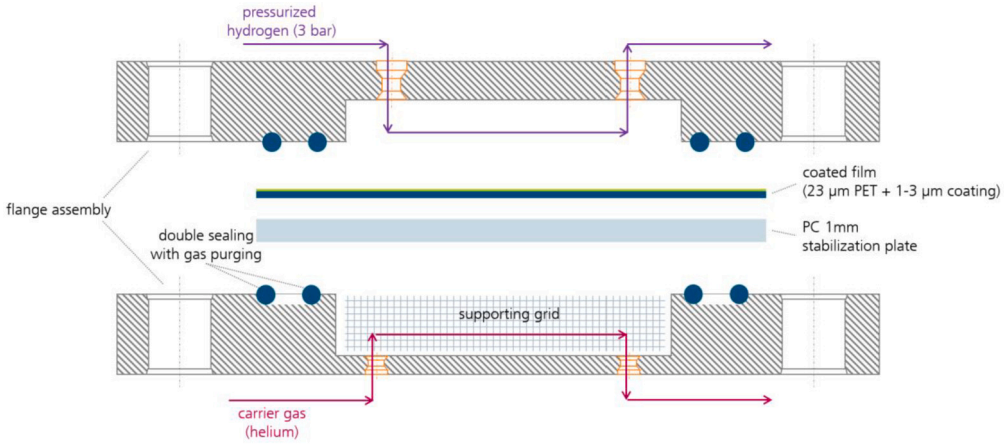

Fig. 1. 2D exploded-view drawing of the measuring cell used to measure hydrogen permeance.

2.3.6. Hydrogen permeability coefficients

The hydrogen permeance Q_{H_2} was measured with the measuring cell shown in Fig. 1. The measurement arrangement between the two cell parts comprised a 1 mm polycarbonate (PC) plate, which was placed on a double sealing ring. On top of the PC plate, a coated PET film was placed. The measuring area, which is the area covered by the inner sealing ring, was 54.45 cm^2. The second part with two sealing rings was fixed with a flange assembly to the first part. In the next step, pressurized hydrogen was conducted to the upper part of the measuring cell. Double sealing with helium gas purging in-between prevented side permeation. Since a total pressure difference of 3 bar was applied between the two chambers, the coated 23 µm thick PET film had to be supported by a 1 mm thick plate made of PC, a stable, but highly hydrogen-permeable material. A supporting grid was also used to prevent deformation of the PC plate. The permeating hydrogen was transported by the helium carrier gas to a mass spectrometer where it was detected. Again, twofold measurements were performed. As the hydrogen permeance of the PC plate $Q_{H_2}^{plate}$ (7.1×10^2 $\frac{cm^3\,(STP)}{m^2\,d\,bar}$) and the PET film $Q_{H_2}^{film}$ (1.8×10^3 $\frac{cm^3\,(STP)}{m^2\,d\,bar}$) are known, the hydrogen permeance of the coating layer can be calculated according to Eq. (4).

$$Q_{H_2}^{coating} = \frac{Q_{H_2}^{film} \cdot Q_{H_2}^{plate} \cdot Q_{H_2}^{total}}{Q_{H_2}^{film} \cdot Q_{H_2}^{plate} - Q_{H_2}^{film} \cdot Q_{H_2}^{total} - Q_{H_2}^{plate} \cdot Q_{H_2}^{total}} \tag{4}$$

Then, the hydrogen permeability coefficients P_{meas} of the different coating layers were calculated via normalization to a layer thickness of 1 µm, using their measured thickness values. The hydrogen permeation was measured at 0 %RH and at 0, 20, 60, and 80 °C to be able to calculate the activation energy E_A via an Arrhenius approach:

$$P_{meas}(T) = P_0 \cdot e^{-\frac{E_A}{RT}} \tag{5}$$

where $P_{meas}(T)$ is the permeability coefficient of the permeating gas at the respective temperature T, P_0 is the pre-exponential factor, and R is the universal gas constant.

2.3.7. Oxygen permeability coefficients

The oxygen permeance of the coated films was measured according to the DIN 53380-3 standard with the oxygen-specific carrier gas method [31]. The measurements were performed using an OX-TRAN 2/21 OTR Analyzer (AMETEK MOCON, Minneapolis, USA) at 20 °C and 0 %RH. Additional measuring temperatures used were 30 and 40 °C, also at a relative humidity of 0 %RH. The measurement was completed when the permeation stayed constant for at least 10 h. Duplicate determinations were performed for all of the coatings. The oxygen permeability coefficient P_{meas} was calculated similarly to the procedure used for helium. The oxygen permeance of the uncoated PET film ($Q_{O_2}^{film}$) was taken as 60.9 $\frac{cm^3\,(STP)}{m^2\,d\,bar}$. The activation energy for oxygen permeation was determined via Arrhenius correlation (Eq. (5)).

2.3.8. Water vapor permeability coefficients

The water vapor permeation rates of the coated films were measured according to the DIN EN ISO 15106-3 standard with the electrolytic detection sensor method [32]. The measurements were performed using an AQUATRAN Model 2 (AMETEK MOCON) at 23 °C and 80 %RH with twofold determinations. The measurement was completed as soon as the measured permeation rate stayed constant for at least 10 h. The water vapor permeability coefficient P_{meas} was calculated similarly to the procedure used for the other gases using the water vapor transmission rate of uncoated PET (8.4 $\frac{g\,(STP)}{m^2\,d}$) at 23 °C and 80 %RH.

2.3.9. Calculation of barrier improvement factor by particle integration

The theoretical barrier values were calculated according to the tortuous path approach for platelet-shaped particles. This approach was developed by Nielsen [25] and describes the barrier improvement of composites through the integration of impermeable platelets in the barrier layer. The elongation of the diffusion path is described by the tortuosity factor τ_{orig}:

$$\tau_{orig} = 1 + \frac{L}{2W} \cdot \eta_{MMT} \tag{6}$$

The aspect ratio of the MMT, i.e. the ratio of particle length L to particle thickness W, and the volume ratio of the silicate particles η_{MMT} define the tortuosity factor. In order to include the particle orientation in Nielsen's equation, Bharadwaj [33] suggested adding an order parameter S, leading to a modified tortuosity factor τ_{mod}. To obtain S, the average angle ζ between the particle plane and the substrate surface was determined as described in Section 2.3.4 from the pole figures of the composites:

$$S = \frac{1}{2} \cdot \left(3 \cdot \cos^2 \zeta - 1\right) \tag{7}$$

An order parameter of 1 ($\zeta = 0$) indicates a perfect perpendicular orientation. With the incorporation of S the tortuosity factor becomes:

$$\tau_{mod} = 1 + \frac{L}{2W} \cdot \eta_{MMT} \cdot \frac{2}{3} \cdot \left(S + \frac{1}{2}\right) \tag{8}$$

A further enhancement of Nielsen's equation, the squaring of the tortuosity factor, was suggested by Shen and Chen [34]. This leads to the following equation to calculate the theoretical permeability coefficients P_{cal} of the composites:

$$P_{cal} = \left(\frac{1 - \eta_{MMT}}{\left(1 + \frac{L}{2W} \cdot \eta_{MMT} \cdot \frac{2}{3} \cdot (S + \frac{1}{2})\right)^2} \right) \cdot P_{meas}^{ref} \tag{9}$$

Table 2
Density and surface energy with shares of polar and dispersive parts of the investigated polymer lacquers and the MMT dispersion before the mixing to produce composite lacquers. Water was included from Janczuk et al. [35] as a reference.

sample	density $\frac{g}{cm^3}$	surface energy $\frac{mN}{m}$	dispersive part	polar part
water	0.997	73	22	51
MMT-ref	1.032	68±0.8	41±0.6	27±0.2
PP-ref	0.949	52±0.4	38±0.2	14±0.2
PAD-ref	1.039	37±0.3	31±0.2	6.4±0.1
PCS-ref	1.041	68±0.4	34±0.2	35±0.2
PVA-ref	1.034	64±0.3	41±0.2	21±0.1

Here P^{ref}_{meas} are the measured permeability coefficients of the reference coating layers without particles. The values for L (494 nm) and W (25 nm) were taken from previous studies of the authors [19]. The volume ratio of the MMT particles with a density of 2.86 $\frac{g}{cm^3}$ is 12 vol% for 3:1 and 29 vol% for 1:1 mixing ratios. The measured (P_{meas}) and calculated (P_{cal}) permeability coefficients were compared according to:

$$\Delta = \left(\frac{P_{cal} - P_{meas}}{P_{cal}} \right) \tag{10}$$

If the value of the deviation Δ is positive, the measured value is lower than the calculated value, and vice versa. To evaluate the effect of the MMT particles on the barrier performance quantitatively, the barrier improvement factor BIF was used.

$$BIF = \frac{P^{ref}_{meas}}{P^{comp}_{meas}} \tag{11}$$

Here P^{comp}_{meas} is the measured permeability coefficient of the composite coating layers.

3. Results and discussion

3.1. Surface energies of coating liquids and dried coating surfaces

Table 2 shows the density and the surface energy, separated into dispersive and polar parts, of the polymer lacquers and the MMT dispersion before mixing to produce the composite lacquers. The total surface energy of the pure MMT dispersion having a solid content of 5 wt% was 68 $\frac{mN}{m}$. This value was in a similar range to the values for the polycarboxylic solution (PCS) and the polyvinyl alcohol solution (PVA) having surface energies of 68 and 64 $\frac{mN}{m}$, respectively. The polypropylene dispersion (PP) and the polyacrylic dispersion (PAD) provided lower values of 52 and 37 $\frac{mN}{m}$, respectively. Similar tendencies are valid for the polar parts.

When MMT is exfoliated in water, a hydration shell is built around the platelets, leading to swelling and further exfoliation of the particles [36]. This hydration shell is very sensitive to changes in the surface energy of the liquid [37]. It is therefore advantageous to mix liquids whose surface energy values differ as little as possible [38]. This difference between the surface energies of the lacquers and the MMT dispersion is lower for both PCS and PVA, whereas PP and PAD vary distinctly in total surface energy as well as in the polar part. PAD contained, for example, up to 2.5 wt% alcohols, which was the reason why the total surface energy was lower than that for a purely water-based system. For ethanol, Habib et al. [39] have shown that it displaces the hydration shell of MMT in the liquid state, which can cause re-agglomeration.

Before drying the composite lacquers, it is required to preserve the hydration shell around the MMT particles in order to maintain a homogeneous dispersion. During drying, the interaction of the polymer matrix and MMT becomes increasingly important since the water molecules evaporate and the hydration shells disappear [16]. Also in the dried state, it was again the case that PCS and PVA provided higher surface energies and also higher polarity parts than PP and PAD (Table 3). This indicates the potential for a stronger attraction between MMT and PCS or PVA.

Table 3
Surface energies of dispersive and polar components of the dried reference polymer and montmorillonite coating layers measured by the sessile drop method.

sample	surface energy	dispersive part	polar part
		$\frac{mN}{m}$	
MMT-ref	58±0.9	30±0.3	29±0.6
PP-ref	18±1.6	17±1.2	0.8±0.4
PAD-ref	31±1.2	31±1.2	0.1±0.0
PCS-ref	44±0.7	35±0.2	9.6±0.5
PVA-ref	43±1.0	39±0.6	4.2±0.4

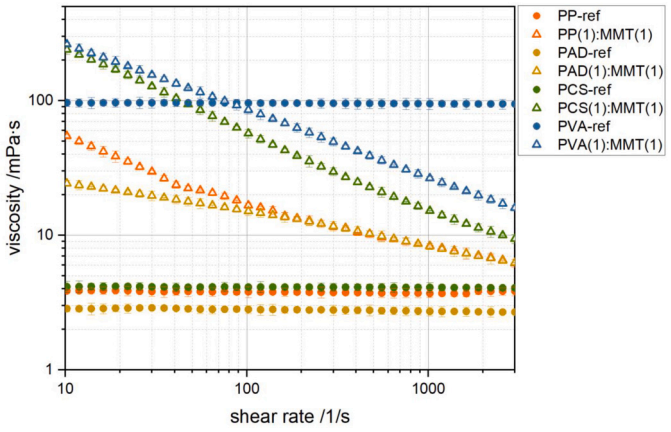

Fig. 2. Viscosity measurement of the polymer and composite lacquers with a mixing ratio of 1:1 as a function of shear rate.

3.2. Rheological investigation

Fig. 2 shows the viscosity of the polymer lacquers and composite lacquers with a mixing ratio of 1:1 by weight as a function of shear rate. When MMT is mixed into the polymer lacquers, the viscosities increase and the composite lacquers exhibit the shear-thinning behavior known for pure MMT dispersions [23,40]. The greater the shear-thinning, the stronger is the interaction between MMT and the polymer matrix [40].

The pure lacquers showed Newtonian behavior at the respective solid contents and measured shear rates. The viscosity increase due to the addition of MMT particles was much more pronounced for PCS (from 4.1 to 36 mPa s) than for PP (from 3.7 to 11 mPa s) or PAD (from 2.8 to 11 mPa s) at a shear rate of 10 $\frac{1}{s}$. The value of 47 mPa s at the same shear rate for PVA(1):MMT(1) also showed a distinct increase due to the addition of MMT. The slope indicates the shear-thinning effect. In this case, the strongest interaction between MMT and the polymer matrix was observed for PCS and PVA.

Similar measurements were carried out for the composite lacquers with a mixing ratio of 3:1 and confirmed this result (Fig. S1).

3.3. Fourier transform infrared spectroscopy

FTIR spectra were measured to examine interactions of polymer matrix material and MMT by identifying single peak shifts. According to Ellerbrock et al. [41], an unshifted peak in the composite spectra needs to be identified when analyzing peak shifts to eliminate the possibility of the whole curve being shifted. As shown in Table 4, every composite exhibits unshifted peaks of MMT and the polymer matrix.

Fig. 3 shows the FTIR spectra of the polymer (PP (A) and PAD (B)) layers, their composites with a mixing ratio of 1:1, and the MMT coating. No peak shifts were observed for composites comprising MMT and

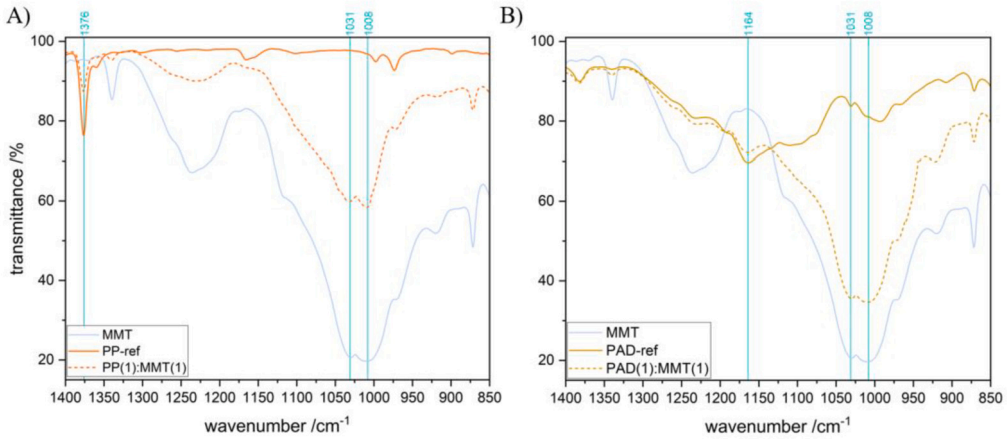

Fig. 3. FTIR spectra of montmorillonite, (A) PP-based and (B) PAD-based composites with a 1:1 mixing ratio of polymer and montmorillonite, and polymer coating layers zoomed in on the range from 1400 to 850 $\frac{1}{cm}$. The total spectrum in the range from 4000 to 600 $\frac{1}{cm}$ is shown in Fig. S2. The turquoise lines represent the unshifted bands indicating no interaction of MMT and polymer.

Table 4
Peak maxima with respective assignments of the polymer matrix materials used and the pure MMT coating layer. Peak shifts appearing in composites with a mixing ratio of 1:1 are assigned.

Material	Maxima ($\frac{1}{cm}$)	Assignment	Peak shift in composite
MMT [42]	3624	-OH stretching, Al-OH in octahedral sheets	no shift
	3425	-OH stretching, absorbed interlayer water	no shift
	1635	-OH bending, absorbed interlayer water	no shift
	1031	-Si-O stretching, Si-O-Si in tetrahedral sheets	blue-shift to 1041 $\frac{1}{cm}$ in PCS(1):MMT(1)
			blue-shift to 1037 $\frac{1}{cm}$ in PVA(1):MMT(1)
	1008	-Si-O stretching, Si-O-Si in tetrahedral sheets	blue-shift to 1018 $\frac{1}{cm}$ in PCS(1):MMT(1)
			blue-shift to 1016 $\frac{1}{cm}$ in PVA(1):MMT(1)
PP [43]	2950, 2867	-CH_3 stretching	no shift
	2919, 2840	-CH_2 stretching	no shift
	1457	-CH_2 bending	no shift
	1376	-CH_3 bending	no shift
PAD [44]	2922, 2849	-CH_2 stretching	no shift
	1730	-C=O stretching	no shift
	1164	-C-O stretching	no shift
PCS [45]	2942, 2832	-CH_2 stretching	no shift
	1713	-C=O stretching	red-shift to 1705 $\frac{1}{cm}$ in PCS(1):MMT(1)
	1092	-C-O stretching	red-shift to 1072 $\frac{1}{cm}$ in PCS(1):MMT(1)
PVA [46]	2933, 2910	-CH_2 stretching	no shift
	1709	-C=O stretching	no shift
	1085	-OH bending	red-shift to 1061 $\frac{1}{cm}$ in PVA(1):MMT(1)

PP. These peaks at 1457 and 1376 $\frac{1}{cm}$ for PP and at 3624 and 1031 $\frac{1}{cm}$ for MMT are similar to those identified previously for PP and MMT based barrier coating layers [47–49]. PP does not provide any functional group with which an interaction with MMT might be possible.

For PAD-based composites, no peak shifts were observed. Compared with PP, an interaction with PAD would be possible in the form of hydrogen bonds with the carbonyl or the ether group of the acrylate. However, these bands stayed unshifted, which indicates that these functional groups are not accessible for interaction with the MMT. Ianchis et al. [50] also observed no peak shifts for composite coating layers with non-modified MMT and polyacrylates.

Fig. 4 shows the FTIR spectra of the polymer layers (PCS (A) and PVA (B)), their composites with a mixing ratio of 1:1, and the MMT coating layer. Peak shifts were identified for both composites. The -C-O stretching band from the carboxylic acid exhibited a red shift when mixed with MMT, as also observed by Smith [51]. Similar red shifts for the -C-O stretching band of the carboxyl group have also been found by Lai et al. [52], Natkański et al. [53], and Yu et al. [54] in composites of polycarboxylic acid and MMT. In addition, the band of the Si-O stretching vibration in MMT showed a blue shift. These peak shifts indicate an interaction of the Si-O group from the Si-tetrahedral layer of MMT with the hydroxy group from the carboxyl group of the carboxylic acid, most likely via hydrogen bonds [55,56].

Similarly to PCS, for PVA composites band shifts also appear for O-H bending and Si-O stretching vibrations of MMT, shown by red and blue colors, respectively. This kind of red shift for the hydroxy group in PVA was also observed by Spoljaric et al. [57] for composites comprising PVA and MMT.

3.4. Pole figures

Fig. 5 shows the average intensity of the MMT 001 peak as a function of tilt angle for the MMT-ref sample and the composite coatings with a mixing ratio of 1:1 based on the pole figure measurements.

The peak shape and position indicate the orientation of the silicate platelets in the coating layer. All peaks provide their maximum at 0°, which suggests that the average orientation is parallel to the surface. The narrower the peak is, the more particles are oriented parallel to

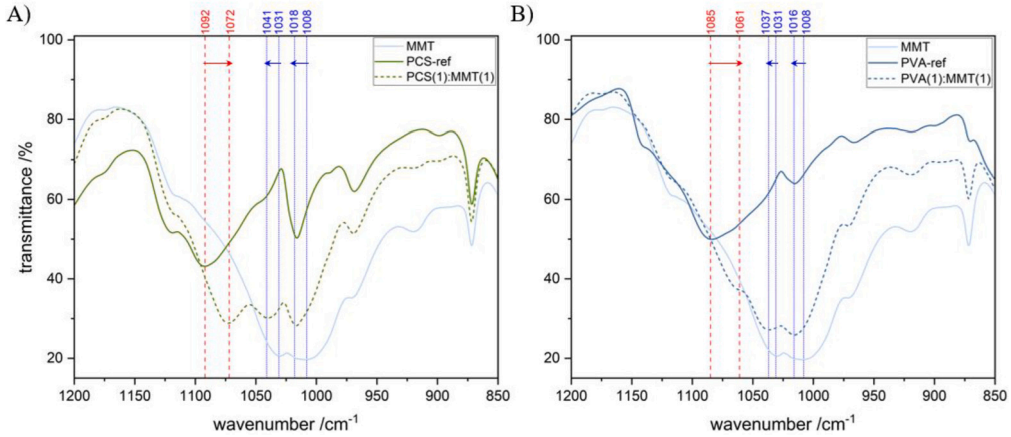

Fig. 4. FTIR spectra of montmorillonite, (A) PCS-based and (B) PVA-based composites with a 1:1 mixing ratio of polymer and montmorillonite, and polymer coating layers zoomed in on the range from 1200 to 850 $\frac{1}{\text{cm}}$. The total spectrum in the range from 4000 to 600 $\frac{1}{\text{cm}}$ is shown in Fig. S3. The red and blue represent peak shifts indicating interaction between MMT and the polymer.

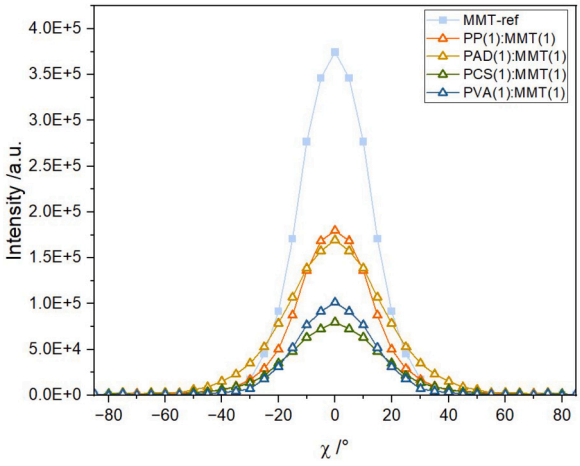

Fig. 5. Average intensity over all rotation angles ϕ from 0 to 360° plotted against the tilt angle χ for the MMT-ref samples and composite coatings with a mixing ratio of 1:1. The underlying pole figures are shown in Figs. S16-S19.

Table 5
Calculated integral breadth and alignment angle for the MMT-ref sample and all composite coatings with mixing ratios of 1:1 and 1:3.

sample	integral breadth	alignment angle ζ (°)
MMT-ref	30	8.32
PP(3):MMT(1)	39	18.4
PP(1):MMT(1)	37	17.7
PAD(3):MMT(1)	45	23.2
PAD(1):MMT(1)	41	20.4
PCS(3):MMT(1)	35	14.2
PCS(1):MMT(1)	34	14.0
PVA(3):MMT(1)	33	11.5
PVA(1):MMT(1)	33	10.6

the substrate surface since the measurement signals indicate the (001) lattice plane, which is the plane perpendicular to the area of the plate. The numerical value describing the peak width is the integral breadth listed in Table 5. The smaller the integral breadth is, the more particles are aligned parallel to the surface.

The particles in the MMT-ref coating layer were aligned the most parallel, followed by the PVA- and PCS-based composite coatings. The orientation became less parallel for PP-based coatings and coating layers based on PAD provided the most heterogeneous alignment.

When coating the pure MMT dispersion, the water molecules do not disturb the platelets from their physically driven behavior to lie parallel to the surface when the solid content of the dispersion is low enough [58]. The shearing during coating even forces the particles to orient parallel to the surface. Adding a polymer as a third ingredient to the lacquer, in addition to MMT and water, impeded the orientation of the platelets. As the PP and PAD lacquers are dispersions, the polymer chains are not dissolved in water, but the polymers are distributed in spherical form and only liquefy during the coating and drying process. The spherical shape of these polymers in water and the fact that particle liquefaction only takes place after shearing could be a reason why the orientation of the particles in PP and PAD was less parallel, as the polymer spheres act as obstacles during application of the coating (Fig. S7-S9). PCS and PVA are solutions, i.e., the polymer chains are completely dissolved in water and embedded between the MMT particles during the coating. This matches on the one hand the steeper slopes of PCS- and PVA-based composites in the viscosity measurements (Fig. 2), which indicate a more pronounced interaction due to the stronger shear-thinning effect. On the other hand, it matches the findings of peak shift investigations in Section 3.3: the interaction of MMT with the polymers, PCS and PVA. A similar investigation, confirming the results, was performed for composite coating layers with mixing ratios of 3:1 (Figs. S16-S20).

The pole figures were also used to determine the alignment angle ζ, which was used to calculate the order parameter S according to Eq. (7). Fig. 6 shows the influence of the alignment angle on the modified tortuosity factor. A change in the particle volume fraction affects the tortuosity more than the alignment angle. The orientation in the investigated composites varies within a range of only 10.6 to 23.2°, leading to a small effect on the tortuosity factor and therefore the permeability coefficients.

3.5. Helium barrier

Fig. 7A shows the values for the helium permeability coefficients of the coating layers.

P_{meas} for helium of the PP-ref sample was 3.7×10^4 $\frac{\text{cm}^3\,(\text{STP})\,1\,\mu\text{m}}{\text{m}^2\,\text{d}\,\text{bar}}$ and decreased to 1.7×10^3 $\frac{\text{cm}^3\,(\text{STP})\,1\,\mu\text{m}}{\text{m}^2\,\text{d}\,\text{bar}}$ when mixed with 50 wt% MMT. This corresponds to a BIF of 21. It has been shown previously that the helium permeability of PP can be reduced by the addition MMT [59,60]. In these previous studies, the MMT was added to PP melt, which is why the amount of MMT was limited to 6 wt%. Hence the BIFs obtained were below 2. The addition of MMT to the aqueous PP dispersion in this study allowed an MMT content of up to 50 wt% in the composite barrier layers. This system was examined for the first time to the best

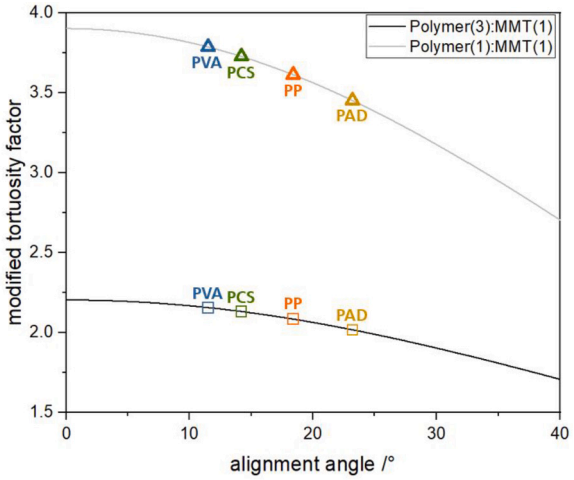

Fig. 6. The black and gray lines show the values of the modified tortuosity factor τ_{mod} calculated according to Eq. (8) for alignment angles ζ from 0 to 40°. The measured alignment angles for the investigated composites from Table 5 are marked for the respective polymer matrices.

of the authors' knowledge. The calculated permeability coefficient P_{cal} according to Eq. (9) was 2.0×10^3 $\frac{cm^3\,(STP)\,1\,\mu m}{m^2\,d\,bar}$. The 11 % deviation between the calculated and the experimentally measured values according to Eq. (10) for PP(1):MMT(1) indicates that the composite performed better than predicted. The calculation used only takes geometrical parameters (such as orientation, particle volume ratio, and aspect ratio) into account and differences in the polymer matrix possibly induced by the MMT are not considered. These differences might be changes in the free volume of the polymer matrix or variations in the crystallinity of the polymer, for example. The XRD pattern (Fig. S21A) of PP-ref and PP(1):MMT(1) showed no distinct variation in the crystallinity of PP due to the addition of MMT. The integration of MMT in the PP matrix might have reduced the free volume slightly in PP and therefore reduced the helium permeation in addition to the tortuosity. The phenomenon of free volume reduction in PP matrix systems on addition of MMT was also observed by Hu et al. [61].

The composites with the PAD matrix showed low BIFs. Since the orientation factors of the MMT in PP and PAD did not differ substantially, the BIFs could be expected to be in the same range. The fact that this is not the case proves that not only the addition of MMT, but also the interaction of MMT with the matrix, the homogeneous distribution, and the influence of the particles on the polymer matrix are important to consider. The calculated P_{cal} for the 1:1 mixture with PAD (8.9×10^2 $\frac{cm^3\,(STP)\,1\,\mu m}{m^2\,d\,bar}$) deviated considerably from the measured P_{meas} (3.3×10^3 $\frac{cm^3\,(STP)\,1\,\mu m}{m^2\,d\,bar}$) with a value of −272 %. The fact that the deviation is negative implies that the particles did not exert their full potential for the He barrier enhancement of the PAD matrix. It is more likely that the particles re-agglomerate when mixed with PAD since the surface energies of PAD lacquer and MMT dispersion differed, as discussed in Section 3.1. From an energetic point of view, a re-agglomeration of particles appears to be favorable in PAD, since neither the viscosity values of its composite lacquers nor the FTIR spectra of the dried composite coating layers indicate an interaction between the two materials. The XRD pattern (Fig. S21B) revealed an increased crystallinity of PAD in the composite coating layers since peaks appear in the range from 10 to 25° compared with PAD-ref. An increase in crystallinity leads to an increase in gas barrier [62]. However, it seems that the re-agglomeration of particles outperformed the increase in crystallinity with respect to barrier properties.

P_{meas} for helium of the PCS-ref sample was measured as 3.7×10^2 $\frac{cm^3\,(STP)\,1\,\mu m}{m^2\,d\,bar}$, which decreased to 7.8 $\frac{cm^3\,(STP)\,1\,\mu m}{m^2\,d\,bar}$ when 50 wt% MMT was added. This corresponds to a barrier improvement factor of 47. Tzeng et al. [63] reported a helium permeance of 4.1 $\frac{cm^3\,(STP)}{m^2\,d\,bar}$ for 10 alternating layers of polyethylenimine, poly(acrylic acid), and MMT with a total layer thickness of 1.6 µm. Herrera-Alonso et al. [64] investigated composites of polybutylmethacrylate with MMT and obtained a BIF of 1.3 for helium with an MMT content of 5 wt%. The higher MMT content is one reason for the higher BIFs in this study. The aqueous lacquers used made it possible to dilute the mixture and thus keep the viscosity in a processable range, even with MMT-rich mixing ratios such as 1:1. The reason for the positive deviation of 58 % from the calculated (1.9×10^1 $\frac{cm^3\,(STP)\,1\,\mu m}{m^2\,d\,bar}$) to the measured (7.9 $\frac{cm^3\,(STP)\,1\,\mu m}{m^2\,d\,bar}$) values for PCS(1):MMT(1) is changes in the polymer matrix. The results reported in Sections 3.1 and 3.3 indicate an interaction between the PCS matrix and the MMT which may have led to a reduced free volume and therefore a better barrier. Additionally, the integration of MMT increased the crystallinity of the PCS matrix (Fig. S22A), which also should lead to an improvement in its gas barrier.

The findings for PVA-based composites are very similar to those for PCS-based composites. The BIFs of 12 and 49 for 3:1 and 1:1 mixing ratios, respectively, were in the same range as for PCS. The PVA molecule also has an accessible hydroxy group that interacts with the Si-O group from the MMT's silicate tetrahedra via hydrogen bonds, similarly to the carboxylic acid's functional group of PCS. That this interaction occurred was concluded from the FTIR spectra in Fig. 4. The XRD pattern (Fig. S22B) indicated also for PVA an increase in crystallinity due to the integration of MMT. Barrier layers of composites comprising PVA and MMT have been well investigated for barrier applications owing to their good compatibility [19,65–67]. A very low P_{meas} of 8.0×10^{-1} $\frac{cm^3\,(STP)\,1\,\mu m}{m^2\,d\,bar}$ was reported by Habel et al. [68] for composite coating layers comprising PVA and synthetic clay sodium fluorohectorite particles applied with multiple layer spray coating. In previous studies, the authors reported a BIF of 17 for a coating layer with a similar composition of 1:1 on oriented PP substrate film [19]. The reason for the observed difference in the BIFs for the same coating lies in the substrate film. The PET used in this study is thermally and mechanically more robust than PP and induces lower stress in the coating layer.

3.6. Hydrogen barrier

The general trends found for helium permeation were also valid for hydrogen permeation, as shown in Fig. 7B. The deviations from the calculated values were positive for PP-, PCS-, and PVA-based coatings and negative for PAD-based coatings for similar reasons. The BIFs for composite coating layers with a 3:1 mixing ratio were constantly lower than the BIFs for coating layers with a 1:1 mixing ratio. The highest BIFs were reached for PCS(1):MMT(1) and PVA(1):MMT(1) with values of 37 and 41, respectively.

Comparing the measured hydrogen and helium permeability coefficients shows the trend that the values of P_{meas} for hydrogen were slightly lower than those for helium. The reason for this is that the helium atom is smaller than the hydrogen molecule in terms of the gas kinetic diameter, while both gases are non-polar [24]. Smaller permeating particles find more permeation paths, therefore the value for the permeability coefficient is higher (Fig. 9). Consequently, the BIFs measured for helium were slightly higher than those for hydrogen, because the generation of an obstacle to permeation, an MMT particle, has a greater influence for smaller permeants.

The permeation of hydrogen through silicate-based composites was investigated previously. Tzeng et al. [63] reported a hydrogen permeance of 3.7 $\frac{cm^3\,(STP)}{m^2\,d\,bar}$ for 10 alternating layers of polyethyleneimine, poly(acrylic acid), and MMT with a total layer thickness of 1.6 µm. In comparison, a value of 9.3×10^{-1} $\frac{cm^3\,(STP)\,1\,\mu m}{m^2\,d\,bar}$ was obtained with a one-time coating in this study with PCS(1):MMT(1). A very low P_{meas} of 6.0×10^{-1} $\frac{cm^3\,(STP)\,1\,\mu m}{m^2\,d\,bar}$ was reported by Habel et al. [68] for composite

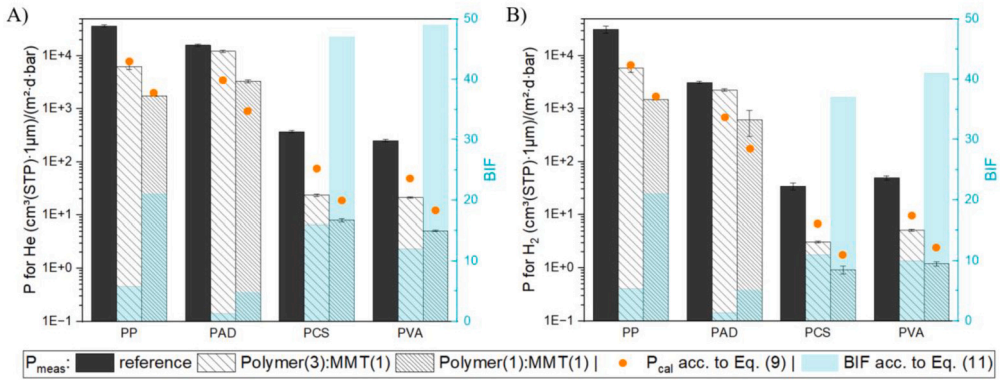

Fig. 7. Helium (A) and hydrogen (B) permeability coefficients of the coating layers of the four different polymer matrices (PP, PAD, PCS, and PVA) and their composites with mixing ratios of 3:1 and 1:1 with MMT. The measurement conditions for helium and hydrogen permeability were 23 °C/0 %RH and 20 °C/0 %RH, respectively. The orange dots represent the P_{cal} values according to Eq. (9). The transparent blue bars show the barrier improvement factors (BIFs) for the respective mixing ratio according to Eq. (11) (right y-axis).

Table 6
Activation energies for hydrogen and oxygen permeation of the reference and composite coating layers. The respective Arrhenius plots are shown in Figs. S23 to S26.

sample	hydrogen $\frac{kJ}{mol}$	oxygen
PP-ref	30.4	30.7
PP(3):MMT(1)	30.9	30.2
PP(1):MMT(1)	29.9	30.2
PAD-ref	21.6	30.5
PAD(3):MMT(1)	23.1	29.7
PAD(1):MMT(1)	24.4	28.6
PCS-ref	42.2	29.3
PCS(3):MMT(1)	39.3	24.5
PCS(1):MMT(1)	36.8	20.6
PVA-ref	47.5	56.5
PVA(3):MMT(1)	45.1	49.8
PVA(1):MMT(1)	39.5	45.8

layers comprising PVA and synthetic clay sodium fluorohectorite particles applied with multiple layer spray coating. The lowest permeability coefficient for hydrogen measured for a single-layer PVA-based composite was 1.2 $\frac{cm^3\,(STP)\,1\,\mu m}{m^2\,d\,bar}$ in their study. Kim et al. [69] recently published a hydrogen permeance of 6.5×10^{-3} $\frac{cm^3\,(STP)}{m^2\,d\,bar}$ at 23 °C for a composite coating comprising MMT and polyvinylpyrrolidone (PVP). The coating with a composition of 63 wt% MMT and 37 wt% PVP was applied on a nylon substrate at a layer thickness of 60 µm. The 63 wt% MMT concentration and the coating layer thickness are the reasons for its higher barrier performance.

In addition to the measurements at 20 °C, the permeation of hydrogen was measured at 0, 60, and 80 °C to calculate the activation energy for permeation according to Eq. (5) (Table 6). The Arrhenius plots for hydrogen and oxygen are linear, indicating no structural changes occurring in the composites, such as hydrogenation or oxidation possibly induced by these gases [70]. It is notable that the activation energy for permeation hardly changed for the two polymer matrices, PP and PAD, with the addition of MMT. For the two polymer matrices, PCS and PVA, where an interaction with MMT was observed, the values of E_A decreased with increasing MMT content.

Kim and Lin [71] have shown that a change in E_A indicates a change in the permeation mechanism. The mechanism of permeation through a pure polymer coating is considered linear and determined by the properties of the polymer matrix [25]. The addition of MMT to the polymer changes the matrix in such a way that boundary areas between MMT and the polymer are created. Erlat et al. [72] showed that the permeation mechanism of gases might occur along these boundary areas, which are not as dense as in the bulk of the matrix because of the shown interaction between MMT and the polymer matrix. The fact that a reduced E_A is measured for the samples with the lowest permeation coefficient indicates that the tortuosity has more influence on the permeation coefficient than changes in the polymer matrix.

3.7. Oxygen barrier

The results for P_{meas} for oxygen followed the trends that were observed for helium and hydrogen permeation (Fig. 8A). The BIFs for a 3:1 mixing ratio were constantly lower than those for a 1:1 mixing ratio. The deviations of the measured values from the calculated values according to Eq. (10) were positive for PP-, PCS-, and PVA-based coating layers and negative for PAD-based coating layers for the aforementioned reasons. The overall best barriers were achieved for PCS- and PVA-based composites with a mixing ratio of 1:1.

The oxygen molecule was the largest permeating non-polar gas compared with the helium atom and the hydrogen molecule, which consequently led to the lowest permeability coefficients (Fig. 9). This is exemplified by the permeability coefficients of the PVA-ref samples. The coefficient for helium was 2.5×10^2 $\frac{cm^3\,(STP)\,1\,\mu m}{m^2\,d\,bar}$, that for hydrogen was 4.9×10^1 $\frac{cm^3\,(STP)\,1\,\mu m}{m^2\,d\,bar}$, and that for oxygen was 1.1×10^{-1} $\frac{cm^3\,(STP)\,1\,\mu m}{m^2\,d\,bar}$. After adding 50 wt% MMT, the coefficients decreased to 5.1 $\frac{cm^3\,(STP)\,1\,\mu m}{m^2\,d\,bar}$ for helium, 1.2 $\frac{cm^3\,(STP)\,1\,\mu m}{m^2\,d\,bar}$ for hydrogen, and 4.2×10^{-3} $\frac{cm^3\,(STP)\,1\,\mu m}{m^2\,d\,bar}$ for oxygen.

Table 6 shows the activation energies for oxygen permeation. The values of E_A showed no substantial changes for PP- and PAD-based polymer matrices when MMT particles were added to the lacquer recipe. For the PCS- and PVA-based composites the values of E_A decreased with increasing MMT content. Hence it is also valid for oxygen that the permeability coefficient decreases with integration of MMT even if the activation energy for permeation decreases. This indicates that even when the energy for permeation along a diffusion path is reduced, the elongation of the diffusion path is the determining factor for the resulting permeability coefficients.

3.8. Water vapor barrier

It is immediately apparent that the trends observed for the non-polar gases differ considerably for water vapor (Fig. 8B). The y-axis is no longer logarithmically scaled. The BIF values are now very low for all polymer matrices, not only for PAD-based coatings. All measured permeability coefficient deviate strongly from the calculated values. For

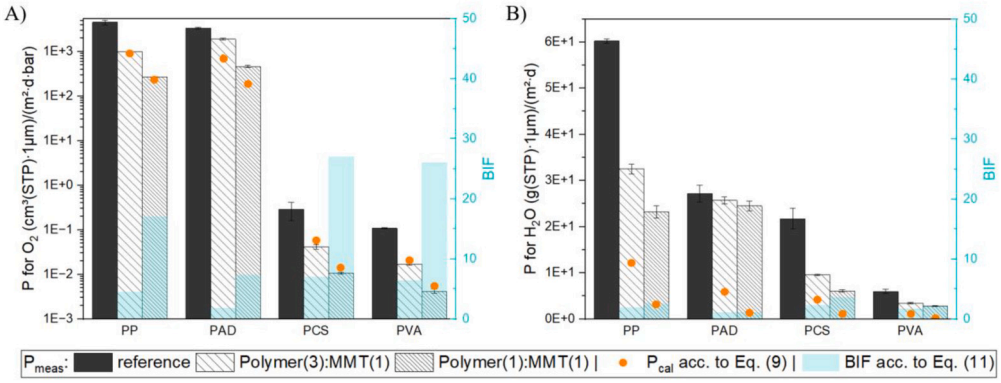

Fig. 8. Oxygen (A) and water vapor (B) permeability coefficients of the coating layers of the four different polymers (PP, PAD, PCS, and PVA) and their composites with mixing ratios of 3:1 and 1:1 with MMT. The measurement conditions for oxygen and water vapor permeability were 23 °C/50 %RH and 23 °C/80 %RH, respectively. The orange dots represent the P_{cal} values according to Eq. (9). The transparent blue bars show the barrier improvement factors ($BIFs$) for the respective mixing ratio according to Eq. (11) (right y-axis).

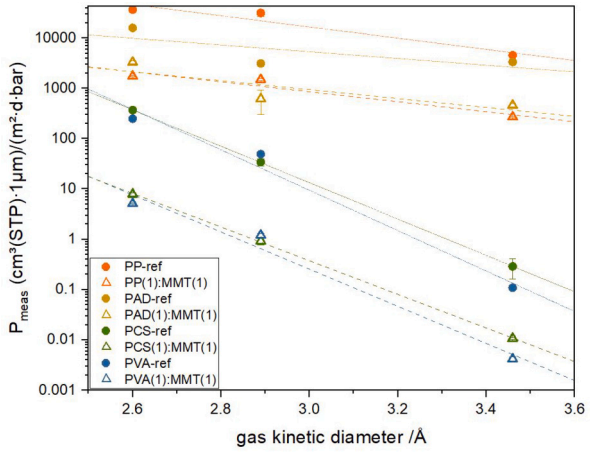

Fig. 9. Permeability coefficients as a function of the gas kinetic diameter for helium (2.60 Å), hydrogen (2.89 Å), and oxygen (3.46 Å). The dotted (reference coatings) and dashed (mixing ratio of 1:1) linear trend lines plotted for the reference and composite coatings, respectively, indicate the correlation between the gas permeability coefficients and gas kinetic diameter.

example, the $BIFs$ of PVA composites with mixing ratios of 3:1 and 1:1 were 6.4 and 26 for oxygen and only 1.9 for water vapor in both cases. Indeed, the measured $BIFs$ for the 3:1 and 1:1 mixing ratios were in the same range for all the matrix materials. This indicates that the permeability of water vapor through composites with MMT are not primarily determined by the tortuosity as is the case for the non-polar gases. The barrier performance of the coating layers against the non-polar gases was additionally supported by changes in the polar matrix, as indicated by the positive deviation values. For water vapor permeation, the BIF values did not differ significantly between the polymer matrices and the values were distinctly lower than expected due to tortuosity. This indicates that even when the particles were distributed homogeneously, which was the case for PP, PCS, and PVA, the possible barrier improvement due to tortuosity was not achieved. Water vapor was the only polar permeant investigated in this study regarding permeability through the composites. MMT also has a high polarity. The similarity of their polarities is one of the reasons why the MMT particles are permeable to the small water molecules (2.65 Å), and the MMT particles might absorb the water molecules. The phenomenon that the absorption of water molecules takes place from MMT particle to MMT particle in the permeation direction was suggested to be called the "polar path effect" by Sankaran et al. [73] and was already described by Nielsen [25]. The permeation of water molecules along these polar paths is assumed to be induced by capillary driving forces next to the concentration gradient [74,75]. Due to its absorption property, the solubility coefficient for water vapor increased in composites when MMT was added to the polymer matrices [76].

The abovementioned permeation mechanism for water vapor, which is not dominated by the tortuous path effect, is the reason why $BIFs$ in silicate-based polymer composites are usually quite low [77,78], as also observed in this study.

4. Conclusion

Composite barrier lacquers based on platelet-shaped MMT and aqueous polymer lacquers were prepared. The polymer matrix materials tested were polypropylene (PP), polyacrylate (PAD), polycarboxylic acid (PCS), and polyvinyl alcohol (PVA). The prepared composite lacquers were coated on PET films and the barrier properties against helium, hydrogen, oxygen, and water vapor were investigated.

The study aimed to investigate the influencing factors for gas and water vapor permeation through the coated films. These factors include the interaction between the polymer matrix and MMT, the orientation of the MMT particles in the coating layer, the change in polymer crystallinity due to its mixing with particles, the permeant type, and the tortuosity. The effect of the tortuosity factor was investigated by comparison of calculated and measured values of permeation, while the calculations were based on the tortuous path theory developed by Nielsen [25].

It was found that the addition of MMT to the aqueous polymers increases the viscosity of the lacquers and adds a shear-thinning property. The shear-thinning effect at shear rates from 3 to 3000 $\frac{1}{s}$ was most pronounced for composites with PVA (reduction of viscosity from 479 to 16.0 mPa s) and PCS (from 680 to 9.39 mPa s), indicating the strongest interaction for those polymer matrices with MMT in the liquid state. For the dried state, it was confirmed via peak shifts in the FTIR spectra that the interaction of MMT and polymer in the form of hydrogen bonds is only apparent for PCS and PVA. These two polymer matrices are indeed the ones in which the orientation of the platelets was more parallel (alignment angle of 10.6 to 14.2°) to the surface in comparison with PP and PAD (alignment angle of 17.7 to 23.2°). For PP- and PAD-based composites, no indication of interaction with MMT was found. Consequently, the barrier properties of PCS- and PVA-based composites outperformed those of the PP- and PAD-based composites. The helium permeability coefficients of the 1:1 mixtures of polymer and MMT for PP and PVA, which are 1.7×10^3 and 5.1 $\frac{cm^3\,(STP)\,1\,\mu m}{m^2\,d\,bar}$, respectively, are given here as examples. These correspond to barrier improvement factors of 21 and 49 for PP and PVA, respectively, when 50 wt% MMT are added to the coating layer. The permeability coefficients were found to be highest for the smallest permeant, the helium. The deviation from

the calculated values was found to be highest for the smallest permeants, helium and hydrogen. The fact that the deviation was found to be positive in the case of PP, PCS, and PVA matrix materials indicates that the addition of MMT not only leads to an elongated diffusion path but also to advantageous changes in the polymer matrix, leading to an even better barrier performance than predicted.

The findings in this study expand the understanding of mechanisms of permeation through composite coating layers and will be of help in developing applications for this technology of wet composite barrier coatings. The coating formulations are to be adapted according to the requirements towards gas barrier, flexibility, sealability, or moisture resistance. The results of this study provide guidelines on how the gas barrier of the coating layer can be improved. If the requirements allow a high MMT concentration (up to 50 wt%), it is advisable to use water-based coatings, which gives the possibility to integrate MMT at higher concentrations. The MMT content has a stronger effect on the barrier of the coating layer than the orientation of the particles. It is also recommended to have polymer matrices with a surface energy of above 50 $\frac{mN}{m}$ (polar content above 20 $\frac{mN}{m}$), as this opens up the possibility of interactions with MMT.

Funding

This work has received funding from the European Union's Horizon 2020 research and innovation program under grant agreement n°862156 FlexFunction2Sustain project.

CRediT authorship contribution statement

Stefan Schiessl: Writing – review & editing, Writing – original draft, Validation, Methodology, Investigation, Data curation, Conceptualization. **Esra Kucukpinar:** Investigation, Funding acquisition, Conceptualization, Methodology, Supervision, Validation, Writing – review & editing. **René Schwiddessen:** Data curation, Investigation, Methodology, Resources, Validation. **Horst-Christian Langowski:** Conceptualization, Methodology, Supervision, Validation, Writing – review & editing. **Peter Eisner:** Conceptualization, Methodology, Supervision, Writing – review & editing.

Declaration of competing interest

The authors declare that they have no known competing financial interests or personal relationships that could have appeared to influence the work reported in this paper.

Data availability

The data presented in this study are available on request from the corresponding author. The data are not publicly available for reasons of confidentiality in the aforementioned EU project, see section "Funding".

Acknowledgements

The authors sincerely thank Ms. Ines Pietsch of BASF, Mr. Hanns Misiak of Henkel, Mr. Samuel Michel of Kuraray, and Mr. Leon Krings of Paramelt, who provided the samples and supported in the form of discussions. Hans Ewender of Fraunhofer IVV is acknowledged for performing the hydrogen barrier measurements. Stephané Cros of CEA Tech is acknowledged for the execution of the helium barrier measurements.

Appendix A. Supplementary material

Supplementary material related to this article can be found online at https://doi.org/10.1016/j.surfcoat.2024.130800.

References

[1] A. Arora, G. Padua, Review: nanocomposites in food packaging, J. Food Sci. 75 (1) (2010) R43–R49, https://doi.org/10.1111/j.1750-3841.2009.01456.x.
[2] M. Manceau, A. Rivaton, J.-L. Gardette, S. Guillerez, N. Lemaître, The mechanism of photo- and thermooxidation of poly(3-hexylthiophene) (P3HT) reconsidered, Polym. Degrad. Stab. 94 (6) (2009) 898–907, https://doi.org/10.1016/j.polymdegradstab.2009.03.005.
[3] K. Choi, S. Nam, Y. Lee, M. Lee, J. Jang, S.J. Kim, Y.J. Jeong, H. Kim, S. Bae, J.-B. Yoo, S.M. Cho, J.-B. Choi, H.K. Chung, J.-H. Ahn, C.E. Park, B.H. Hong, Reduced water vapor transmission rate of graphene gas barrier films for flexible organic field-effect transistors, ACS Nano 9 (6) (2015) 5818–5824, https://doi.org/10.1021/acsnano.5b01161, pMID: 25988910.
[4] M. Muthukumar, N. Rengarajan, B. Velliyangiri, M. Omprakas, C. Rohit, U. Kartheek Raja, The development of fuel cell electric vehicles – a review, Mater. Today Proc. 45 (2021) 1181–1187, https://doi.org/10.1016/j.matpr.2020.03.679, International Conference on Advances in Materials Research - 2019.
[5] M. Mariello, K. Kim, K. Wu, S.P. Lacour, Y. Leterrier, Recent advances in encapsulation of flexible bioelectronic implants: materials, technologies, and characterization methods, Adv. Mater. 34 (34) (2022) 2201129, https://doi.org/10.1002/adma.202201129.
[6] N. Liu, J. Zheng, D.B. Bogy, Thermal flying-height control sliders in hard disk drives filled with air-helium gas mixtures, Appl. Phys. Lett. 95 (21) (2009), https://doi.org/10.1063/1.3268468.
[7] S.-H. Schulze, C. Ehrich, R. Meitzner, M. Pander, Helium permeation as a fast quality indicator for barrier properties of solar cell encapsulates, Prog. Photovolt. 25 (12) (2017) 1051–1058, https://doi.org/10.1002/pip.2922.
[8] F. Herbst, S. Großer, P.C. With, L. Prager, M. Pander, Helium transmission rate as a rapid and reliable method for assessing the water vapour transmission rate of transparent PET-SiOx barrier foils, Packag. Technol. Sci. 34 (8) (2021) 497–504, https://doi.org/10.1002/pts.2576.
[9] K. Miller, J. Krochta, Oxygen and aroma barrier properties of edible films: a review, Trends Food Sci. Technol. 8 (7) (1997) 228–237, https://doi.org/10.1016/S0924-2244(97)01051-0.
[10] C. Charton, N. Schiller, M. Fahland, A. Holländer, A. Wedel, K. Noller, Development of high barrier films on flexible polymer substrates, Thin Solid Films 502 (1) (2006) 99–103, https://doi.org/10.1016/j.tsf.2005.07.253, Selected Papers from the 5th International Conference on Coatings on Glass (ICCG5) - Advanced Coatings on Glass and Plastics for Large-Area or High-Volume Products.
[11] M.A. Priolo, K.M. Holder, T. Guin, J.C. Grunlan, Recent advances in gas barrier thin films via layer-by-layer assembly of polymers and platelets, Macromol. Rapid Commun. 36 (10) (2015) 866–879, https://doi.org/10.1002/marc.201500055.
[12] S. Kiese, E. Kücükpinar, O. Miesbauer, H.-C. Langowski, Time-dependent water vapor permeation through multilayer barrier films: empirical versus theoretical results, Thin Solid Films 672 (2019) 199–205, https://doi.org/10.1016/j.tsf.2019.01.001.
[13] J.G. Acheson, A. McFerran, D. Xu, M. Ziminska, S. Goel, A.B. Lennon, N. Dunne, A.R. Hamilton, Hydrated behavior of multilayer polyelectrolyte-nanoclay coatings on porous materials and demonstration of shape memory effect, Surf. Coat. Technol. 458 (2023) 129335, https://doi.org/10.1016/j.surfcoat.2023.129335.
[14] T. Gulin-Sarfraz, M.S. Grøvlen, E. Rosqvist, M.K. Pettersen, J. Peltonen, J. Sarfraz, Optimized multilayer coating using layer-by-layer assembly method for excellent oxygen barrier of poly(lactic acid) based film, Colloids Surf. A, Physicochem. Eng. Asp. 664 (2023) 131155, https://doi.org/10.1016/j.colsurfa.2023.131155.
[15] B. Tan, N. Thomas, A review of the water barrier properties of polymer/clay and polymer/graphene nanocomposites, J. Membr. Sci. 514 (2016) 595–612, https://doi.org/10.1016/j.memsci.2016.05.026.
[16] S.-L. Bee, M. Abdullah, S.-T. Bee, L.T. Sin, A. Rahmat, Polymer nanocomposites based on silylated-montmorillonite: a review, Prog. Polym. Sci. 85 (2018) 57–82, https://doi.org/10.1016/j.progpolymsci.2018.07.003.
[17] L. Alves, E. Ferraz, J. Gamelas, Composites of nanofibrillated cellulose with clay minerals: a review, Adv. Colloid Interface Sci. 272 (2019) 101994, https://doi.org/10.1016/j.cis.2019.101994.
[18] A. Cabrini, A. Ghalayani Esfahani, A. Petraconi, M. Lavorgna, L. De Nardo, G.G. Buonocore, R.J.E. Andrade, P. Cerruti, Ultrasonic spray deposition of PEGDE-crosslinked chitosan/graphene oxide coatings for enhancing gas barrier properties of polybutylene succinate films, Prog. Org. Coat. 183 (2023) 107760, https://doi.org/10.1016/j.porgcoat.2023.107760.
[19] S. Schiessl, E. Kucukpinar, S. Cros, O. Miesbauer, H.-C. Langowski, P. Eisner, Nanocomposite coatings based on polyvinyl alcohol and montmorillonite for high-barrier food packaging, Front. Nutr. 9 (2022), https://doi.org/10.3389/fnut.2022.790157.
[20] G. Zehetmeyer, R.M.D. Soares, A. Brandelli, R.S. Mauler, R.V.B. Oliveira, Evaluation of polypropylene/montmorillonite nanocomposites as food packaging material, Polym. Bull. 68 (8) (2012) 2199–2217, https://doi.org/10.1007/s00289-012-0722-1.
[21] M. Sirousazar, M. Yari, B.F. Achachlouei, J. Arsalani, Y. Mansoori, Polypropylene/montmorillonite nanocomposites for food packaging, e-Polymers 7 (1) (2007) 027, https://doi.org/10.1515/epoly.2007.7.1.305.
[22] J. Condé-Wolter, M.G. Ruf, A. Liebsch, T. Lebelt, I. Koch, K. Drechsler, M. Gude, Hydrogen permeability of thermoplastic composites and liner systems for future

mobility applications, Composites, Part A, Appl. Sci. Manuf. 167 (2023) 107446, https://doi.org/10.1016/j.compositesa.2023.107446.
[23] S. Schiessl, E. Kucukpinar, N. Rivollier, H.-C. Langowski, P. Eisner, A comparative study on the roll-to-roll processing of a silicate–polyvinyl alcohol composite barrier lacquer using slot-die and reverse gravure coating techniques, Polymers 15 (13) (2023), https://doi.org/10.3390/polym15132761.
[24] S. Matteucci, Y. Yampolskii, B.D. Freeman, I. Pinnau, Transport of Gases and Vapors in Glassy and Rubbery Polymers, John Wiley & Sons, Ltd, 2006, pp. 1–47, Ch. 1.
[25] L.E. Nielsen, Models for the permeability of filled polymer systems, J. Macromol. Sci., Part A, Chem. 1 (1967) 929–942, https://doi.org/10.1080/10601326708053745.
[26] DIN Deutsches Institut für Normung e.V., Paints and varnishes – wettability – part 3: determination of the surface tension of liquids using the pendant drop method (iso 19403-3:2017), DIN EN ISO 19403-3 (April 2020).
[27] D.K. Owens, R. Wendt, Estimation of the surface free energy of polymers, J. Appl. Polym. Sci. 13 (8) (1969) 1741–1747, https://doi.org/10.1002/app.1969.070130815.
[28] DIN Deutsches Institut für Normung e.V., Paints and varnishes – wettability – part 2: determination of the surface free energy of solid surfaces by measuring the contact angle (iso 19403-2:2017), DIN EN ISO 19403-2 (April 2020).
[29] M. Firon, S. Cros, P. Trouslard, Method and device for measurement of permeation, U.S. Patent US2007186622, 2007.
[30] R.M. Barrer, Diffusion in and Through Solids, University Press, 1941.
[31] DIN Deutsches Institut für Normung e.V., Determining the gas transmission rate of plastic film, sheeting and mouldings by the carrier gas method, DIN 53380-3 (June 1998).
[32] DIN Deutsches Institut für Normung e.V., Plastics - film and sheeting - determination of water vapour transmission rate, DIN EN ISO 15106-3 (May 2005).
[33] R.K. Bharadwaj, Modeling the barrier properties of polymer-layered silicate nanocomposites, Macromolecules 34 (26) (2001) 9189–9192, https://doi.org/10.1021/ma010780b.
[34] L. Shen, Z. Chen, Critical review of the impact of tortuosity on diffusion, Chem. Eng. Sci. 62 (2007) 3748–3755, https://doi.org/10.1016/j.ces.2007.03.041.
[35] B. Jańczuk, T. Białopiotrowicz, W. Wójcik, The components of surface tension of liquids and their usefulness in determinations of surface free energy of solids, J. Colloid Interface Sci. 127 (1) (1989) 59–66, https://doi.org/10.1016/0021-9797(89)90007-6.
[36] K. Norrish, The swelling of montmorillonite, Discuss. Faraday Soc. 18 (1954) 120–134, https://doi.org/10.1039/DF9541800120.
[37] A.M. Atta, H.A. Al-Lohedan, Z. Alothman, A.A. Abdel-Khalek, A.M. Tawfeek, Characterization of reactive amphiphilic montmorillonite nanogels and its application for removal of toxic cationic dye and heavy metals water pollutants, J. Ind. Eng. Chem. 31 (2015) 374–384, https://doi.org/10.1016/j.jiec.2015.07.012.
[38] V. Khoshkava, M.R. Kamal, Effect of surface energy on dispersion and mechanical properties of polymer/nanocrystalline cellulose nanocomposites, Biomacromolecules 14 (9) (2013) 3155–3163, https://doi.org/10.1021/bm400784j, pMID: 23927495.
[39] A. Habib, M. Abd-El-Megeed, A. Saafan, R. Issa, The catalytic conversion of n-pentanol to dialkylether by some cation-exchanged montmorillonite catalysts, J. Incl. Phenom. 4 (1986) 185–189, https://doi.org/10.1007/BF00655933.
[40] S. Abend, G. Lagaly, Sol–gel transitions of sodium montmorillonite dispersions, Appl. Clay Sci. 16 (3) (2000) 201–227, https://doi.org/10.1016/S0169-1317(99)00040-X.
[41] R.H. Ellerbrock, A. Höhn, J. Rogasik, Functional analysis of soil organic matter as affected by long-term manurial treatment, Eur. J. Soil Sci. 50 (1) (1999) 65–71, https://doi.org/10.1046/j.1365-2389.1999.00206.x.
[42] A.A. Tireli, I.d.R. Guimarães, J.C.d.S. Terra, R.R. da Silva, M.C. Guerreiro, Fenton-like processes and adsorption using iron oxide-pillared clay with magnetic properties for organic compound mitigation, Environ. Sci. Pollut. Res. 22 (2) (2015) 870–881, https://doi.org/10.1007/s11356-014-2973-x.
[43] V. Krylova, N. Dukštienė, Synthesis and characterization of Ag_2S layers formed on polypropylene, J. Chem. 2013 (2013) 987879, https://doi.org/10.1155/2013/987879.
[44] D. Xiao, D. Chen, Z. Zhou, A. Zhong, Three-group type mechanism in the curing behavior of polyacrylate and blocked toluene diisocyanate, J. Appl. Polym. Sci. 83 (2002) 112–120, https://doi.org/10.1002/app.2233.
[45] D. Liang, C. Du, F. Ma, Y. Shen, K. Wu, J. Zhou, Characterization of nano FeIII-tannic acid modified polyacrylate in controlled-release coated urea by Fourier transform infrared photoacoustic spectroscopy and laser-induced breakdown spectroscopy, Polym. Test. 64 (2017) 101–108, https://doi.org/10.1016/j.polymertesting.2017.09.037.
[46] A.S. Asran, S. Henning, G.H. Michler, Polyvinyl alcohol–collagen–hydroxyapatite biocomposite nanofibrous scaffold: mimicking the key features of natural bone at the nanoscale level, Polymer 51 (4) (2010) 868–876, https://doi.org/10.1016/j.polymer.2009.12.046.
[47] H. Qin, S. Zhang, C. Zhao, M. Feng, M. Yang, Z. Shu, S. Yang, Thermal stability and flammability of polypropylene/montmorillonite composites, Polym. Degrad. Stab. 85 (2) (2004) 807–813, https://doi.org/10.1016/j.polymdegradstab.2004.03.014.
[48] B. Albach, M. Munaro, P.H. Santos, S.F. Zawadzki, W.H. Schreiner, D.S. Rampon, R.V. Barbosa, Thermal, mechanical, and water vapor barrier behavior of polypropylene composite containing modified kaolinite, J. Appl. Polym. Sci. 135 (5) (2018) 45785, https://doi.org/10.1002/app.45785.
[49] N. Bunekar, T.-Y. Tsai, J.-Y. Huang, S.-J. Chen, Investigation of thermal, mechanical and gas barrier properties of polypropylene-modified clay nanocomposites by micro-compounding process, J. Taiwan Inst. Chem. Eng. 88 (2018) 252–260, https://doi.org/10.1016/j.jtice.2018.04.016.
[50] R. Ianchis, L. Cinteza, D. Donescu, C. Petcu, M. Corobea, R. Somoghi, M. Ghiurea, C. Spataru, Implications of silylated montmorillonite on montmorillonite–polyacrylate nanocomposites, Appl. Clay Sci. 52 (1) (2011) 96–103, https://doi.org/10.1016/j.clay.2011.02.004.
[51] B. Smith, Infrared spectroscopy of polymers X: polyacrylates, Spectroscopy 38 (01) (2023) 10–14, https://www.spectroscopyonline.com/view/infrared-spectroscopy-of-polymers-x-polyacrylates.
[52] M.-C. Lai, K.-C. Chang, J.-M. Yeh, S.-J. Liou, M.-F. Hsieh, H.-S. Chang, Advanced environmentally friendly anticorrosive materials prepared from water-based polyacrylate/Na+-MMT clay nanocomposite latexes, Eur. Polym. J. 43 (10) (2007) 4219–4228, https://doi.org/10.1016/j.eurpolymj.2007.05.008.
[53] P. Natkański, P. Kuśtrowski, A. Białas, Z. Piwowarska, M. Michalik, Controlled swelling and adsorption properties of polyacrylate/montmorillonite composites, Mater. Chem. Phys. 136 (2) (2012) 1109–1115, https://doi.org/10.1016/j.matchemphys.2012.08.061.
[54] C. Yu, R. Liao, X. Cai, X. Yu, Sodium polyacrylate modification method to improve the permeant performance of bentonite in chemical resistance, J. Clean. Prod. 213 (2019) 242–250, https://doi.org/10.1016/j.jclepro.2018.12.179.
[55] B. Behera, P.K. Das, Blue- and red-shifting hydrogen bonding: a gas phase FTIR and ab initio study of RR'CO· · ·DCCl3 and RR'S· · ·DCCl3 complexes, J. Phys. Chem. A 122 (18) (2018) 4481–4489, https://doi.org/10.1021/acs.jpca.7b11962, pMID: 29683668.
[56] A. Błoniarz, J. Marchewka, M. Sitarz, K. Drożdż, T. Gosiewski, M. Brzychczy-Włoch, T. Moskalewicz, Effect of adding selected carboxylic acids to the solution on electrophoretic deposition, adhesion strength, morphology and antibacterial properties of chitosan coatings on titanium, Prog. Org. Coat. 189 (2024) 108258, https://doi.org/10.1016/j.porgcoat.2024.108258.
[57] S. Spoljaric, A. Salminen, N. Dang Luong, P. Lahtinen, J. Vartiainen, T. Tammelin, J. Seppälä, Nanofibrillated cellulose, poly(vinyl alcohol), montmorillonite clay hybrid nanocomposites with superior barrier and thermomechanical properties, Polym. Compos. 35 (6) (2014) 1117–1131, https://doi.org/10.1002/pc.22759.
[58] M.A. Mballa Mballa, S.I. Ali, J.P. Heuts, A.M. van Herk, Control of the anisotropic morphology of latex nanocomposites containing single montmorillonite clay particles prepared by conventional and reversible addition-fragmentation chain transfer based emulsion polymerization, Polym. Int. 61 (6) (2012) 861–865, https://doi.org/10.1002/pi.4185.
[59] M.-J. Dumont, A. Reyna-Valencia, J.-P. Emond, M. Bousmina, Barrier properties of polypropylene/organoclay nanocomposites, J. Appl. Polym. Sci. 103 (1) (2007) 618–625, https://doi.org/10.1002/app.25253.
[60] J. Villaluenga, M. Khayet, M. López-Manchado, J. Valentin, B. Seoane, J. Mengual, Gas transport properties of polypropylene/clay composite membranes, Eur. Polym. J. 43 (4) (2007) 1132–1143, https://doi.org/10.1016/j.eurpolymj.2007.01.018.
[61] D. Hu, J. Chen, S. Sun, T. Liu, L. Zhao, Solubility and diffusivity of CO2 in isotactic polypropylene/nanomontmorillonite composites in melt and solid states, Ind. Eng. Chem. Res. 53 (7) (2014) 2673–2683, https://doi.org/10.1021/ie403580x.
[62] D.-S. Chen, G.-H. Hsiue, C.-S. Hsu, Gas permeation through two side-chain liquid-crystalline polyacrylate-based membranes containing 4-methoxyphenyl 4-hexyloxybenzoate or 4-cyanophenyl 4-hexyloxybenzoate mesogenic side groups, Makromol. Chem. 193 (6) (1992) 1469–1479, https://doi.org/10.1002/macp.1992.021930623.
[63] P. Tzeng, E.L. Lugo, G.D. Mai, B.A. Wilhite, J.C. Grunlan, Super hydrogen and helium barrier with polyelectrolyte nanobrick wall thin film, Macromol. Rapid Commun. 36 (1) (2015) 96–101, https://doi.org/10.1002/marc.201400559.
[64] J.M. Herrera-Alonso, Z. Sedláková, E. Marand, Gas transport properties of polyacrylate/clay nanocomposites prepared via emulsion polymerization, J. Membr. Sci. 363 (1) (2010) 48–56, https://doi.org/10.1016/j.memsci.2010.07.014.
[65] J.C. Grunlan, A. Grigorian, C.B. Hamilton, A. Mehrabi, Effect of clay concentration on the oxygen permeability and optical properties of a modified poly(vinyl alcohol), J. Appl. Polym. Sci. 93 (2004) 1102–1109, https://doi.org/10.1002/app.20564.
[66] Y. Song, J. Gerringer, S. Qin, J.C. Grunlan, High oxygen barrier thin film from aqueous polymer/clay slurry, Ind. Eng. Chem. Res. 57 (2018) 6904–6909, https://doi.org/10.1021/acs.iecr.8b01077.
[67] S. Schiessl, P. Eisner, E. Kucukpinar, Gasbarriereschicht, Nanokomposit-Lack zur Erzeugung der Gasbarriereschicht sowie Verfahren zur Herstellung des Lacks, Patent WO23072628 A1, 2023.
[68] C. Habel, E.S. Tsurko, R.L. Timmins, J. Hutschreuther, R. Kunz, D.D. Schuchardt, S. Rosenfeldt, V. Altstädt, J. Breu, Lightweight ultra-high-barrier liners for helium and hydrogen, ACS Nano 14 (6) (2020) 7018–7024, https://doi.org/10.1021/acsnano.0c01633, pMID: 32374585.
[69] H. Kim, W. Choi, S.E. Choi, K. Nomura, J.-W. Kwark, C.J. Ellison, D.W. Kim, Tailored self-assembly of semi-transparent polymer/clay nanocomposites for gas-barrier applications assisted by aqueous liquid crystalline scaffolds, Prog. Org. Coat. 186 (2024) 108003, https://doi.org/10.1016/j.porgcoat.2023.108003.

[70] M.C. Celina, A. Quintana, Oxygen diffusivity and permeation through polymers at elevated temperature, Polymer 150 (2018) 326–342, https://doi.org/10.1016/j.polymer.2018.06.047.

[71] J. Kim, Y. Lin, Synthesis and oxygen permeation properties of ceramic-metal dual-phase membranes, J. Membr. Sci. 167 (1) (2000) 123–133, https://doi.org/10.1016/S0376-7388(99)00273-2.

[72] A.G. Erlat, B.-C. Wang, R.J. Spontak, Y. Tropsha, K.D. Mar, D.B. Montgomery, E.A. Vogler, Morphology and gas barrier properties of thin SiOxcoatings on polycarbonate: correlations with plasma-enhanced chemical vapor deposition conditions, J. Mater. Res. 15 (3) (2000) 704–717, https://doi.org/10.1557/JMR.2000.0103.

[73] K. Sankaran, P. Manoharan, S.R. S, S. Chattopadhyay, A brief insight into the prediction of water vapor transmissibility in highly impermeable hybrid nanocomposites based on bromobutyl/epichlorohydrin rubber blends, Open Chem. 16 (1) (2018) 1207–1213, https://doi.org/10.1515/chem-2018-0124.

[74] S. Kumar, S. Chattopadhyay, A. Sreejesh, S. Nair, G. Unnikrishnan, G.B. Nando, Analysis of air permeability and WVTR characteristics of highly impermeable novel rubber nanocomposite, Mater. Res. Express 2 (2) (2015) 025001, https://doi.org/10.1088/2053-1591/2/2/025001.

[75] J. Li, X. Li, K. Wu, D. Feng, T. Zhang, Y. Zhang, Thickness and stability of water film confined inside nanoslits and nanocapillaries of shale and clay, Int. J. Coal Geol. 179 (2017) 253–268, https://doi.org/10.1016/j.coal.2017.06.008.

[76] D. Murima, H. Pfukwa, I. Tiggelman, P.C. Hartmann, H. Pasch, Novel polymer clay-based nanocomposites: films with remarkable optical and water vapor barrier properties, Macromol. Mater. Eng. 301 (7) (2016) 836–845, https://doi.org/10.1002/mame.201600080.

[77] T.T.T. Ho, T. Zimmermann, S. Ohr, W.R. Caseri, Composites of cationic nanofibrillated cellulose and layered silicates: water vapor barrier and mechanical properties, ACS Appl. Mater. Interfaces 4 (9) (2012) 4832–4840, https://doi.org/10.1021/am3011737, pMID: 22928612.

[78] U.M. Garusinghe, S. Varanasi, V.S. Raghuwanshi, G. Garnier, W. Batchelor, Nanocellulose-montmorillonite composites of low water vapour permeability, Colloids Surf. A, Physicochem. Eng. Asp. 540 (2018) 233–241, https://doi.org/10.1016/j.colsurfa.2018.01.010.

A.4. Unpublished results

Calculation of applied energy via ball milling

Calculation of applied energy E_{app} to MMT according to Garcia et al.[196] for the ball mill used in Section 3.1

$$\begin{aligned} E_{\mathrm{app}} =& \frac{1}{2} \cdot \left(\rho_{\mathrm{b}} \frac{\pi d_{\mathrm{b}}^2}{6} \right) \cdot W_{\mathrm{d}}^2 \cdot \left[\left(\frac{W_{\mathrm{v}}}{W_{\mathrm{d}}} \right)^2 \cdot \left(\frac{D_{\mathrm{v}} - d_{\mathrm{s}}}{2} \right)^2 \cdot \left(1 - 2 \frac{W_{\mathrm{v}}}{W_{\mathrm{d}}} \right) \right. \\ & \left. - R_{\mathrm{d}} \left(\frac{W_{\mathrm{v}}}{W_{\mathrm{d}}} \right) \cdot \left(\frac{D_{\mathrm{v}} - d_{\mathrm{s}}}{2} \right) - \left(\frac{W_{\mathrm{v}}}{W_{\mathrm{d}}} \right)^2 \cdot \left(\frac{D_{\mathrm{v}} - d_{\mathrm{s}}}{2} \right)^2 \right] \end{aligned} \tag{A.1}$$

Table A.1.: List of parameters and values used to calculate the applied energy by the used ball mill in Section 3.1 and the result in the last line.

Parameter	Symbol	Value
Density of zirconium dioxide balls and vial	ρ_{b}	$6.06\,\frac{\mathrm{g}}{\mathrm{cm}^3}$
Diameter of balls	d_{b}	3.0 mm
Diameter of vial	D_{v}	10 cm
Distance between the center of the main disk an the center of the vial	R_{d}	15 cm
Speed of the main disk	W_{v}	400 rpm
Main disk/vial speed ratio	$\frac{W_{\mathrm{v}}}{W_{\mathrm{d}}}$	-0.5495
Applied energy to MMT	E_{app}	$9.1\,\frac{\mathrm{J}}{\mathrm{g}}$

Calculation of volume ratio of weak boundary area

The percentage of the weak boundary area ν_{wb} in a reference volume V_{ref} is calculated as with

$$\nu_{\mathrm{wb}} = \frac{V_{\mathrm{wb}}}{V_{\mathrm{ref}}} \tag{A.2}$$

where V_{wb} is the volume of the weak boundary areas. This volume of the weak boundary area is defined by the distance of the chemical interaction ε, which is in the range from 1 to 10 nm for hydrogen bonds and van der Waals forces given by Ito and Nakashima [224]. Due to the aspect ratio of the MMT particles, the interaction between polymer and MMT mainly takes place on the particle plane, the edges are neglected. Mathematically the MMT platelets are described as cylinders. The volume of the weak boundary area within the reference volume

is therefore

$$V_{\mathrm{wb}} = N_{\mathrm{MMT}} \cdot \pi \cdot \left(\frac{L}{2}\right)^2 \cdot \varepsilon \cdot 2 \tag{A.3}$$

where N_{MMT} is number of MMT particles and L the average length of an MMT particle. The number of MMT particles is calculated via the quotient of MMT volume in the composite layer and the volume for one MMT particle.

$$N_{\mathrm{MMT}} = \frac{V_{\mathrm{MMT}}}{V_{\mathrm{particle}}} = \frac{V_{\mathrm{ref}} \cdot \nu_{\mathrm{MMT}}}{\pi \cdot \left(\frac{L}{2}\right)^2 \cdot W} \tag{A.4}$$

Inserting the Equations A.3 and A.4 into A.2 yields that the volume ratio of the weak boundary areas is only dependent on the value for the interaction distance, the volume ratio of MMT particles, and their thickness W:

$$\nu_{\mathrm{wb}} = \frac{\nu_{\mathrm{MMT}}}{W} \cdot \varepsilon \cdot 2 \tag{A.5}$$

Table A.2.: List of parameters and values used to calculate the volume ratio of the weak boundary area.

ν_{MMT}	W	ε	ν_{wb}
vol%	nm	nm	vol%
30	25	1	2.4
30	25	10	24
7	25	1	0.6
7	25	10	5.6